MULTI-LEVEL MODELLING OF GAS-LIQUID TWO-PHASE FLOW IN A BUBBLE COLUMN

Samenstelling promotiecommissie:

Prof.dr.ir. W.P.M. van Swaaij, voorzitter	Universiteit Twente
Prof.dr.ir. J.A.M. Kuipers, promotor	Universiteit Twente
Dr.ir. N.G. Deen, assistent-promotor	Universiteit Twente
Prof.dr.ing. B.H. Hjertager	Aalborg University Esbjerg
Prof.dr. R.F. Mudde	TU Delft
Prof.dr.ir. M.M.C.G. Warmoeskerken	Universiteit Twente
Prof.dr.ir. G.F. Versteeg	Universiteit Twente
Dr.ir. M.J.V. Goldschmidt	Akzo Nobel

The research in this thesis was financially supported by Akzo Nobel

Omslag: S.J. Timmer

ISBN 90-365-2020-7

Multi-level modelling of gas-liquid two-phase flow in a bubble column

PROEFSCHRIFT

ter verkrijging van
de graad van doctor aan de Universiteit Twente,
op gezag van de rector magnificus,
prof.dr. F.A. van Vught,
volgens besluit van het College van Promoties
in het openbaar te verdedigen
op donderdag 26 februari 2004 om 15.00 uur

door

Esther Iris Viola van den Hengel

geboren op 26 mei 1976

te Tubbergen

Dit proefschrift is goedgekeurd door de promotor

Prof.dr.ir. J.A.M. Kuipers

en de assistent-promotor

Dr.ir. N.G. Deen

Contents

Summary

Bubble columns are used in a variety of industrial processes and are commonly used as gas-liquid reactors. Therefore the design and scale-up of this type of process equipment is of great economic interest. Detailed hydrodynamic models can give insight in the hydrodynamics of bubbly flows occurring in these reactors. Despite the widespread application of bubbly flows and substantial research efforts on their behaviour, detailed knowledge on fluid dynamics is still lacking. The models incorporated for the forces acting on bubbles are usually based on spherical bubbles, while the shape of most bubbles in a column is non-spherical. Due to the increased computer capacity the fundamental modelling of multi-fluid problems have come within reach. In this study effort has been made to develop detailed computer models that can provide detailed information about the hydrodynamics of bubble columns.

In this thesis a 'hierarchy of models' is employed, which consists of a set of three types of CFD models. Each model is used to study specific hydrodynamic phenomena. The models have been validated with experimental data. The results of each model will be shortly presented.

Interface tracking models

Interface tracking models are the most detailed models in the hierarchy of models. To study in detail the time-dependent behaviour of large bubbles in an initially quiescent liquid, 2D volume of fluid (VOF) and 2D and 3D front tracking models have been used. A known drawback of the VOF model is the evaluation of the surface tension force by the continuum surface force model, especially at points where the interface has a strong curvature compared to the computational mesh size. In this thesis a new surface tension model, the tensile force model, has been introduced into the VOF model. With this model is it possible to perform simulations for very small bubbles in an air-water system.
The mentioned interface tracking models were used to determine the forces acting on a bubble, i.e. the drag, lift and virtual mass forces by evaluating the force balance for a

single bubble. The results were compared to relations from literature. The drag coefficients for small bubble diameters (< 2 mm), calculated with the 2D VOF model, are very close to the relations of Tomiyama (1998) and Ishii and Zuber (1979). For larger bubble diameters (> 2 mm) the drag coefficients are very close to the relation of Grace *et al.* (1976). The drag coefficients in the 3D front tracking model for bubbles larger than 7 mm are higher than in the 2D VOF model where the equation for a sphere is used to calculate the drag coefficient. When the equation for a cylinder is used to calculated the drag coefficient for the 2D VOF model, the drag coefficients of the 3D front tracking model and the 2D VOF model are close together.

The virtual mass force was calculated during the acceleration of the bubble. For the 2D VOF model the virtual mass coefficient is about 1.1. For the 3D case the value of the virtual mass force is 0.6. These values for bubbles in 2D and 3D systems are in agreement with literature.

The lift force was studied using a 2D front tracking model. A bubble in a linear shear field does not rise in a straight line, but oscillates in the horizontal direction and moves to one side of the column. An 8 mm bubble moves to the side with the highest slip velocity and a 10 mm bubbles moves to the side with the lowest slip velocity. When using a lower shear rate, the movement of the bubble is smaller. The horizontal velocity and thus the sign of the lift coefficient shows large oscillations due to the oscillating movement of the bubble in the column. The average lift coefficient for a bubble of 8 mm is positive and the average lift coefficient for a bubble of 10 mm is negative. The values are larger than the values reported in literature (Tomiyama, 1998).

Euler-Lagrange model

The next level in the hierarchy of models is the Euler-Lagrange model, also called discrete bubble model (DBM). The DBM was used to investigate the hydrodynamics, coalescence and break-up occurring in bubble columns. The 3D DBM code, originally developed by Delnoij (1999), was extended to incorporate models describing the coalescence and break-up along with a closure model for the turbulence. The model incorporates all relevant forces acting on a bubble in a liquid. The DBM is used to calculate the liquid flow in a square column. The simulation results of the DBM with

closures for the sub-grid stresses were compared to experimental particle image velocimetry (PIV) results.
The calculated liquid velocity and velocity fluctuations of the DBM are overpredicted compared to the PIV results. The difference between the simulation results and the experiments is about 7 %. The differences between the simulations and the PIV results are marginal when using a smaller time step. The influence of a smaller grid size is small.
In the DBM in which the sub-grid scale stresses are not accounted for the liquid velocity and velocity fluctuations are much lower. In this case the effective viscosity is lower due to the absence of the turbulent viscosity. Due to the low viscosity the bubble plume is more spread over the column cross-sectional area and the average velocity profile is flatter. When the turbulence induced by the bubbles is accounted for in the effective viscosity, the bubble plume is less dynamic and the velocity profile is steeper. The incorporation of the sub-grid scale velocity in the evaluation of the force balance has a negligible influence on the results of the model.
When the lift coefficient is changed from 0.3 to 0.5 the results are similar to the results obtained for the case with the bubble induced turbulence.
The best results are obtained when using a time step of $0.5 \cdot 10^{-3}$ s, a grid size of 0.01 m in all directions and a lift coefficient of 0.5.

To investigate the influence of the coalescence and break-up of bubbles, the DBM was extended with the coalescence model of Chesters (1991) and Lee *et al.* (1987) and the break-up model of Luo and Svendsen (1996). The break-up model of Luo and Svendsen (1996) was developed for energy dissipations larger than 0.5 $m^2 s^{-3}$. However, in bubble columns with low gas flow rates and low turbulence intensities the energy dissipation is in the order of 10^{-2} $m^3 s^{-1}$. When these energy dissipations are used in the break-up model, hardly any break-up occurs. In the simulations break-up only occurs in the top of the column, when the energy dissipation exceeding than 10^{-1} $m^3 s^{-1}$ and the diameter of the bubble is large (> 5 mm).
The number of collisions between two bubbles that result in coalescence is 43 % with the coalescence model of Chesters and 85 % with the coalescence model of Lee *et al.* (1987). Most of the coalescence occurs in the lower part of the column. The higher the superficial gas velocity, the more collisions occur and thus the more coalescence takes place.
Due to the fact that hardly any break-up of bubbles occurs, both coalescence models overpredict the mean diameter of the bubbles. The results of the coalescence model of Chesters (1991) combined with the break-up model of Luo and Svendsen (1996) shows the best agreement with experimental results.

Euler-Euler model

In Euler-Euler models the different phases are treated as interpenetrating fluids and the ensemble averaged mass and momentum conservation equations are solved to describe the time-dependent motions of the phases. For the simulations using the Euler-Euler model the commercial code CFX 4.4 was used. Three different Euler-Euler models have been used to describe two-phase flows in bubble columns: A gas-liquid model, a gas-liquid model with the MUSIG model for the gas phase and a gas-gas-liquid model. In all three Euler-Euler models a sub-grid scale model for the sub-grid turbulence is incorporated. The gas phase in the MUSIG model is divided in a number of classes depending on the bubble size. For each class a population balance is used to account for the consequences of break-up and coalescence of bubbles. To study the effect of the different rise velocities of the bubbles a three-phase gas-gas-liquid system is used. The bubbles in the two gas phases have different diameters and different drag relations.
Good agreement was reached comparing the simulation results of the gas-liquid model to the experimental PIV measurements. When using a smaller grid size the liquid velocity and velocity fluctuations are lower, but the differences between the velocity profiles of the case with smaller grid sizes and the standard case are marginal. In the case with a smaller time step the average velocity profile is lower than in the standard case. The velocity fluctuations in the vertical direction are lower, but the difference between the fluctuations in the horizontal direction between the case with smaller time step and the standard case is negligible. When the SGS model is not implemented the liquid velocity and velocity fluctuations are much lower, which is in agreement with the results of DBM.
The default break-up model used in the MUSIG model was that of Luo and Svendsen (1996), the default coalescence model was that of Prince and Blanch (1990). The difference of the velocity and velocity fluctuations between the gas-liquid models with and without MUSIG model is very small. This is as expected, because the MUSIG model combined with the used drag relation does not influence the interface momentum transport. The calculated velocities of the gas-gas-liquid model are lower than for the gas-liquid model. This is due to the presence of the smaller bubbles with a different drag relation. There is very little movement of the bubble plume, as can be concluded from the velocity fluctuations. This is not in agreement with the experimental data.
Simulation results of two different coalescence models, of Prince and Blanch (1990) and Chesters (1991), are compared with simulation results of the DBM with the coalescence model of Chesters (1991) in a square column. In all models the break-up model of Luo and Svendsen (1996) is incorporated. The bubbles in the DBM are the smallest and the

bubble size distribution is the narrowest. The bubbles in the model of Prince and Blanch (1990) are the largest and the bubble size distribution is the widest. As mentioned previously the results of the DBM with the coalescence model of Chesters (1991) and the break-up model of Luo and Svendsen (1996) shows the best agreement with experimental results. The results of the Euler-Euler model with the models of Chesters (1991) and Luo and Svendsen (1996) show the best agreement with the results of the DBM. The bubbles in the Euler-Euler model with the models of Prince and Blanch (1990) and Luo and Svendsen (1996) are too large.

Experiments

A video-imaging technique is used to measure the bubble size distribution and mean diameter in a pseudo 2D lab-scale bubble column. The results of these experiments are used to validate the simulation results of the DBM. In this thesis it is shown that the imaging technique gives valuable information about the bubble size distribution and mean diameter at different flow rates and at different heights in the column. In a column filled with distilled water the bubble size distribution moves to larger diameters, with increasing height because of coalescence of the bubbles. The same trend is observed for increasing flow rates.
When a very small amount of octanol ($2.4 \cdot 10^{-4}$ M) is added to the water, coalescence is inhibited. In this case the mean diameter only shows a weak increase with increasing height in the column due to the decrease in hydrostatic pressure. The mean diameter decreases with increasing flow rate. When the flow rate is higher, more bubbles are present in the column and more turbulence and eddies are generated. The number of collisions between bubbles and eddies is larger. Therefore the chance for breakage of the bubbles is higher and the mean diameter of the bubbles decreases. The bubble size distribution moves to larger diameters with increasing height and moves to smaller diameters with increasing flow rate.

Samenvatting

Bellenkolommen worden in veel industriële processen toegepast en gebruikt als gas-vloeistof reactoren. Daarom is het ontwerp en de scale-up van dit type procesapparatuur van groot economisch belang. Gedetailleerde hydrodynamische modellen kunnen inzicht geven in het hydrodynamische stromingsgedrag van bellen in deze reactoren. Ondanks de veelvuldige toepassing van stromingen met bellen en de aanzienlijke hoeveelheid onderzoek naar het gedrag hiervan, ontbreekt er gedetailleerde kennis over de stromingsdynamica. De modellen voor de beschrijving van de krachten die op bellen werken, zijn gebaseerd op ronde bellen, hoewel de vorm van de meeste bellen in een kolom niet rond is. Door de toenemende computer capaciteit komt de fundamentele modellering van meer-fase systemen binnen bereik. In deze studie is inspanning verricht om gedetailleerde modellen te ontwikkelen, die gedetailleerde informatie over de hydrodynamica van bellenkolommen kunnen geven.

In dit proefschrift wordt het concept van de 'hiërarchie van modellen' toegepast, die bestaat uit een set van drie CFD modellen. Elk model wordt gebruikt om specifieke hydrodynamische verschijnselen te bestuderen. De modellen zijn gevalideerd met experimentele data. De resultaten van elke van deze modellen worden hieronder kort beschreven.

Interface tracking modellen

De 'interface tracking' modellen zijn de meest gedetailleerde modellen in de hiërarchie van modellen. Voor het in detail bestuderen van het tijdsafhankelijke gedrag van grote bellen in een initieel stilstaande vloeistof zijn een 2D 'volume of fluid' (VOF) model en 2D en 3D 'front tracking' modellen gebruikt. Een bekend nadeel van het VOF is de evaluatie van de oppervlaktespanning middels het 'continuum surface force' model, met name bij punten waar het interface een sterke kromming heeft in vergelijking tot de grootte van het grid. In dit proefschrift is een nieuw oppervlaktespanningsmodel in het VOF model geïntroduceerd, het 'tensile force model' Met behulp van dit model is het

mogelijk om simulaties voor zeer kleine bellen in een water-lucht systeem uit te voeren. De genoemde interface tracking modellen zijn gebruikt om de krachten op bellen, d.w.z. de wrijvingskracht, de liftkracht en de kracht ten gevolge van de toevoegde massa van de vloeistof, te bepalen door het evalueren van de krachtenbalans voor een enkele bel. De resultaten zijn vergeleken met relaties uit de literatuur. De waarden van de coëfficiënten van de wrijvingskracht voor kleine bellen (< 2 mm), berekend met het 2D VOF model, komen nauw overeen met de relaties van Tomiyama (1998) en Ishii en Zuber (1979). Voor grotere bellen (> 2 mm) komen de waarden van deze coëfficiënten goed overeen met de relatie van Grace *et al.* (1976). De waarden van weerstandscoëfficiënten in het 3D front tracking model voor bellen groter dan 7 mm zijn hoger dan die van het 2D VOF model, waarbij de vergelijking voor een cirkel werd gebruikt om de weerstandscoëfficiënten te berekenen. Als de vergelijking voor een cylinder wordt gebruikt om de weerstandscoëfficiënten voor het 2D VOF model uit te rekenen, komen de waarden van de weerstandscoëfficiënten voor het 3D front tracking model en het 2D VOF model goed overeen.

De kracht ten gevolge van de toegevoegde massa van de vloeistof werd berekend tijdens de versnelling van de bel. Voor het 2D VOF model is de waarde van de coëfficiënt van deze ongeveer 1.1. Voor 3D front tracking model is de waarde van de coëfficiënt gelijk aan 0.6. Deze waarden komen overeen met waarden uit de literatuur voor 2D en 3D modellen.
De liftkracht werd bestudeerd met behulp van een 2D front tracking model. Een bel in een lineair afschuifveld stijgt niet in een rechte lijn, maar oscilleert in horizontale richting en verplaatst zich naar een kant van de kolom. Een 8 mm bel verplaatst zich naar de kant met de grootste slipsnelheid en een 10 mm bel naar de kant met de kleinste slipsnelheid. Bij een kleinere afschuifsnelheid is de verplaatsing van de bel kleiner. De horizontale snelheid en dus ook het teken van de lift coëfficiënt vertonen grote oscillaties ten gevolge van de oscillaties van de bel in de kolom. De gemiddelde lift coëfficiënt van een bel van 8 mm is positief en de gemiddelde lift coëfficiënt van een bel van 10 mm is negatief. De waarden van deze lift coëfficiënten zijn groter dan de literatuurwaarden (Tomiyama, 1998).

Euler-Lagrange model

Het volgende niveau in de hiërarchie van de modellen is het Euler-Lagrange model, ook wel het discrete bellen model (DBM) genoemd. Het DBM werd gebruikt om de hydrodynamica, coalescentie en het breken van bellen in een bellenkolom te bestuderen. De 3D DBM code, origineel ontwikkeld door Delnoij (1999), werd uitgebreid met modellen die de coalescentie en het breken van bellen beschrijven en er werden sluitingswetten voor de turbulentie in het model geïmplementeerd. Het model bevat vergelijkingen van alle relevante krachten die op bellen in een vloeistof werken. Het DBM is gebruikt om de stroming in een vierkante kolom te berekenen. De resultaten van de simulaties met het DBM, voorzien van een sluitingsmodel voor de sub-grid spanningen, zijn vergeleken met experimentele 'particle image velocimetry' (PIV) resultaten.
De door het DBM gesimuleerde snelheid en de snelheidsfluctuaties zijn hoger dan de PIV resultaten. Het verschil tussen de resultaten van de simulaties en de experimenten is ongeveer 7 %. De verschillen tussen de simulaties en de PIV resultaten zijn marginaal als er een kleinere tijdstap wordt gebruikt. De invloed van een kleiner grid op de resultaten is zeer klein.
In DBM simulaties waarin de sub-grid schaal spanningen niet worden verdisconteerd zijn de snelheid en de snelheidsfluctuaties lager. In dat geval is de effectieve viscositeit in het model lager ten gevolge van de afwezigheid van turbulente viscositeit. Lage viscositeiten geven een grotere verspreiding van de bellenpluim over het oppervlak van de kolom en een meer vlakker gemiddelde snelheidsprofiel. Wanneer de door de bellen geïnduceerde turbulentie middels de effectieve viscositeit wordt meegenomen, leidt dit juist tot een minder dynamische bellenpluim en dientengevolge een spitser snelheidsprofiel. Het verdisconteren van een sub-grid schaal snelheid in de evaluatie van de krachtenbalans blijkt een verwaarloosbare invloed te hebben op de uitkomsten van het model.
Wanneer de coëfficiënt van de liftkracht wordt veranderd van 0,3 naar 0,5 geeft dit gelijke resultaten als bij het gebruik van de door de bellen geïnduceerde turbulentie.
De simulaties geven de beste overeenkomsten met de experimentele data wanneer een tijdstap van $0{,}5 \cdot 10^{-3}$ s, een gridgrootte van 0,01 m in alle richtingen en een liftcoëfficiënt van 0,5 worden gebruikt.

Om de invloed van coalescentie en opbreken van bellen te onderzoeken werd het DBM uitgebreid met de coalescentiemodellen van Chesters (1991) en Lee *et al.* (1987) en het

breekmodel van Luo and Svendsen (1996). Het breekmodel van Luo and Svendsen (1996) werd ontwikkeld voor een energiedissipatie groter dan 0,5 $m^2 s^{-3}$. In bellenkolommen met een lage gas flow snelheden en lage turbulentie is de energiedissipatie echter in de orde van grootte van $10^{-2} m^3 s^{-1}$. Als deze energiedissipaties worden gebruikt in de breekmodellen vindt het breken van bellen nauwelijks plaats. In de simulaties breken de bellen alleen in de top van de kolom als de energiedissipatie groter is dan $10^{-1} m^3 s^{-1}$ en de diameter van de bel groot is (> 5 mm).
Het aantal botsingen tussen twee bellen dat leidt tot coalescentie is 43 % in het coalescentiemodel van Chesters (1991) en 85 % in het coalescentiemodel van Lee *et al.* (1987). De meeste coalescentie vindt plaats in het onderste gedeelte van de kolom. Hoe hoger de superficiële gassnelheid, des te meer botsingen en coalescentie er plaatsvinden.
Doordat het breken van bellen nauwelijks plaatsvindt, leiden deze twee coalescentiemodellen tot een overschatting van de gemiddelde beldiameter. Ondanks deze tekortkoming komen de resultaten van het coalescentiemodel van Chesters (1991) gecombineerd met het breekmodel van Luo en Svendsen (1996) het beste overeen met de experimentele resultaten.

Euler-Euler model

In Euler-Euler modellen worden de fasen behandeld als interpenetrerende fasen. De tijdsafhankelijke bewegingen van de verschillende fasen worden beschreven door het oplossen van de ensemble gemiddelde massa- en impulsvergelijking. Voor de simulaties met het Euler-Euler model is de commerciële code CFX 4.4 gebruikt. Er werden drie verschillende Euler-Euler modellen gebruikt om de twee-fasestroming in een bellenkolom te beschrijven: Een gas-vloeistof model, een gas-vloeistofmodel met het MUSIG model voor de gasfase en een gas-gas-vloeistofmodel. In alle drie modellen is een sub-gridschaal model voor de sub-grid turbulentie geïmplementeerd. In het MUSIG model wordt de gasfase op basis van belgrootte in een aantal klassen opgedeeld. Voor elk van de klassen wordt een populatiebalans bijgehouden welke de gevolgen van het breken en coalesceren van bellen verdisconteerd. Om het effect van verschillende stijgsnelheden van de bellen te bestuderen wordt het driefasemodel gas-gas-vloeistof gebruikt. De bellen in de twee gasfasen hebben verschillende diameters en verschillende relaties voor de wrijvingskracht.

De overeenkomst tussen de simulatieresultaten van het gas-vloeistofmodel en PIV metingen is goed. Wanneer een kleiner grid wordt gebruikt zijn de snelheid en de snelheidsfluctuaties kleiner, maar het verschil tussen het model met een fijner grid en het standaard model is klein. Bij het gebruik van een kleinere tijdstap is de gemiddelde snelheid lager dan in de standaard case. De snelheidsfluctuaties in de verticale richting zijn lager, maar de verschillen tussen de fluctuaties in de horizontale richting voor de standaard case en de case met de kleinere tijdstap zijn verwaarloosbaar. Wanneer het SGS model buiten beschouwing wordt gelaten, zijn de snelheidsprofielen voor de gemiddelde snelheid en de snelheidsfluctuaties beduidend lager, hetgeen in overeenstemming is met de DBM resultaten.
Het standaard breekmodel dat in het MUSIG model wordt gebruikt is het model van Luo and Svendsen (1996), het standaard coalescentiemodel is het model van Prince and Blanch (1990). Het verschil van de snelheid en de snelheidsfluctuaties tussen het gas-vloeistofmodel met en zonder MUSIG is heel klein. Dit is naar verwachting, aangezien het MUSIG model in combinatie met het gebruikte wrijvingskrachtmodel geen gevolgen heeft voor de implusvergelijkingen.
De berekende snelheid van het gas-gas-vloeistofmodel is lager dan voor het gas-vloeistofmodel. Dit is het gevolg van de aanwezigheid van de kleinere bellen met een andere relatie voor de weerstandskracht. Uit de snelheidsfluctuaties kan worden geconcludeerd, dat de bewegingen van de bellenpluim in dit geval klein is, hetgeen niet in overeenstemming is met de experimentele data.
De simulatieresultaten van twee verschillende coalescentiemodellen, van Prince en Blanch (1990) en Chesters (1991), worden vergeleken met simulatieresultaten van het DBM met het coalescentiemodel van Chesters (1991) in een vierkante kolom. In alle modellen is het breekmodel van Luo en Svendsen (1996) geïmplementeerd. De bellen in het DBM zijn het kleinst en de belgrootteverdeling is het smalst. De bellen in het model van Prince en Blanch (1990) zijn het grootst en de belgrootteverdeling is het breedst. Zoals eerder gezegd komen de resultaten van het DBM met het coalescentiemodel van Chesters (1991) en het breekmodel van Luo en Svendsen (1996) het best overeen met de experimentele resultaten. De resultaten van het Euler-Euler model met de modellen van Chesters (1991) en Luo en Svendsen (1996) komen het best overeen met de resultaten van DBM. De bellen in het Euler-Euler model met de modellen van Prince en Blanch (1990) en Luo en Svendsen (1996) zijn te groot.

Experimenten

Om de belgrootteverdeling en de gemiddelde beldiameter in een pseudo 2D bellenkolom te bepalen werd een video-techniek gebruikt. De resultaten van deze experimenten werden gebruikt voor de validatie van het DBM. In dit proefschrift is aangetoond, dat de video-techniek waardevolle informatie geeft over de belgrootteverdeling en de gemiddelde diameter bij verschillende gasstromen en op verschillende hoogtes in de kolom. In gedestilleerd water verplaatst de belgrootteverdeling zich naar grotere diameters bij toenemende hoogte ten gevolge van coalescentie. Hetzelfde effect werd gezien bij toenemende gasstroom.
Als een zeer kleine hoeveelheid octanol ($2.4 \cdot 10^{-4}$ M) aan het water wordt toegevoegd, wordt coalescentie afremd. In dit geval neemt de gemiddelde diameter een klein beetje toe met toenemende hoogte in de kolom ten gevolge van de afnemende hydrostatische druk met toenemende hoogte. De gemiddelde diameter neemt af met toenemende gasstroom. Als de gasstroom groter is, zijn er meer bellen aanwezig in de kolom. Het aantal botsingen tussen bellen en wervels is groter. De breekkans voor de bellen is daardoor ook groter en de gemiddelde beldiameter wordt kleiner. De belgrootteverdeling verschuift naar grotere beldiameters bij toenemende hoogte in de kolom en verschuift dus naar kleinere beldiameters bij toenemende gasstroom.

Chapter 1

GENERAL INTRODUCTION

Abstract

In this chapter a brief introduction to bubbles columns is presented. The hydrodynamics of gas-liquid bubble columns is very complex and despite the widespread application of bubble columns, detailed knowledge on the fluid dynamics is still lacking. Therefore fundamental hydrodynamic models are required to study the fluid dynamics. A 'hierarchy of models' is used which consists of a set of three CFD models. In this thesis each model is used to study specific hydrodynamic phenomena. The flow regimes and the different shapes of the bubbles in a bubble column are described, together with the experimental techniques used in this thesis. In addition the research objectives are presented and the chapter is concluded with an outline of the thesis.

1.1 Bubble Columns

Bubble columns are used in a variety of industrial processes including large-scale production of base chemicals and synthetic fuels. Many processes involve gas-liquid mass transfer with accompanying reactions between the gas and the liquid phase itself or with components dissolved or suspended in it. Bubble columns in industry are operated for a wide range of fluid properties.
Gas-liquid bubble columns offer distinct advantages over other gas-liquid contactors. Two characteristic aspects of bubble columns are their simple construction and the absence of complex (moving) mechanical parts. Therefore the column is easy to construct and maintain. The bubble column is a relatively cheap reactor and can be built in large sizes. The aspect ratio L/d, i.e. the ratio between length and diameter, may vary enormously. Aspect ratios between 3 and 6 are common and a $L/d \approx 10$ is not infrequent. The columns have good heat transfer characteristics, with nearly uniform temperature, even under strong exothermal reaction conditions. Bubble columns work equally well when the gas throughput is high. The high rate of liquid circulation (due to rising gas bubble entrainment) ensures that when any solids such as catalysts are involved they can be uniformly distributed. As the liquid phase has a significantly higher density than the gas phase, the liquid flow rate passing through a bubble column is low and the gas flow rate is the most important parameter. Gas throughput may vary widely according to the methods used and the specified conversion level. The superficial gas is normally in the region of 0.03-0.12 m s^{-1}, although in practice, very high rates in excess of 1 m s^{-1} are also used. The dispersed gas passing upwards through the reactor entrains liquid with it, which then moves downwards again, forming distinctive flow patterns. The bubbles and entrained liquid tend to rise through the centre, the larger bubbles in particular. Therefore a radial gas hold-up and velocity profile results, despite an initial uniform distribution of gas across the whole cross-section of the reactor. Liquid close to the wall moves downwards, transporting smaller bubbles with it for a certain distance. A radial cross-exchange of fluid elements is superimposed on the axial circulation pattern. This gives a high radial mixing, so practically no liquid phase concentration gradients can be found in the radial direction (Deckwer et al, 1992).

Despite the widespread application of bubble columns and substantial research efforts on their behaviour, detailed knowledge on the fluid dynamics is still lacking. Flow phenomena that are difficult to describe are bubble coalescence, bubble break-up and the resulting bubble size distribution in a bubble column as a function of the operating

conditions. From experimental results it can be concluded that these phenomena have a distinct impact on the performance of a gas-liquid bubble column as a chemical reactor, through for instance the interfacial area. To illustrate the difficulties that arise in the prediction of those flows, two very similar gas-liquid systems are shown in Figure 1.1. The only difference is that in one system only distilled water is used and in the other system distilled water with a very small amount of n-octanol. In Figure 1.1 it can be seen that bubbles in distilled water are larger than bubbles in distilled water with octanol. Octanol inhibits coalescence and the smaller bubbles influence the rate of mass transfer.

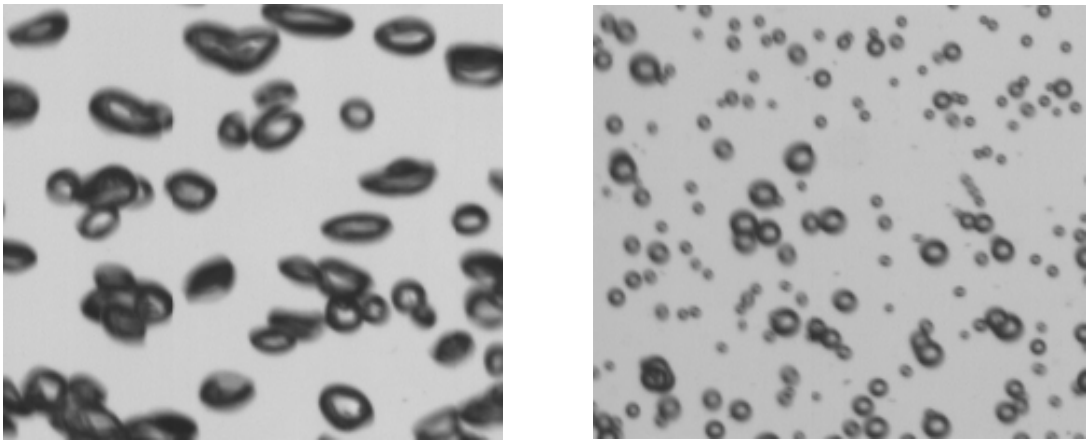

Figure 1.1: Experimental images of bubbles in a bubble column; left: distilled water, right: distilled water and octanol. Superficial gas velocity = 2.78 m s^{-1}.

An advantage of computer models over experiments is the ease at which the different parameters can be varied and the effects can be studied. Experimental programs are very time consuming and the usage of validated computer models can significantly reduce the costs of experimental work. The ongoing developments in computer hardware give the opportunity to develop advanced mathematical models to study the hydrodynamic behaviour of gas-liquid flows in bubble columns. Once these models have been thoroughly validated with experiments, they can be used to study the flow phenomena in bubble columns.

1.2 Hierarchy of models

The gas-liquid flow prevailing in a bubble column is very complex. Because of large differences in time and length scales involved, it seems almost impossible to develop a generalised computational fluid dynamics (CFD) model that accounts for all hydrodynamic phenomena in bubble columns. Therefore a 'hierarchy of models' is employed in which each model is used to study specific hydrodynamic phenomena (Delnoij, 1999), prevailing at a particular scale. The 'hierarchy of models' used in this thesis comprises of three CFD models (Figure 1.2): Interface tracking models, the Euler-Lagrange and the Euler-Euler models. The spatial resolution decreases from $O(10^{-4}$ m) for the interface tracking models to $O(10^{-2})$ for the Euler-Euler models.

In the hierarchy of models information is exchanged between the three levels. The interface tracking models can describe the bubbles in much more detail than the Euler-Lagrange and the Euler-Euler models and require no assumptions and thus no closure relations. The Euler-Lagrange and Euler-Euler models contain unclosed parts, which can be closed by constitutive equations, derived from the results of the interface tracking models. Each of these models will now be briefly introduced.

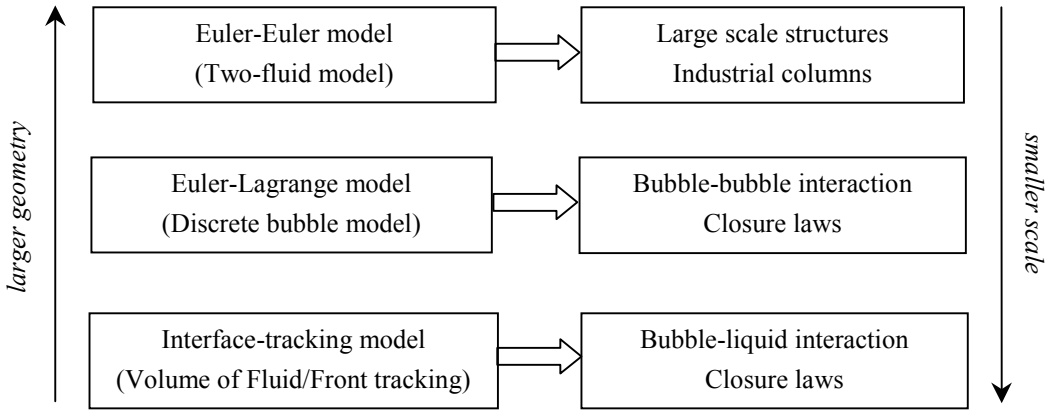

Figure 1.2: Multi-level modelling concept for fundamental hydrodynamic models of gas-liquid bubble columns.

The interface tracking models solve the instantaneous Navier-Stokes equations to obtain the gas and liquid flow field with a very high spatial resolution. The model tracks the motion and deformation of the gas-liquid interface by using an interface tracking scheme. This scheme has to be very accurate to avoid numerical diffusion of the gas-liquid interface and to account for the substantial changes in the interface topology. The interface tracking models do not require any empirical constitutive equations. The number of bubbles that can be simulated simultaneously is limited (<10 bubbles). Different methods can be used for this interface tracking technique. Delnoij (1999) used a volume of fluid (VOF) technique (Youngs, 1982; Rudman, 1997) that tracks the volume of the bubble. Tryggvason *et al*. (2001) used a front tracking technique, which tracks the gas-liquid interface. Sankaranarayanan *et al*. (1999, 2002) implemented a volume tracking technique in the Lattice Boltzmann method.

The Euler-Lagrange model (Sokolichin *et al*., 1997; Delnoij, 1999; Lapin and Lübbert, 1994; Laín *et al*., 2001), also called discrete bubble model (DBM), tracks the individual bubbles by solving the equation of motion for each bubble. The bubble dynamics are described by incorporating the relevant forces acting on a bubble rising in a liquid. To solve the liquid flow field the volume-averaged Navier-Stokes equations are used. The model has a two-way coupling for the exchange of momentum between the gas and liquid phase which may be obtained with the use of interface tracking models. Each individual bubble is tracked in the computational domain accounting for encounters with other bubbles and walls. Therefore it can be used to implement a break-up and coalescence model. The model calculates the break-up or coalescence efficiency and determines whether the bubbles will break, coalesce or bounce.
The Euler-Euler model (Sokolichin *et al*., 1997; Sokolichin and Eigenberger, 1994), also called two-fluid Model, solves the volume averaged mass and momentum conservation equations to describe the time-dependent motions of both the liquid and gas phase. In this model the exchange of momentum through the interface also needs to be modelled. This exchange can consist of several forces, like drag, lift and virtual mass. The equations for the closure of this part of the model are derived using the interface tracking model. For a proper implementation of the break-up and coalescence model the same equations as studied in the Euler-Lagrange model are employed.

1.3 Flow regimes

In literature three different flow regimes encountered in bubble column operations are reported (Figure 1.3). These flow regimes affect the hydrodynamics, transport and mixing properties in the column. When the gas flow rate is low the bubble size distribution is relatively narrow and small, spherical gas bubbles are uniformly distributed in the column. This is known as the homogeneous flow regime. The rise velocity of the bubbles in this regime is about 0.18-0.30 m s^{-1} (Levich, 1962). Liquid up-flow is observed in the wake of the bubbles and liquid down flow in between the bubbles and near the walls. However, this state is not maintained when the superficial gas velocity is higher. In this flow regime, bubbles coalesce and break-up and bubbles of different sizes and shapes can be observed. The larger bubbles rise in the centre of the column and the smaller bubbles are moving along the wall of the column and in the wakes of the larger bubbles. This type of flow regime is known as the heterogeneous regime and commonly used in the industry. The liquid flow field is unsteady and dominated by a variety of vortices and turbulent structures.

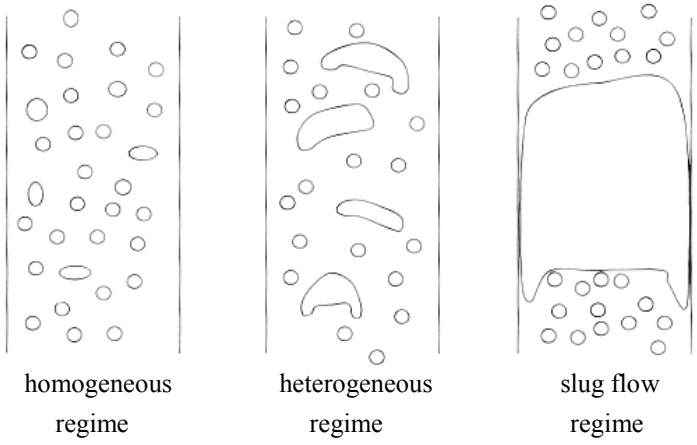

Figure 1.3: Flow regimes observed in gas-liquid bubble columns.

At still high superficial gas velocity and in bubble columns with a diameter smaller than 0.15 m the slug flow regime can be observed. In this regime very large bubbles, the so-called slugs, span the entire cross section of the bubble column. In the operation of bubble columns this slug flow regime is undesirable due to its excessive gas by-pass effect.

In this thesis only the homogeneous and the heterogeneous regime will be considered.

1.4 Experiments

It is very important to validate the results of the aforementioned models. To validate these models experimental data are compared to simulation results.
For the validation of the break-up and coalescence models in both the Euler-Lagrange and Euler-Euler models, information about the bubble size distribution is typically of interest. The bubble size distribution in a bubble column can be measured by imaging techniques and a number of probe techniques. In this thesis an imaging technique is used in a pseudo 2D column to measure the bubble size distribution and the number, volume and Sauter mean diameter. The advantage of the imaging technique is the non-intrusiveness. A disadvantage of this technique is that it can only be applied in pseudo 2D systems at relatively low gas hold-up. Despite this disadvantage the imaging technique is applied in many studies.
It is also important to validate the hydrodynamics predicted by the Euler-Lagrange and Euler-Euler models. The flow in a bubble column can be measured using particle image velocimetry (PIV). PIV is a powerful non-intrusive imaging technique developed in the field of experimental fluid dynamics to study fluid motion using tracer particles. It can be used to measure whole field information of the mean and fluctuating velocities.

1.5 Objective

Detailed knowledge on the fluid dynamics in bubble columns is still lacking. The objective of this work is to develop and improve computational models that describe the time-dependent flow behaviour of gas-liquid flows in bubble columns. The models will be validated with experimental data.
The hierarchy of models concept is used in this work. The detailed models, i.e. interface tracking models and the Euler-Lagrange model, will be used to develop closure laws for the Euler-Euler model.

1.6 Outline

Chapter 2 describes the most detailed level in the ‘hierarchy of models’. In this chapter two interface tracking models, i.e. the volume of fluid model and the front tracking model

are presented. First the fundamentals of the models will be given as well as a description of the numerical techniques. Furthermore the forces acting on a bubble are described. The simulation results of the drag, lift and virtual mass force acting on a bubble are given and discussed.

Chapter 3 deals with the extension of the discrete bubble model, originally developed by Delnoij (1999). The DBM is extended with a LES turbulence model and with models describing the coalescence and break-up of bubbles. The theory of these models will be given and the simulation results will be discussed. The predicted bubble size resulting from the coalescence and break-up models, are compared to experimental data.

In Chapter 4 the Euler-Euler model, used to study the dynamics of large-scale bubble columns, is compared to experimental PIV results. In this model the LES turbulence model is implemented as well as models to describe the bubble size distribution. The simulation results are compared to experimental data.

In Chapter 5 the experimental technique is presented. The video-imaging technique is used to measure the bubble size distribution and mean bubble diameters. This technique is used in a pseudo 2D column. The theory and validation of the technique is described and the results obtained with the technique are presented. These results can, in turn, be used to validate the DBM and Euler-Euler model.

In Chapter 6 the main conclusions of this thesis are presented and recommendations for future work are given.

Chapter 2

VOLUME OF FLUID AND FRONT TRACKING MODEL

Abstract

In this chapter two interface tracking models are presented, i.e. the 2D volume of fluid model and the 2D and 3D front tracking model. These models are used to study the detailed time-dependent behaviour of bubbles rising in a liquid. The models solve the incompressible Navier-Stokes equation on a staggered Cartesian mesh to obtain the flow field. In the Youngs' VOF method the interface is 'tracked' through the Eulerian mesh by reconstruction of the gas-liquid interface from the local liquid fraction data. The calculation of the surface tension force is based on a model, which was adapted from the front tracking technique instead of the frequently used continuum surface force model. The front tracking method uses an unstructured dynamic mesh to represent the interface surface and tracks this interface explicitly by the interconnected marker points. With these models the forces acting on a bubble have been calculated and compared to relations from literature. The drag coefficients in the 2D model agree very well with relations from literature. The drag coefficients for larger bubbles in the 3D model differ from these relations. The agreement between 2D and 3D simulations and literature for the virtual mass coefficient was good. A bubble in a shear field does not rise in a straight line, but oscillates in the horizontal direction and moves to one side of the column. An 8 mm bubble moves to the side with highest slip velocity, a 10 mm bubble moves to the side with the lowest slip velocity. When using a lower shear rate, the movement of the bubble is smaller. Due to the horizontal oscillations, the lift coefficient changes accordingly. The values of the lift coefficient are higher than the values in literature (Tomiyama, 1998). The shape of a bubble of 8 mm is approximately ellipsoidal during the oscillations. The shape of a bubble of 10 mm changes during the oscillations. The bubble is ellipsoidal and during the turn the shape changes to wobbling.

2.1 Introduction

Bubble columns are encountered in a variety of industrial processes and are commonly used as reactors for gas-liquid reactions. Therefore the design and scale-up of these bubble columns is of great economic interest. Gas-liquid bubble columns can operate in several regimes, depending on the superficial gas velocity, the physical properties of the phases and the aspect ratio of the column. In the homogeneous regime the superficial gas velocity is low and the bubbles are small, spherical and of approximately the same size. The heterogeneous regime is the most important regime for industrial bubble columns. In this regime break-up and coalescence of bubbles occurs. Due to bubble break-up and coalescence bubbles of widely varying size and shape can be observed. This regime is characterised by intermediate gas velocities and the liquid flow field is characterised by inherent unsteadiness and dominated by a variety of vortical and turbulent structures. The larger bubbles in this regime are important because of their significant impact on the contact between gas and liquid and thus on the overall performance of the bubble column as a chemical reactor. The fundamental knowledge regarding the hydrodynamics of bubble column operation in the heterogeneous regime is still lacking.
Due to the increased computer capacity the fundamental modelling of multi-fluid problems have come within reach. Significant research effort has been made to develop detailed computer models that can provide detailed information about the hydrodynamics of bubble columns.

2.2 Shapes of the bubbles

The shape of the bubble is dependent on the properties of the liquid and the gas. Grace (1973) and Grace *et al*. (1976) presented a diagram, which shows the (experimentally determined) effect of fluid properties and the bubble diameter on the shape and the terminal rise velocity of a single bubble. This so-called Grace diagram is reproduced in Figure 2.1. Three dimensionless numbers, which are related to each other, are presented in this diagram, i.e. the Reynolds number (the ratio of the inertial to the viscous force), the Eötvos number (the ratio of gravity to surface tension force) and the Morton number (combination of the properties of the liquid and the gas phase).

$$\mathrm{Re} = \frac{\rho_l v_B d_B}{\mu_l} \tag{2. 1}$$

$$\mathrm{Eo} = \frac{g d_B^2 \left(\rho_l - \rho_g\right)}{\sigma} \tag{2. 2}$$

$$\mathrm{M} = \frac{\mathrm{g}\mu_l^4 \left(\rho_l - \rho_g\right)}{\rho_l^2 \sigma^3} \tag{2. 3}$$

Another dimensionless number, that gives the ratio of inertial to surface tension force, is the Weber number. This number is a function of the Reynolds, Eötvos and Morton number.

$$\mathrm{We} = \frac{\mathrm{Re}^2 \mathrm{M}^{1/2}}{\mathrm{Eo}^{1/2}} = \frac{\rho_l v_B^2 d_B}{\sigma} \tag{2. 4}$$

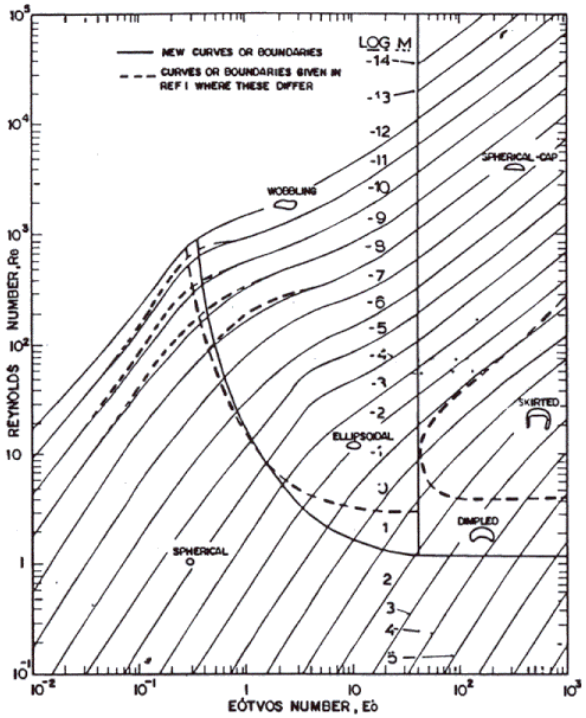

Figure 2.1: Graphical correlation by Grace (1973) and Grace *et al*. (1976).

The Grace diagram contains three main regimes in which the bubbles have different shapes: The spherical, ellipsoidal and spherical-cap regime. The boundaries between the

spherical-cap regime and the other two regimes are relatively well defined. The spherical-cap regime consists of three sub-regimes: Spherical-cap, skirted and dimpled. The ellipsoidal regime consists of two sub-regimes: Wobbling and ellipsoidal. Bubbles are spherical at low Re, no matter how large the value of Eo. It is more difficult to distinguish clearly between the spherical and ellipsoidal regime. This arises partly because of a lack of data, but also because the amount of eccentricity, which can be tolerated before a bubble is considered ellipsoidal, is arbitrary. A further complication is that bubble deformation is affected somewhat by the amount of surface-active species present. The boundary in the diagram in somewhat arbitrary, but is thought to give a reasonable estimate in case the ratio of minor to major semi-axis is about 0.9 (Grace, 1973).

2.3 Interface tracking methods

Interface tracking methods can be divided into front tracking and volume tracking models. Rider and Kothe (1995) gave a good overview of the different tracking methods. In this section a brief overview of the latest developments is given.

To indicate the location of the interface in the front tracking methods an unstructured mesh is generated at the gas-liquid interface. The interface consists of elements, usually a connected set of points or triangles to form a continuous moving surface (Unverdi and Tryggvason, 1992; Tryggvason *et al*., 2001). The calculation of the interface in front tracking methods is very accurate. A disadvantage is that the volume of the bubble is not intrinsically conserved. Front tracking methods are very complex, because of the interaction between the moving boundary and the Eulerian mesh employed to solve the flow field. Front tracking is best suited for well-defined fronts that are easily identifiable in the initial conditions.

Volume tracking methods track the motion of the volume of both fluids separated by an interface and not the motion of the interface itself. The motion of the interface is tracked indirectly through the motion of the fluids. Volume tracking methods are popular, because they are reasonably accurate and generally relatively simple to implement. In these methods a marker particle or marker function, used to reconstruct the interface, is advected with the flow. Examples of volume tracking models are shock capturing methods, level set methods, marker particle methods and volume of fluid methods.

Shock capturing methods discretise the transport equation of the liquid using a high order (usually second order) shock-capturing scheme. These methods work less well for the sharp discontinuities generally encountered in multiphase flows. They require a relatively fine grid to obtain accurate solutions. Rider and Kothe (1995) used a high order Godunov method and evaluated this method by several numerical tests. They concluded that in all cases the use of shock capturing methods was inadequate.

Ida (2000, 2003) proposed an improved unified solver for compressible and incompressible fluids involving free surfaces, based on the CIP-CUP (Cubic Interpolated Propagation/Combined Unified Procedure) method, by adapting several improvements and modifications. This is a pressure-based semi-implicit solver for the Euler equations. Ida (2000) proposed an improved scheme for the convection terms in the equations. Ida (2003) adapted the multi-time step integration technique, which makes the determination of the time interval very flexible. High accuracy and excellent robustness of the improved methods have been demonstrated.

Numerical diffusion generated near discontinuities by high-resolution shock-capturing schemes is often too excessive for interface tracking. Level set methods are designed to minimise the numerical diffusion. These methods draw upon existing advection algorithms, but employ them in a manner that minimises the problematic diffusion. Fundamental to the level set approach is the definition of the interface as the zero level set of a distance function from that interface. The advection of this distance function evolves through the solution of the transport equation of the liquid fraction. Level set methods are conceptually simple and relatively easy to implement. In case of simple flows these methods give accurate results. When the interface is significantly deformed or with appreciable vorticity in the flow field, level set methods suffer from severe loss of mass and thus loss of accuracy.

Marker particle methods are perhaps the simplest volume tracking methods. They use marker particles that are assigned an identity (‘colour’) based on the fluid in which they reside. The marker particles are pegged to the particular fluid and their motion is tracked in time. The instantaneous positions of the marker particles are used to derive the relevant Eulerian fluid properties and the position of the gas-liquid interface. Marker particle methods are extremely accurate and robust, but they are complex and expensive (in terms of CPU time and storage). These complexities arise when the interface stretches

considerably. This requires additional marker particles, which have to be generated during the computation.

In the VOF methods a fractional volume or marker 'colour' function is defined that indicates the fraction of the liquid in mesh cell and thus the gas-liquid interface. This marker function is advected by the flow. Several different interfaces might correspond to the field of liquid fractions. To calculate the interface configuration from these fractions an interface orientation is assumed. The interface is represented as a straight line that truncates the cell with a volume equal to the liquid fraction in that cell. A number of different techniques have been proposed that differ in their assumptions about this interface geometry. The better known volume advection methods are the simplified line interface calculation (SLIC) method of Noh and Woodward (1976) and the donor-acceptor algorithm published by Hirt and Nichols (1981). Youngs (1982) significantly improved the VOF methods by allowing a multi-dimensional and piecewise linear interfaced geometry. The Youngs' algorithm and its extension (Pilliod, 1992) is referred to as the PLIC (piecewise linear interface calculation) algorithm. The PLIC method has been improved considerably since its introduction including second-order reconstruction and unsplit advection. The accuracy and capability of these modern PLIC VOF algorithms greatly exceeds that of the older VOF algorithms such as Hirt and Nichols (Kothe and Rider, 1995a and 1995b, Rider *et al*., 1995, Rider and Kothe, 1995, Rudman, 1997). PLIC methods have inherent mass conservation and can be made to rigorously conserve mass. A negative point is that these methods exhibit strong numerical surface tension when a body becomes too thin for the mesh it resides on.

Shahbazi *et al*. (2003) presented a second order accurate piecewise linear volume tracking based on remapping for triangular meshes. This approach avoids the complexity of extending unsplit second order volume of fluid algorithms on triangular meshes. The method is based on Lagrangian-Euler methods. The details of the normal line finding are given for two methods: Differential least squares (DLS), which has a first order accuracy and geometric least squares (GLS), which had a second order accuracy. GLS is superior to the DLS method in both error values and convergence rate. However, the volume is not conserved.
Sussman and Puckett (2000) and Sussman (2003) developed a coupled level set/volume of fluid (CLSVOF) method for representing the free surface in two-phase flow problems. This method combines some of the advantages of the volume of fluid method with the level set method to obtain a method, which is generally superior to either of the

individual methods. They tested the CLSVOF method on two-dimensional, axi-symmetric and fully three-dimensional flows and for all problems the CLSVOF method produces results that are as good as or better than those produced by the individual methods. The CLSVOF method conserves mass as well as or better than the level set method while retaining the advantage of the simpler, and probably more accurate, method of computing surface tension that characterise level set methods. For problems with surface tension the CLSVOF method is generally superior to the VOF methods.

Ginzburg and Wittum (2001) developed a two-phase 2D model that combines the VOF method with implicit staggered finite volume discretisation of the Navier-Stokes equation. This model adaptively refines the interface or produces a grid that is aligned with it. In computations with the interface aligned grids, the jumps of the pressure and the continuity of the viscous stresses are kept on the front. The surface tension force on cubic spline aligned grids is accurately computed and the parasite currents disappear when the interface is represented as a true circle. Although the current representation of the interface is based on the VOF method, on regular grid, the model can work with other front descriptions. One can reconstruct the zero level set from the level set function provided by the level set approach.

The main progress witnessed over the past years is the advent of many three-dimensional calculations for volume tracking techniques (Scardovelli and Zaleski, 1999; Gunsing et al, 2004). At the moment two-dimensional calculations produce either highly accurate results or calculations over impressively large grids. The level set method seems attractive due to its simplicity but has not yet produced the wide range of results, especially in three-dimensions, achieved by the older methods. The VOF method has been considerably improved by the systematic use in the scientific literature of the higher order piecewise linear calculation method. For engineering applications new methods need to be developed that could adapt to complex geometries.

To study the time-dependent behaviour of the larger bubbles in a fundamental way, the 2D volume of fluid model (Youngs, 1982; Rudman, 1997) and the 2D and 3D front tracking models (Unverdi and Tryggvason, 1992) are used in this work. The VOF model is used to study the forces acting on bubbles, i.e. the drag and virtual mass force in more detail in a 2D model. The lift force is studied using a 2D front tracking model. The results of the drag and virtual mass coefficient of the 2D VOF model are compared to results of the 3D front tracking model to study the 3D effects.

The 2D VOF model resolves the time-dependent motion of the gas and liquid phases and of the interface between the two phases. This finite difference model is robust, accurate and has a very good mass conservation. The VOF model is able to account for substantial changes in the topology of the gas-liquid interface induced by the relative liquid motion due to its advanced interface tracking scheme.
One of the main advantages of the front tracking model is the accurate calculation of the interface, which has significant effect on the bubble shape and bubble dynamics. A disadvantage of the Front Tracking model is that the volume of the bubble is not intrinsically conserved. The bubble volume slowly changes in time, due to the method used to move the interface and the re-meshing of the interface mesh.

In this chapter the existing numerical approaches to interface tracking will be reviewed and the Youngs' VOF model and the Front Tracking model will be described in detail. A known drawback of the Youngs' VOF model is the poor calculation of the surface tension force by the continuum surface force model (Brackbill *et al*., 1992), especially at points where the interface has a strong curvature compared to the computational mess size. In this chapter a new surface tension model, the tensile force model, will be introduced into the model.

2.4 Volume of fluid model

The 2D volume of fluid model, described in this chapter, resolves the time-dependent motion of the gas and liquid phases and of the interface separating the two phases. In this chapter the 2D Youngs' VOF model, developed at the University of Twente (Delnoij, 1999), will be described. With this model the velocity of a rising bubble in horizontal and vertical direction can be determined. The velocity can be used to describe the forces acting on a bubble rising in a liquid. For spherical bubbles it is relatively simple to calculate the forces exerted by the liquid on the bubble. For non-spherical bubbles it is more complicated to calculate these forces.

The VOF model used in this thesis consists of two coupled parts: A part that 'tracks' the liquid volume through the Eulerian mesh and a part that solves the gas and liquid flow field. The model describes the hydrodynamics of the gas-liquid flow based on a single set of conservation equations for mass and momentum. A 'colour' function is used to identify the gas and liquid phases. Each of these parts will now be introduced.

2.4.1 Gas-liquid interface

The VOF model defines a volume fraction or 'colour' function F, which specifies the liquid volume fraction in the computational cell. Only for $0<F<1$ the grid cell contains a gas-liquid interface. Within one cell only one interface segment is permitted. Cells without interfaces have a volume fraction F equal to zero (gas) or unity (liquid).

The motion of the liquid and thus of the interface can be calculated by solving the incompressible equation for the F-transport:

$$\frac{DF}{Dt} = \frac{\partial F}{\partial t} + \mathbf{u} \cdot \nabla F = 0 \tag{2. 5}$$

The value of F at the new time level is related to its value at the previous time level and to the fluxes of F through the four cell faces by the finite difference approximation of this equation. In order to maintain the rigidity of the interface the calculation of the convective fluxes needs to be done with great care. The reconstruction of the interface is done according to the Youngs' method also referred to as the PLIC VOF method (Youngs, 1982). This method is relatively easy to implement, very accurate and has a very good inherent volume (mass) conservation, especially in flow fields with considerable spatial and temporal variations. The method is robust and able to account for significant changes in the topology of the gas-liquid interface, and implicitly accounts for mergers between different interfaces or between different parts of the same interface.
The model used is derived from the method published by Rudman (1997) and implemented by Delnoij (1999). This model is preferred because of its relatively simple implementation compared to higher order methods (Zaleski, 1999) and because of its superior performance compared to the classical model proposed by Hirt and Nichols (1981). Good overviews of the accuracy of the different VOF methods are given by Rudman (1997) and Zaleski (1999).
Exact interface locations are not known, at any time in the solution, i.e. a given distribution of volume data does not guarantee a unique interface. Youngs' VOF method approximates the interface within a cell by a straight-line segment with a slope determined from the interface normal **n**. The number of possible interface element types needed to reconstruct the interface in a two-dimensional case is equal to 4. This gives 16 possible interface configurations, based on the orientation of the interface normal with

respect to the co-ordinate axis. In the figure below the 4 possible interface elements are shown. Rotating these 4 figures gives 16 possible configurations.
To reconstruct the interface of a computational cell first the normal **n** to the interface of that cell has to be calculated. In the two-dimensional case this normal **n** is calculated from the gradient of the liquid fraction of the computational cell itself and the eight surrounding cells, resulting in a nine-point stencil. From the normal **n** and the liquid fraction F the interface is reconstructed. The interface cuts the computational cell (i,j) in such a way that the fractional volume of the liquid in the cell is equal to $F_{i,j}$.

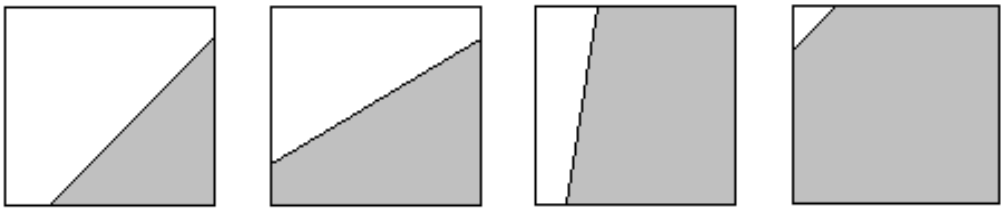

Figure 2.2: Possible configurations of the gas-liquid interface in a cell.

Once the interface orientation and the velocities on the cell boundaries are known the four side fractions of the cell containing an interface are calculated. With the use of these side fractions, the fluxes through the four cell faces can be calculated. From these fluxes the liquid fraction F at the new time step can be calculated and at the new time step the flow field is solved again. The fluxes through the cell faces of cells that do not contain a gas-liquid interface are calculated using second order accurate the Barton scheme (Centrella and Wilson, 1984; Hawley *et al*., 1984).

2.4.2 Mass and momentum equations

To solve the flow field a one-fluid approach is used with local density and viscosity variation to account for the different phases. The conservation equations for mass and momentum for an incompressible fluid are given as follows:

$$\nabla \cdot \mathbf{u} = 0 \tag{2. 6}$$

$$\frac{\partial \rho \mathbf{u}}{\partial t} + \nabla \cdot \rho \mathbf{u}\mathbf{u} = -\nabla P + \nabla \cdot \mu \left((\nabla \mathbf{u}) + (\nabla \mathbf{u})^T \right) + \rho \mathbf{g} + \mathbf{F}_{SF} \tag{2. 7}$$

in which $\mathbf{F}_{SF}$ is the surface tension force, which only acts in the vicinity of the interface.

Often (Rudman, 1998) simple linear weighing is used to calculate the local density and viscosity as a function of the liquid fraction *F*:

$$\rho = F \cdot \rho_l + (1 - F) \cdot \rho_g \tag{2. 8}$$

$$\mu = F \cdot \mu_l + (1 - F) \cdot \mu_g \tag{2. 9}$$

Prosperetti (2001) derived another equation to calculate the viscosity. He showed that the flow along the gas-liquid interface can be considered analogous to an electrical current with two parallel resistances. When the Reynolds number is not too small, at an interface, normal viscous stresses are usually negligible in comparison with pressure and surface tension effects. With the neglect of normal viscous stresses and surface tension, the pressure (the analogue of voltage) is equal on both sides of the interface. The two phases (analogous to current) flow in parallel along the interface under the action of the same pressure gradient. Thus the total resistance is a combination of two resistances in parallel, which results in:

$$\frac{\rho}{\mu} = F \frac{\rho_l}{\mu_l} + F \frac{\rho_g}{\mu_g} \tag{2. 10}$$

2.4.3 Surface tension force

Continuum surface force model

In many VOF models (Rudman, 1997; Delnoij, 1999) the surface tension force $\mathbf{F}_{SF}$ in equation 2.7 is computed using the continuum surface force (CSF) model of Brackbill

et al. (1992). This model interprets surface tension as a continuous, three-dimensional effect across an interface, rather than a boundary value condition on the interface.

In the CSF model the surface force per unit interfacial area can be written as:

$$\mathbf{F}_{SF} = 2 \cdot F \cdot \sigma \cdot \kappa \cdot \mathbf{n} \tag{2. 11}$$

in which σ is the surface tension force, κ is the curvature and $\mathbf{n}$ is the normal to the interface given by:

$$\mathbf{n} = \nabla F \tag{2. 12}$$

The volumetric surface tension force $\mathbf{F}_{SF}$ is calculated at cell centres and interpolated to the cell faces.

The local surface curvature κ is given by:

$$\kappa = -\left(\nabla \cdot \tilde{\mathbf{n}}\right) = \frac{1}{|\mathbf{n}|}\left[\left(\frac{\mathbf{n}}{|\mathbf{n}|} \cdot \nabla\right)|\mathbf{n}| - \left(\nabla \cdot \mathbf{n}\right)\right] \tag{2. 13}$$

in which $\tilde{\mathbf{n}}$ is the unit normal at the gas-liquid interface.

The implementation of the CSF model in the Youngs' VOF model, including wall adhesion, is similar to the implementation followed by Kothe *et al*. (1991) in their RIPPLE code. The surface curvature κ is calculated at the cell centres and the normal vector $\mathbf{n}$ is calculated at the cell vertices.

The CSF model uses a nine-point stencil to calculate the normal $\mathbf{n}$ to the interface as well as the derivatives of the normal, $\nabla\mathbf{n}$. Both are used for the calculation of the surface curvature, which is needed to calculate the surface tension force. The derivatives of the normal make the model sensitive to numerical errors in the liquid fraction field. Therefore the curvature can only be calculated accurately if the curvature is relatively small compared to the mesh size.
The errors in the surface tension force calculation, due to the calculation of the derivatives of the normal and the curvature from this normal, cause the presence of

unavoidable 'parasite currents' (Rudman, 1998). Figure 2.3 shows the simulation result of the VOF model with a 4 mm air bubble positioned in water under zero gravity conditions (Eo = 2.15 and M = $2.52 \cdot 10^{-11}$) and the simulation result of Lafaurie *et al*. (1994). In both cases the bubble is surrounded by a small amplitude velocity field having a four-fold symmetry of lattice. These 'parasite currents' are due to the slight unbalance between the stresses at the sites in the interfacial region (Lafaurie *et al*., 1994).

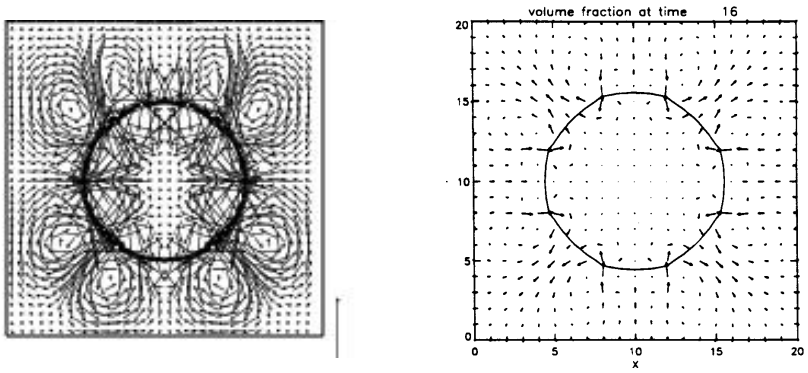

Figure 2.3: Parasite currents in bubble simulations. Left: simulation of 4 mm bubble; right: simulation by Lafaurie *et al*. (1994). Reference vector with length comparable to 0.10 m s^{-1}.

Tensile force model

In this thesis, a new surface tension model, inspired by the model used by Bunner and Tryggvason (1997) in their front tracking codes, is used. This model avoids the calculation of the derivative of the normal **n**. The new model calculates the surface tension force on the edge of the surface elements using the normal vectors to the adjacent surface elements. This enables an accurate computation of the surface tension force over a large range of curvatures. This method produces significantly smaller parasite currents.

In this tensile force model the surface tension force is directly calculated from the interfacial tensile forces acting on the interface segment in the computational cell by the interface segments of the adjacent cells. The model uses the orientation of the interface in the computational cell and the four side fractions. When a cell contains an interface two of the four side fractions of that cell are unequal to zero. Once these side fractions are known, the starting and end point (point 1 and 2) of the interface segment in the cell are known (see Figure 2.4).

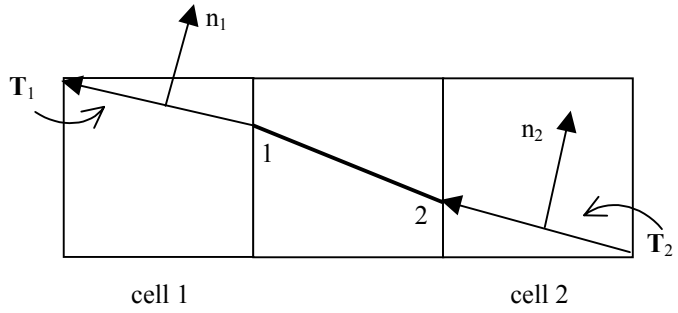

Figure 2.4: Start and end point of interface segment in cell.

At points 1 and 2 the tensile forces $\mathbf{T}_1$ and $\mathbf{T}_2$ in the directions $\mathbf{t}_1$ and $\mathbf{t}_2$ are acting on the interface segment in the computational cell by the interface segments of the adjacent cells, where $\mathbf{t}_1$ and $\mathbf{t}_2$ are the tangential unit vectors of the adjacent cells defined by the two interface segments of the adjacent cells.

The force exerted on the interface segment between the points 1 and 2 is calculated by:

$$\mathbf{F}_{1-2} = \sigma \cdot (\mathbf{t}_1 - \mathbf{t}_2) \cdot l_{\perp} \tag{2. 14}$$

with $l_{\perp}$ the length perpendicular to the x,y-surface.
The x- and y-components of the force are calculated at the centres of the interface segment in the cell. They can be subsequently distributed to the cell centres or the Peskin function (Peskin, 1977) can be used for the distribution. In the simulations in this work the Peskin function (Peskin, 1977) is used.

Peskin function

The x- and y-components of the surface tension force can be distributed to the Eulerian nodes with the use of an area-weighed technique or the method developed by Peskin (1977). The last method is used to avoid instabilities due to steep gradients near the interface.
When using the Peskin method the surface tension force is smoothed. This smoothed surface tension force $\overline{\mathbf{F}}_{SF}$ is computed from the following expression:

$$\overline{\mathbf{F}}_{SF} = \sum D(\mathbf{x} - \overline{\mathbf{x}})\mathbf{F}_{SF} \tag{2. 15}$$

where the smoothing function $D(\mathbf{x} - \overline{\mathbf{x}})$ is an integrated version of the one given by Peskin (1977):

$$D(\mathbf{x} - \overline{\mathbf{x}}) = \frac{1}{2nh}\left[1 + \cos\left(\frac{\pi}{nh}(\mathbf{x} - \overline{\mathbf{x}})\right)\right] \tag{2. 16}$$

in which *2n* is the number of grid cells over which the Peskin function is smoothed, **x** is the position of the data which will be smoothed, $\overline{\mathbf{x}}$ is the centre of the distribution function and *h* is the grid spacing in the particular direction.

The function used in the VOF model uses an integrated version of equation 2.16:

$$D(\mathbf{x} - \overline{\mathbf{x}}) = \frac{1}{2h}\left[\mathbf{x}_j - \mathbf{x}_i + \frac{nh}{\pi}\left(\sin\left(\frac{\pi}{nh}(\mathbf{x}_j - \overline{\mathbf{x}})\right) - \sin\left(\frac{\pi}{nh}(\mathbf{x}_i - \overline{\mathbf{x}})\right)\right)\right] \tag{2. 17}$$

where $\mathbf{x}_i$ and $\mathbf{x}_j$ are the boundaries of the integration step.

Comparison of the two models

A first check on the performance of the tensile force model is the reduction of the 'parasite currents'. In the CSF model these 'parasite currents' are computed for a 4 mm air bubble positioned in water under zero gravity conditions (Figure 2.3).
In Figure 2.5 a simulation result with the tensile force model is the same case. The 'parasite currents' are reduced when using the tensile force model, as can be seen in Figure 2.5. The asymmetric parasite currents in the right figure can probably be caused by round off or break off errors.

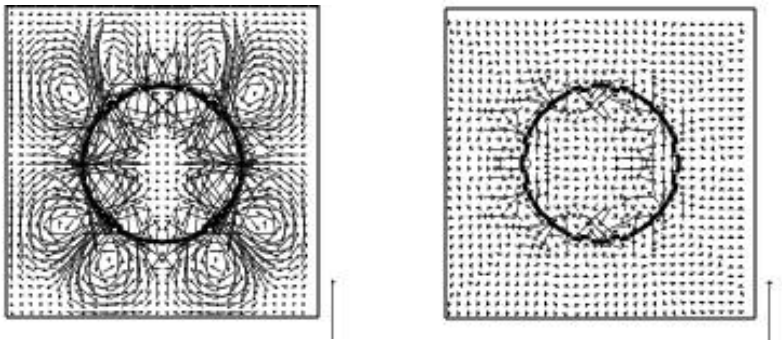

Figure 2.5: Simulation results of bubble simulation of 4 mm. Left: continuum surface force model; right: tensile force model. Reference vector with length comparable to 0.10 m s^{-1}.

Another check has been carried out by comparing the tensile force model simulation results for the excess pressure inside a bubble to the analytical solution, calculated by the Youngs-Laplace equation, given by:

$$P_1 - P_2 = \frac{2\sigma}{r_b} \tag{2. 18}$$

For an air bubble in water with a radius of 2 mm the analytical solution of the pressure difference is 73.0 Pa. The pressure difference for the simulation results of the tensile force model is 73.0 Pa and for the simulation results of the CSF model 32.0. In Figure 2.6 the different results can be seen. Since the Youngs-Laplace equation can only be used for spherical bubbles these results are for the initial part of the simulation, when the bubble is still spherical. The tensile force model gives much better results than the CSF model. When comparing the pressure difference predicted by CSF model and the tensile force model, the tensile force model shows a steeper gradient at the interface (see Figure 2.6).

A final check is the comparison of shapes of rising bubbles. Grace (1973) and Grace *et al*. (1976) presented a diagram, which shows the (experimentally determined) effect of fluid properties and the bubble diameter on the shape and the terminal rise velocity of a single bubble (Figure 2.1). In Figure 2.7 the simulation results of a rising air bubble in water with a diameter of 4 mm (Eo = 2.15 and M = $2.52 \cdot 10^{-11}$) using the CSF model and the tensile force model are shown. In Figure 2.8 the results of a 6 mm bubble (Eo = 4.84

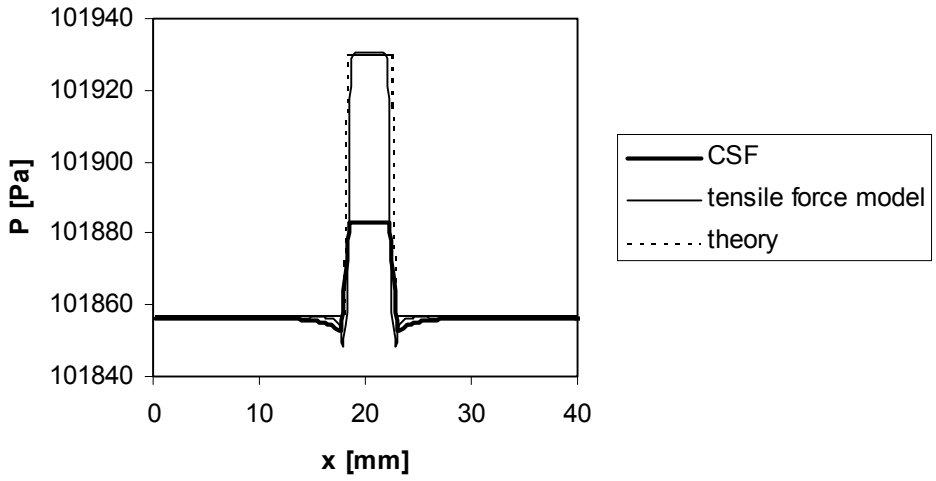

Figure 2.6: Pressure difference.

and M = $2.52 \cdot 10^{-11}$) can be seen. In both figures also the results of the 3D front tracking model are shown. These results are compared to the Grace diagram (Figure 2.1). An air bubble with a diameter of 4 mm or 6 mm in water is in the wobbling regime, according to this figure. From the simulation results can be concluded, that the bubble shape of a 4 mm computed by the CSF model is in the ellipsoidal regime. A 6 mm bubble computed by the CSF model is in the spherical cap regime. The bubble shape computed by the tensile force model is in line with the results in the Grace diagram.

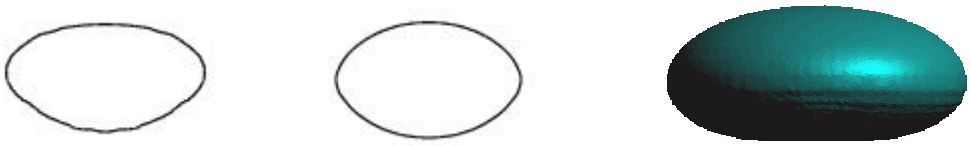

Figure 2.7: Simulation results of a bubble with a diameter of 4 mm. Left: CSF model; middle: tensile force model; right: 3D front tracking.

Figure 2.8: Simulation results of a bubble with a diameter of 6 mm. Left: CSF model; middle: tensile force model; right: 3D front tracking.

2.5 Front tracking

To compare the 2D VOF simulation results to 3D simulation results and to study 3D effect the 3D front fracking model is used. The front fracking technique is based on direct numerical simulation and has been introduced by Unverdi and Tryggvason (1992). The front tracking method uses an unstructured dynamic mesh to represent the interface surface and tracks this interface explicitly by the interconnected marker points. This technique has excellent capability to calculate the surface tension forces, which have significant effect on the bubble shape and bubble dynamics. Other models like the VOF, level set or MAC models show less good and detailed calculations of the surface tension forces.

2.5.1 Model description

The conservation equations for mass and momentum for an incompressible fluid (one-fluid approach) are given by equation 2.6 and 2.7. These equations have been solved with a finite volume technique on a staggered rectangular three-dimensional grid using a two-step projection-correction method with an implicit treatment of the pressure gradient and explicit treatment of the convection and diffusion term. For the calculation of the density and the viscosity equations 2.8 and 2.9 are used.
For the local liquid fraction the indicator function F is used. In the front tracking model it is assumed that this indicator function is conserved:

$$\frac{DF}{Dt} = 0 \tag{2. 19}$$

In the Front Tracking method this conservation equation, based on the incompressibility, is not solved directly, but evaluated from the position of the interface (mesh), which is moved every time step.

2.5.2 Interface description

Generally a front structure is used that consists of points connected by elements. In the three-dimensional fronts the three points are connected by a triangular element to form a

continuous interface. From this mesh the indicator function F, on the Cartesian grid, is computed.

The local distribution of the indicator function F is computed from the location of the triangulated interface by solving a Poisson-equation, following the method proposed by Unverdi and Tryggvason (1992):

$$\nabla^2 F = \nabla \cdot \sum_m D\left(\mathbf{x} - \mathbf{x}_m\right)\mathbf{n}_m \Delta s_m \tag{2. 20}$$

where m the interface element, $\mathbf{n}_m$ is the outwardly pointing normal on the interface element m and Δs_m is the surface area of this element. The function D represents a numerical approximation of the Dirac-function normalised to the cell volume. In the used model volume weighing proofed to be sufficiently stable (Van Sint Annaland *et al*., 2003). A robust incomplete Cholesky conjugated gradient (ICCG) algorithm has been used to solve the Poisson-equation for the F-field.

2.5.3 Surface tension force

One of the main advantages of the front tracking model is the accurate calculation of the interface. The surface tension forces are computed from the tensile forces on the three edges l of all interface elements m (see Figure 2.9). In previous work (Van Sint Annaland *et al.*, 2003) these forces were subsequently distributed to the Eulerian grid via volume weighing.

$$\mathbf{F}_{SF} = \sum_m \sum_\ell D\left(\mathbf{x} - \mathbf{x}_{m,\ell}\right)\sigma\left(\mathbf{t}_{m,\ell} \otimes \mathbf{n}_{m,\ell}\right) \tag{2. 21}$$

where $\mathbf{t}_{m,l}$ is the tangential vector to edge ℓ of marker m. In this model the normal and tangent vectors of the edges of the elements are used, which can be obtained directly from the interface marker data, in contrast to the method used by Tryggvason *et al*. (2001), where a polynomial fit for the interface is constructed from which the normal and tangent vectors to the element are calculated. In order to avoid distribution the surface tension force to cells that have very low liquid volume fractions, which would results in

large distortions of the velocity field near the interface, a “mass weighing” function has been used (Deen *et al.*, 2004):

$$\mathbf{F}_\sigma = \frac{\sum_m \sum_\ell \rho_{m,\ell} D\left(\mathbf{x}-\mathbf{x}_{m,\ell}\right)\sigma\left(\mathbf{t}_{m,\ell}\otimes\mathbf{n}_{m,\ell}\right)}{\sum_m \sum_\ell \rho_{m,\ell} D\left(\mathbf{x}-\mathbf{x}_{m,\ell}\right)} \tag{2. 22}$$

2.5.4 Restructuring the interface mesh

When the surface of a bubble is moved, the shape of the bubble can change due to the flow in the column and the surface mesh deforms. If too many elements are used stretching and shrinking of the surface elements can cause numerical problems after some simulation time.

To restructure the surface mesh methods used by Tryggvason (2001) are implemented. The most evident restructuring is the addition or the removal of new surface elements when one of the edges of an element becomes too long or too short.

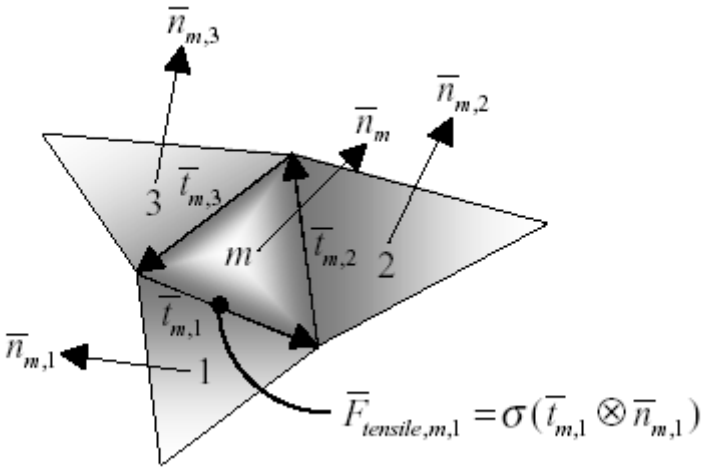

Figure 2.9: Schematic representation of the calculation of the three tensile forces acting on the three edges of interface marker *m*.

2.6 Forces acting on bubbles

The VOF model can be used to study the time-dependent behaviour of bubbles rising in a liquid in a fundamental way. This model can be used to develop closure relations, which can be used in models, which can simulate the flow in industrial bubble columns. Closure relations for the forces acting on bubbles are used in the Euler-Euler and Euler-Lagrange models.

The total force acting on a bubble rising in a liquid flow can be decomposed of separate and uncoupled contributions of gravity ($\mathbf{F}_G$), pressure gradient ($\mathbf{F}_P$), drag ($\mathbf{F}_D$), lift ($\mathbf{F}_L$), virtual or added mass force ($\mathbf{F}_{VM}$) (Auton, 1983):

$$\mathbf{F}_{tot} = \mathbf{F}_G + \mathbf{F}_P + \mathbf{F}_D + \mathbf{F}_L + \mathbf{F}_{VM} \tag{2. 23}$$

The acceleration of a rising bubble can be calculated by Newton's second law:

$$m_B \frac{d\mathbf{v}}{dt} = \mathbf{F}_{tot} \tag{2. 24}$$

Each of the forces in equation 2.23 will be discussed in the following sections.

2.6.1 Gravity and pressure gradient

The force acting on a bubble due to gravity and pressure gradient, also called the buoyancy force, results in a net upward force. The equation for the gravity force is given by:

$$\mathbf{F}_G = \rho_g \mathbf{g} V_B \tag{2. 25}$$

The force acting on a bubble due to the pressure gradient in the liquid phase incorporate contributions from the Archimedes displacement force, inertial forces and viscous strain in the liquid:

$$\mathbf{F}_P = -V_B \nabla P = -\rho_l \mathbf{g} V_B \tag{2. 26}$$

It is noted that **g** points in the negative y-direction. The combination of equation 2.25 and 2.26 gives the equation for the buoyancy force:

$$\mathbf{F}_{Buoyancy} = \mathbf{F}_G + \mathbf{F}_P = \left(\rho_g - \rho_l\right)\mathbf{g}V_B \tag{2. 27}$$

2.6.2 Drag force

A bubble, moving in a column with a uniform flow field, experiences a drag force exerted by the liquid on the moving bubble. This drag force consists of a form drag and friction drag. Odar and Hamilton (1964) gave the following relation for the drag force acting on a sphere. The force is proportional to the relative velocity between the bubble and the fluid (**v** - **u**) and acts in the opposite direction to the path of the bubble.

$$\mathbf{F}_D = -\frac{1}{2}C_D\rho_l\frac{1}{4}\pi d_B^2\left|\mathbf{v}-\mathbf{u}\right|\left(\mathbf{v}-\mathbf{u}\right) \tag{2. 28}$$

The drag force in this equation depends on the bubble size and the flow regime (laminar or turbulent).

The former is characterised by the dimensionless Eötvös number:

$$\mathrm{Eo} = \frac{gd_B^2\Delta\rho}{\sigma} \tag{2. 29}$$

while the latter is represented by the Reynolds number:

$$\mathrm{Re} = \frac{\rho_l d_B v}{\mu_l} \tag{2. 30}$$

Tomiyama (1998) derived some equations for the drag coefficient of single bubbles for a wide range of fluid properties, bubble diameters and acceleration of gravity. These equations are based on a balance of forces acting on a single bubble in an infinite stagnant liquid and on available empirical correlations for the terminal rise velocities of single bubbles.

Tomiyama (1998) proposed three equations, which corresponds to a pure, slightly-contaminated and contaminated system, and are respectively given by:

$$C_D = \max\left[\min\left[\frac{16}{\mathrm{Re}}\left(1+0.15\,\mathrm{Re}^{0.687}\right),\frac{48}{\mathrm{Re}}\right],\frac{8}{3}\frac{\mathrm{Eo}}{\mathrm{Eo}+4}\right] \tag{2. 31}$$

$$C_D = \max\left[\min\left[\frac{24}{\mathrm{Re}}\left(1+0.15\,\mathrm{Re}^{0.687}\right),\frac{72}{\mathrm{Re}}\right],\frac{8}{3}\frac{\mathrm{Eo}}{\mathrm{Eo}+4}\right] \tag{2. 32}$$

$$C_D = \max\left[\frac{24}{\mathrm{Re}}\left(1+0.15\,\mathrm{Re}^{0.687}\right),\frac{8}{3}\frac{\mathrm{Eo}}{\mathrm{Eo}+4}\right] \tag{2. 33}$$

The difference between the pure and contaminated systems is due to the difference in internal circulation inside the bubble, which does not occur for bubbles in contaminated liquid.

Tomiyama compared the results of the calculated terminal rise velocities of single bubbles in stagnant liquids using the proposed C_D with measured data (Grace et al, 1973) under the condition of $10^{-2} < \mathrm{Eo} < 10^{3}$, $10^{-14} < \mathrm{M} < 10^{7}$ and $10^{-3} < \mathrm{Re} < 10^{5}$. Figure 2.10 shows the results of the comparison. The calculated terminal rise velocity agreed well with the measured data.

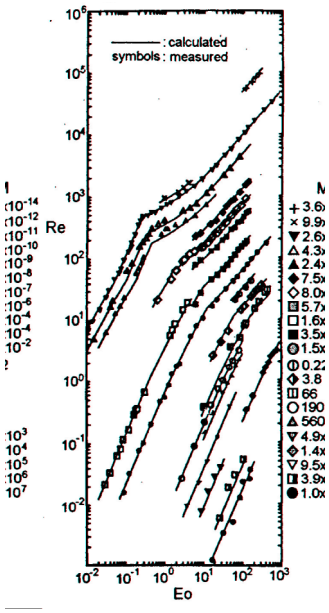

Figure 2.10: Verification of the C_D model: measured data were quoted from Grace *et al.* (1973) (Tomiyama, 1998).

As can be seen in Figure 2.10 at some point the slope of the different lines changes. This is due to the change of shape of the bubbles. For small bubbles the standard drag curve is applicable. For larger bubbles surface tension effects become dominant and the Eötvös curve is used.

2.6.3 Lift force

A bubble, rising in a non-uniform liquid flow field, experiences a transverse lift force due to vorticity, rotations of bubbles or shear. The lift force consists of two parts: The classical shear-induced lateral lift force and the wake induced lift force. Both forces act simultaneously on the bubble. For small, spherical bubbles the classical shear-induced lateral lift force dominates and for large, deformed bubbles the transverse lift force dominates.

Auton (1987) derived that the lift force is proportional to the cross product of the slip velocity and the curl of the liquid velocity. This implies that the lift force is perpendicular to the path of the bubble.

$$\mathbf{F}_L = -C_L \rho_l V_B \left(\mathbf{v} - \mathbf{u}\right) \times \Omega \qquad (2.\ 34)$$
$$\Omega = \nabla \times \mathbf{u}$$

The expression for the lift force is valid under the assumption of local homogeneity of the flow. This assumption is satisfied throughout the homogeneous regime where both bubble radius and liquid velocity gradients are rather small.

In Figure 2.11 the values for the lift coefficient for an air bubble in water for different diameters of the bubble is shown (Tomiyama, 1998). In this figure can be seen, that the value of the lift coefficient changes from 0.3 to -0.3 depending on the size of the bubble.

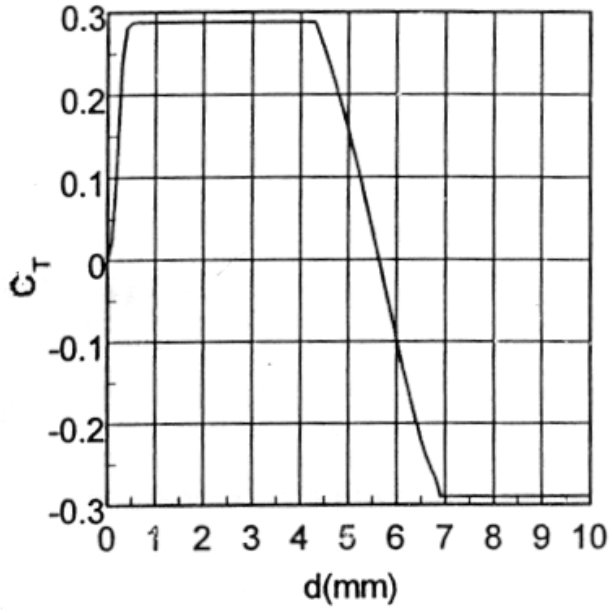

Figure 2.11: Transverse lift coefficient for air bubble in water (Tomiyama, 1998).

2.6.4 Virtual mass force

The virtual mass force, also called the added mass force, is especially important in cases of unsteady rise when a bubble accelerates or decelerates, e.g. near the nozzle or in a turbulent field. When the velocity of the bubble changes, the velocity of the liquid around the bubble changes accordingly. The force can be seen as a resistance to acceleration, as the 'added mass' of the liquid also has to be accelerated along with the bubble. According to Auton (1983) the virtual mass force can be modelled by:

$$\mathbf{F}_{VM} = -\left(\frac{D\mathbf{I}}{Dt} + \mathbf{I} \cdot \nabla \mathbf{u} \right) \qquad (2.\ 35)$$

$$\mathbf{I} = C_{VM} \rho_l V_B \left(\mathbf{v} - \mathbf{u} \right)$$

The value of the virtual mass force is considered to be independent of the void fraction and for spherical bubbles C_{VM} is taken equal to 0.5 in 3D systems and 1.0 in 2D systems (Auton, 1988; Lamb, 1932).

2.7 Derivation of drag, lift and virtual mass coefficient

In this section expressions for the drag, lift and virtual mass force coefficient will be derived. These expressions will be used in the other models in the 'hierarchy of models'. The drag and lift forces are the most important forces acting on a bubble rising in a liquid. The virtual mass force is only important during acceleration or deceleration of the bubble.

2.7.1 Drag coefficient

The relation for the drag coefficient for spherical and non-spherical bubbles can be derived by solving a force balance for a single bubble rising steadily in a quiescent liquid. The contribution of the virtual mass can be neglected, as the virtual mass is only important during the acceleration of the bubble (when a bubble starts to rise in the liquid) or in a turbulent field. In absence of a shear field the lift force is zero and because of the presence of only one bubble there is no hydrodynamic interaction between neighbouring bubbles. For this system the force balance is given by

$$\mathbf{F}_{tot} = \mathbf{F}_P + \mathbf{F}_G + \mathbf{F}_D \tag{2. 36}$$

The total force $\mathbf{F}_{\text{tot}}$ equals zero when the bubble reaches its stationary rise velocity.
In case the bubble only moves in the vertical direction the force balance reduces to:

$$\left(\rho_l - \rho_g\right)|g|V_B - \frac{1}{2}C_D\rho_l A_p\left|\mathbf{v}-\mathbf{u}\right|\left(v_y - u_y\right) = 0 \tag{2. 37}$$

The volume of the bubble is $\frac{1}{6}\pi d_B^3$,with d_B the equivalent diameter of a spherical bubble. The projected surface A_p is defined as $\frac{1}{4}\pi d_p^2$, with d_p the projected diameter during steady rise. For spherical bubbles d_p is the same as d_B, however, for non-spherical bubbles d_p differs from d_B.

Rearrangement of equation 2.37 leads to the following equation for the drag coefficient:

$$C_{D,3D} = \frac{4}{3}\left(\frac{\rho_l - \rho_g}{\rho_l}\right)\frac{d_B^3|g|}{d_p^2|\mathbf{v}-\mathbf{u}|(v_y - u_y)} \tag{2. 38}$$

As some of the simulation are carried out in 2D, it would be more accurate to derive a C_D equation for a cylinder because a 2D bubble stretches out to a cylinder in 3D with a volume of $\frac{1}{4}\pi d_B^2 L$ and a projected surface of $d_p L$. The resulting C_D is:

$$C_{D,2D} = \frac{1}{2}\left(\frac{\rho_l - \rho_g}{\rho_l}\right)\frac{\pi d_B^2|g|}{d_p|\mathbf{v}-\mathbf{u}|(v_y - u_y)} \tag{2. 39}$$

These equations will be used to calculate the drag coefficient for bubbles of different sizes in an air-water system.

2.7.2 Lift coefficient

For spherical and non-spherical bubbles the lift coefficient is calculated by solving the force balance on a bubble rising in a shear field. In this case again the virtual mass can be neglected and the hydrodynamic interaction is neglected.
The forces due to drag and lift have an x- and y-component. When the bubble has reached a stationary rise velocity two force balances can be derived, one for each direction. The x-balance in stationary state is:

$$F_{D,x} + F_{L,x} = 0 \tag{2. 40}$$

Substitution of the equations for the x-component of the drag and lift forces gives:

$$-\frac{1}{2}C_D\rho_l\frac{1}{4}\pi d_p^2|\mathbf{v}-\mathbf{u}|(v_x - u_x) - C_L\rho_l\frac{1}{6}\pi d_B^3(v_y - u_y)\frac{du_y}{dx} = 0 \tag{2. 41}$$

After rearrangement an equation for C_L is obtained:

$$C_L = \frac{-\frac{3}{4} C_D d_p^2 |\mathbf{v}-\mathbf{u}| (v_x - u_x)}{d_B^3 (v_y - u_y) \frac{du_y}{dx}} \tag{2. 42}$$

The balance for the y-direction consists of the y-component of the drag and lift force and the forces due to a pressure gradient and gravity.

$$F_P + F_G + F_{D,y} + F_{L,y} = 0 \tag{2. 43}$$

Substituting the equations for these forces gives a second equation for the lift coefficient:

$$C_L = \frac{-\frac{(\rho_l - \rho_g)}{\rho_l} |g| d_B^3 + \frac{3}{4} C_D d_p^3 |\mathbf{v}-\mathbf{u}| (v_y - u_y)}{d_B^3 (v_x - u_x) \frac{du_y}{dx}} \tag{2. 44}$$

Equation 2.42 and 2.44 can be combined to derive an equation for both the lift and drag coefficient

$$C_L = \frac{-\frac{\rho_l - \rho_g}{\rho_l} |g| (v_x - u_x)}{|\mathbf{v}-\mathbf{u}|^2 \left(\frac{du_y}{dx} \right)} \tag{2. 45}$$

$$C_D = \frac{\frac{4}{3} \frac{(\rho_l - \rho_g)}{\rho_l} |g| d_B^3 (v_y - u_y)}{d_p^2 |\mathbf{v}-\mathbf{u}|^3} \tag{2. 46}$$

Note that equation 2.46 reduces to equation 2.39 in absence of a shear field.
As can be seen in equation 2.45 the lift coefficient is independent of the diameter of the bubble, d_B. Therefore it can be concluded that $C_{L,3D} = C_{L,2D}$.

2.7.3 Virtual mass coefficient

The virtual mass coefficient can be obtained from the first part of the simulation. At t=0 s the bubble is placed in the column and starts to rise in the liquid. First an acceleration of the bubble can be seen, before it reaches a stationary rise velocity. The virtual mass coefficient can be obtained by fitting the simulated bubble acceleration with the equation of motion. In absence of a shear field the lift force is zero and the hydrodynamic interaction can be neglected.

$$\mathbf{F}_{tot} = \mathbf{F}_P + \mathbf{F}_G + \mathbf{F}_D + \mathbf{F}_{VM} \tag{2. 47}$$

Substituting the equations for the drag, lift and virtual mass force gives for the acceleration in a 3D system:

$$\frac{d\mathbf{v}}{dt} = \frac{\left(\rho_l - \rho_g\right)|g| - \frac{3}{4d_B} C_D \rho_l \mathbf{v}^2}{\left(\rho_g + C_{VM}\rho_l\right)} \tag{2. 48}$$

The acceleration for a 2D system is:

$$\frac{d\mathbf{v}}{dt} = \frac{\left(\rho_l - \rho_g\right)|g| - \frac{2}{\pi d_B} C_D \rho_l \mathbf{v}^2}{\left(\rho_g + C_{VM}\rho_l\right)} \tag{2. 49}$$

The acceleration can be calculated from the simulations. When the drag coefficient is known, the virtual mass coefficient can be determined.

2.8 Boundary conditions and numerical method

2.8.1 Volume of fluid model

The 2D VOF mode is used to calculate the drag and virtual mass force. In the VOF simulations the bubble column is initially filled with a quiescent liquid. During the initialisation step the pressure is set to the hydrostatic pressure. The initial position of a

spherical gas bubble is specified in the middle of the column at one bubble diameter from the bottom (see Figure 2.12).
The liquid fraction of each cell is computed by first setting the cell values at 1 and subtracting the fraction of gas present in each cell from that value. When the liquid fraction is computed, the local density and viscosity are calculated and the bubble interface is reconstructed. This interface is needed to calculate the surface tension force. In the main loop the Navier-Stokes equations are solved and the second step is to determine the interface information from the liquid fraction of each cell from the previous time step. Once the velocity field and the interface data are determined, the fluxes through the cell faces can be calculated. These fluxes are used to compute the new liquid fractions in the cells. The last step in the main loop is updating the density, viscosity and surface tension force. The final step at the end of the simulation releases the computer memory and stores the final data.

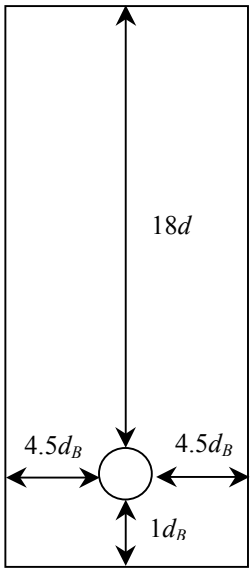

Figure 2.12: Simulation set-up for the VOF-simulations.

In Figure 2.13 the computational flow diagram of the VOF model is shown.
The boundary conditions required to solve the system are imposed using a flag matrix concept (Kuipers *et al.*, 1993). On all the boundaries of the computational domain, except the top, free slip conditions were applied. For the top the inflow/outflow conditions (zero gradient) were used.

For the discretisation of the convection term of the Navier-Stokes equation the second order accurate Barton scheme (Centrella and Wilson, 1984; Hawley et al, 1984; Goldschmidt, 2001) is used. The diffusive terms are computed using the second order finite difference scheme.

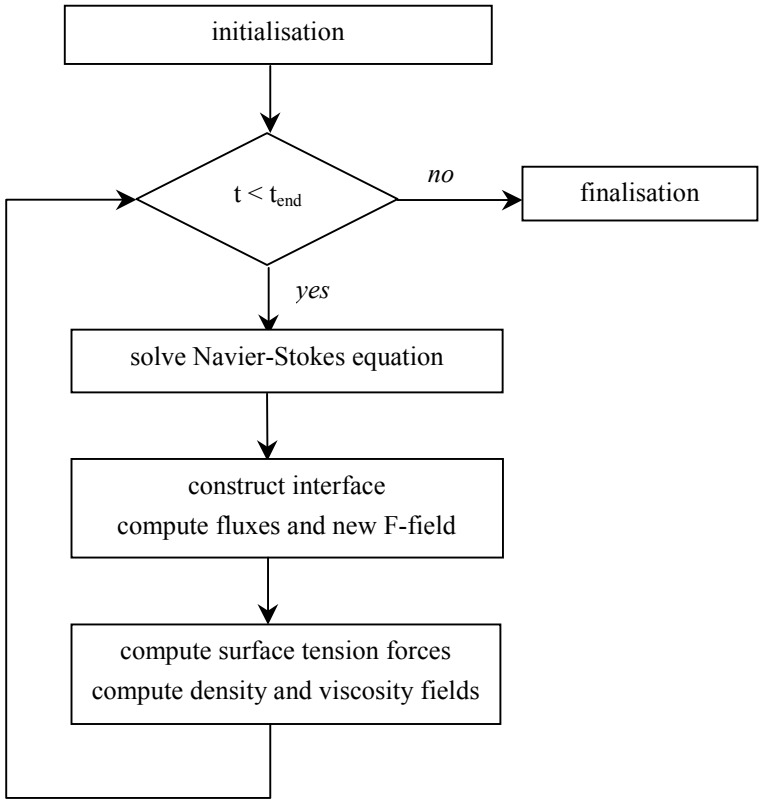

Figure 2.13: Computational flow diagram of the VOF model.

The equations are discretised on a two-dimensional staggered mesh. The pressure-Poisson equation is solved using the incomplete Choleski conjugate gradient (ICCG) method.

The stabilility of the code is highly dependent on the choice of the time step. Three stability criteria can be used for this code: Courant stability, viscosity stability and the surface tension stability condition. For very small bubbles (1.0 and 2.0 mm) the time step is $1.0 \cdot 10^{-6}$ s, according to these three criteria. For bubbles > 2.0 mm the used time step is $1.0 \cdot 10^{-5}$ s.

To avoid wall effects the diameter of the column is set equal to 10 times the bubble diameter. The number of cells initially assigned to the bubble diameter is 16. This is in correspondence with the work of Tomiyama (1998).
In order to avoid numerical instabilities due to very steep gradients in the density or viscosity the interface is extended over four Eulerian grid cells. In this transition zone the fluid properties change smoothly from one side of the interface to the other.

2.8.2 Front tracking model

In the initialisation step of the front tracking model the velocities are set to zero, the pressure is set to the hydrostatic pressure and the initial interface mesh is constructed. From this interface mesh the surface tension forces are computed and the indicator field is calculated. From the indicator field the local density and viscosity are calculated.

As shown in Figure 2.14 in the main loop the Navier-Stokes equations are first solved yielding the flow and pressure fields. Then the interface nodes are tracked with the local interpolated fluid velocity, which gives the new position of the interface nodes and implicitly the new bubble shape. Finally the new surface tension forces, indicator field and the density and viscosity are calculated.

In order to be able to handle very large density variations in gas-liquid flows the Navier-Stokes equations 2.7 are rewritten in their non-conservative form using the continuity equation given in equation 2.6:

$$\rho\left(\frac{\partial \mathbf{u}}{\partial t}+\nabla\cdot\mathbf{uu}\right)=-\nabla P+\nabla\cdot\mu\left(\left(\nabla\mathbf{u}\right)+\left(\nabla\mathbf{u}\right)^{T}\right)+\rho\mathbf{g}+\mathbf{F}_{SF} \qquad (2.\ 50)$$

For the discretisation of the convection term of the Navier-Stokes equation the second order accurate Barton scheme (Centrella and Wilson, 1984; Hawley et al, 1984; Goldschmidt, 2001) is used. The diffusive terms are computed using the second order finite difference scheme.

The Navier-Stokes equations are solved on a staggered rectangular two- or three-dimensional grid using a finite-volume method with a SIMPLE algorithm (Patankar,

1980). The pressure-Poisson equation is solved using the incomplete Choleski conjugate gradient (ICCG) method.

To limit the computational costs of the simulations a moving window concept is used. The simulation domain travels along with the movement of the bubble. If the centre of mass of the bubble moves to a neighbouring grid cell, e.g. in the positive z-direction, a plane of grid cells is removed from the bottom of the simulation domain, while a plane of grid cells is added to the top. The properties in the newly added grid cell are obtained by extrapolating the local data.

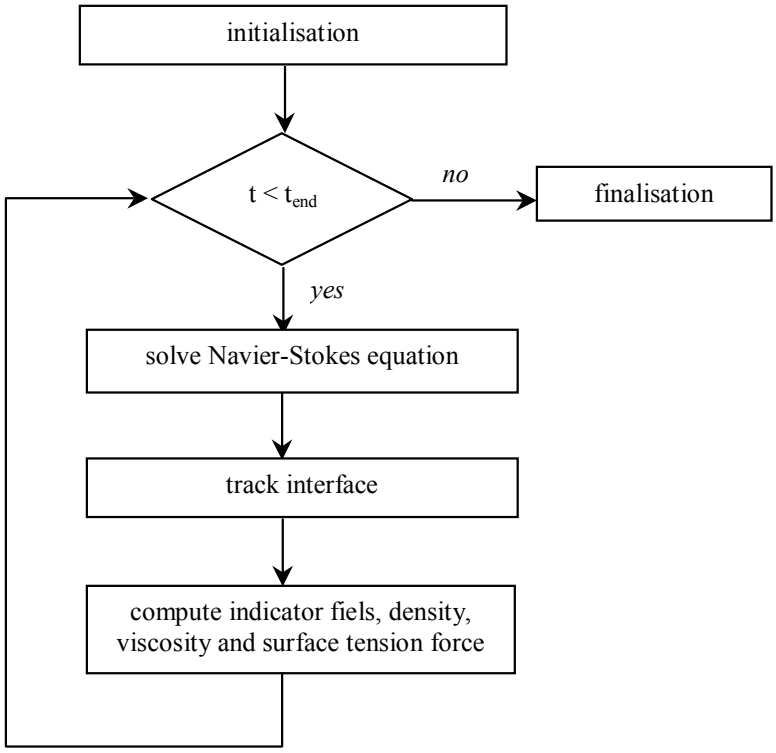

Figure 2.14: Computational flow diagram of the front tracking model.

The lift force is calculated with the 2D front tracking model. No slip boundary conditions are used for all walls except for the bottom of the computational domain, where a free slip boundary condition is applied. The liquid flow in the shear field flows from the top of the column to the bottom. This reduced the number of Eulerian computational cells in the vertical direction. During the computation the computational domain is shifted in

such a way, that the centre of mass of the total gas content is kept more or less at 1/4 from the top of the domain (see Figure 2.15). This also reduces the number of Eulerian computational cells to simulate a fast rising gas bubble. The diameter of the column is set equal to 5 times the bubble diameter. The number of cells initially assigned to the bubble diameter is 10. The time step used in the calculations for the lift force is $2.0 \cdot 10^{-5}$ s.

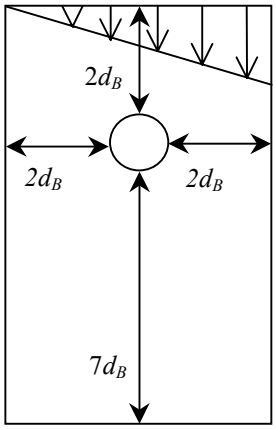

Figure 2.15: Simulation set-up 2D front tracking simulations.

The 3D front tracking model is used to calculate the drag and virtual mass force in a 3D system. In the 3D front tracking model no slip boundary conditions are used for all walls except for the top of the computational domain, where a free slip boundary condition is applied. During the computation the computational domain is shifted in such a way, that the centre of mass of the total gas content is kept more or less at 1/5 from the top of the domain (see Figure 2.16).

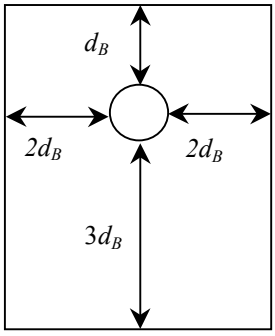

Figure 2.16: Simulation set-up 3D front tracking simulations.

This reduces the number of Eulerian computational cells to simulate a fast rising gas bubble. The diameter of the column is set equal to 5 times the bubble diameter. The number of cells initially assigned to the bubble diameter is 10. The time step used in the calculations for the lift force is $2.0 \cdot 10^{-5}$ s.

2.9 Results

The most important information for the determination of the drag, lift and virtual mass coefficient is the velocity of the bubble in the x- and y-direction. In the Youngs' VOF model this velocity is calculated from the position of the centre of mass of the bubble for each time step. The bubble velocity is obtained by differentiating the position with respect to time.
The x- and y-co-ordinates of the centre of mass of the bubble are calculated from the colour function data as follows:

$$x_{masscentre} = \frac{\sum_{i=1}^{NX}\sum_{j=1}^{NY}(1-F)\cdot i}{\sum_{i=1}^{NX}\sum_{j=1}^{NY}(1-F)} \tag{2. 51}$$

$$y_{masscentre} = \frac{\sum_{i=1}^{NX}\sum_{j=1}^{NY}(1-F)\cdot j}{\sum_{i=1}^{NX}\sum_{j=1}^{NY}(1-F)} \tag{2. 52}$$

2.9.1 Results drag coefficient

To calculate the drag curve for air bubbles in water, simulations were carried out for bubbles of different diameters (1-10 mm). From the results of the calculations the velocity and thus the Reynolds number and the drag coefficient were calculated.
The simulated drag curve is compared to the drag relations of Tomiyama (1998) (equation 2.31), Ishii and Zuber (1979) and Grace *et al.* (1976). The relation of Ishii and Zuber (1979) is given by:

$$C_D = \frac{2}{3}\sqrt{\mathrm{Eo}} \tag{2. 53}$$

Grace *et al.* (1976) gave the following correlation for the terminal rise velocity of ellipsoidal bubbles in contaminated systems:

$$v_{b,contaminated} = \frac{\mu_l}{\rho_l d_b}\mathrm{Re} \tag{2. 54}$$

For pure bubbles at low Re, the terminal velocity is related to that for the same system under contaminated conditions by:

$$v_{b,pure} = v_{b,contaminated}\left(1+\frac{1}{2+3\left(\frac{\mu_g}{\mu_l}\right)}\right) \qquad (\mathrm{Re} < 0.2) \tag{2. 55}$$

For systems with higher Re, equation 2.55 is an upper bound for the terminal rise velocity of the system.
Re in equation 2.54 is given by:

$$\mathrm{Re} = \frac{\mathrm{J} - 0.857}{\mathrm{M}^{0.149}} \tag{2. 56}$$

where the correlation for J is:

$$J = 0.94H^{0.757} \qquad (2 < \mathrm{H} \leq 59.3) \tag{2. 57}$$

$$J = 3.42H^{0.441} \qquad (\mathrm{H} > 59.3) \tag{2. 58}$$

with:

$$H = \frac{4}{3}\frac{\mathrm{Eo}}{\mathrm{M}^{0.149}\left(\frac{\mu_l}{\mu_w}\right)^{0.14}} \tag{2. 59}$$

μ_w in equation (2.59) is the viscosity of water and may be taken as 0.0009 kg m^{-1} s^{-1} (Braida, 1956).

The relation of Grace *et al.* (1976) was derived for the following conditions:

$$\left.\begin{array}{l} \mathrm{Eo} < 40, \mathrm{M} < 10^{-3}, \mathrm{Re} > 0.2 \\ \dfrac{d_e}{D_c} < 0.08 + 0.02\, log\,\mathrm{Re} \quad \text{for } 0.2 < \mathrm{Re} < 100 \\ \text{or} \\ \dfrac{d_e}{D_c} < 0.12 \qquad\qquad \text{for } \mathrm{Re} > 100 \end{array}\right\} \tag{2. 60}$$

The discontinuity in the slope at H=59.3 corresponds approximately to the transition between non-oscillating and oscillating drops or bubbles.

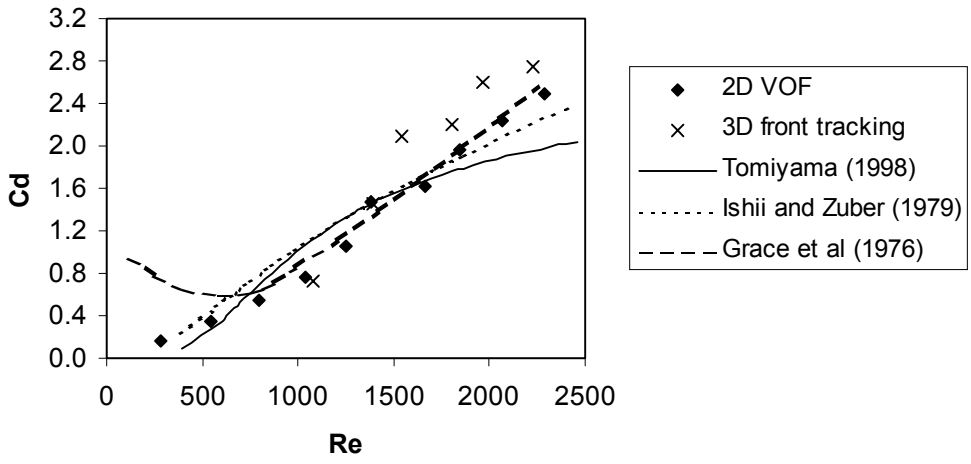

Figure 2.17: Simulations results of C_D compared to drag curve from Tomiyama (1998), Ishii and Zuber (1979) and Grace (1973) for a system with sphere.

The results of the drag coefficient for the 2D VOF simulations can be seen in Figure 2.17. In this figure equation 2.38 is used for a sphere without deformation ($d_p = d_B$). The values of the first two points (Re < 500) are very close to the values of Tomiyama (1998) and Ishii and Zuber (1979). For Re > 800 the C_D calculated from the simulations is very close to the values of Grace *et al.* (1976).

The results of the 2D VOF model are compared to results of a 3D front tracking model. As can be seen in Figure 2.17 the 3D front tracking results and the 2D VOF results are the same for low Re (Re < 1500). For higher Re (Re > 1500) the differences between the 3D front tracking results and the 2D VOF results are larger.

In Figure 2.18 the VOF results of the drag coefficient, using equation 2.39 for a cylinder without deformation are shown. The values of the drag coefficients for a cylinder without deformation are higher than the values of the drag coefficient for a sphere without deformation, as can also be concluded from equation 2.38 and 2.39. The differences between the 2D VOF simulation results and the drag relations from literature are larger than for a system with a sphere (Figure 2.17). The 2D VOF and the 3D front tracking results are close together in Figure 2.18.

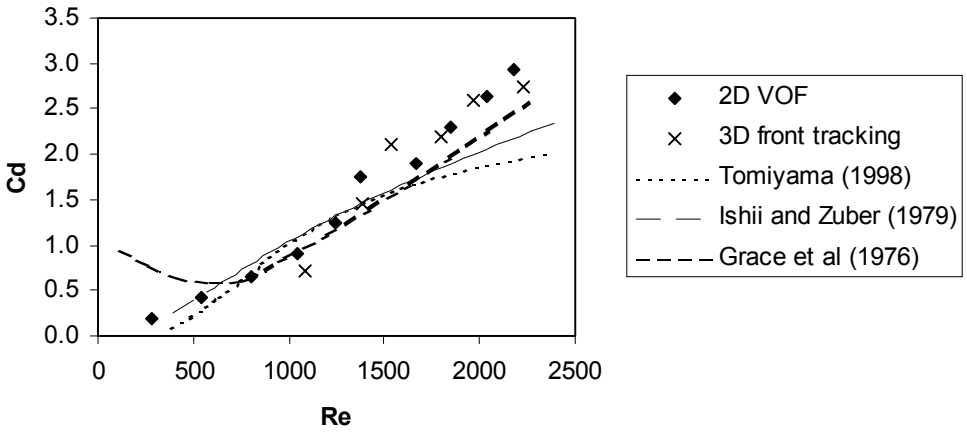

Figure 2.18: Simulations results of C_D compared to drag curve from Tomiyama (1998), Ishii and Zuber (1979) and Grace (1973) for a system with cylinder.

2.9.2 Results virtual mass coefficient

To calculate the virtual mass coefficients for air bubbles in water, simulations were carried out for bubbles of different diameters (1 - 10 mm). When the drag coefficients are calculated the virtual mass coefficients can be determined for the first part of the simulation when the bubble accelerates. The bubble is placed in the domain as a sphere. During the first part of the simulation the bubble deforms. To exclude this effect as much as possible, only the first 0.1 s in the 3D front tracking and 0.2 s in the 2D VOF simulations were considered.

In Table 2.1 the values of the virtual mass coefficient for the 2D VOF 3D front tracking simulations are given. The virtual mass coefficient for the 2D VOF model for a sphere and for a cylinder is the same.
As can be concluded from Table 2.1 the virtual mass coefficients for bubbles in 2D VOF are around 1.1. This value for bubbles in 2D systems is in agreement with literature (Auton, 1988; Lamb, 1932). For the 3D front tracking model the virtual mass coefficient is around 0.6, the value for 3D systems (Auton, 1983).
The small deviation from the theoretical value of spherical bubbles is probably caused by the deformation of the bubble.

Table 2.1: Virtual mass coefficient for 2D VOF and 3D front tracking.

d_B [mm]	C_{VM} 2D VOF	C_{VM} 3D FT
1	1.3	-
2	1.3	-
3	1.3	-
4	1.2	0.6
5	1.1	-
6	1.1	0.6
7	1.1	0.6
8	1.0	0.6
9	1.0	0.6
10	1.0	0.6

2.9.3 Results lift coefficient

To calculate the lift coefficients simulations were carried out with the 2D front tracking model for two bubbles of different diameters (8 and 10 mm). Due to problems with the mass conservation for small bubbles, only large bubbles subjected to a linear shear field were studied.
In both cases the shear rate was 5 s^{-1}. For the bubble with a diameter of 10 mm the results of two different shear rates were compared (2 s^{-1} and 5 s^{-1}). All cases were simulated for a period of 3 s. The three different cases and the final results are presented in Table 2.2.

Table 2.2: Lift coefficient for 2D front tracking.

case	d_B **[mm]**	**shear rate** [s^{-1}]	C_L
1	8	5	0.6
2	10	5	-0.7
3	10	2	-1.0

In Figure 2.19 the x- and y-position of the bubble for case 1 is presented. Figure 2.20 shows the slip velocity in horizontal and vertical direction and Figure 2.21 shows the values of the drag and lift coefficient for the bubble in case 1.

The slip velocity in horizontal direction is given by:

$$v_{x,slip} = v_x - u_x \qquad \text{with} \qquad u_x = 0 \tag{2. 61}$$

The slip velocity in vertical direction is given by:

$$v_{y,slip} = v_y - u_y \qquad \text{with} \qquad u_x = -\gamma \cdot x_B \tag{2. 62}$$

As can be seen in Figure 2.19 the bubble is constantly rising in the column for t < 2 s. For t > 2 s the bubble is moving to the right side of the column with a high negative liquid velocity and the y-position of the bubble is constant. The bubble is oscillating in the horizontal direction and on average moving to the right of the column. During these oscillations the bubble first moves to the left side of the column and after 1 s it moves to

the right side of the column. The right side of the column is the side with the highest slip velocity.
The vertical velocity shows small oscillations, but is more of less constant, as is shown in Figure 2.20. The horizontal velocity shows large oscillations due to the oscillating movement of the bubble in the column. The bubble is oscillating from left to right and the horizontal velocity is changing accordingly. Due to the change in horizontal velocity, the lift coefficient shows the same oscillations (Figure 2.21). The average value of the lift coefficient is given in Table 2.2.

Figure 2.22 shows the x- and y-position of the bubble in case 2. In this case the shear rate remains the same (5 s^{-1}), while the bubble size is increased from 8 to 10 mm. Figure 2.23 shows the velocity in horizontal and vertical direction and Figure 2.24 shows the values of the drag and lift coefficient for the bubble in case 2.
The difference between case 1 and 2 is the movement of the bubble. In case 2 the bubble is moving to the left side of the column, the side with the lowest slip velocity. The average value of the lift coefficient is therefore negative (see Table 2.2). Tomiyama (1998), who also studied the behaviour of large bubbles in shear fields, concluded that the lift coefficient is dependent on the shape of the bubble.

The lift coefficient is positive for small bubbles and negative for large bubbles (see Figure 2.11). He found that the mean lift coefficient varies from between 0.3 to -0.3 for small and large bubbles respectively. The results in this work are different from the results of Tomiyama (1998). The values of the lift coefficient in the simulations are higher. Therefore the lift coefficient of a bubble of 8 mm is positive, which is not the case in the results of Tomiyama (1998).

Figure 2.25, 2.26 and 2.27 shows the position of the bubble, the velocity and the drag and lift coefficient of the bubble in case 3, respectively. Here the shear rate is reduced to a value of 2 s^{-1}.
The lateral movement of the bubble in case 2 and 3 is in the same direction, both to side with the highest slip velocity. The lateral movement in case 3 is smaller in the same time. In case 2 the movement in 3 s is 0.55 m and in case 3 the movement is 0.25, which is in approximate agreement with the change in shear rate.

Figure 2.28 shows the liquid flow around the bubble in the three cases. Figure 2.29, 2.30 and 2.31 are close-ups of Figure 2.28. In these three figures the change of the bubble

shape during one cycle of the oscillations in the column can be seen. The time between two images is 0.03 s.
The liquid is flowing downwards due to the shear rate from the top as is shown in Figure 2.28. In the neighbourhood of the bubble the liquid is moving from the top of the bubble to the wake of the bubble, which is the same as in the case without shear field. During the turn of the bubble the liquid is circulating, as can be seen in the vortices in the column. In Figure 2.28 right the three vortices can be seen very clearly.

The shape of the bubble changes during the rise and oscillation through the column. The shape of the bubble with a diameter of 8 mm is approximately ellipsoidal during the oscillations, as can be seen in Figure 2.29. When the bubble is going from one side to the other the bubble is rotated to a more vertical ellipsoidal position. During the turn the ellipsoidal position of the bubble changes 180°, as can be seen when the third and the seventh image are compared to each other. The shape of the bubble with a diameter of 10 mm is different (see Figure 2.30 and 2.31). During the oscillation the shape of the bubble is ellipsoidal, but during the turn the shape of the bubble is wobbling (first image). In Figure 2.30 the bubble starts turning in the last image. In the case with a smaller shear rate the oscillation is smaller. In Figure 3.31 the first and last image are almost the same. In both images the bubble is turning.

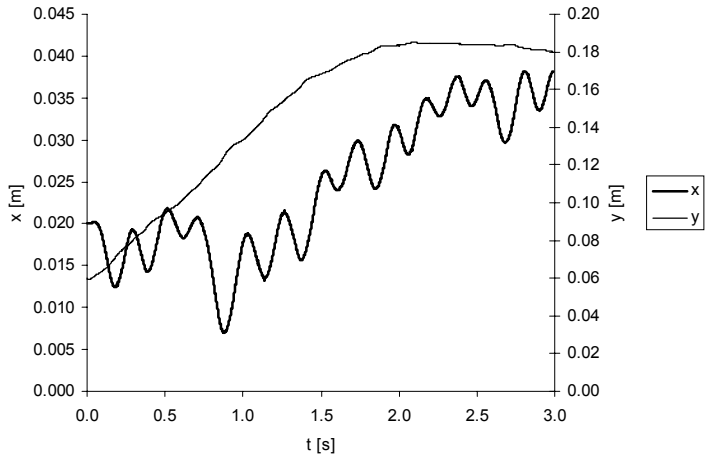

Figure 2.19: x- and y-position of the bubble for case 1 (see Table 2.2).

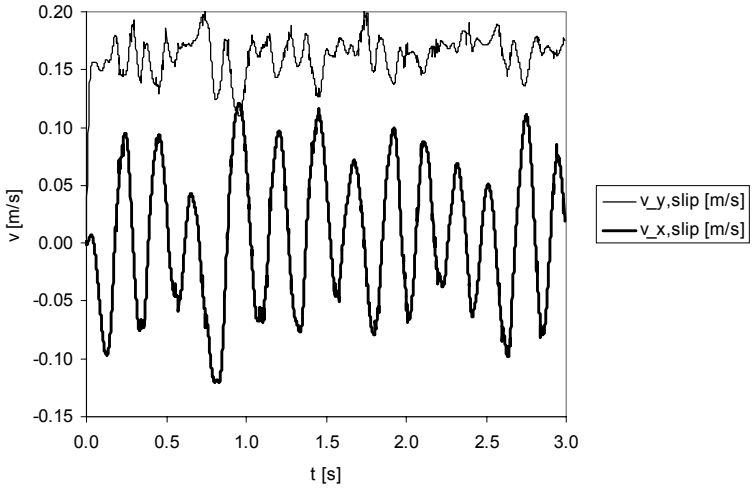

Figure 2.20: Horizontal and vertical slip velocity of the bubble for case 1 (see Table 2.2).

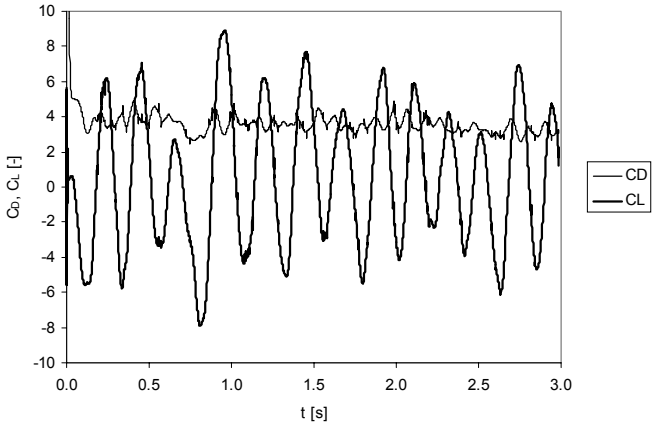

Figure 2.21: Drag and lift coefficient of the bubble for case 1 (see Table 2.2).

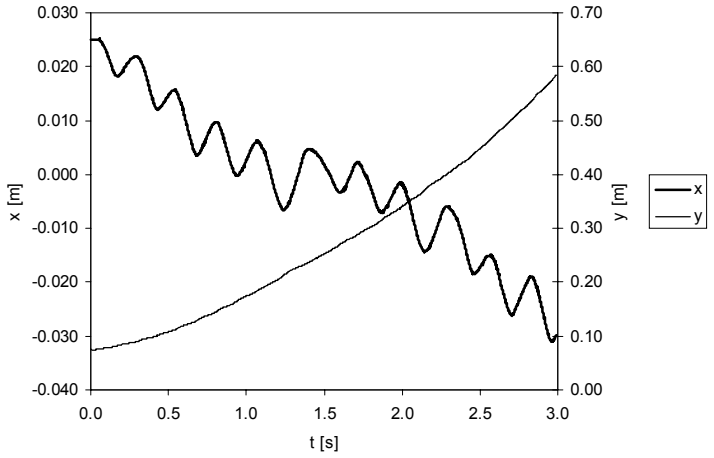

Figure 2.22: x- and y-position of the bubble for case 2 (see Table 2.2).

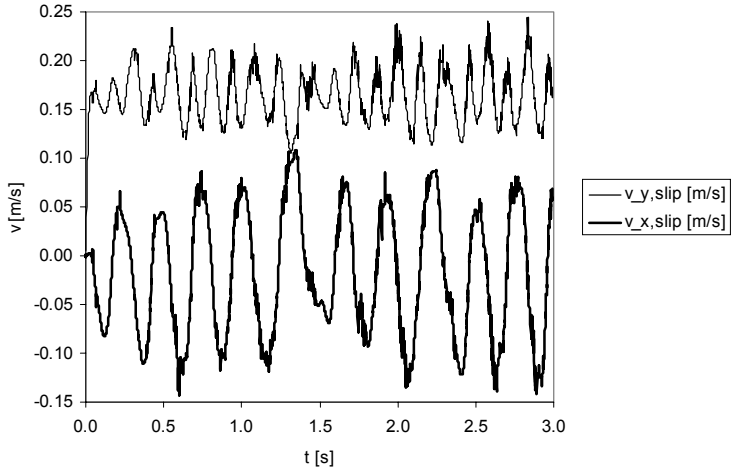

Figure 2.23: Horizontal and vertical slip velocity of the bubble for case 2 (see Table 2.2).

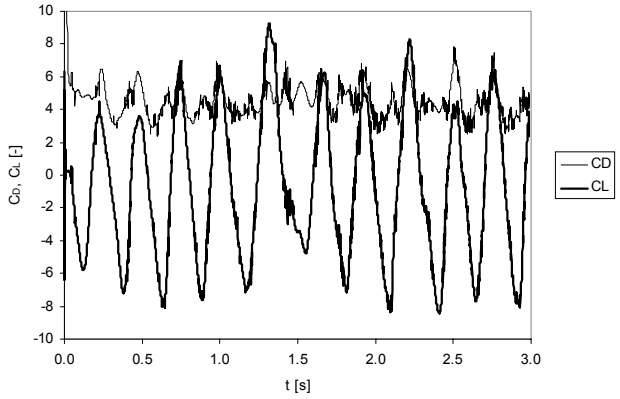

Figure 2.24: Drag and lift coefficient of the bubble for case 2 (see Table 2.2).

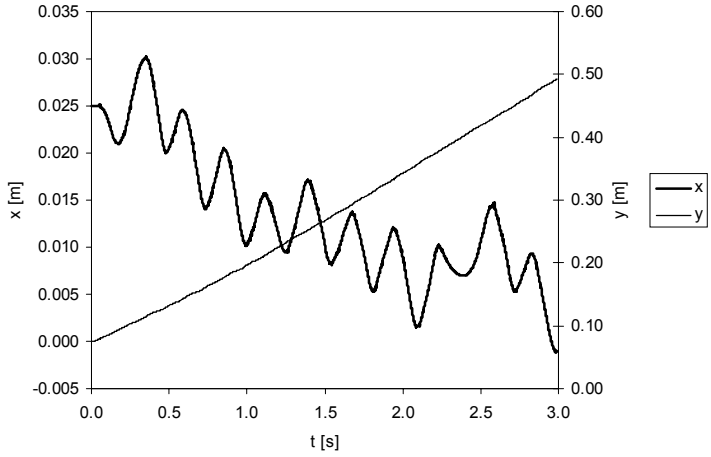

Figure 2.25: x- and y-position of the bubble for case 3 (see Table 2.2).

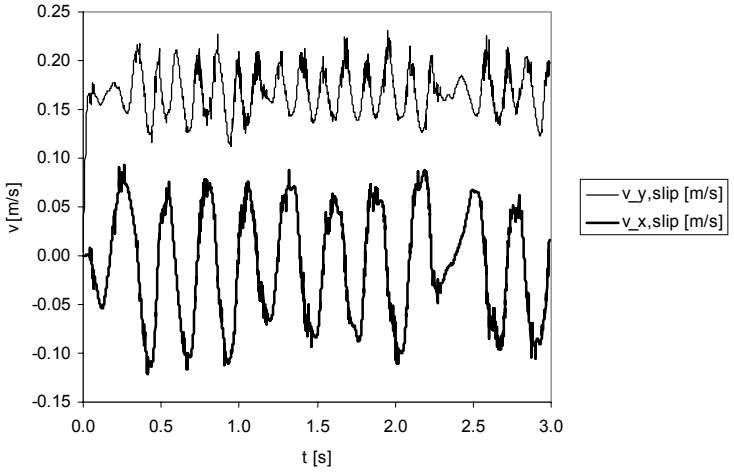

Figure 2.26: Horizontal and vertical slip velocity of the bubble for case 3 (see Table 2.2).

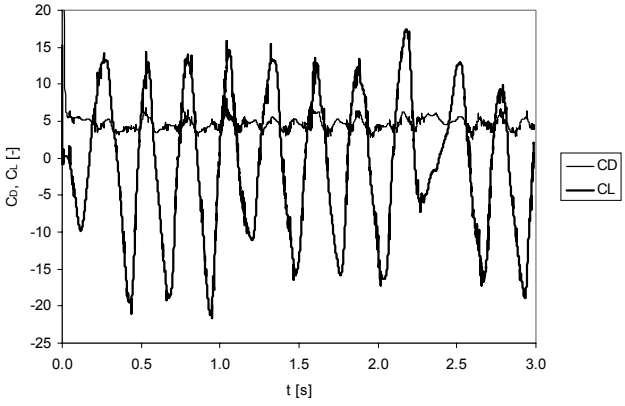

Figure 2.27: Drag and lift coefficient of the bubble for case 3 (see Table 2.2).

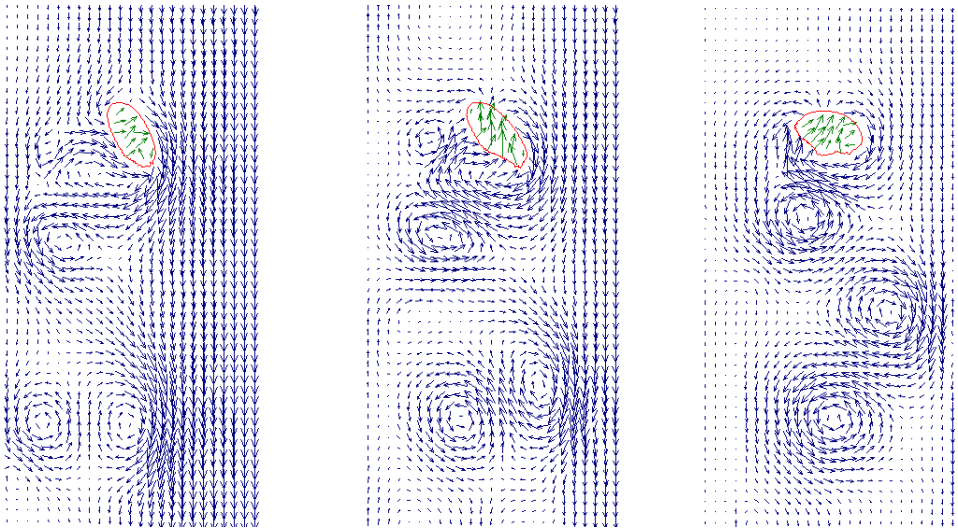

Figure 2.28: Liquid flow around a bubble in a shear field. Left: d_B = 8 mm, shear field = 5 s^{-1}; middle: d_B = 10 mm, shear field = 5 s^{-1}; Right: d_B = 10 mm, shear field = 2 s^{-1}.

2.10 Conclusions

The 2D volume of fluid (VOF) model and 2D and 3D front tracking model have been used to study the time-dependent behaviour of large bubbles rising in an initially quiescent liquid in a fundamental way. Both models solve the incompressible Navier-Stokes equation on a staggered Cartesian mesh using a one-fluid formulation to obtain the gas and liquid flow fields. The Youngs' VOF method reconstructs the gas-liquid interface from the local liquid fraction and the interface is 'tracked' through the Eulerian mesh. The calculation of the surface tension force is based on a model, which was adapted from the front tracking technique instead of the frequently used continuum surface force model.
The front tracking method uses an unstructured dynamic mesh to represent the interface surface and tracks this interface explicitly by the interconnected marker points.

With these models the forces acting on a bubble, i.e. the drag, lift and virtual mass forces have been calculated by using a force balance for a single bubble. The results are compared to relations from literature.
The drag coefficients for small bubble diameters (< 2 mm), calculated with 2D VOF model, are very close to the relations of Tomiyama (1998) and Ishii and Zuber (1979).

For larger bubble diameters (> 2 mm) the drag coefficients are very close to the relation of Grace *et al.* (1976). The drag coefficients in the 3D front tracking model for bubbles larger than 7 mm are higher than in the 2D VOF model where the equation for a sphere is used to calculate the drag coefficient. When the equation for a cylinder is used to calculated the drag coefficient for the 2D VOF model, the drag coefficients of the 3D front tracking model and the 2D VOF model are close together.
The virtual mass force can only be calculated for the first part of the simulation when the bubble accelerates. For the 2D VOF model the virtual mass coefficient is around 1.1 whereas for the 3D front tracking model the virtual mass coefficient is 0.6. These values of the virtual mass coefficient are in agreement with literature. The deviation from the theoretical value of spherical bubbles is probably caused by the deformation of the bubble.

A bubble in a shear field does not rise in a straight line, but oscillates in the horizontal direction and moves to one side of the column. A bubble with a diameter of 8 mm first moves to the side with the lowest slip velocity and after some time it moves to the side with the highest slip velocity. The bubble with a diameter of 10 mm moves to the side with the lowest slip velocity. When using a lower shear rate, the movement of the bubble is smaller, which is in agreement with theory. The horizontal velocity shows large oscillations due to the oscillating movement of the bubble in the column and is oscillating between a negative to a positive value. Due to the oscillations in horizontal velocity, the lift coefficient changes accordingly. The average lift coefficient for the bubble of 8 mm is positive and the lift coefficient for the bubble of 10 mm is negative. The values are higher than the values in literature (Tomiyama, 1998).
The shape of a bubble of 8 mm is approximately ellipsoidal during the oscillations. The shape of a bubble of 10 mm changes during the oscillations. The bubble is ellipsoidal and during the turn the shape changes to wobbling. This is probably the reason for the differences in the lift coefficient.

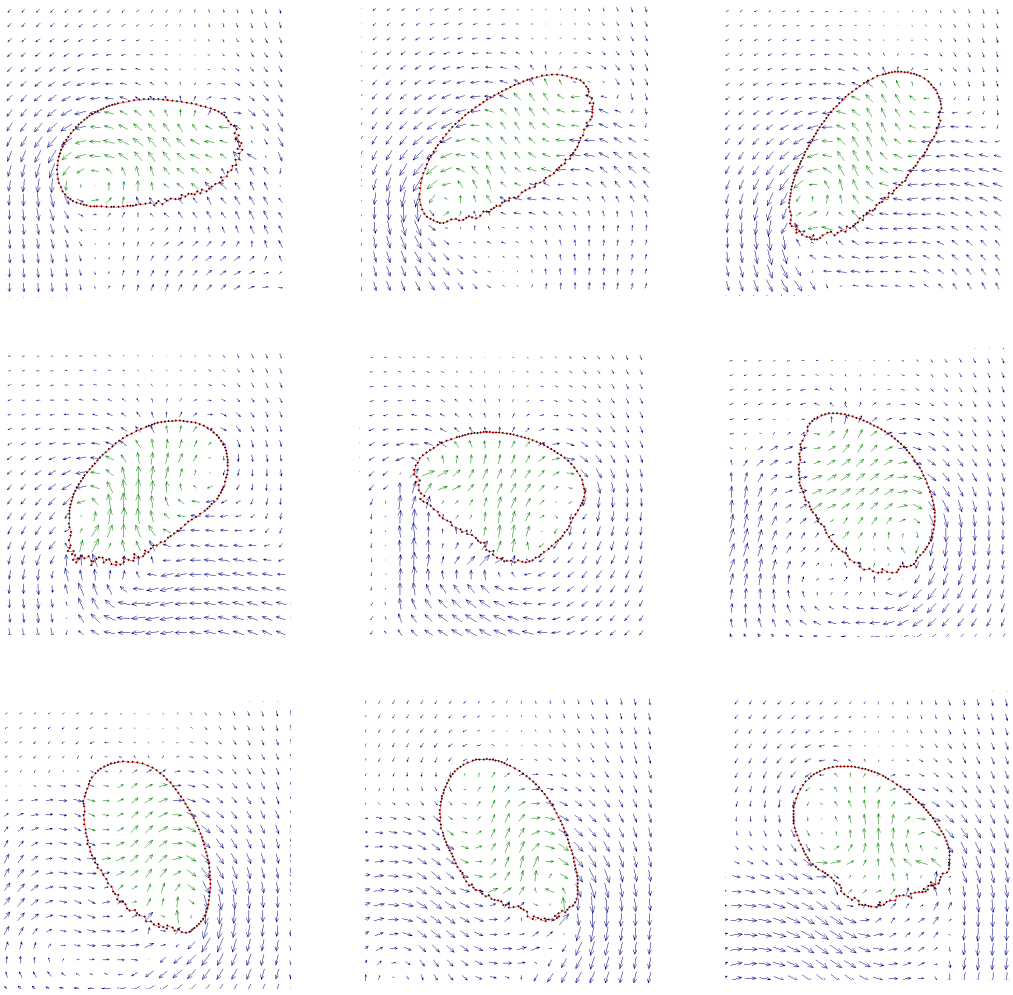

Figure 2.29: Bubble shape for bubble with a diameter of 8 mm in a shear field of 5 s^{-1}.

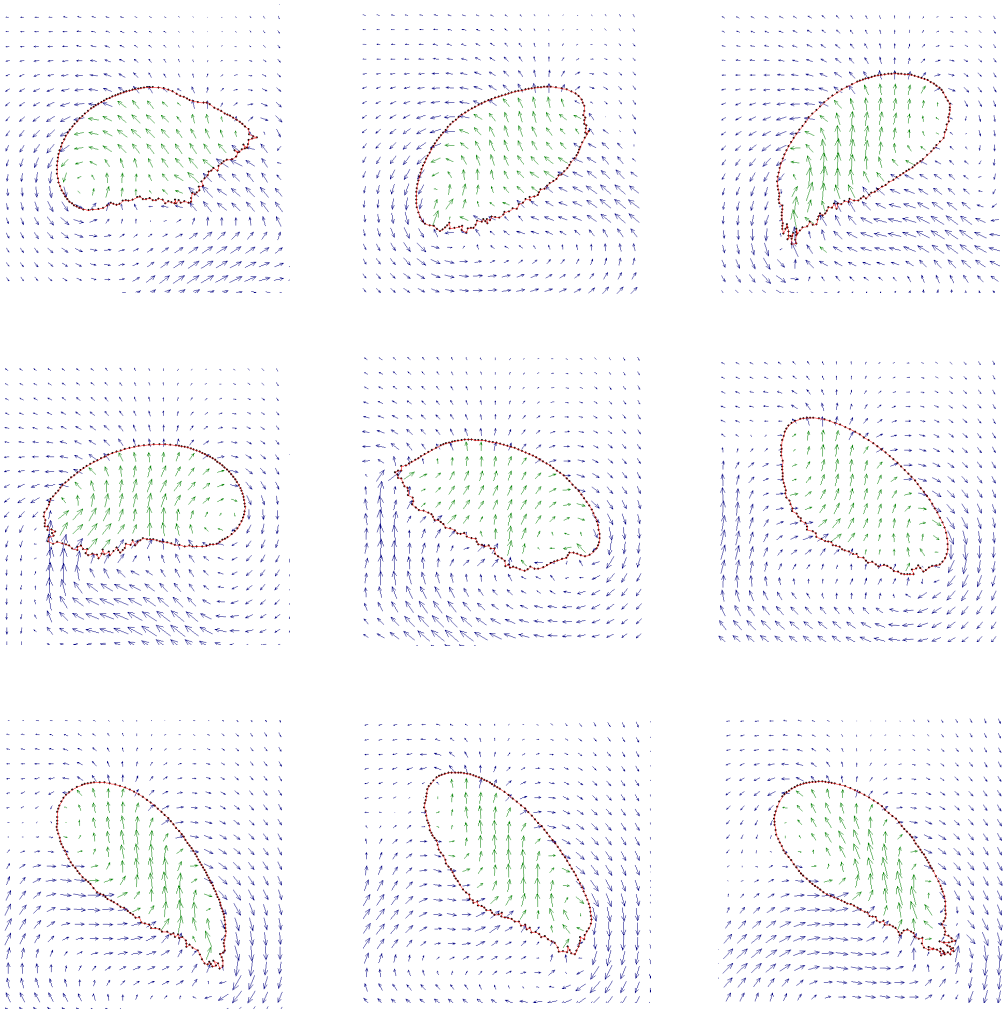

Figure 2.30: Bubble shape for bubble with a diameter of 10 mm in a shear field of 5 s^{-1}.

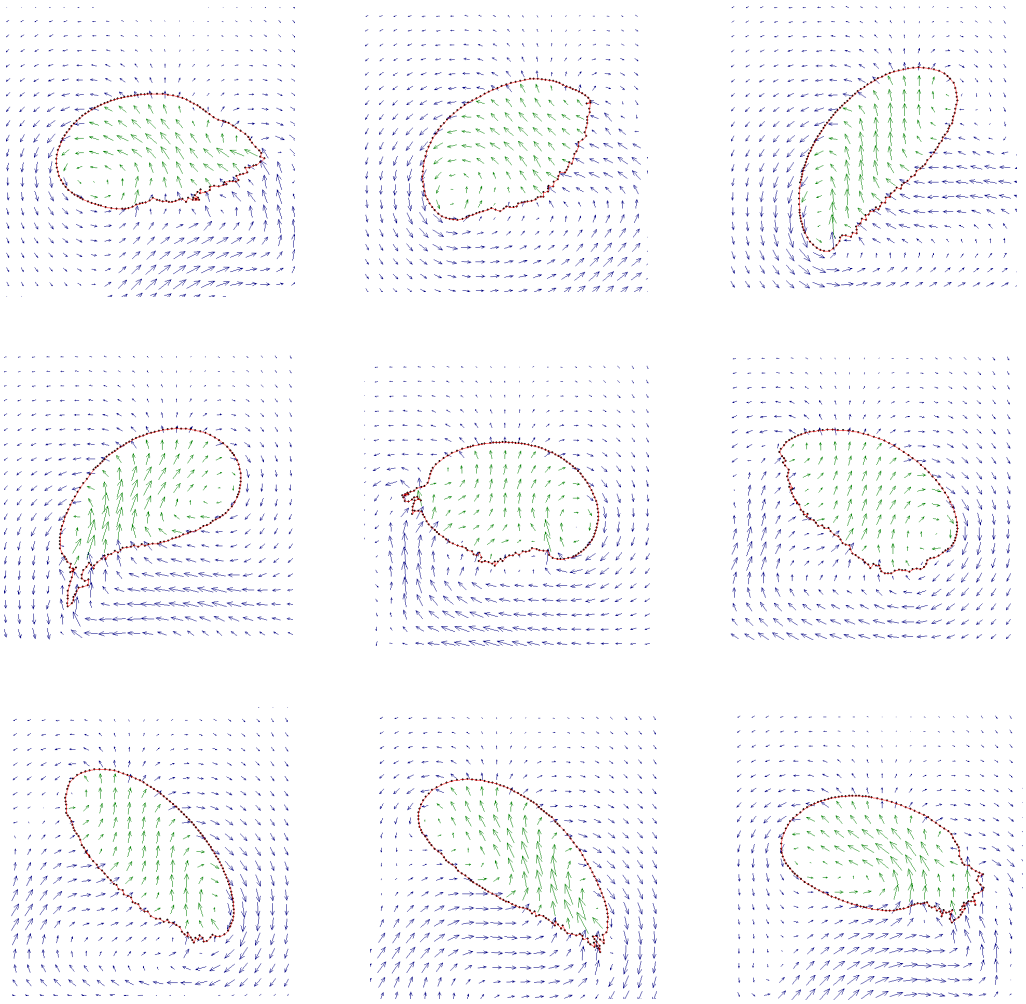

Figure 2.31: Bubble shape for bubble with a diameter of 10 mm in a shear field of 2 s^{-1}.

Chapter 3

DISCRETE BUBBLE MODEL

Abstract

In this chapter a discrete bubble model (DBM) will be used to investigate the hydrodynamics, coalescence and break-up occurring in a bubble column. The DBM will be extended to incorporate models describing the break-up and coalescence along with a closure model for the turbulence.

Simulation results of the DBM with LES model are compared to experimental PIV results of Deen (2001). LES influences the velocity and velocity fluctuations in the bubble column due to an increase of the effective viscosity. The influence of the sub-grid scale velocity is marginal. The average velocity increases due to bubble induced turbulence.

The theory of break-up and coalescence models is given presented and the models are implemented into the DBM. The coalescence model of Chesters (1991) and Lee et al. (1987) showed different results. The number of collisions between two bubbles that result in coalescence is 43 % with the model of Chesters (1991) and 85 % with the model of Lee et al. (1987). Coalescence occurs in the lower part of the column. The mean diameter obtained from the DBM is higher than the experimental mean diameter. The bubble size distribution is narrower. The energy dissipation in the simulated bubble column is too low and hardly any break-up occurs.

3.1 Introduction

In important processes in the chemical industry contact of multiple phases is involved. In these processes gas-liquid mass transfer takes place with accompanying chemical reactions. The specific area is very important for the rate of mass transfer and therefore the bubble size is very important. Processes like break-up and coalescence of bubbles have an enormous impact on the bubble size distribution and thus on the specific area and the rate of mass transfer.
Detailed hydrodynamic models can give insight in the hydrodynamics of bubbly flows. Despite the widespread application of bubble columns and substantial research efforts on their behaviour, detailed knowledge on break-up and coalescence of bubbles is still lacking and is not implemented into the hydrodynamic models.

Flows in industrial bubble columns can be simulated using Euler-Euler or Euler-Lagrange models. The Euler-Euler models treat the different phases as interpenetrating fluids. The Euler-Lagrange model is the next and more detailed level. This model, also called the discrete bubble models (DBM), follows each bubble separately. The liquid phase is described on basis of the volume-averaged Navier-Stokes equations.
In the Euler-Lagrange model each bubble can be followed separately. This can be very useful for studying the behaviour of the bubbles in case of break-up and coalescence and collisions between the bubbles. The incorporation of a bubble size distribution in this model is straightforward. The number of bubbles in the Euler-Lagrange model is limited to a number of about 10^5 and it needs a lot of storage requirements and computer power.
With the Euler-Euler model an industrial bubble column can be simulated and the flow and volume fraction of both phases can be seen in the column. In the Euler-Euler model the number of bubbles is not limited and storage requirements and demand of computer power depend only on the number of volume elements considered and not on the number of bubbles.

Sokolichin *et al*. (1997) compared the results of the Euler-Euler and the Euler-Lagrange model. They noticed that the Euler-Euler approach suffers from numerical diffusion. This is due to the fact, that in the Euler-Euler model the gas fraction is smeared out over the entire cell, whereas in the Euler-Lagrange model no numerical diffusion will be introduced into the dispersed phase since each bubble trace can be calculated accurately within a given volume element. They suggested the use of higher order discretisation scheme for the Euler-Euler model to reduce the numerical diffusion in this approach.

When using an appropriate discretisation scheme the Euler-Euler method provides results, which are in the same order of accuracy as the solution obtained with the Euler-Lagrange method, which is not affected by numerical diffusion.
Sokolichin and Eigenberger (1999) concluded this once more by comparing the results of the Euler-Euler model with the results of Delnoij *et al*. (1997).
Also Lapin and Lübbert (1994) concluded that the Euler-Euler method is very sensitive to numerical diffusion and Euler-Lagrange methods are much better in this respect.

In many calculations turbulence of the continuous phase was not considered. Only an effective viscosity was used in order to match calculated results with measurements.
Laín *et al*. (2001) used the k-ε model to predict the flow in a bubble column. The values for the mean velocities showed reasonable agreement with PIV experiments for both phases, the fluctuating components are overpredicted.
Laín *et al*. (1999) found some problems in prescribing the appropriate drag coefficient. The bubble rise velocity is considerably under-predicted compared to experimental results. This effect is the result of a reduced drag in a bubble swarm.

Euler-Lagrange models for bubble columns, also called discrete bubble models, were first used by Trapp and Mortensen (1993), Lapin and Lübbert (1994) and Devanathan *et al*. (1995). The models developed by these authors differ in their description of the bubble dynamics and in the representation of the coupling between the phases. Lapin and Lübbert (1994) developed a 2D Euler-Lagrange model of a bubble column using a simple description of the bubble dynamics. Coupling between the gas and the liquid phases was achieved through the effective density of the mixture. No exchange of momentum between the phases was incorporated in their model.
The Euler-Lagrange model needs closure relations to account for phenomena at sub-grid scale level. This information can be given by e.g. the VOF model and the front tracking model, as was shown in Chapter 2.

In this study, a 3D DBM model, originally developed by Delnoij (1999) was extended. In the DBM the encounters between bubbles are taken into account. Therefore this model can be used very well to study break-up and coalescence of bubbles. In this chapter the DBM model, developed by Delnoij *et al*. (1997) will be extended to account for turbulence effects, break-up and coalescence and state of the art closures for the forces acting on bubbles will be implemented.

3.2 Theory of the discrete bubble model

The discrete bubble model consists of two coupled parts: A part describing the bubble motion and a part describing the liquid phase motion. The model requires constitutive equations for the forces acting on a bubble. The exchange of momentum between the gas and the liquid phase and vice versa is incorporated as a source term in the momentum equation. The interaction between the bubbles is modelled via an encounter model, including bouncing, break-up and coalescence of bubbles.

3.2.1 Bubble dynamics

With the discrete bubble model the transient behaviour can be simulated. The bubbles are tracked by solving an equation of motion for each individual bubble. The bubble dynamics are described by incorporating all relevant forces acting on a bubble rising in a liquid. The total force $\mathbf{F}_{\text{tot}}$ is assumed to be composed of separate and uncoupled contributions from pressure, gravity, drag, lift and virtual mass (Auton, 1983):

$$\mathbf{F}_{tot} = \mathbf{F}_P + \mathbf{F}_G + \mathbf{F}_D + \mathbf{F}_L + \mathbf{F}_{VM} \tag{3. 1}$$

The force acting on a bubble due to the gravity and pressure gradient, also called the buoyancy force, results in a net upward force.
The equation for the buoyancy force is given by:

$$\mathbf{F}_{Buoyancy} = \mathbf{F}_G + \mathbf{F}_P = \left(\rho_g - \rho_l\right)\mathbf{g}V_B \tag{3. 2}$$

It is noted that **g** points in the negative y-direction.

The relation for the drag force acting on a sphere is given by equation 3.3. The force is proportional to the relative velocity between the bubble and the fluid (**v** - **u**) and acts in the opposite direction to the path of the bubble. **u** in this equation is the instantaneous velocity:

$$\mathbf{F}_D = -\frac{1}{2}C_D\rho_l\frac{1}{4}\pi d_B^2\left|\mathbf{v}-\mathbf{u}\right|\left(\mathbf{v}-\mathbf{u}\right) \tag{3. 3}$$

Tomiyama (1998) proposed three equations, which correspond to a pure, slightly contaminated and contaminated system. These equations are based on a balance of forces acting on a single bubble in an infinite stagnant liquid and on available empirical correlations of terminal rise velocities of single bubbles and are respectively given by:

$$C_D = \max\left[\min\left[\frac{16}{\mathrm{Re}}\left(1+0.15\,\mathrm{Re}^{0.687}\right),\frac{48}{\mathrm{Re}}\right],\frac{8}{3}\frac{\mathrm{Eo}}{\mathrm{Eo}+4}\right] \tag{3. 4}$$

$$C_D = \max\left[\min\left[\frac{24}{\mathrm{Re}}\left(1+0.15\,\mathrm{Re}^{0.687}\right),\frac{72}{\mathrm{Re}}\right],\frac{8}{3}\frac{\mathrm{Eo}}{\mathrm{Eo}+4}\right] \tag{3. 5}$$

$$C_D = \max\left[\frac{24}{\mathrm{Re}}\left(1+0.15\,\mathrm{Re}^{0.687}\right),\frac{8}{3}\frac{\mathrm{Eo}}{\mathrm{Eo}+4}\right] \tag{3. 6}$$

In our DBM equation 3.4 for the pure system is used.

The lift force consists of two parts: the classical shear-induced lateral lift force and the wake induced lift force. Both forces act simultaneously on the bubble.
Auton (1983) derived that the lift force is proportional to the cross product of the slip velocity and the curl of the liquid velocity. This implies that the lift force is perpendicular to the path of the bubble.

$$\mathbf{F}_L = -C_L \rho_l V_B \left(\mathbf{v}-\mathbf{u}\right)\times\Omega \tag{3. 7}$$
$$\Omega = \nabla\times\mathbf{u}$$

The virtual mass force, also called the added mass force, is especially important in cases of unsteady rise when a bubble accelerates or decelerates, e.g. near the nozzle or in a turbulent field. The force can be seen as a resistance to acceleration, as the 'added mass' of the liquid also has to be accelerated when the bubble accelerates. According to Auton (1983) the virtual mass force can be modelled by:

$$\mathbf{F}_{VM} = -\left(\frac{D\mathbf{I}}{Dt}+\mathbf{I}\cdot\nabla\mathbf{u}\right) \tag{3. 8}$$
$$\mathbf{I} = C_{VM}\rho_l V_B\left(\mathbf{v}-\mathbf{u}\right)$$

The value of the virtual mass force is considered to be independent of the void fraction and C_{VM} is taken equal to 0.5 in 3D systems.

For more details about the forces acting on bubbles the reader is referred to Chapter 2.

The acceleration of the bubble can be described by Newton's second law:

$$m_B \frac{d\mathbf{v}}{dt} = \mathbf{F}_{tot} \tag{3. 9}$$

The new bubble velocity can be calculated by using an explicit integration formula:

$$\mathbf{v}^{t+1} = \mathbf{v}^{t} + \left(\frac{d\mathbf{v}}{dt} \right)^{t} dt_{bub} \tag{3. 10}$$

where t and $t+1$ are the old and new time levels respectively.
Once the new velocity is obtained, the bubble position can be calculated as follows:

$$\mathbf{x}^{t+1} = \mathbf{x}^{t} + \mathbf{v}^{t+1} dt_{bub} \tag{3. 11}$$

To resolve the time-dependent motion of the gas and liquid phases, the discrete bubble model uses three different time scales. The biggest time step (dt_{flow}) is employed to solve the Navier-Stokes equations to obtain the macroscopic liquid flow field induced by the rising bubbles. The forces acting on a bubble, as described above, are resolved on a smaller time scale (dt_{bub}). To account for the possible collision between the bubbles and the displacement of the bubbles an even smaller time step t_{ab} is used. During this time step t_{ab} the position of all bubbles in the column changes.

After an encounter of two bubbles in a bubble column the bubbles either coalesce or bounce. In the DBM model, developed by Delnoij (1999), it was assumed that bubbles only collide and bounce, so no coalescence could occur. This assumption is valid for small bubbles. The hard sphere collision model, developed by Hoomans *et al*. (1996), is used to describe the collisions between bubbles. The model describes one collision at a time.

In the collision model a search area is determined in which the possible collision partners of the bubble under consideration are located. The collision partner can be another bubble or a column wall. These collision partners are stored in a so-called 'neighbour list'.
The next step is to calculate the collision time, t_{ab} of the bubble (a) under consideration with all its possible collision partners (b) in the 'neighbour list'.
The collision time t_{ab} of two bubbles can be calculated using the initial position of the bubbles and their velocities:

$$t_{ab} = \frac{-b_{ab} - \sqrt{b_{ab}^2 - \left|\mathbf{v}_a - \mathbf{v}_b\right|^2 \left(\left|\mathbf{r}_a - \mathbf{r}_b\right|^2 - \left(r_a + r_b\right)^2\right)}}{\left|\mathbf{v}_a - \mathbf{v}_b\right|^2} \tag{3. 12}$$

where:

$$b_{ab} = \mathbf{r}_{ab} \cdot \mathbf{v}_{ab} \tag{3. 13}$$

When the collision time t_{ab} of the bubble with all its possible collision partners is calculated, the smallest collision time for each bubble is determined. So each bubble has one most likely collision partner and one collision time. The next step is to determine the smallest collision time of all bubble pairs in the whole column. The bubble positions of all bubbles are updated using the smallest collision time and the known bubble velocities:

$$\mathbf{r}_a(t + t_{ab}) = \mathbf{r}_a(t) + \mathbf{v}_a t_{ab} \tag{3. 14}$$

Two bubbles, with the smallest collision time in the column, collide in the time interval t_{ab}. Their velocity and momentum change due to this collision must be updated. When the bubbles bounce, the velocities of both bubbles are splitted into a normal and a tangential component with respect to the line connecting the centres of mass of both bubbles. The normal component does not change due to a collision between the bubbles a and b, so the tangential component can be calculated using:

$$\left(\mathbf{v}\right)_{aftercollision} = 2\frac{m_a \mathbf{v}_a + m_b \mathbf{v}_b}{m_a + m_b} - \mathbf{v}_a \tag{3. 15}$$

3.2.2 Liquid phase hydrodynamics

The liquid phase hydrodynamics are described using the equations of motion:

$$\frac{\partial(\alpha_l \rho_l)}{\partial t} + \nabla \cdot \alpha_l \rho_l \mathbf{u} = 0 \tag{3. 16}$$

$$\frac{\partial(\alpha_l \rho_l \mathbf{u})}{\partial t} + \nabla \cdot \alpha_l \rho_l \mathbf{u}\mathbf{u} = -\alpha_l \nabla P - \nabla \cdot \alpha_l \tau_l + \alpha_l \rho_l \mathbf{g} + \Phi \tag{3. 17}$$

The influence of the gas phase on the hydrodynamics of the liquid phase is expressed in two ways. First, the presence of the bubbles alters the liquid volume fraction α_l and second, the interface momentum transfer is represented by the term Φ.

The liquid phase stress tensor τ_l is assumed to obey the general Newtonian form given by

$$\tau_l = -\mu_{eff,l}\left(\nabla \mathbf{u}_l + (\nabla \mathbf{u}_l)^T - \frac{2}{3}\mathbf{I}(\nabla \mathbf{u}_l)\right) \tag{3. 18}$$

where $\mu_{eff,l}$ represents the effective shear viscosity.
The effective viscosity $\mu_{eff,l}$ in the equation is composed of three different contributions: The molecular viscosity, the turbulent viscosity and the viscosity due to bubble induced turbulence:

$$\mu_{eff,l} = \mu_{L,l} + \mu_{T,l} + \mu_{BIT,l} \tag{3. 19}$$

There are several models available to take turbulence induced by the movement of the bubbles into account. In this study the model proposed by Sato and Sekoguchi (1975) was used:

$$\mu_{BIT,l} = \rho_l C_{\mu,BIT} \alpha_g d_B \left|\mathbf{v} - \mathbf{u}\right| \tag{3. 20}$$

with a model constant $C_{\mu,BIT}$ which is equal to 0.6.

To calculate the turbulent viscosity $\mu_{T,l}$ a SGS model is used. This model represents the small scale turbulent structures, which are smaller than the grid scale. In the DBM model the model proposed by Smagorinsky (1963) has been used.

The resulting turbulent viscosity is formulated as follows:

$$\mu_{T,l} = \rho_l \left(C_S \Delta\right)^2 |\mathbf{S}| \tag{3. 21}$$

in which C_S is a constant with the value of 0.1, **S** the characteristic filtered rate of strain and $\Delta=(\Delta_x\Delta_y\Delta_z)^{1/3}$ the filter width.

In order to incorporate the influence of the SGS liquid velocity on the bubble dynamics, the following liquid velocity is used in the evaluation of the force balance:

$$\mathbf{u} = \mathbf{u}_{gs} + \mathbf{I} \cdot u_{sgs} \tag{3. 22}$$

The sub-grid scale part of the LES model is mimicked by a uniform random, isotropic process with zero average and RMS value u_{sgs} given by:

$$u_{sgs} = \sqrt{\tfrac{2}{3} k_{sgs}} \tag{3. 23}$$

This equation is used for the x-, y- and z-velocity directions.

The sub-grid kinetic energy k_{sgs} is calculated according to

$$k_{sgs} = C_k \left(C_S \Delta\right)^2 |\mathbf{S}|^2 \tag{3. 24}$$

with C_k a constant with the value of 5 (Mason and Callen, 1986).

By combining equations 3.21, 3.23 and 3.24 the following expression for the sub-grid scale velocity is obtained:

$$u_{sgs} = \frac{\mu_{T,l}}{\left(C_S \Delta\right) \rho_l} \sqrt{\tfrac{2}{3} C_k} \tag{3. 25}$$

3.2.3 Grid mapping

For the calculation of the coupling terms α_l and Φ a so called Euler-Lagrange mapping technique is required. This mapping consists of bubble volume fraction mapping, Euler to Lagrange mapping and Lagrange to Euler mapping.
The mapping technique used by several authors (Delnoij, 1999 and Tomiyama *et al*., 1997) cannot handle bubbles, which are bigger than the Eulerian cell. The size of the bubbles in the DBM is changing due to coalescence and break-up and therefore in the DBM a mapping technique is used, which can handle bubbles, which are smaller as well as larger than the Eulerian grid cell.

The gas volume fraction α_g of a computational cell is calculated from the volume occupied by the bubbles present in the cell under consideration and the volume of the cell itself:

$$\alpha_g = \frac{1}{V_{cell}} \sum_{\forall q \in cell} \zeta^q_{cell} V^q_B \tag{3. 26}$$

where ζ^q_{cell} is the volume fraction of the q^{th} bubble in the cell (see Figure 3.1)

The liquid volume fraction is then easily calculated as:

$$\alpha_l = 1 - \alpha_g \tag{3. 27}$$

Equation 3.26 requires a value of ζ^q_{cell}, which is strongly dependent of the bubble shapes. The bubble shape depends on various parameters, e.g. fluid properties, bubble volume, gravity and the time-dependent flow field around the bubble, so the prediction of the shape is quite difficult. Even for simple shapes such as spherical or ellipsoidal, the calculation of ζ^q_{cell} requires significant computational effort especially if the size of the bubble is larger than the size of the computational grid cell (Darmana, 2004). According to Tomiyama *et al*. (1997) a cubic shape can be used to represent the bubble for two reasons: (1) the calculation of ζ^q_{cell} is easy and takes little CPU time; (2) since the actual bubbles take time-dependent complex shapes, there may be little difference between the cubic approximation and other more sophisticated approximations such as spherical and ellipsoidal shapes.

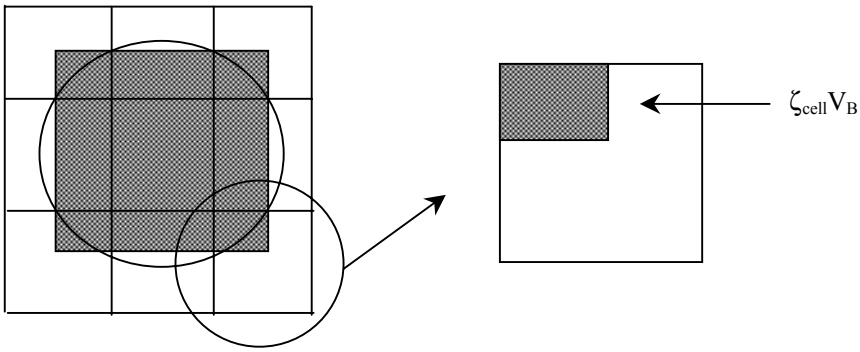

Figure 3.1: Porosity mapping.

Special treatment should be given to cells that are entirely occupied by the bubble, since this breaks the basic assumption of continuum liquid for the liquid phase. To overcome this problem the liquid phase porosity in such a case is set to a minimum value $\alpha_l = \alpha_{low}$. The value of α_{low} influences the accuracy as well as the computational cost to solve the problem. Here $\alpha_{low} = 5\%$ is used.

The momentum transfer rate of the bubbles to the liquid per unit volume Φ, is the opposite of the momentum transfer rate due to drag, lift and virtual mass exerted by the liquid on the bubble in the computational cell. It can be calculated from:

$$\Phi = -\sum_{\forall q \in cell} \left(\mathbf{F}_{D,q} + \mathbf{F}_{VM,q} + \mathbf{F}_{L,q} \right) \zeta_{cell}^{q} \tag{3. 28}$$

To calculate the momentum transfer from the liquid to the bubble (the forces acting on bubbles), all local values of the liquid properties (i.e. pressure and velocity) have to be available at the centre of mass position of the bubble. The closures for the forces acting on bubbles are derived using the far field or undisturbed flow. The Eulerian quantity is not taken at the same place as the mapping region of the bubble but one cell outward (Figure 3.2). In this region the Eulerian quantity is expected to be numerically less disturbed than in the mapping region. Thus under these conditions the bubble experiences the undisturbed liquid flow field as used in the derivation of the closures of the forces.

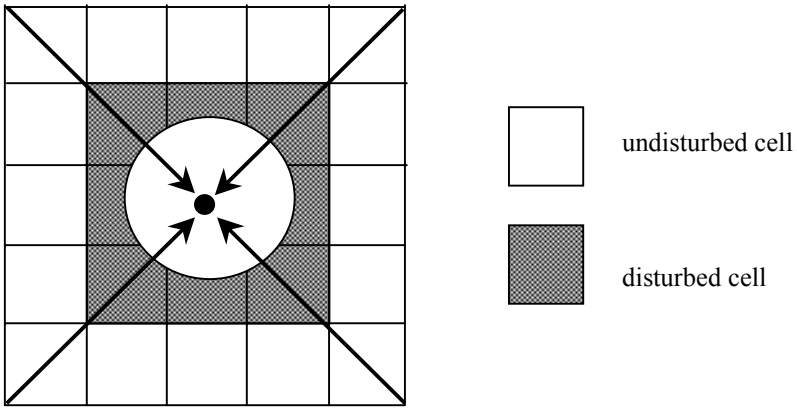

Figure 3.2: Eulerian grid at bubble position.

3.3 Coalescence

In literature many models, which describe coalescence, can be found. Usually the coalescence process is modelled with the coalescence frequency Q. This function is often written as the product of the collision frequency θ and the coalescence efficiency λ:

$$Q(d_a, d_b) = \theta(d_a, d_b)\lambda(d_a, d_b) \tag{3. 29}$$

where d_a and d_b are the diameters of the bubbles considered in the coalescence process.

The coalescence efficiency $\lambda(d_a,d_b)$ is the probability that coalescence occurs between two bubbles with diameter d_a and d_b once collision has occurred. Thus, the efficiency can be described as the fraction of bubbles, which coalesce after collision. The coalescence efficiency is a function of the coalescence time and the contact time, which will be described in the subsequent sections.

The collision frequency $\theta(d_a,d_b)$ is determined by the DBM, because this model accounts for the collisions between bubbles.

3.3.1 Coalescence time

Two main approaches for the coalescence efficiency can be distinguished: One assuming instantaneous coalescence after collision and one involving a drainage process.
In the first process coalescence is assumed to be governed by the impact of the collision of the bubbles: Kinetic collision (Sovová, 1981). The latter type, which includes a drainage process, is most often considered. In this case coalescence can be seen as a three-step process:

1. Collision: Approach of two bubbles to within a distance of 10-100 μm;
2. Drainage: Further thinning of the liquid layer between the bubbles to the so-called critical film thickness;
3. Rupture: Rupture of the thin liquid layer via an instability mechanism which leads to the actual coalescence of the bubbles

The first two steps are rate controlling.

1. Collision
In general only the collision between two bubbles is considered. The turbulent inertial forces are assumed to cause collision. The correct mechanism of the collision is not known explicitly, because no general expression for the trajectory of a bubble in a turbulent flow field exists.

2. Drainage
After collision of the bubbles drainage of the intervening liquid film between the bubbles may take place if a compressive net force on a bubble pair exists. Usually a hydrodynamic force is considered, but also models regarding intermolecular interactions, presence of surfactants or influence of electrical effects have been developed. The coalescence process generally considered in literature for turbulent dispersions is that bubbles, embedded in eddies of inertial range, experience a squeezing force for a finite time (Kumar *et al*., 1993). The acting force is described by the turbulent dynamic pressure, which fluctuates randomly in time. Therefore the film-drainage process can be interrupted any time. The longer the drainage takes the greater the probability of interruption. Before rupture can occur the film has to be thinned to a certain thickness. Several models for this thinning process under influence of a compressive force have been proposed. This thinning process depends on several factors, such as the shape of the

bubble and the flow regime of the drainage flow. Most thinning mechanisms are based on the 'parallel disc model': the surfaces of the coalescing bubbles are modeled at the 'contact side' initially as two parallel plates.

The thinning process may be either inertial or viscous. When inertial forces are predominant, which will be the case for low viscosity turbulent systems, the thinning process is called inertial. In this case the film surface is completely immobile. If only inertial terms are considered, the Bernoulli equation can be used to obtain a thinning rate equation. The inertial thinning time required for removing all liquid from the film between two equally sized bubbles is (Sagert and Quinn, 1976):

$$t_d = \frac{r_d}{4}\left(\frac{\rho_l r_B}{\sigma}\right)^{1/2} \ln\left(\frac{h_i}{h_f}\right) \tag{3. 30}$$

In this equation h_i is the initial thickness of the film in air-water systems is given by Kirkpatrick and Locket (1974) to be 10^{-4} m. The final film thickness h_f is typically taken as 10^{-8} m, where r_d is the radius of the liquid film disc.

For the case of bubbles of unequal size, r_B and r_d in the former equation should be replaced by the equivalent radius (r_{ab}). The equivalent radius is given by Chesters and Hoffman (1982) as:

$$r_{ab} = 2\left(\frac{1}{r_a} + \frac{1}{r_b}\right)^{-1} \tag{3. 31}$$

3. Rupture

If the bubbles remain in contact after collision for sufficient time, the drainage will lead to rupture and coalescence. When the film has become sufficiently thin, the effects of Van der Waals forces and electrostatic double layer forces become significant (Li, 1994). These forces can either enhance or retard drainage. Also the Hamaker force may be considered, which represents the mutual attraction of molecules on opposite sides of the liquid film. Usually the time for rupture is much smaller than the drainage time (time of rupture is about 5% the time of drainage). Therefore there is no need to consider rupture to estimate the time of the coalescence process (Prince and Blanch, 1990). However impurities which act as surface-active agents may increase the time of rupture to the time scale of the drainage process (Lee *et al*., 1987).

The rupture of a free liquid film has been studied by Ruckenstein and Jain (1974) using hydrodynamic stability theory. They have established a kind of wave motion equation, which allows one to calculate the critical wavelength of the perturbations and the time of rupture. Their result for a pure liquid is given by:

$$t_r \approx 6\pi\mu_l h_f^3 A_h^{-1} \tag{3. 32}$$

where A_h is the Hamacker constant which range between 10^{-20} and 10^{-19} joules.

This equation is the lower bound of the time in real systems of the breaking time for a liquid film.

In presence of surface-active impurities the time of rupture depends strongly on the surface concentration of surfactants and can be several orders of magnitude longer than for a pure liquid. Ruckenstein and Jain (1974) have derived an expression for the upper bound of the time of rupture in the system where the surface-active agent is present. The result is given by:

$$t_r \approx 96\pi^2\sigma\mu_l h_f^5 A_h^{-2} \tag{3. 33}$$

Since the breakage time for a liquid film increases with the concentration of the surfactant, Lee *et al*. (1987) proposed a general expression for the breakage time of the liquid film in a real system:

$$t_r = kf(M)\sigma\mu_l h_f^5 A_h^{-2} \tag{3. 34}$$

The simplest representation for *f(M)* is *M*, where *M* is the surface immobility parameter, which usually takes the value 0,1 or 4 depending on whether there are 0, 1 or 2 immobile interfaces, respectively. When there is a surfactant present, *M* can take any value between 0 and 4, and it does not need to be an integer. In general, its value is determined empirically in order to account for the experimental coalescence time. However, it is expected that *M* will increase with the concentration of the surfactant since high surfactant concentration will definitely increase the immobility of the interfaces and therefore increase the film thinning time.

When replacing *f(M)* for *M* this equation can be written as:

$$t_r = 24\pi^2 M \sigma \mu_l h_f^5 A_h^{-2} \tag{3. 35}$$

3.3.2 Contact time

The contact time τ_c is the time two bubbles actually stay together and can be estimated by assuming it is proportional to the characteristic period of velocity fluctuations of an eddy of size d_i+d_j. From Levich (1962) it can be shown that the average contact time is:

$$\overline{\tau}_c = C_1 \frac{\left(d_a + d_b\right)^{2/3}}{\varepsilon^{1/3}} \tag{3. 36}$$

where C_1 is a constant with the value 1 and ε is the energy dissipation.

3.3.3 Coalescence efficiency

In the two preceding sections relations for the coalescence time and the contact time were given. Coalescence will take place if the contact time exceeds the coalescence time ($\tau_c > t_c$).
Ross and Curl (1973) derived an expression for the coalescence efficiency of a particular collision:

$$\lambda = exp\left(-\frac{t_c}{\tau_c}\right) \tag{3. 37}$$

where τ_c is the contact time between two bubbles and t_c is the coalescence time, the time required for coalescence upon collision.
Ross and Curl (1973) assumed that both the contact time and coalescence time are random variables and the contact time is normally distributed.

Most authors consider the coalescence time t_c as the time required for drainage. Lee *et al*. (1987) considered the coalescence time, as the time required for thinning plus the time of rupture:

$$\lambda = \exp\left(-\frac{\frac{r_{ab}}{4}\left(\frac{\rho_l r_{ab}}{\sigma}\right)^{1/2} \ln\left(\frac{h_i}{h_f}\right) + 24\pi^2 M \sigma h_f^5 A_h^{-2}}{\frac{\left(d_a + d_b\right)^{2/3}}{\varepsilon^{\frac{1}{3}}}} \right) \tag{3. 38}$$

Chesters (1991) used the following equation for the coalescence time (drainage time) of two bubbles:

$$t_c \approx \frac{0.5\rho_l v_{rel} r^2}{\sigma} \tag{3. 39}$$

The collision time according to Chesters (1991) is:

$$\tau_c = \left[\frac{\frac{4\rho_g}{3\rho_l} + 1}{2\sigma} \rho_l r^3 \right]^{1/2} \tag{3. 40}$$

When assuming $\rho_l >> \rho_g$:

$$\frac{t_c}{\tau_c} = \frac{1}{2}\sqrt{We} \tag{3. 41}$$

The resulting coalescence efficiency is a function of the Weber number:

$$\lambda = exp\left[-\frac{C_2}{2}\sqrt{We} \right] \tag{3. 42}$$

where C_2 is a constant of order unity.

For high Weber number collisions, the chance of coalescence is small as the bubbles tend to bounce. Only equal sized collisions were considered by Chesters (1991), for he asserted that the equations governing axi-symmetrical film drainage between two unequal bubbles are the same as those for equal bubbles that have a so-called equivalent diameter.

3.4 Break-up

Walter and Blanch (1986) postulated that the turbulent break-up process in a bubble consists of three stages:

1. oscillation of the bubble surface and rippling due to fluctuating pressure forces
2. stretching into the shape of a dumb-bell with two large centers of mass connected by a thin fluid neck
3. two independent bubbles are formed when the neck is pinched off.

The deformation of a bubble due to turbulent fluctuations is three-dimensional. As there seems to be no clear picture of the three-dimensional turbulent flow field in the vicinity of a bubble, only one-dimensional models have been developed in literature.
For breakage two conditions should be fulfilled:

1. the dispersive forces should exceed the stabilizing forces
2. the energy input should be large enough to provide the increase of surface energy; the time duration of the interaction should be long enough to communicate the required energy

Bubble break-up occurs through bubble interaction with turbulent eddies. The eddies responsible for break-up are equal to or marginally smaller than the bubble size. Larger eddies simply transport the bubble without causing break-up, while very small eddies do not contain sufficient energy to affect breakage.

In the DBM the break-up model reported by Luo and Svendsen (1996) is implemented. They did not make any distinction between drops and bubbles in the derivation of their theoretical model. The turbulence in this model is assumed to be isotropic. For bubble columns, the turbulence is non-isotropic (Menzel, 1990). Nevertheless, the isotropic

turbulence assumption has often been used also for these systems (Lee *et al*., 1987a; Prince and Blanch, 1990).
The model of Luo and Svendsen (1996) contains no unknown or adjustable parameters. Their equation for the total breakage rate of a bubble with volume V is:

$$g(V) = \frac{1}{2}\int_0^1 \Omega\left(V : Vf_{BV}\right) df_{BV} \tag{3. 43}$$

where $\Omega(V:Vf_{BV})df$ is the breakage rate of bubbles of volume V into two bubbles, one with volume Vf_{BV} and one with the complementary volume. The factor 0.5 has to be added because $\Omega(V:Vf_{BV})$ and $\Omega(V:V(1-f_{BV}))$ refer to the same event. Analogous to the coalescence frequency the rate function Ω has been defined as a function of the eddy-bubble collision $\vec{\omega}_{\lambda_e}(V)$ and the break-up probability (efficiency) P_{BU}:

$$\Omega\left(V : Vf_{BV}\right) = \int_{\lambda_{min}}^{d_b} P_{BU}\left(V : Vf_{BV}, \lambda_e\right) \vec{\omega}_{\lambda_e}\left(V\right) d\lambda_e \tag{3. 44}$$

where $P_{BU}(V:Vf_{BV},\lambda_e)$ is the probability for a bubble of volume V to break into two bubbles, one with volume Vf_{BV} and one with volume $V(1-f_{BV})$, when the bubble is hit by an eddy of size λ_e; $\vec{\omega}_{\lambda_e}(V)$ is the arrival frequency of eddies of size between λ_e and $\lambda_e+d\lambda_e$ on bubbles of volume V. λ_{min} is the minimum size of eddies in the inertial range.

3.4.1 Arrival frequency

The arrival frequency of eddies with a given size λ_e on the surface of bubbles with size d_b, is equivalent to the collision frequency between the same eddies and the bubbles. The motion of eddies is considered random and the collision frequency of eddies of a size between λ_e and $\lambda_e+d\lambda_e$ with bubbles of size d can be expressed by:

$$\vec{\omega}_{\lambda_e}\left(d_B\right) = \frac{\pi}{4}\left(d_B + \lambda_e\right)^2 \mathbf{u}_{\lambda_e} \dot{n}_{\lambda_e} n_B \tag{3. 45}$$

where $\dot{n}_{\lambda_e}$ is the number of eddies of size between λ_e and $\lambda_e+d\lambda_e$ per unit reactor volume, n_B is the number of bubbles per unit dispersed phase and $\mathbf{u}_{\lambda_e}$ is the turbulent velocity of eddies of size λ_e. The mean turbulent velocity of eddies with size λ_e in the inertial sub-range of isotropic turbulence can be expressed by (Kuboi *et al*., 1972).

$$\mathbf{u}_{\lambda_e} = \left(\frac{8\mathbf{u}^2}{3\pi}\right)^{1/2} = \left(\frac{8\tilde{\beta}}{3\pi}\right)^{1/2} (\varepsilon\lambda)^{1/2} = \beta^{1/2}(\varepsilon\lambda)^{1/3} \tag{3. 46}$$

where the constant $\tilde{\beta} = (3/5)\Gamma(1/3)\alpha_c$. Γ is the gamma function and α_c is a universal constant, as given by Batchelor (1982), based on turbulence energy. $\tilde{\beta}$ becomes about 2.41 when α is 1.5 (Tennekes and Lumley, 1972). The measured value of $\tilde{\beta}$ is 2.0 (Kuboi *et al*., 1972).

The energy spectrum *E(k)* gives the kinetic energy per unit mass contained in eddies of wave number between *k* and *k+dk*, or equivalently of size between λ_e and $\lambda_e+d\lambda_e$ (Tennekes and Lumley, 1972). When this is known, a relationship between $\dot{n}_{\lambda_e}$ and *E(k)* can be obtained as follows:

$$\dot{n}_{\lambda_e}\rho_l\frac{\pi}{6}\lambda_e^3\frac{\mathbf{u}_{\lambda_e}^2}{2}d\lambda_e = E(k)\rho_l(1-\alpha_g)(-dk) \tag{3. 47}$$

where α_g is the local fraction of gas phase.

The functional form of the energy spectrum for the whole range of isotropic turbulence is not available, but in the inertial sub-range it is well described (Tennekes and Lumley, 1972) by:

$$E(k) = \alpha\varepsilon^{2/3}k^{-5/3} \tag{3. 48}$$

The relationship between the wave number and the size of an eddy is $k=2\pi/\lambda_e$ (Tennekes and Lumley, 1972). Therefore, the number of eddies of size between λ_e and $\lambda_e+d\lambda_e$ per unit reactor volume, or the number density of eddies is:

$$\dot{n}_{\lambda_e} = \frac{C_3\left(1-\alpha_g\right)}{\lambda_e^4} \tag{3. 49}$$

where

$$C_3 = \frac{9\alpha}{2\left(2\pi\right)^{2/3}\tilde{\beta}} = \frac{15}{2\left(2\pi\right)^{2/3}\Gamma\left(\frac{1}{3}\right)} \approx 0.822 \tag{3. 50}$$

Equation 3.49 indicates that smaller eddies have higher number densities. However, the equation is only valid for eddies in the inertial sub-range of isotropic turbulence because the used turbulent energy spectrum function and the turbulent velocity are only valid in this range. This limitation will probably have an insignificant effect on the eddy bombarding consideration, since the very small eddies have very low energy contents and very short lifetimes.

The bombarding frequency of the eddies with size between λ_e and $\lambda_e+d\lambda_e$ can be expressed as:

$$\vec{\omega}_{\lambda_e}\left(d_b\right) = \vec{\omega}_{\xi}(\xi) = C_4(1-\alpha_g)n_B(\varepsilon d_B)^{\frac{1}{3}}\frac{(1+\xi)^2}{d_B^2\xi^{\frac{11}{3}}} \tag{3. 51}$$

where $\xi=\lambda_e/d_b$ is the size ratio between an eddy and a bubble and

$$C_4 = \frac{C_3\pi\beta^{1/2}}{4} \approx 0.923 \tag{3. 52}$$

3.4.2 Probability function

The time scale of bubble oscillation is assumed to be smaller than that associated with the eddy bombardment. This implies that once an eddy of sufficiently high energy arrives, this leads to bubble breakage.

Then the condition for an oscillating deformed bubble to break is that the kinetic energy of the bombarding eddy of size λ_ε ($e(\lambda_\varepsilon)$) exceeds the increase in surface energy required for bubble breakage ($\overline{e}_i(\lambda_e)$):

$$e(\lambda_e) \geq \overline{e}_i(d_B) = c_f \pi d_B^2 \sigma \tag{3. 53}$$

where c_f is defined as the increase coefficient of the surface area:

$$c_f = f_{BV}^{2/3} + (1 - f_{BV})^{2/3} - 1 \tag{3. 54}$$

The increase in surface energy is a function of the sizes of the new bubbles.
f_{BV} is the volume ratio of the newly created bubble, with $0 \leq f_{BV} \leq 1$ and c_f in equation 3.54 is symmetrically around $f_{BV} = 0.5$.

This increase in surface energy is determined by the number and the sizes of the daughter bubbles formed in the breakage process.

The probability function $P_{BU}(V:Vf_{BV},\lambda_e)$ for a bubble of size V breaking into a bubble of size $V_1 = Vf_{BV}$ and a bubble of size $V_2 (=V-V_1)$ is then given by:

$$P_{BU}(V : Vf_{BV}, \lambda_e) = 1 - \int_0^{\chi_c} exp(-\chi)\, d\chi = exp(-\chi_c) \tag{3. 55}$$

where χ is the dimensionless energy $(e(\lambda_e)/\overline{e}(\lambda_e))$ and χ_c is the critical dimensionless energy for break-up given by:

$$\chi_c = \frac{\overline{e}_i(d_B)}{\overline{e}(\lambda_e)} \tag{3. 56}$$

A distribution function of the kinetic energy for eddies in turbulence is required to determine the energy contained in eddies of different scales. Lee *et al*. (1987) used Maxwell's law for this function. However, Maxwell's law is especially for free-gas molecular motion and may not be suitable for turbulent eddies. Angelidou *et al*. (1979) have developed an energy-distribution density function for fluid particles in liquids,

which satisfies a natural exponential function. Actually for the kinetic energy of turbulent eddies, this exponential-energy density function is found to be equivalent to the common assumption that the velocity distribution of turbulent eddies is a normal density function (Saffman and Turner, 1956; Coulaloglou and Tavlarides (1977); Narsimhan *et al*. (1979)). This assumption of a normal velocity distribution is also supported by the experimental results of Kuboi *et al*. (1972) for a turbulent liquid-liquid dispersion system.

Hence, this distribution function is also used by Luo and Svendsen (1996) to describe the kinetic energy distribution of the eddies in turbulence:

$$p_e(\chi) = \frac{1}{\overline{e}(\lambda_e)} exp(-\chi); \qquad \chi = \frac{e(\lambda_e)}{\overline{e}(\lambda_e)} \tag{3. 57}$$

The mean kinetic energy of an eddy with size λ_e, $\overline{e}(\lambda_e)$, is given by:

$$\overline{e}(\lambda_e) = \rho_l \frac{\pi}{6} \lambda_e^3 \frac{\mathbf{u}_{\lambda_e}^2}{2} = \frac{\pi\beta}{12} (\varepsilon d_B)^{2/3} d_B^3 \xi^{11/3} \tag{3. 58}$$

When a bubble of size V breaks into two bubbles the increase in surface energy is:

$$\overline{e}_i(d_B) = \left[f_{BV}^{2/3} + (1 - f_{BV})^{2/3} - 1 \right] \pi d_B^2 \sigma = c_f \pi d_B^2 \sigma \tag{3. 59}$$

The choice of daughter particle size distribution has usually been more or less arbitrary by different authors. Most of the functions used, except the uniform distribution, have the same characteristics: equal size breakage has the highest probability and the breakage percentage decreases when $V_1 \downarrow 0$ or $V_1 \uparrow V$. Nambiar *et al*. (1992) have pointed out that these models may not be representative of the underlying physical situation. This is physically correct, because more energy is required for binary equal-sized breakage then for binary unequal-sized breakage. The experimental results of Hesketh *et al*. (1991a) have also shown that equal-sized breakage has the lowest breakage probability, while the highest breakage probability occurs when $V_1 \downarrow 0$ or $V_1 \uparrow V$. Luo and Svendsen (1996) assumed a U-shaped function of the dimensionless daughter size distribution and the lowest breakage probability (which is non-zero) is found for equal-sized breakage for any given original particle size (see Figure 3.3).

To include this phenomenon in the breakage model in the DBM is a continuous function for f_{BV} is used, given by:

$$f_{BV} = 0.5 + 0.5\tanh\left(\frac{10\cdot\left(x_{random} - 0.5\right)}{\pi}\right); \qquad 0 < x_{random} < 1 \tag{3. 60}$$

where x_{random} is determined using the standard random function in C.

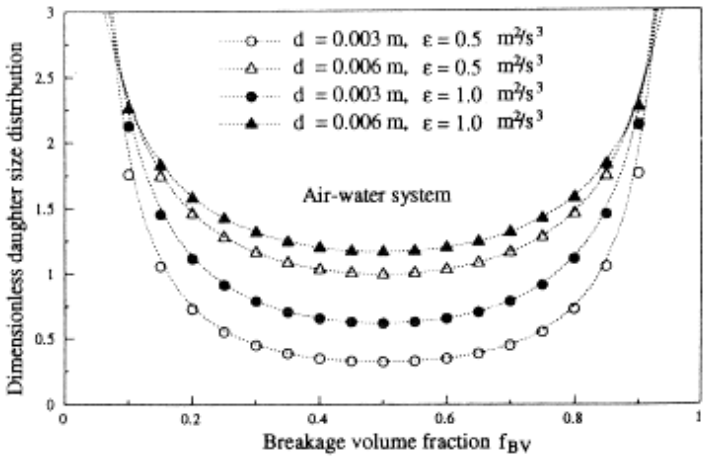

Figure 3.3: Effect of bubble size and energy dissipation rate per unit mass on the dimensionless daughter bubble-size distribution for an air-water system (Luo and Svendsen, 1996).

Substituting equations 3.58 and 3.59 in equation 3.56 gives the following equation for the critical dimensionless energy for break-up:

$$\chi_c = \frac{\overline{e}_i(d_B)}{\overline{e}(d_B)} = \frac{12 c_f \sigma}{\beta \rho_l \varepsilon^{2/3} d_B^{5/3} \xi^{1/3}} \tag{3. 61}$$

Substituting equations 3.51 and 3.55 into equation 3.44 the breakup rate of a bubble with volume V into bubble volumes of Vf_{BV} and $V(1\text{-}f_{BV})$ can be obtained as

$$\frac{\Omega_B\left(V:Vf_{BV}\right)}{\left(1-\alpha_g\right)n_B}=C_4\left(\frac{\varepsilon}{d_B^2}\right)^{1/2}\int_{\xi_{min}}^{1}\frac{\left(1+\xi\right)^2}{\xi^{11/3}}exp\left(-\frac{12c_f\sigma}{\beta\rho_l\varepsilon^{2/3}d_B^{5/3}\xi^{11/3}}\right)d\xi \qquad (3.\ 62)$$

where $\xi_{min} = \lambda_{min}/d_B$.

In the preceding integral the micro-scale of eddies, λ_{ms}, should actually be used as the lower limit, but it has been replaced by the minimum size of eddies in the inertial sub-range of isotropic turbulence λ_{min}:

$$\lambda_{min}=11.4\lambda_{ms} \qquad (3.\ 63)$$

$$\lambda_{ms}=\left(\frac{\left(\frac{\mu_l}{\rho_l}\right)^3}{\varepsilon}\right)^{0.25} \qquad (3.\ 64)$$

The reason for this replacement is that the expression for bombarding frequency of eddies and breakage probability developed earlier are only valid for the inertial sub-range. This change is acceptable since the very small eddies have very low energy contents and very short lifetimes and therefore they have a negligible effect on the breakage of bubbles.

In Table 3.1 an overview of the equations for coalescence and break-up, incorporated in the DBM is given.

Table 3.1: Overview of the equations for coalescence and break-up, incorporated in the DBM

	model	**number equation**
coalescence	Chesters (1991)	3.42
	Lee *et al.* (1987)	3.38
break-up	Luo and Svendsen (1996)	3.62

3.5 Boundary conditions and numerical method

During the initialisation step of the simulation the pressure is set to the hydrostatic pressure in a quiescent liquid without bubbles. The boundary conditions required to solve the system are incorporated using the flag matrix concept (Kuipers *et al*., 1993). With this concept the boundary conditions can be set for each individual computational cell. At all the boundaries of the computational domain, except the top, no slip conditions were applied. For the top the free-slip boundary condition is used. At one grid cell from the top the column contains slids with predescribed pressure cells at all sides of the column. These slids occupy 1/3 of the top row of the column (see Figure 3.4).

Table 3.2: Cell flags and corresponding cell types used in defining boundary conditions.

flag	boundary condition
1	interior cell, no boundary condition specified
2	impermeable wall, free-slip boundary
3	impermeable wall, no-slip boundary
4	fluid phase influx cell, normal velocity has to be specified
5	prescribed pressure cell, free-slip boundary
6	continuous outflow cell, free-slip boundary
7	corner cell, no boundary condition specified

In Figure 3.5 a computational flow diagram of the DBM is shown. After entering the main loop the forces acting on the bubbles present in the computational domain are computed and the bubbles are moved according to the Newtonian laws of motion. The encounter model is used to avoid bubbles to have overlap. Bubbles can bounce of coalesce, depending on the actual local conditions (radius of the bubble, approach velocity). When the bubbles are in a strong turbulent field, the bubbles can break. Bubbles leave the computational domain if they hit the top of the domain.
From the position of the bubbles the local liquid fractions are calculated. As described previously the two-way coupling is achieved by the liquid volume fraction α_l and the interface momentum transfer, represented by the term Φ. This last term is splitted in two parts: a velocity-dependent and a velocity-independent part. The velocity-independent part is taken explicitly, the velocity-dependent part of the velocity is computed implicitly.

The Navier-Stokes equations are discretised on a staggered Eulerian grid. The incomplete Choleski conjugate gradient (ICCG) method is used to solve the pressure-Poisson equation.

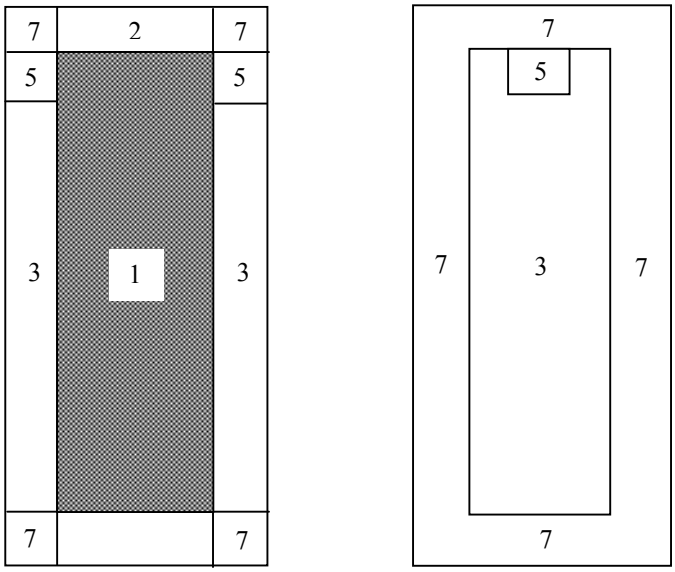

Figure 3.4: Grid lay-out in a simulation with the DBM. The cell flags are explained in Table 3.2. Left: cross-section; right: wall.

For the discretisation of the convection term of the Navier-Stokes equation the second order accurate Barton scheme (Centrella and Wilson, 1984; Hawley *et al.*, 1984; Goldschmidt, 2001) is used.

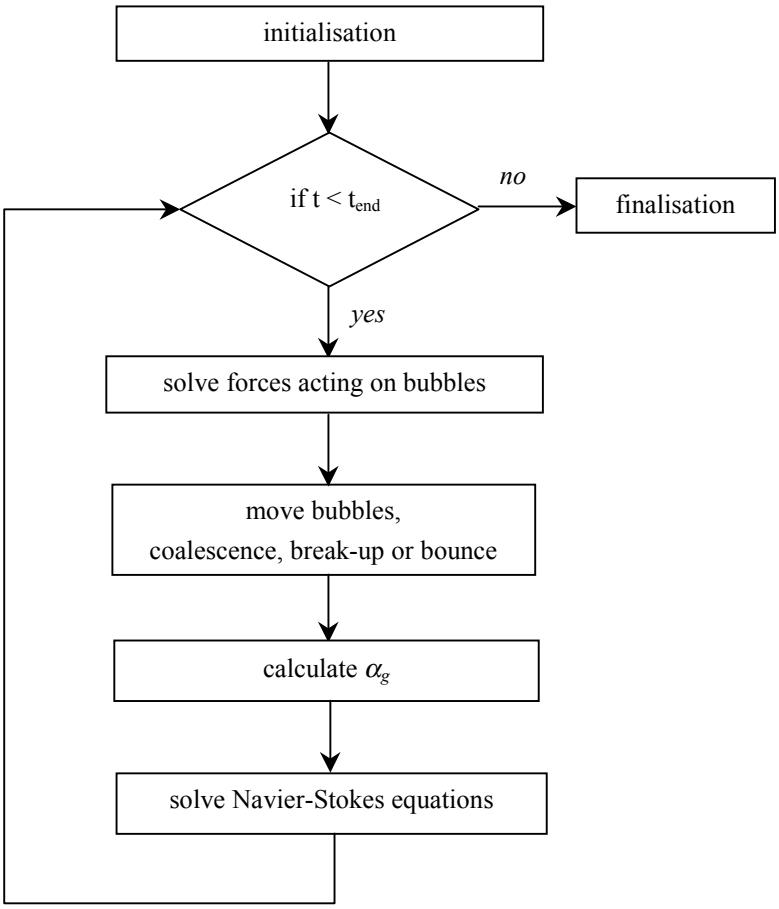

Figure 3.5: Computational flow diagram of the DBM.

3.6 Results grid size, time step and turbulence

The gas-liquid flow in a bubble column is modelled with the DBM as described in the previous sections. In this section the results of the simulations are discussed. First the grid and time step dependence of the model are checked. Next the results of the DBM with and without the LES turbulence model and sub-grid scale velocity are discussed. The different computational cases are listed in Table 3.3.

A standard case (case 0) is used as starting point for the simulations. The results of this standard case are compared to experimental PIV results measured by Deen (2001). The bubble column used by Deen (2001) had a square cross section of 0.15 x 0.15 m^2 and a

height of 1 m. The column was filled with distilled water upto an initial liquid height of 0.45 m. Air was introduced into the column through a perforated plate. The plate contained 49 holes, with a diameter of 1 mm, which were positioned in the middle of the column at a square pitch of 6.25 mm. The superficial gas velocity was 4.9 mm/s, corresponding to a gas flow rate of $2.25 \cdot 10^{-6}$ m^3 s^{-1} per hole.

The simulated bubble column had the same dimensions as the column in the experimental PIV set-up. The perforated plate in the simulated column was also the same as for the experimental set-up. The initial bubble diameter was set to a constant value of 4.0 mm. The grid of the computational domain consisted of 15 x 15 x 45 grid cells and the time step was $1.0 \cdot 10^{-3}$ s.
In the standard case the LES turbulence model (turbulence viscosity $\mu_{T,l}$) and the sub-grid scale velocity are implemented.

Each case was simulated for 180 s and the time-averaged mean velocity and the velocity fluctuations were calculated starting from 20 s.

The time-averaged mean velocity is calculated as:

$$\overline{u} = \frac{1}{N_t} \sum_{\hbar=1}^{N_t} u_{\hbar} \tag{3. 65}$$

where N_t is the number of time steps used in the averaging.
The large scale velocity fluctuations resolved by the model are calculated as follows:

$$\overline{u'} = \frac{1}{N_t} \sqrt{\sum_{\hbar=1}^{N_t} \left(u_{\hbar} - \overline{u} \right)^2} \tag{3. 66}$$

Table 3.3: Overview of different simulation cases for hydrodynamics.

Case	ΔxΔyΔz [mm]	Δt [ms]	$\mu_{T,l}$	$\mu_{BIT,l}$	u_{sgs}
0	10	1.0	Eq. 3.21	0	Eq. 3.23
1	10	0.5	Eq. 3.21	0	Eq. 3.23
2	5	1.0	Eq. 3.21	0	Eq. 3.23
3	10	1.0	Eq. 3.21	0	0
4	10	1.0	0	0	0
5	10	1.0	Eq. 3.21	Eq. 3.20	Eq. 3.23

3.6.1 Grid size and time step

In Figure 3.6, 3.7, 3.8 and 3.9 snapshots of the bubble positions and the liquid phase velocity are displayed for case 0, 1, 2 and 5, respectively. It is found that the flow is driven by a bubble plume, which moves through the column in an oscillatory manner, which is in agreement with experimental observations by Deen (2001). The snapshots of the four cases are about the same. The difference between these cases can be seen in the next section.

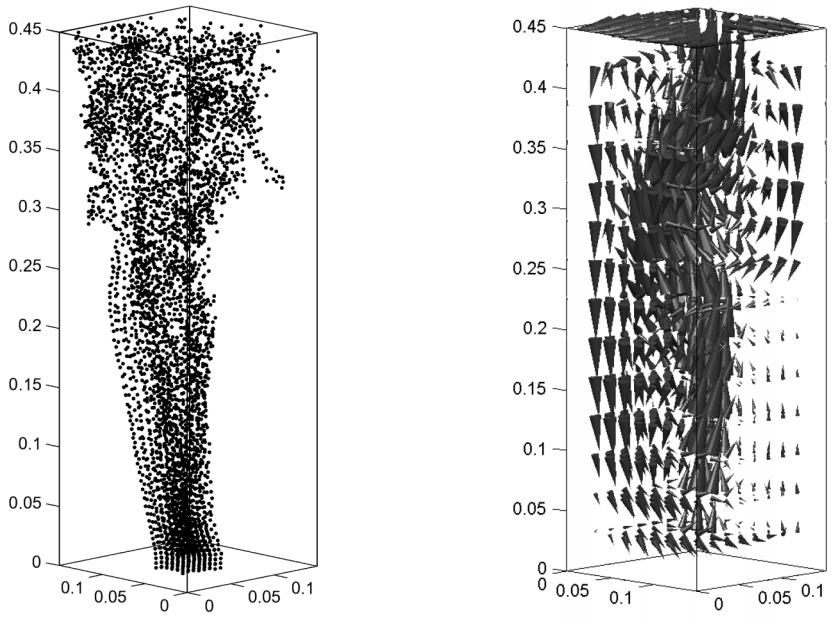

Figure 3.6: Snapshots of the bubble position and the liquid phase velocity after 70 s for the standard case (case 0, see Table 3.3).

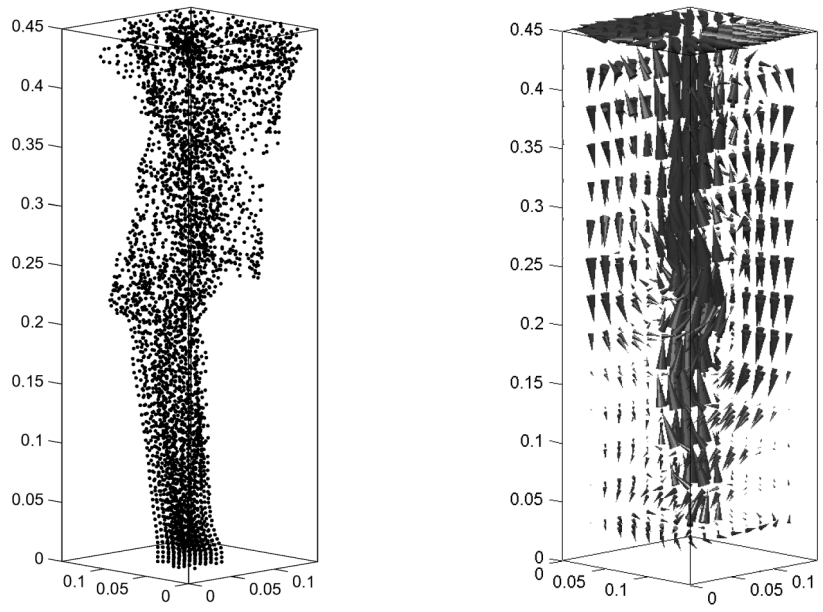

Figure 3.7: Snapshots of the bubble position and the liquid phase velocity after 70 s in the case of a smaller time step (case 1, see Table 3.3).

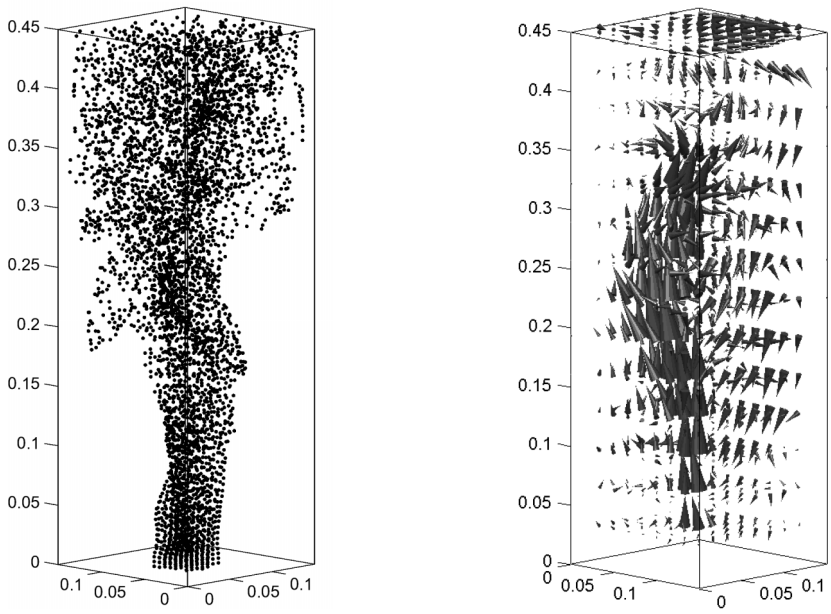

Figure 3.8: Snapshots of the bubble position and the liquid phase velocity after 70 s in the case of a smaller grid (case 2, see Table 3.3).

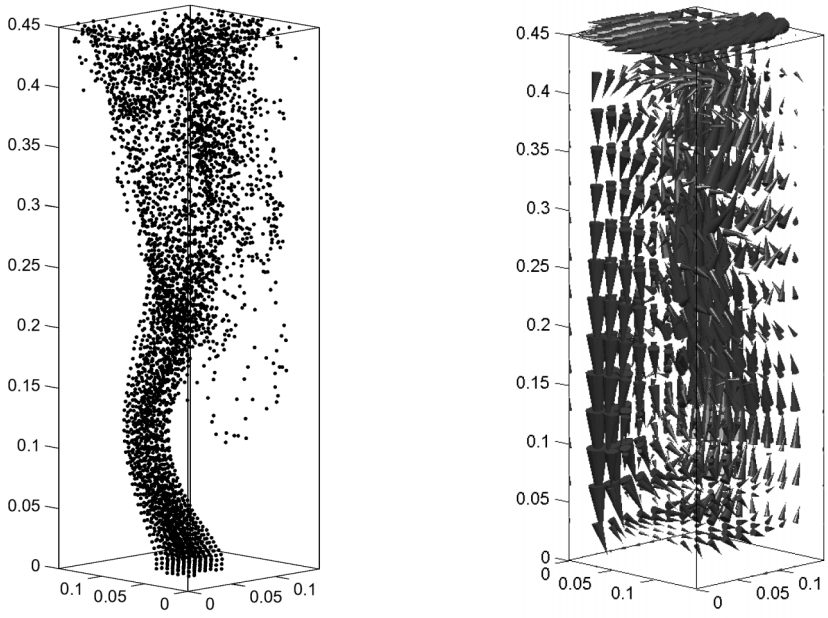

Figure 3.9: Snapshots of the bubble position and the liquid phase velocity after 70 s in the without LES (case 5, see Table 3.3).

Figure 3.10 shows the results of the average liquid velocity at different times, compared to the PIV results. The average velocity is stable after 130 s. The simulated average velocity is higher than the PIV results. In Figure 3.11 the average gas velocity is compared to PIV results. In this figure it can be seen, that also the simulated average gas velocity is higher than the PIV results.

The vertical and horizontal liquid velocity fluctuations of the simulations are shown in Figure 3.12. The vertical fluctuations are of the same order of magnitude compared to the PIV results. The velocity fluctuations, measured with PIV, show a local minimum in the middle, which is not seen in the simulation results. The horizontal fluctuations are lower compared to the PIV results, which indicates an underprediction of the horizontal plume dynamics.

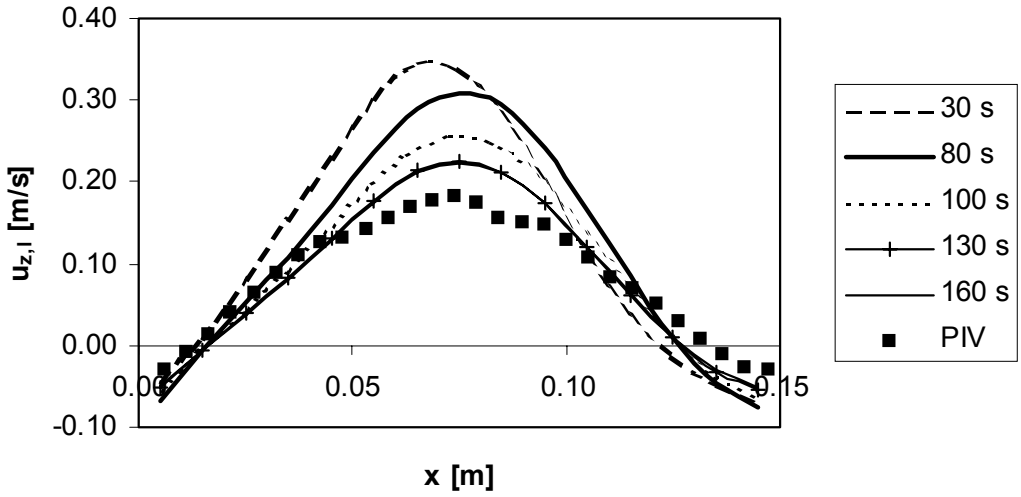

Figure 3.10: Comparison of the simulated and experimental average liquid velocity profiles for the standard case (see Table 3.3) at a height of 0.255 m and a depth of 0.075 m: Effect of the averaging period.

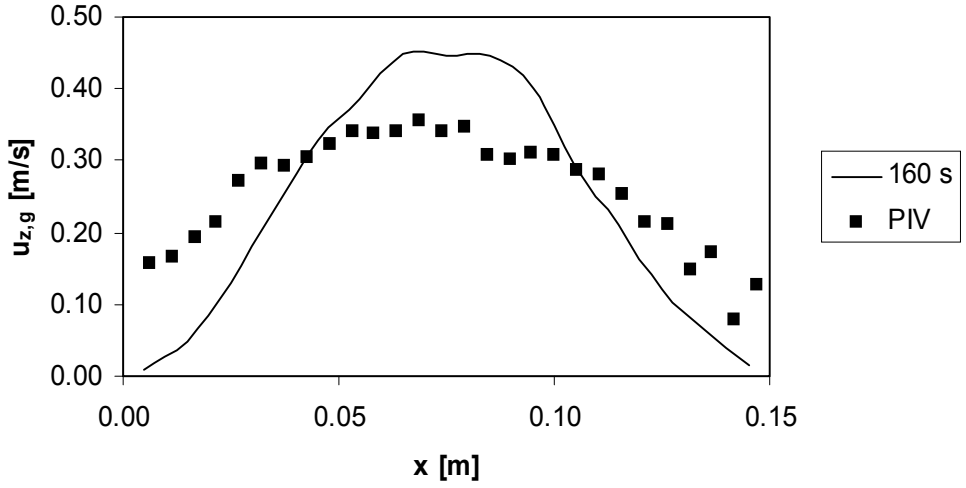

Figure 3.11: Comparison of the simulated and experimental average gas velocity profiles for the standard case (see Table 3.3) at a height of 0.255 m and a depth of 0.075 m.

In Figure 3.13 the average liquid phase velocity profiles and the liquid phase velocity fluctuations for a smaller time step (case 1) are compared to the standard case. The difference between the standard case and the case with the smaller time step is about 25 %. The difference may be attributed to small differences in the pertaining dynamics. The difference between the simulation results with smaller time step and the PIV results is marginal.

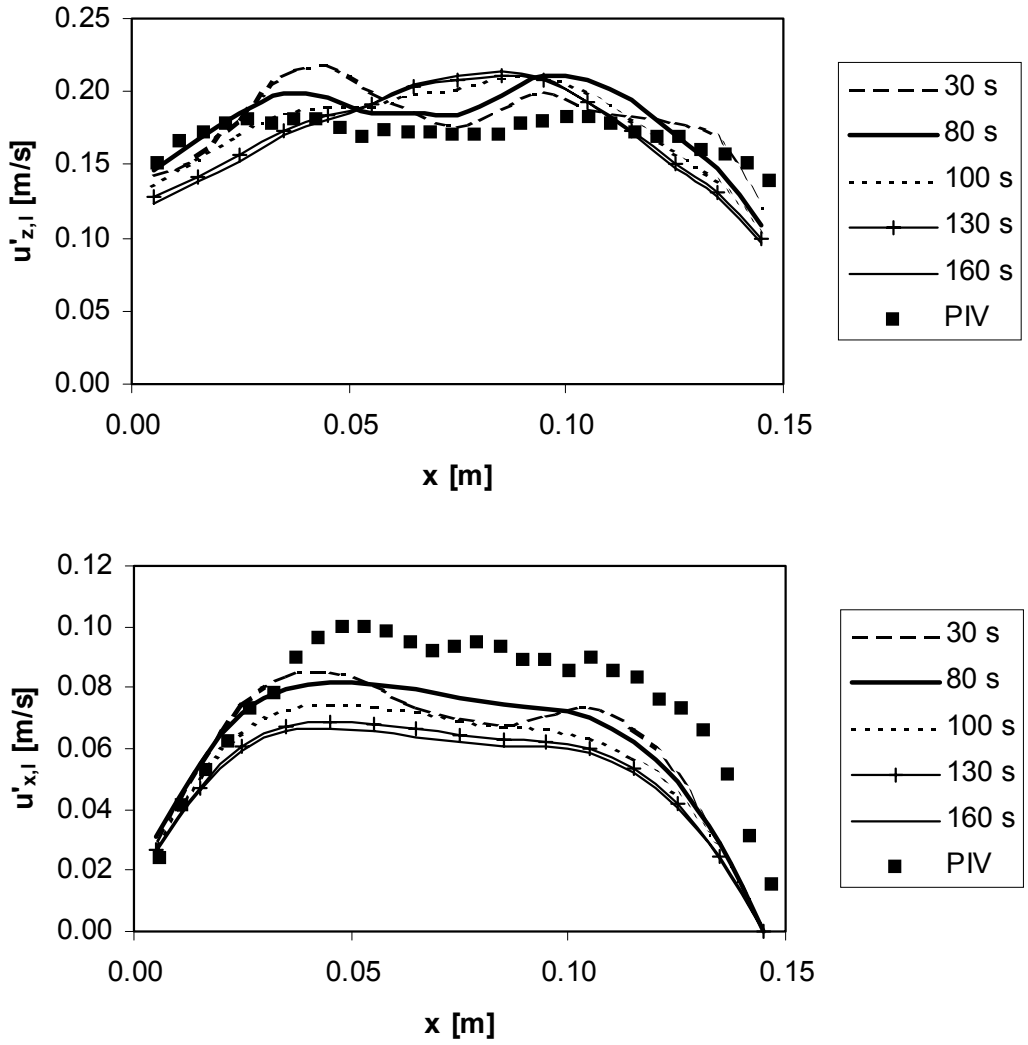

Figure 3.12: Comparison of the simulated and experimental average liquid velocity fluctuations for the standard case (see Table 3.3) at a height of 0.255 m and a depth of 0.075 m.

Figure 3.14 shows the average velocity profiles and the velocity fluctuations results of the liquid phase for a smaller grid size (case 2) compared to the standard case. The difference of the average velocity between the standard case and the case with the smaller grid is about 25 %. The difference between the average liquid velocity profiles of the simulation results with smaller grid size and the PIV results is marginal. The velocity fluctuations of the standard case and the case with smaller time step are about the same.

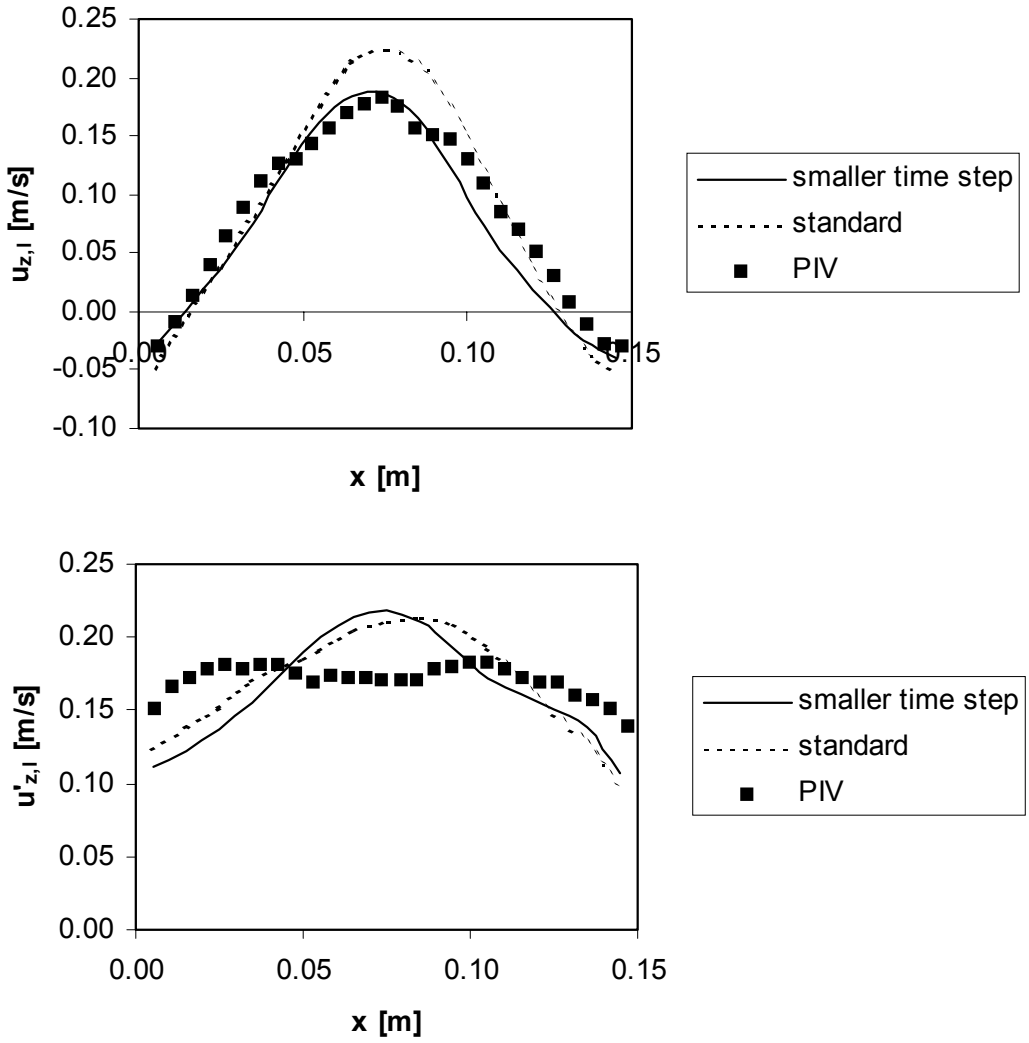

Figure 3.13: Comparison of the simulated and experimental average liquid velocity and velocity fluctuations for case 0 and 1 (see Table 3.3) at a height of 0.255 m and a depth of 0.075 m: Effect of the time step.

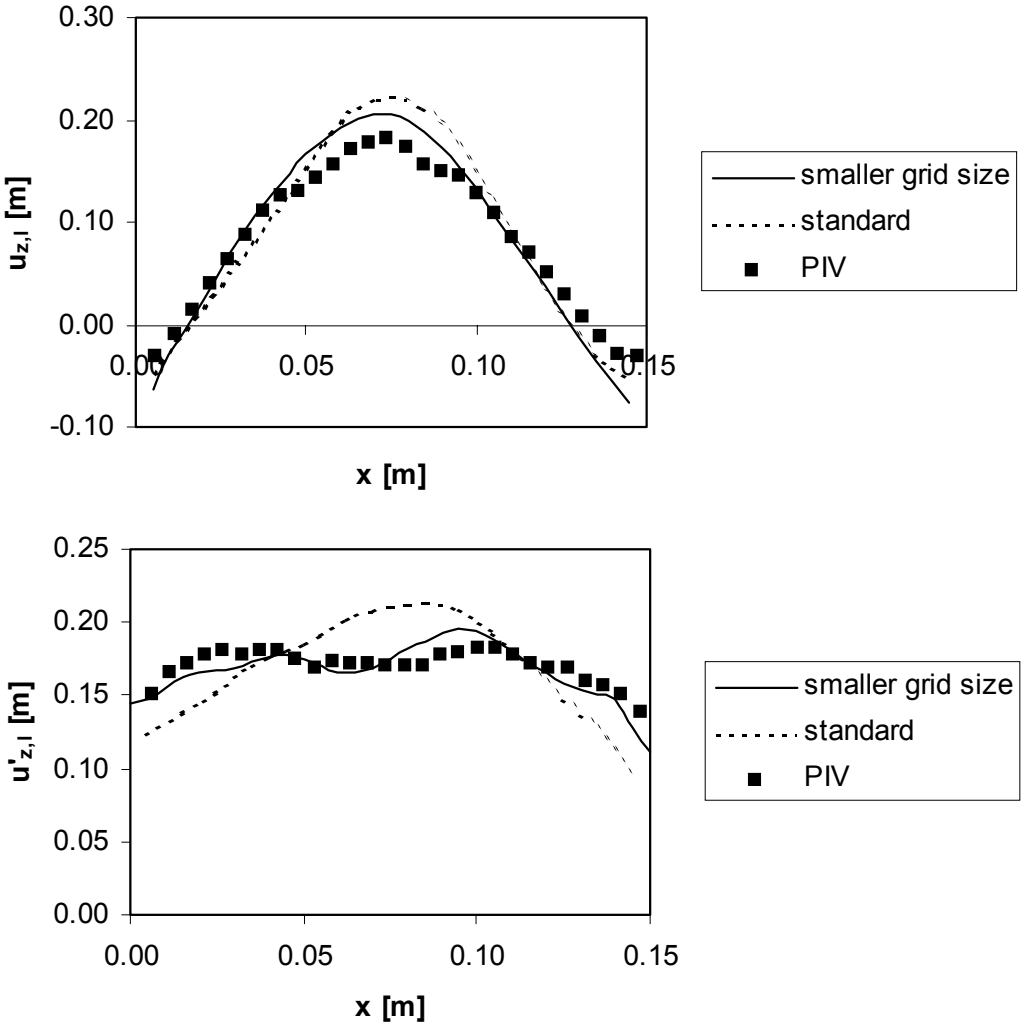

Figure 3.14: Comparison of the simulated and experimental average liquid velocity and velocity fluctuations for case 0 and 2 (see Table 3.3) at a height of 0.255 m and a depth of 0.075 m: Effect of the grid size.

3.6.2 Turbulence

In case 3 the influence of the sub-grid scale velocity is investigated. The simulation results of the standard case are compared to simulation results of the case without sub-grid scale velocity.

In Figure 3.15 the results of the simulated profiles of the average velocities and velocity fluctuations are shown. The differences between the cases with and without sub-grid

scale velocity are marginal, about 8 %. Apparently the unresolved part of the liquid velocity can be neglected as compared to the resolved grid scale liquid velocity.

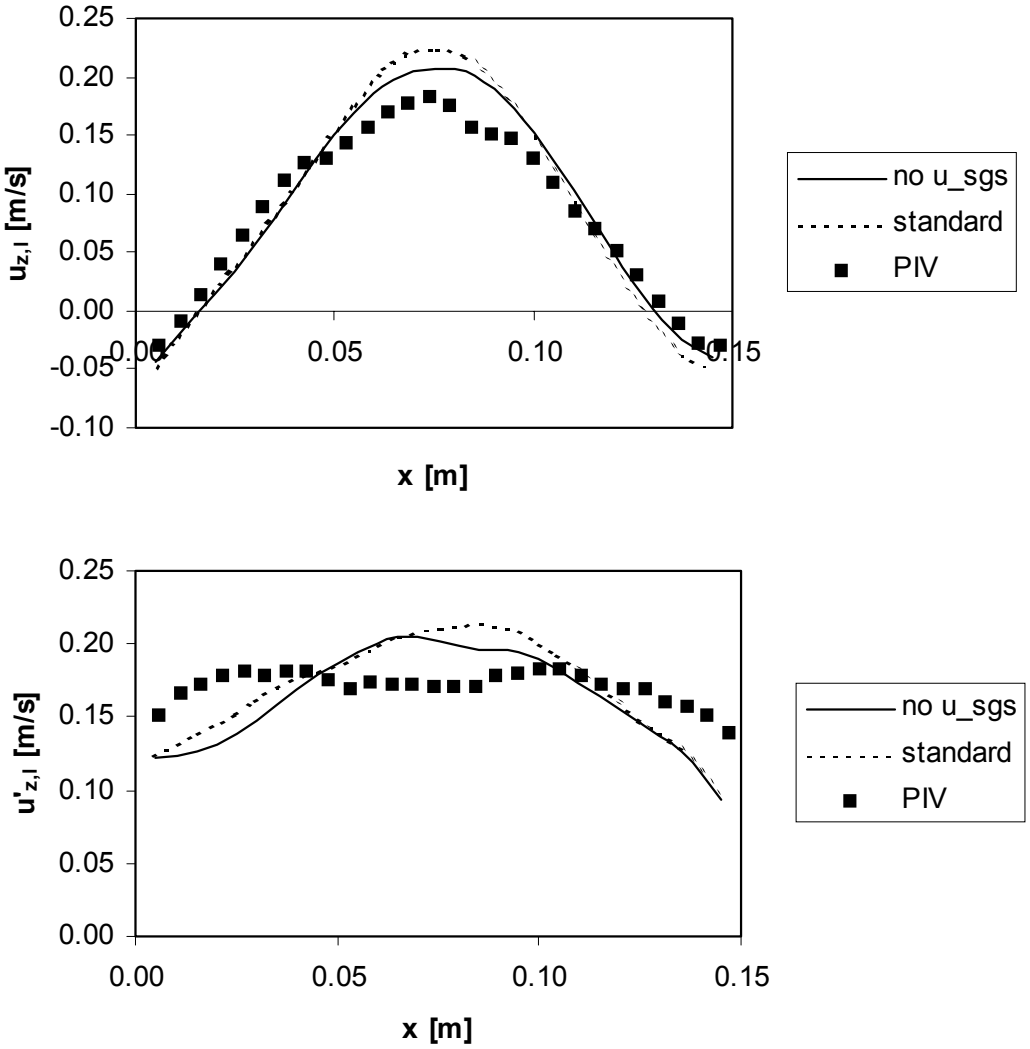

Figure 3.15: Comparison of the simulated and experimental average liquid velocity and velocity fluctuations for case 0 and 3 (see Table 3.3) at a height of 0.255 m and a depth of 0.075 m: Effect of the sub-grid scale velocity.

In case 4 the simulation results of the average velocity profiles and the velocity fluctuations of the case with LES are compared to the case without LES. As can be seen in Figure 3.16 the average velocity profiles of the case with LES are much higher than in the case without LES. When a turbulence model is incorporated, the effective viscosity is considered higher than when only the molecular viscosity is active. Low viscosities lead

to less dampening of the bubble plume dynamics. This in turn leads to flatter average liquid velocity profiles. It appears that the vertical velocity fluctuations are less influenced by the choice of the turbulence model. The horizontal velocity fluctuations are higher in the case without LES, which indicates less underprediction of the horizontal plume dynamics.

In case 5 the influence of the bubble induced turbulence is investigated. The simulation results of the average velocity profile and the velocity fluctuations of the standard case are compared to the simulation results of the case with bubble induced. As can be seen in Figure 3.17, the average velocity profiles in the case with bubble induced turbulence are higher than in the case without bubble induced turbulence. The difference is about 10 %. When the bubble induced turbulence is incorporated, the effective viscosity is higher than without bubble induced turbulence. This leads to more dampening of the bubble plume dynamics and to a higher maximum of the average liquid velocity profiles. As a consequence the velocity fluctuations for the horizontal and the vertical direction are lower when bubble induced turbulence is incorporated.

3.6.3 Lift coefficient

The value of the lift coefficient in the standard case is 0.5. To study the influence of the lift coefficient this value is reduced to 0.3, which is the value suggested by Tomiyama (1998). In Figure 3.18 the results of the average velocity profile and the velocity fluctuations can be seen. It is found that the average velocity profiles in the case of C_L=0.3 are much higher than in the case of C_L=0.5. In the case of C_L=0.3, the spreading of the plume is less and therefore the dynamics of the plume are reduced, which leads to a higher average velocity in the centre of the column. This observation can also be confirmed by the velocity fluctuations. The velocity fluctuations in the vertical direction in the case with C_L=0.3 are higher than in the case with C_L=0.5. The velocity fluctuations in the horizontal direction are lower in the case with C_L = 0.3. The observed behaviour is in agreement with the findings of Deen *et al.* (2001), who showed that a lift coefficient of zero leads to a significant overprediction of the liquid velocities in the centre of the column.

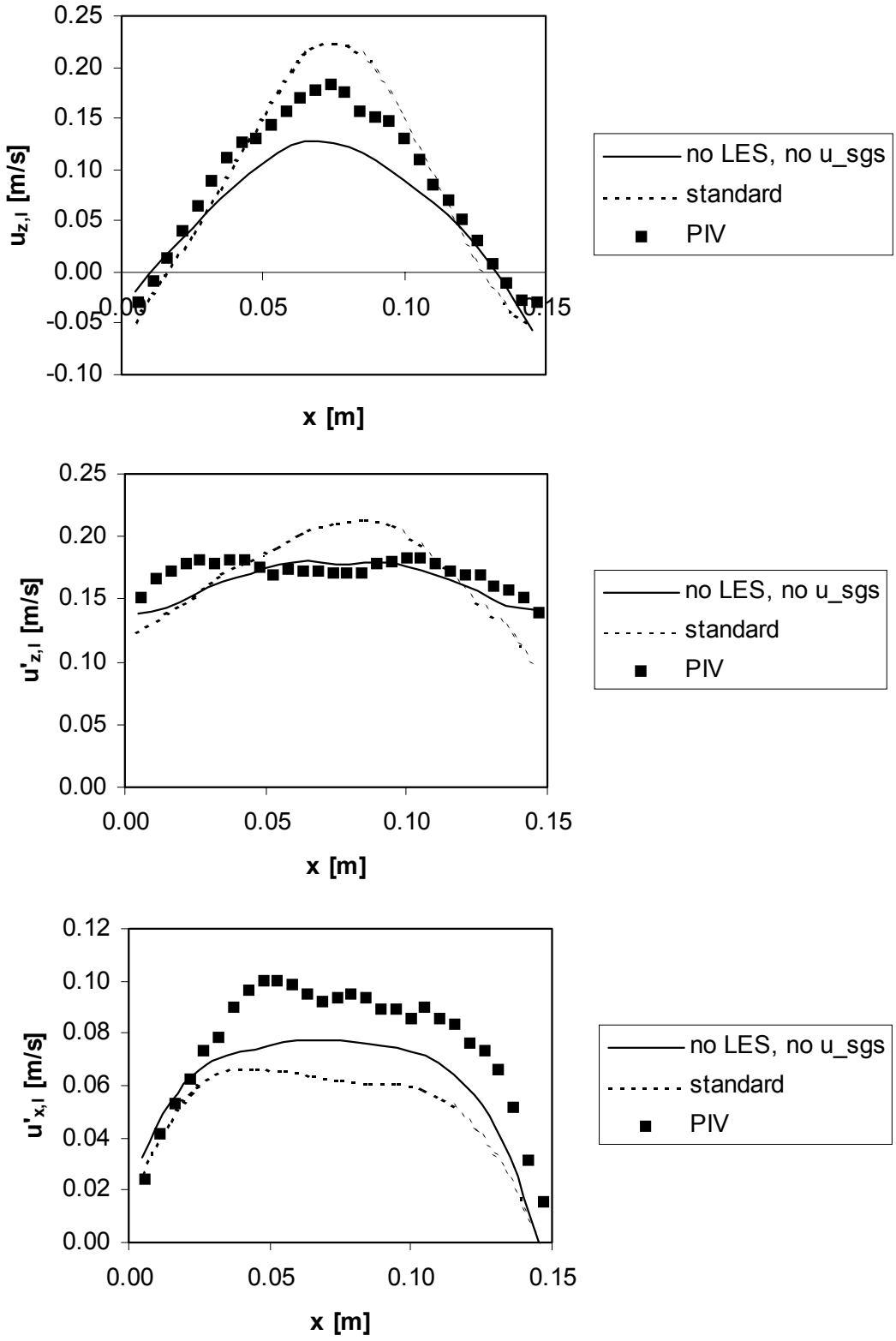

Figure 3.16: Comparison of the simulated and experimental liquid velocity and velocity fluctuations for case 0 and 4 (see Table 3.3) at a height of 0.255 m and a depth of 0.075 m: Effect of the LES model.

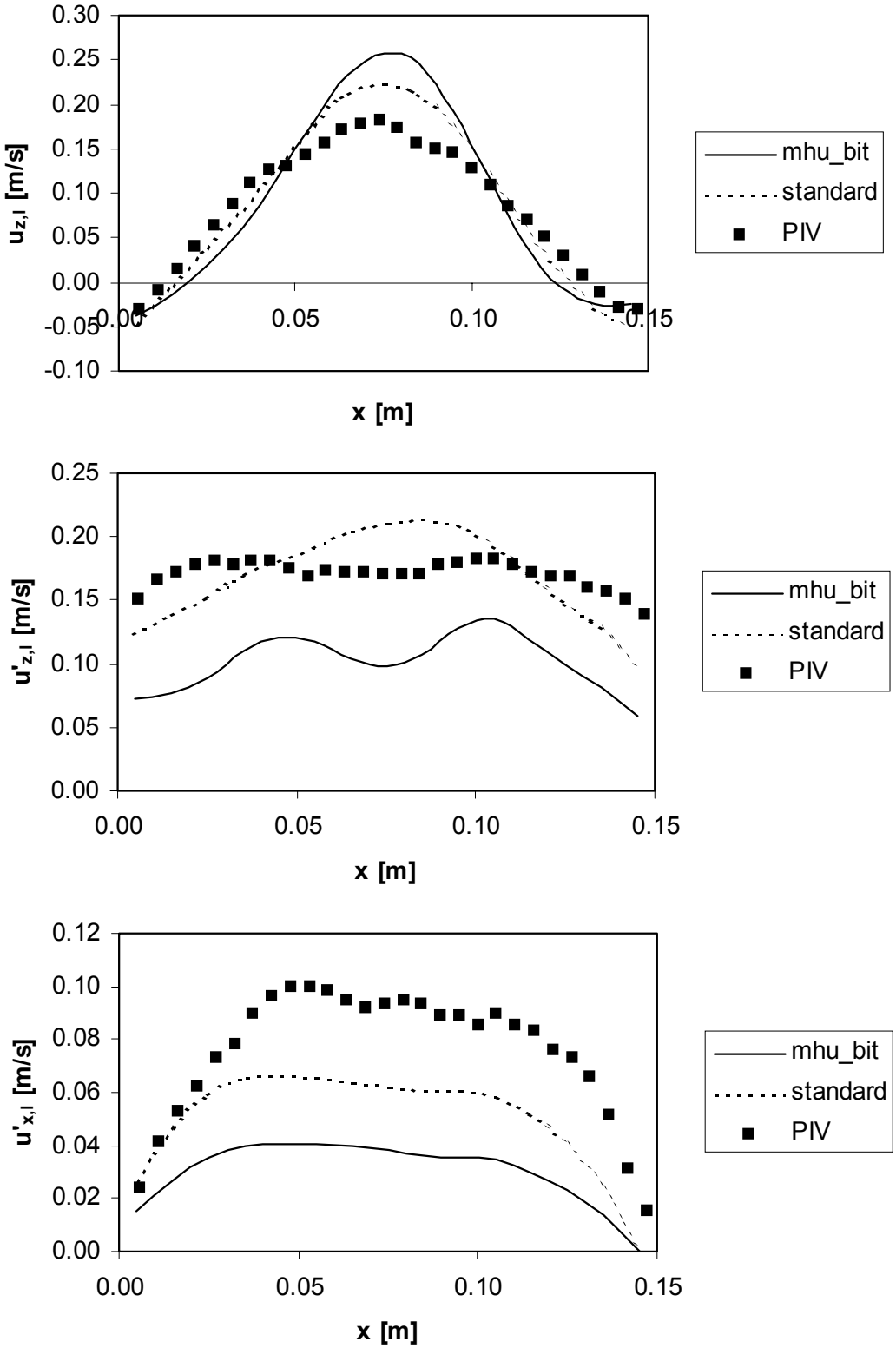

Figure 3.17: Comparison of the simulated and experimental liquid velocity and velocity fluctuations for case 0 and 5 (see Table 3.3) at a height of 0.255 m and a depth of 0.075 m: Effect of the bubble induced turbulence.

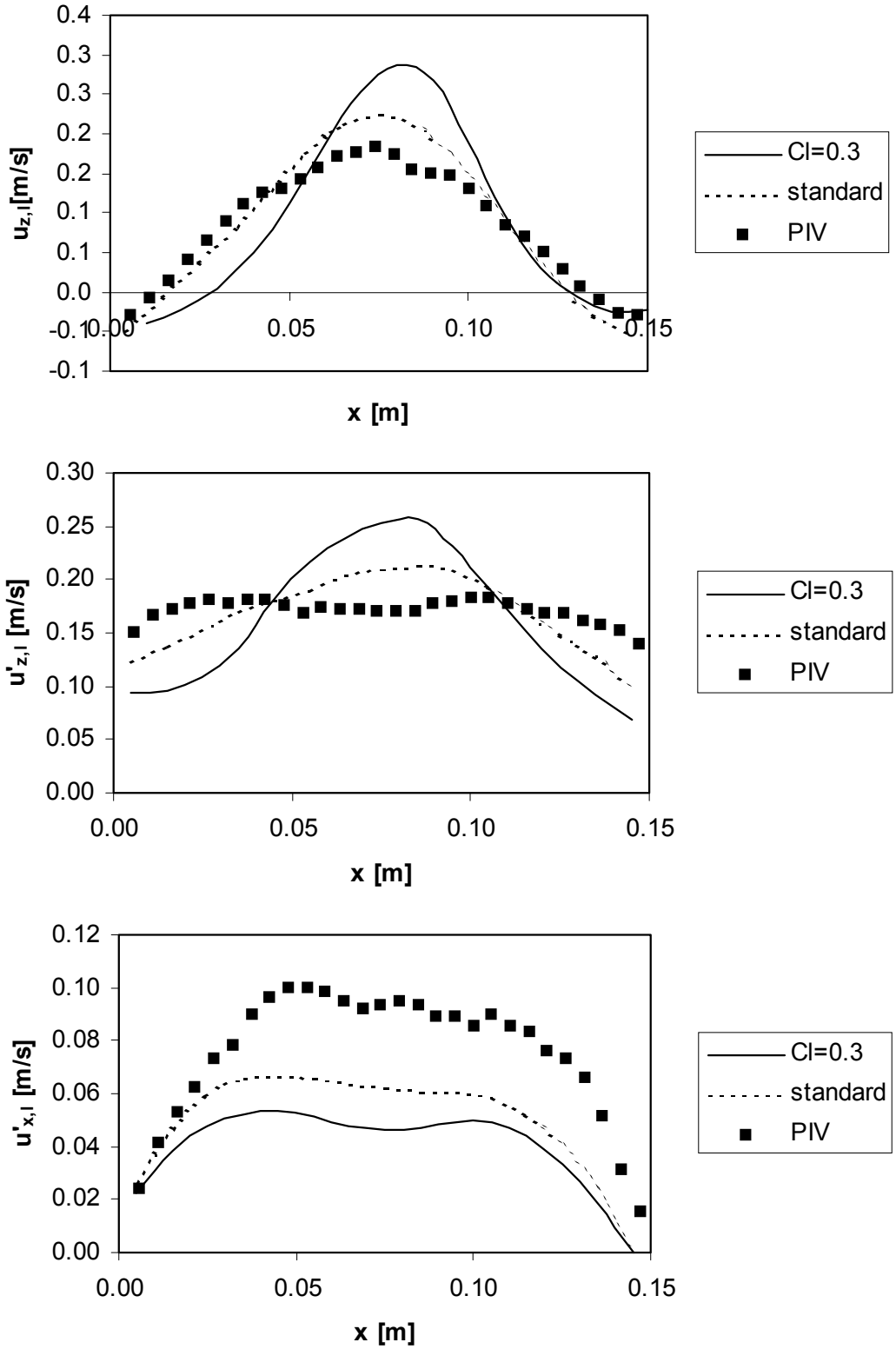

Figure 3.18: Comparison of the simulated and experimental liquid velocity and velocity fluctuations for case 0 and 5 (see Table 3.3) at a height of 0.255 m and a depth of 0.075 m: Effect of the lift coefficient.

3.7 Results break-up and coalescence

3.7.1 Break-up

For the break-up of bubbles the energy dissipation is an important parameter. The break-up model of Luo and Svendsen (1996) and others were developed for $\varepsilon > 0.5$ m^2 s^{-3}. In bubble columns with low gas flows and low turbulence the energy dissipation is in the order of 10^{-2}. This was also observed in simulations where the model of Luo and Svendsen (1996) was implemented. When this energy dissipation rates are used in the break-up model, hardly any break-up occurs. The simulation results indicate, that break-up only occurs in the top of the column. The energy dissipation in case of break-up is larger than 10^{-1} and the bubble diameters are generally large (> 5 mm). In this case the break-up rate is around 10^{-4}, which is high enough for break-up to occur. In order to further validate the break-up model, cases experiencing a higher energy dissipation rate should be considered in future research.

3.7.2 Coalescence

In the DBM the coalescence model of Chesters (1991) (equation 3.42) and Lee *et al.* (1987) (equation 3.38) are implemented. In this section the results of the simulations are discussed and compared to with experimental results, which were obtained with digital image analysis, which is described in Chapter 5. The different computational cases are listed in Table 3.4. In all cases also the break-up model of Luo and Svendsen (1996) was implemented.

The break-up and coalescence model are verified with the use of a pseudo 2D bubble column. The bubble column has the dimensions of 0.20 x 0.03 x 1.40 m. The bottom of the column contains a nozzle of 2 cm with a membrane. By using a membrane in the nozzle the incoming bubbles in the plume have a bubble size distribution around 3 mm. This value was used as the initial bubble size in the simulations.
The grid of the computational domain consists of 20 x 3 x 140 grid cells and the time step is $1.0 \cdot 10^{-3}$ s. In the simulation the sparger is modelled as 8 nozzles in two rows of four nozzles. The distance between the nozzles is 1 cm. The bubbles are entering the column with a normal bubble diameter distribution. The LES model is used to model the sub-grid

scale turbulence. Each case was simulated for 130 s., which appears to be sufficient, as was found in the previous section.
The simulation results of the two coalescence models are compared with the experimental results by means of the bubble size distribution. The number of classes used in the bubble size distribution is 10. Furthermore the number mean, volume mean and Sauter mean diameter are calculated at 4 different heights of the column. These three diameters are respectively given by:

The number mean diameter (average diameter of all bubbles in the sample):

$$d_{10} = \frac{1}{N_B} \sum_{k=1}^{N_B} d_k \tag{3. 67}$$

The volume mean diameter (diameter of a bubble whose volume, if multiplied by the total number of bubbles, equals the total volume of the sample):

$$d_{30} = \left(\frac{1}{N_B} \sum_{k=1}^{N_B} d_k^3 \right)^{\frac{1}{3}} \tag{3. 68}$$

The Sauter mean diameter (diameter of a bubble whose ratio of volume to surface area is the same as the complete sample):

$$d_{32} = \frac{\sum_{k=1}^{N_B} d_k^3}{\sum_{k=1}^{N_B} d_k^2} \tag{3. 69}$$

Table 3.4: Overview of different simulation cases coalescence.

case	**coalescence model**	**superficial gas velocity [m/s]**
1	eq. 3.42	$2.78 \cdot 10^{-3}$
2	eq. 3.38	$2.78 \cdot 10^{-3}$
3	eq. 3.42	$1.39 \cdot 10^{-3}$
4	eq. 3.42	$4.17 \cdot 10^{-3}$

Two important parameters for coalescence to occur are the collision rate and the coalescence efficiency. The collision frequency is determined by the DBM. For every collision the coalescence efficiency is calculated. It was found that in the simulations for the coalescence model of Chesters (1991) (case 1) that 43 % of all collisions results in coalescence. The coalescence efficiency is around 0.43 for the whole column.
Most of the collisions and thus of the coalescence occur in the lower part of the column because in this part the bubbles stay together in a plume. In the upper part of the column the bubbles are more spread over the column and the change for collision is smaller. Most of the collisions occurs in the lower part of the column (see Figure 3.19).
For the coalescence model of Lee *et al.* (1987) (case 2) the results are different. 85 % of all collisions results in coalescence. Most coalescence occurs in the lower part of the column, in the same area as in the model of Chesters (1991) (see Figure 3.20).

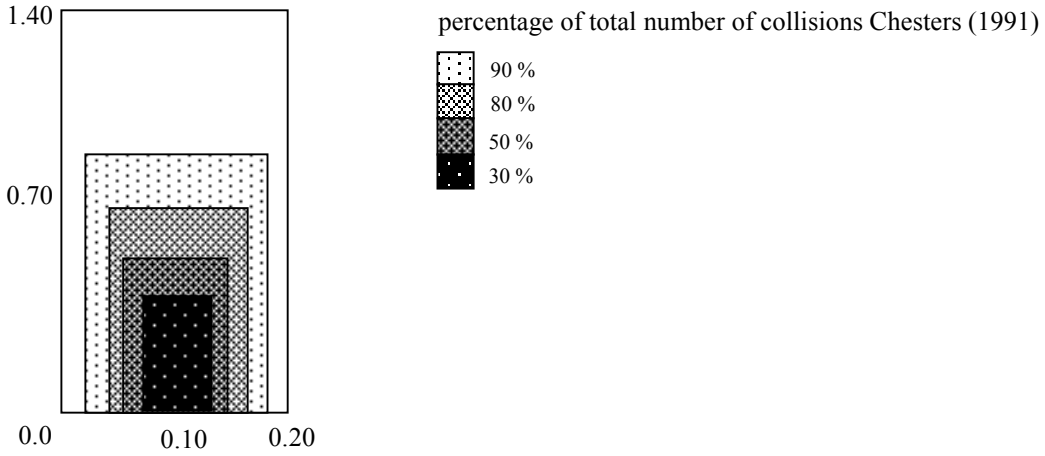

Figure 3.19: Percentage of collisions in bubble column with the model of Chesters (1991).

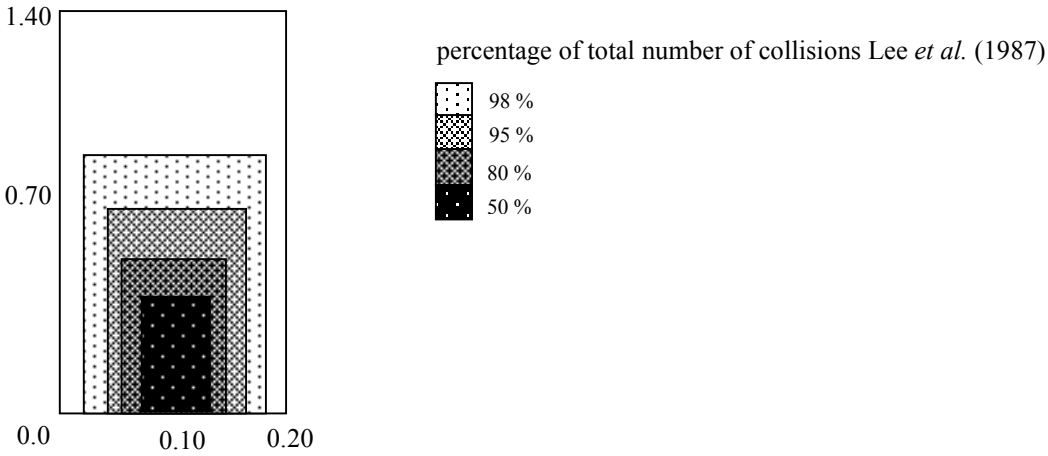

Figure 3.20: Percentage of collisions in bubble column with the model of Lee *et al.* (1987).

Figure 3.21 shows the number mean, volume mean and Sauter mean diameter vs. the height in the column. The two coalescence models are compared to the experimental results (see Chapter 5). It can be concluded from the definition of the three different mean diameters, that number mean diameter < volume mean diameter < Sauter mean diameter.

The mean diameter increases with increasing height in the column, because the higher their position in the column, the longer bubbles generally have resided in the column and the more opportunity they have had to coalesce. The increase in diameter can also be seen in the experiments. The difference in mean diameter between the simulation results of model of Chesters (1991) and the experiments is 15 %. For the model of Lee *et al.* (1987) the difference is around 35 %.

In Figure 3.22 the bubble size distribution at different heights in the column for the simulations and the experiments can be seen. As can be observed in this figure the bubble size distribution moves to larger diameters, with increasing height. In the lower part of the column the bubble size distribution is narrower and the maximum is higher. Most of the bubbles in the lower part of the column have a diameter around 2.8 mm. The number of coalesced bubbles is small. The bottom contains a large number of small bubbles and therefore the bubble size distribution is narrow. In the higher part of the column the bubble size distribution is broader than in the bottom part due to coalescence.
The bubble size distribution in the experiments also moves to larger diameters when increasing the height due to coalescence. However, the bubble size distribution in the top of the column in the experiments is narrower and the maximum is higher than in the simulations. The difference is due to the larger number of small bubbles in the top of the column in the simulations.
In the simulation results the maximum of the bubble size distribution is found at lower diameters. The maximum is higher and the distribution is narrower compared to the experimental results. In the experiments the bubbles immediately coalesce when they leave the nozzle and the maximum shifts to higher diameters.

In both models the mean diameter is overpredicted, probably due to the fact that hardly any break-up occurs. The results of the coalescence model of Chesters (1991) combined with the break-up model of Luo and Svendsen (1996) are closer to the experimental results.

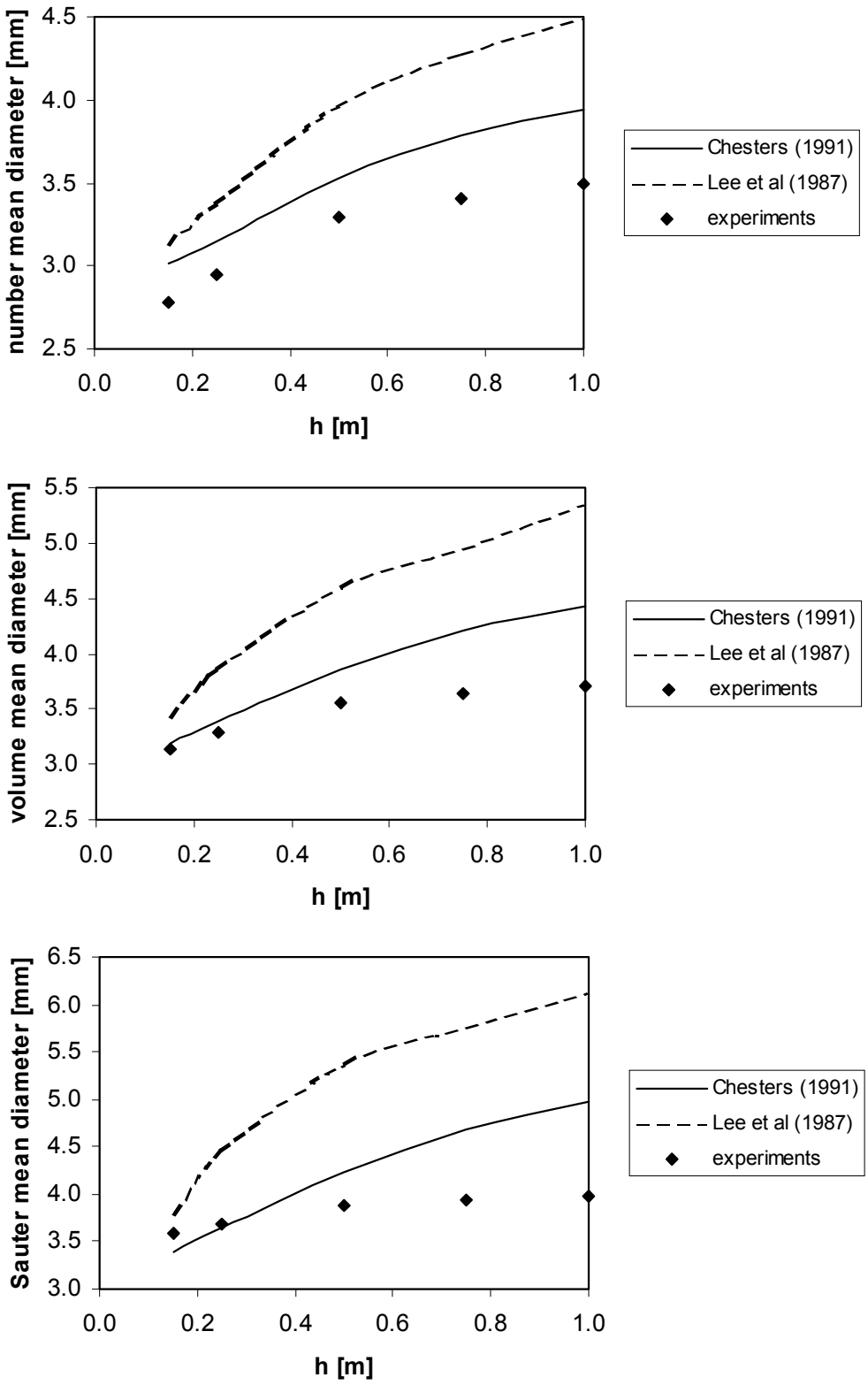

Figure 3.21: Comparison of simulation and experimental results of mean diameter vs. height for case 1 and 2 (see Table 3.4). Top: number mean diameter; middle: volume mean diameter; bottom: Sauter mean diameter.

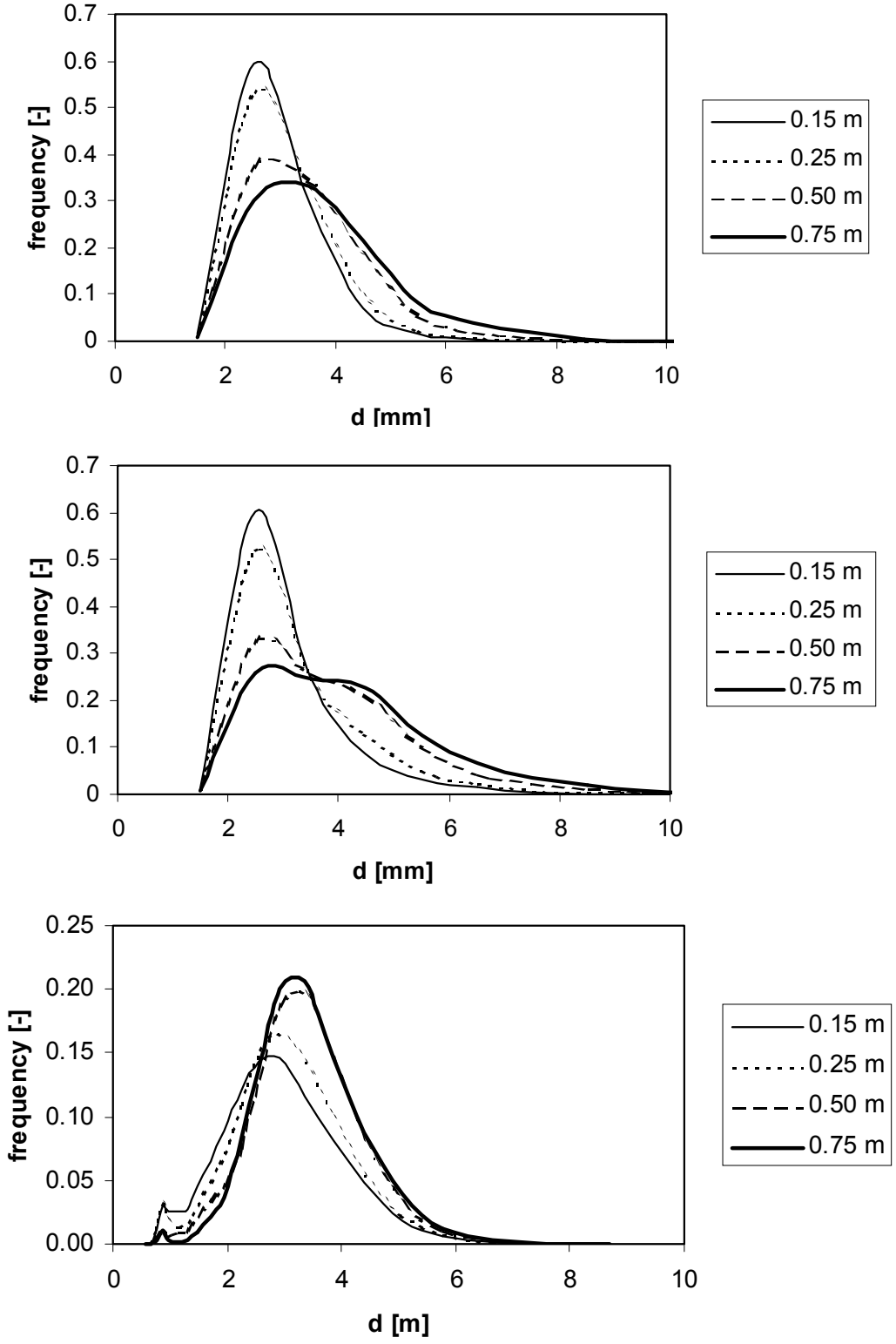

Figure 3.22: Simulated and experiments bubble size distribution after 130 s. Top: case 1; middle: case 2 (see Table 3.4); bottom: experiments.

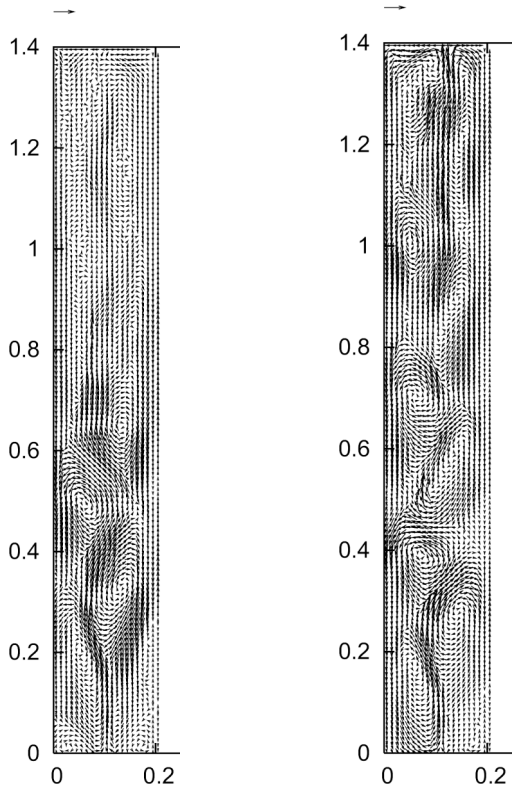

Figure 3.23: Snap shots of the liquid phase velocity of the DBM in a pseudo 2D column after 70 s. Left: case 1; right: case 2 (see Table 3.4). Reference vector = 0.2 m s^{-1}.

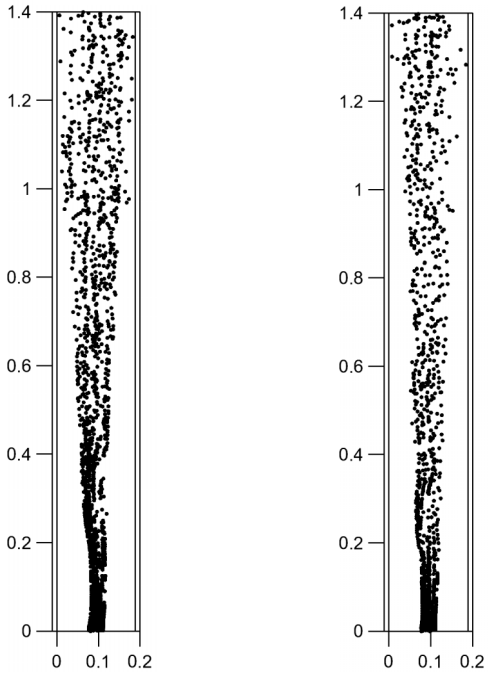

Figure 3.24: Snap shots of the bubble plume of the DBM in a pseudo 2D column after 70 s. Left: case 1; right: case 2 (see Table 3.4).

In Figure 3.23 and 3.24 snap shots of the liquid phase velocity and the bubble position in the DBM with Chesters (1991) (case 1) and Lee *et al.* (1987) (case 2) are presented. In these figures it is found that the flow is driven by a bubble plume, which moves through the column in an oscillatory manner. The total number of bubbles present in the column is less when the model with Lee *et al.* (1987) is used, due to the higher coalescence efficiency. In the simulations and the experiments it is observed that in the lower part of the column the bubbles are close together forming a bubble plume. In the upper part of the column the bubbles are more uniformly distributed. In Figure 3.22 can be seen, that in the case with Chesters (1991) the liquid phase velocity is higher in the upper part of the column. In the case with Lee *et al.* (1987) the liquid phase velocity is the same in the lower and upper part of the column. The bubble plume can be seen in the liquid phase velocity.

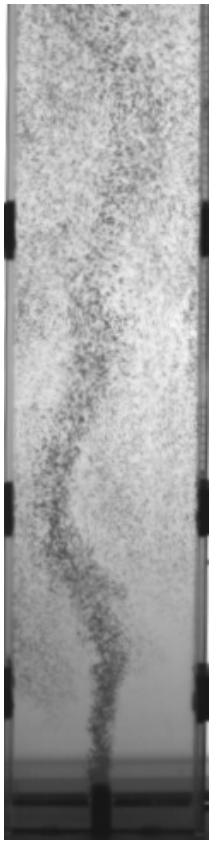

Figure 3.25: Experimental images of bubble plume in pseudo 2D column at a superficial gas velocity of $5.56 \cdot 10^{-3}$ m s^{-1}.

In case 3 the model of Chesters (1991) is used with a lower superficial gas velocity ($1.39 \cdot 10^{-3}$ m s^{-1}). The number of collisions between two bubbles that result in coalescence at a lower superficial gas velocity is around 43 %, which is the same number as in case 1. Around 65% of the coalescence occurs in the lower part of the column (< 0.70 m).
Figure 3.26 shows the number mean, volume mean and Sauter mean diameter vs. the height in the column for case 3. The mean diameters of the simulations are smaller than the experimental results with lower superficial gas velocity. The bubble size distribution of case 3 in Figure 3.27 is narrower and the maximum of the distribution is found at smaller bubble diameter than in the case of higher superficial gas velocity. The bubbles stay together in a bubble plume. Compared to experimental results and the case with higher superficial velocity the number of collisions is lower when using a lower superficial velocity. Due to the low number of collisions the number of coalescence is much lower. A possible explanation is that the zig-zag and spiral movement of bubbles is not implemented in the model.

In Figure 3.28 snap shots of the liquid phase velocity and the bubble plume of case 3 are presented. The number of bubbles is less than with higher superficial gas velocity (case 1). The horizontal distribution of the bubble plume is less than in case 1. As can be seen in this figure, the bubbles in the plume are rising in 'lines' behind each other. This can be the effect of the large grid size. The liquid phase velocity is smaller in the case with lower superficial gas velocity.

In case 4 the model of Chesters (1991) is used with a higher superficial gas velocity ($4.17 \cdot 10^{-3}$ m s^{-1}) than in case 1. The number of collisions between two bubbles that result in coalescence is the same number as in case 1. Around 88% of the coalescence occurs in the lower part of the column (< 0.70 m).
In Figure 3.29 the number mean, volume mean and Sauter mean diameter vs. the height in the column are presented for case 4. The mean diameter increases with increasing flow rate. This is due to the fact that when the flow rate is higher, the gas fraction increases and the bubbles are closer together. The differences between the simulated mean diameters and the experiments in case 4 are higher than in case 1. In both the experimental and simulation results it can be seen, that the slope of the line in the lower part of the column is steeper than in the higher part. The number of collisions resulting in coalescence decreases higher in the column.

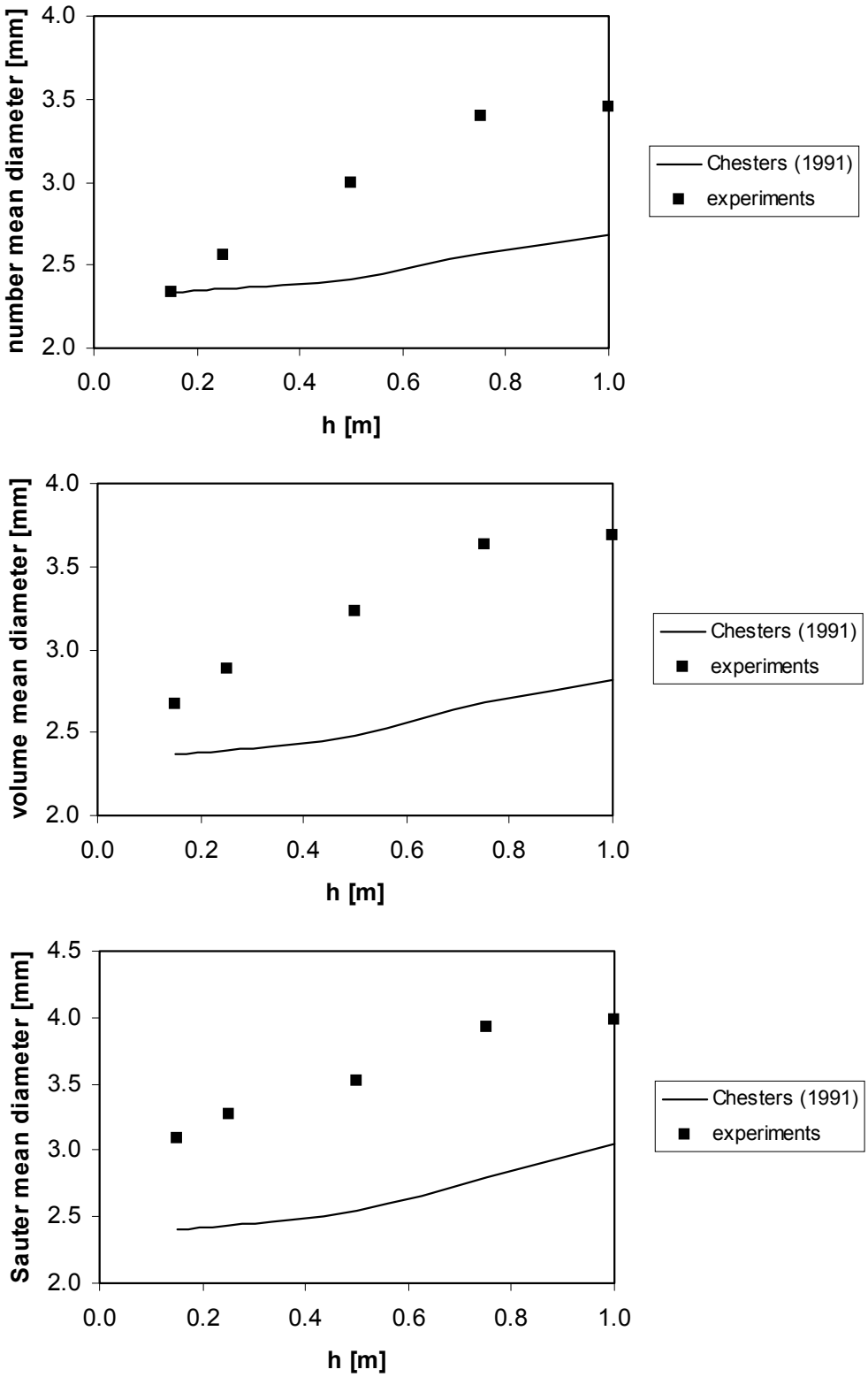

Figure 3.26: Comparison of simulation and experimental results of mean diameter vs. height for case 3 (see Table 3.4). Top: number mean diameter; middle: volume mean diameter; bottom: Sauter mean diameter.

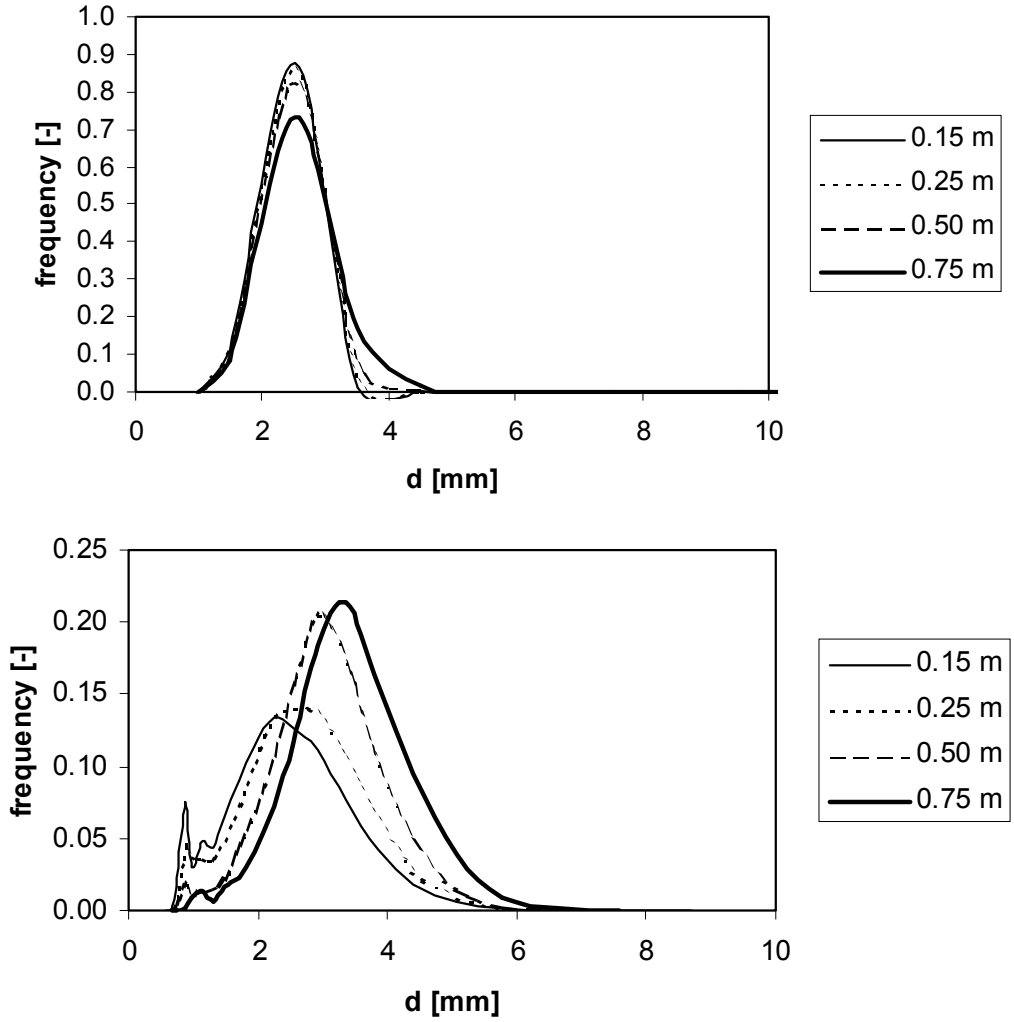

Figure 3.27: Bubble size distribution after 130 s. Top: case 3 (see Table 3.4); bottom: experimental results.

In Figure 3.30 it can be seen that in the lower part of the column the bubbles stay together in a plume. The bubbles are close together and they collide very often and coalescence can occur. In the higher part of the column, the bubbles are spread through the whole column and no coalescence is observed. The hold-up is low and therefore there is more space between the bubbles. The bubbles do not collide very often and the chance for coalescence is lower. The liquid phase velocity is much higher in the case with a higher superficial gas velocity.

The bubble size distribution of case 4 in Figure 3.31 is wider and the maximum is at larger bubble diameter than in the experimental results. This is opposite to case 1. The higher the superficial gas velocity, the more collisions and coalescence takes place and the higher the bubble diameter in the column. Due to the fact that hardly any break-up occurs, the bubble diameter can increase to large diameter.

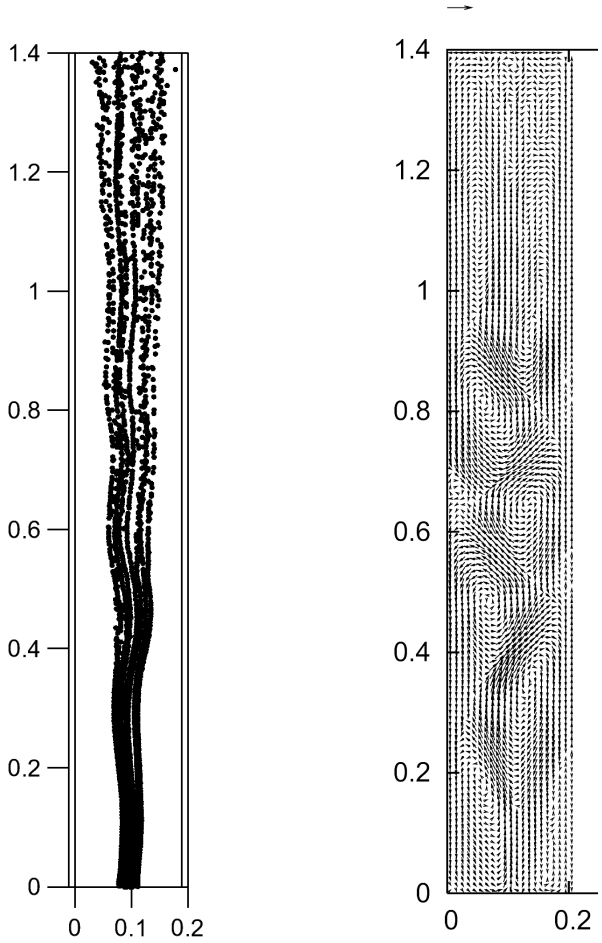

Figure 3.28: Snap shots of the bubble plume and liquid phase velocity for case 3 in a pseudo 2D column after 70 s.

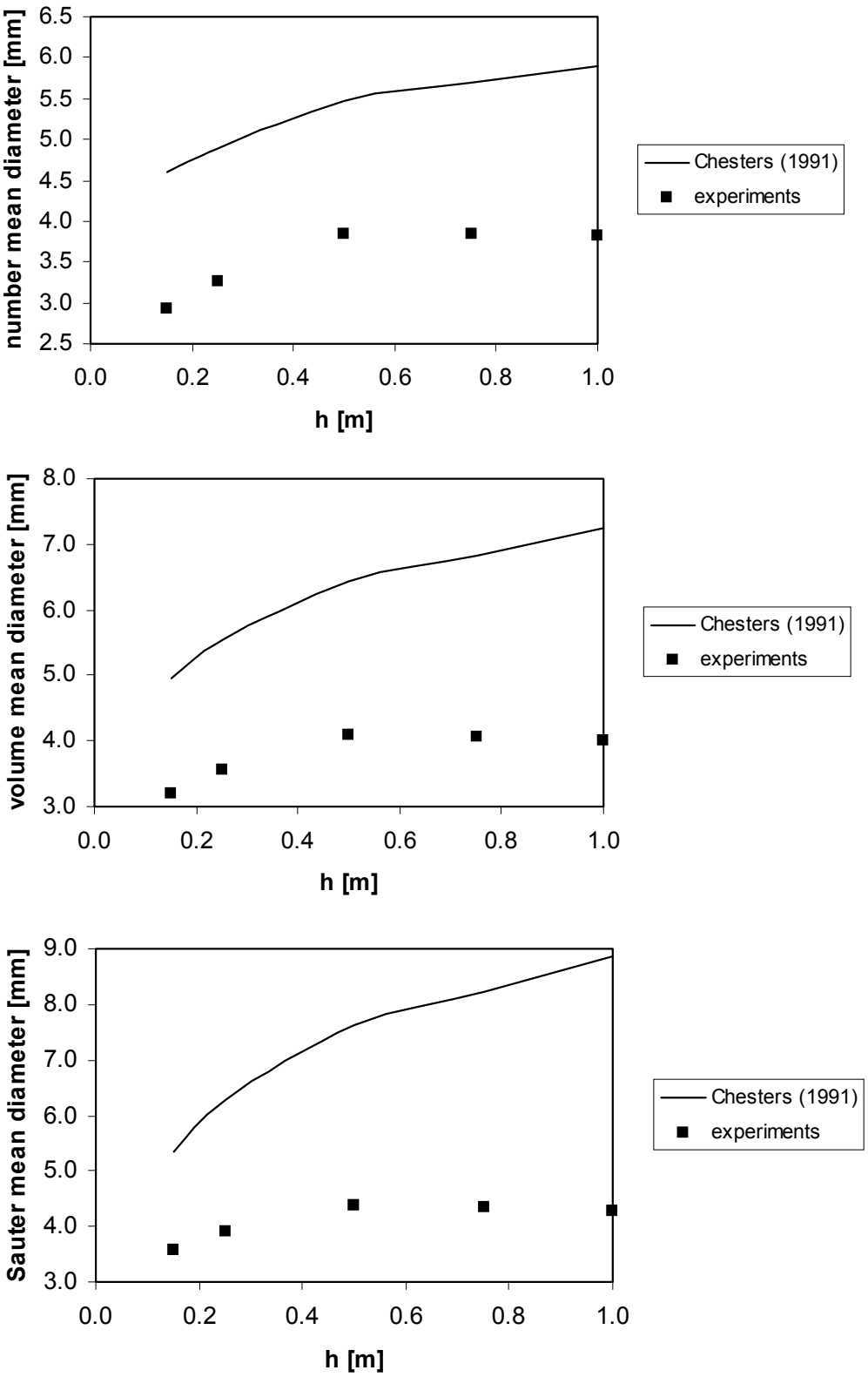

Figure 3.29: Comparison of simulation and experimental results of mean diameter vs. height for case 4 (see Table 3.4). Top: number mean diameter; middle: volume mean diameter; bottom: Sauter mean diameter.

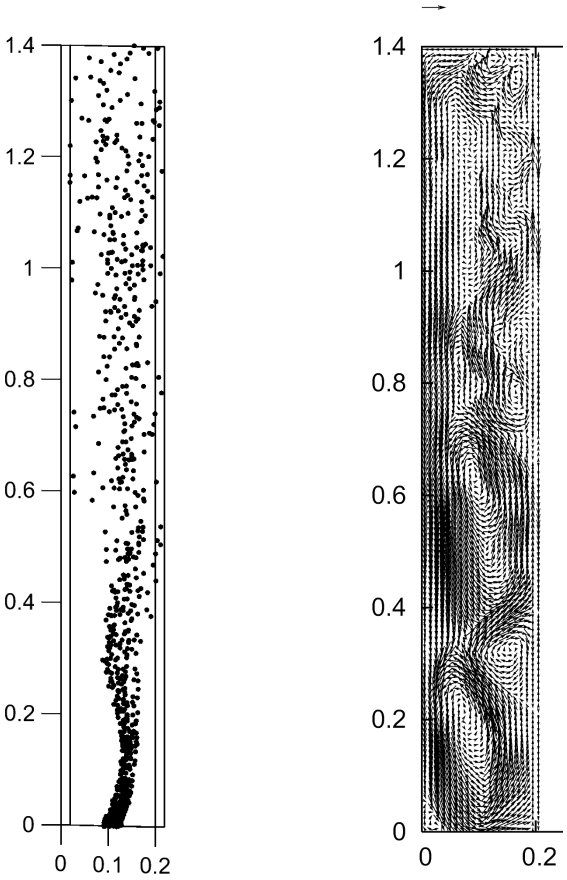

Figure 3.30: Snap shots of the bubble plume and liquid phase velocity for case 4 in a pseudo 2D column after 70 s.

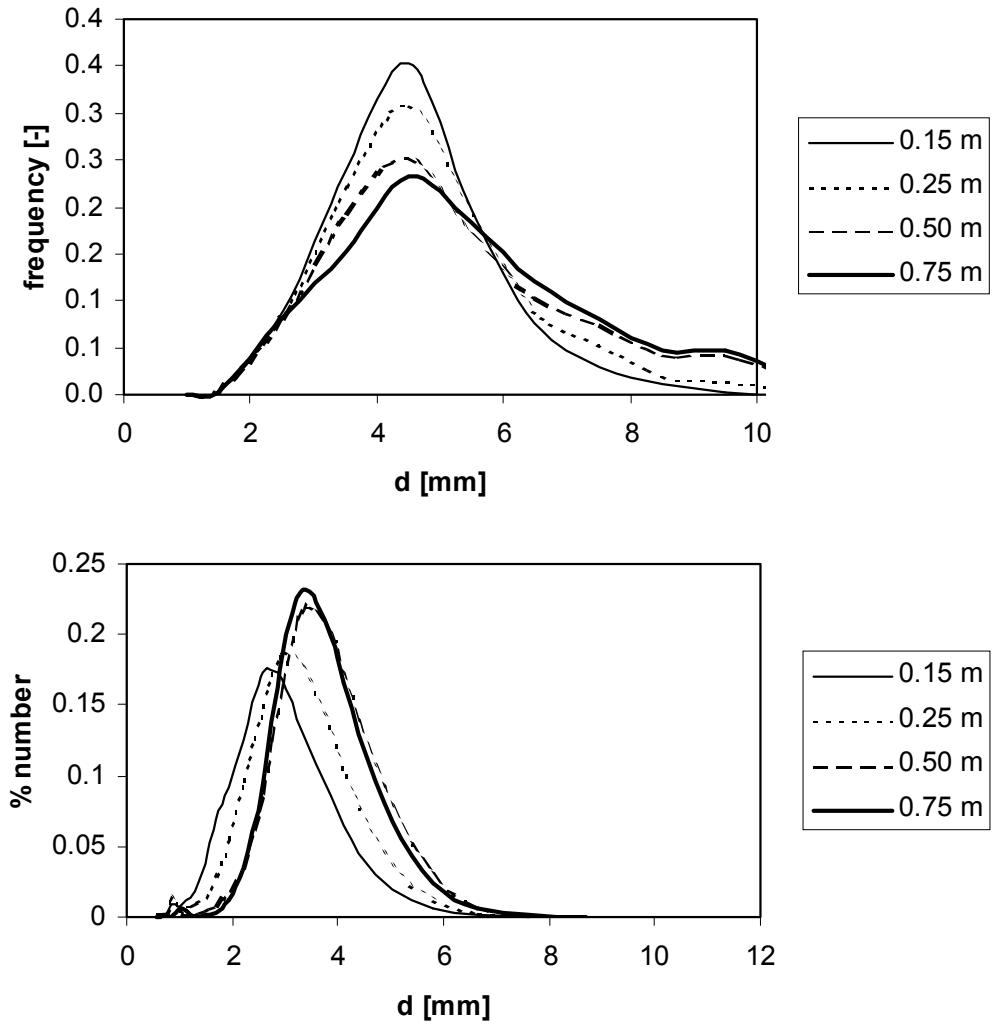

Figure 3.31: Bubble size distribution after 90 s. Top: case 4 (see Table 3.4); bottom: experimental results.

3.8 Conclusions

In this chapter a discrete bubble model (DBM) was used to investigate the hydrodynamics, coalescence and break-up occurring in bubble columns. The 3D DBM code, developed by Delnoij (1999) was extended to incorporate models describing the coalescence and break-up along with a closure model for the turbulence.
Simulation results of the model with LES are compared to experimental PIV results measured by Deen (2001) in a square column. The velocity and velocity fluctuations of the simulation are predicted somewhat too high compared to the PIV results. The difference between the simulation results and the experiments is 7 %. When using a

smaller time step or grid size the difference between simulation and PIV results is marginal.

When no LES model is used the average velocity and velocity fluctuations of the liquid phase are much lower than in the case with LES. The effective viscosity in case without LES is lower due to the absence of the turbulent viscosity. Low viscosities lead to less dampening of the bubble plume dynamics and this in turn leads to flatter average liquid phase velocity profiles. The opposite effect is observed when accounting for bubble induced turbulence, due to an increase in the effective viscosity. The influence of the sub-grid scale velocity is negligible.

When the lift coefficient is reduced from 0.5 to 0.3 the average velocity and velocity fluctuations are much higher. In case of a smaller lift coefficient the spreading of the plume is less and therefore the dynamics of the plume are reduced, which leads to a higher average velocity in the centre of the column.

The best results are obtained when a LES model is incorporated, using a time step of $0.5 \cdot 10^{-3}$ s, a grid size of 1.0 cm in all directions and a lift coefficient of 0.5.

In the DBM the coalescence model of Chesters (1991) and Lee *et al.* (1987) and the break-up model of Luo and Svendsen (1996) are implemented. The results are compared to experimental results, measured in a pseudo 2D bubble column with an air-water system.
The break-up model of Luo and Svendsen (1996) and others were developed for energy dissipations larger than 0.5 $m^2 s^{-3}$. In bubble columns with low gas flows and low turbulence the energy dissipation is in the order of 10^{-2} $m^3 s^{-1}$. When these energy dissipation rates are used in the break-up model, hardly any break-up occurs. In the simulations break-up only occurs in the top of the column, when the energy dissipation is larger than 10^{-1} $m^3 s^{-1}$ and the diameter of the bubble is large (> 5 mm).
The number of collisions between two bubbles that result in coalescence is 43 % with the coalescence model of Chesters and 85 % with the coalescence model of Lee *et al.* (1987). Most of the coalescence occurs in the lower part of the column. When either of the coalescence models is used, the mean diameter is overpredicted, due to the fact that hardly any break-up occurs. The results of the coalescence model of Chesters (1991) combined with the break-up model of Luo and Svendsen (1996) are closer to the experimental results.

When changing the superficial gas velocity the coalescence efficiency is still the same, but the number of collisions and thus of coalescence changes. The higher the superficial gas velocity, the more collisions occur in the column. Therefore the differences between the simulated mean diameters and the experiments at higher superficial gas velocity are higher. The bubble size distribution is wider at higher superficial gas velocity.
Further research is necessary to resolve the differences between the experiments and the simulations.

Chapter 4

TWO-FLUID MODEL

Abstract

In this chapter three different Euler-Euler models will be used to describe two-phase flows in bubble columns: a gas-liquid model, a gas-liquid model with the MUltiple-Size-Group (MUSIG) model for the gas phase and a gas-gas-liquid model. For the simulations of the Euler-Euler model in this thesis the commercial code CFX 4.4 will be used. In the Euler-Euler models a LES-turbulence model will be incorporated. The MUSIG model, including population balances with a break-up and coalescence model, can be used to study the bubble size distribution in the column. The effect of the different rise velocities of 'small' and 'large' bubbles is studied with a three-phase gas-gas-liquid model. The gas phase is divided into two groups, one with smaller bubble diameters and one with larger bubble diameters with different drag relations. Simulation results are compared to experimental PIV results of Deen (2001). Good agreement was found when comparing the simulation results of the gas-liquid model to the experimental results. The difference between the results of the gas-liquid model and the gas-liquid model with MUSIG mode is small. When the LES model is implemented the average velocity and velocity fluctuations of the liquid phase are much higher than in the case without LES, due to an increase of the effective viscosity in the case with LES. The magnitude of the average liquid velocities of the gas-gas-liquid model is smaller than for the gas-liquid model.
In the gas-liquid model with MUSIG model the bubbles in the gas phase are divided into 10 equally sized bubble size groups from 0.0 - 10.0 mm. The difference between the models with and without MUSIG model is very small, because the model that was used for the calculation of the drag force does not depend on the bubble size. The results of the Euler-Euler model with MUSIG with the coalescence model of Chesters (1991) and the break-up model of Luo and Svendsen (1996) are the best in agreement with the results of the DBM.

4.1 Introduction

Bubble column reactors are commonly used as reactors in chemical, biochemical and petrochemical processes. The applications usually involve gas-liquid mass transfer and (exothermal) chemical reactions.
Flows in industrial bubble columns can be simulated using Euler-Lagrange models or Euler-Euler models. The Euler-Lagrange model follows each bubble separately and is described in Chapter 3. The Euler-Euler model, also called two-fluid model models treats the different phases as interpenetrating fluids. It solves the ensemble averaged mass and momentum conservation equations to describe the time-dependent motion of both the liquid and gas phase.
The Euler-Euler model requires closure relations for the unclosed parts of the model, like the Euler-Lagrange model, e.g. closures for the forces acting on a bubble, the break-up and coalescence of bubbles and the turbulence.
In the Euler-Lagrange direct bubble-bubble interaction is described using an encounter model. Here the incorporation of a bubble size distribution is straightforward. The number of bubbles in the Euler-Lagrange model is limited to a number of about 10^5 and significant storage requirements and CPU power are required.
The Euler-Euler model can be used to simulate the flow in an industrial bubble column. In the Euler-Euler model the number of bubbles is irrelevant and storage requirements and demand of computer power depend only on the number of grid cells required. Furthermore in this model a break-up and coalescence model can be incorporated and the bubble size distribution can be calculated using a population balance.

By comparing the Euler-Euler and Euler-Lagrange model Sokolichin *et al*. (1997) concluded that the Euler-Euler model suffers from numerical diffusion when first order discretisation schemes were used for the convective fluxes. In the Euler-Euler model the gas fraction is smeared out over the entire grid cell, whereas in the Euler-Lagrange model no numerical diffusion will be introduced into the dispersed phase since each bubble is tracked individually. They recommended the use of higher order discretisation schemes for the Euler-Euler model to reduce the numerical diffusion. When using an appropriate discretisation scheme the Euler-Euler method provides results, which are quite simular to these obtained with the Euler-Lagrange method.
Sokolichin and Eigenberger (1994) concluded this once more by comparing the results of their Euler-Euler model to the Euler-Lagrange model of Delnoij *et al*. (1997).

Also Lapin and Lübbert (1994) concluded that the Euler-Euler method is very sensitive to false diffusion when using first order schemes.

Some authors introduced a turbulence model into the Euler-Lagrange or Euler-Euler model. Laín *et al* (2001) predicted the flow in a cylindrical bubble column using the *k*-*ε* model. The values of the mean velocities showed reasonable agreement with the experiments for both phases, but the fluctuating components were overpredicted. Also the axial liquid velocity and the turbulent kinetic energy differed from the experimental findings.
Sokolichin and Eigenberger (1999), Pfleger *et al*. (1999) and Mudde and Simonin (1999) showed that the turbulent viscosity in 2D models is overestimated. This is probably due to an overprediction of the turbulent kinetic energy.
Sokolichin and Eigenberger (1999) used 3D simulations and the *k*-*ε* model. They used three different grids and observed that the solution was basically the same for all grids.
Pfleger *et al*. (1999) reported that bubble induced turbulence may play an important role, which can be modelled by introducing an extra term in the *k*-equation (Friberg, 1998). However, in their paper they used the standard *k*-*ε* model in an air-water system. They investigated the use of a turbulent dispersion term in the continuity equation instead. They concluded that most of the gas dispersion was already obtained by numerical diffusion, so there was no need for an additional dispersion term anymore. The use of turbulent dispersion also reduced the dynamic behaviour. Pfleger *et al*. (1999) therefore concluded that the use of a turbulent dispersion term is not necessary. It is important to realise that the use of schemes with less numerical diffusion or finer grids may still need turbulent dispersion terms though.
Although some of the authors have obtained good results using the k-ε model, the model still fails in case of flows in complex geometries. Furthermore the assumption of isotropic turbulence is not valid in gas-liquid flows. In these cases advanced models are required. Kuipers and Van Swaaij (1997) and Jakobsen *et al*. (1997) suggested the use of large eddy simulations (LES). LES can be used well in the area of 3-dimensional dynamic flows. It is clear that problems of turbulent multiphase flow are within this area. Deen (2001) compared results of the k-ε model and the LES model with experimental results. The simulation results of Deen (2001) of the flow of a bubble plume in a flat bubble column, using the k-ε turbulence model corresponded well with both the experiments of Becker *et al*. (1994) and the numerical results obtained by Sokolichin and Eigenberger (1999). The large difference between the simulations and the experiments was the overestimation of the oscillation period by 20 s. Both the velocity and the

velocity fluctuations were in quantitative agreement with the measurement data of Becker *et al*. (1994). In the simulations of the 3D bubble column the LES model showed better agreement with experimental PIV results than the k-ε model. Contrary to the simulations with the k-ε model, the LES model captured the transient movement of the bubble plume. Furthermore, the velocity and the velocity fluctuations were in good quantitative agreement with the measurements.

To study the bubble size distribution in a bubble column a break-up and coalescence model will be incorporated in the Euler-Euler model. In literature many models are available to describe the break-up of bubbles. Most of the published literature on bubble break-up is based on the early work of Hinze (1955). Bubble break-up occurs through bubble interaction with turbulent eddies. The responsible eddies are equal or marginally smaller than the bubble size. Most models define a breakage efficiency and breakage frequency to calculate the number of bubbles breaking. Coulaloglou and Tavlarides (1977) developed a model for break-up rates of liquid drops based on the fraction of drops undergoing break-up and the time required for break-up to occur. The fraction of drops in the breakage frequency is assumed proportional to the fraction of turbulent eddies colliding with the droplet that have a turbulent kinetic energy greater than the droplet surface energy. They assumed that the droplet sizes formed upon breakage are represented by a normal density function. Two unequal droplets were assumed to form. Prince and Blanch (1990) derived a coalescence model based on the model of Coulaloglou and Tavlarides (1977). Their estimate of the eddy-bubble collision frequency is based on isotropic turbulence. The criterion for break-up relates the energy of the eddy to the surface tension force of the bubble. Shimizu derived almost the same model as Prince and Blanch (1990). Tsouris and Tavlarides (1994) criticized their original model because it predicted a critical diameter whose break-up frequency is maximized. The Prince and Blanch model (1990) exhibits the same behavior. Tsouris and Tavlarides (1994) proposed a new model which predicted a monotonic increase of the break-up frequency. Luo and Svendsen (1996) did not make any distinction between drops and bubbles in the derivation of their theoretical model. The turbulence in this model is assumed to be isotropic. The model of Luo and Svendsen (1996) contains no unknown or adjustable parameters and favores unequal breakage.
Coalescence of two bubbles in turbulent flow occurs in three steps: Collisions of the two bubbles, drainage of the liquid film between the bubble until this film reaches a critical thickness and rupture resulting in coalescence. Modeling of the coalescence process requires only one function for the coalescence frequency, which is the product of the

collision frequency and the coalescence efficiency. The efficiency can be described as the fraction of drops, which coalesce after collision. Coulaloglou and Tavlarides (1977) derived the expression for the collision frequency of drops by assuming that the mechanism of collision in a locally isotropic field is analogous to collisions between molecules as in the kinetic theory of gases. The force, which compresses the drops, must act for a sufficient time that the intervening film drains to a critical thickness so that film rupture and coalescence will take place. The time for this process to occur, the contact time, must exceed the coalescence time of the droplets. In contrast to Coulaloglou and Tavlarides (1977), Sovová (1981) stated that the kinetic energy of a collision is the controlling factor for coalescence. Coalescence has been found to follow in a very short time after collision and its probability increases with increasing energy of collision. This model predicts a decreasing efficiency with decreasing drop size, in contrast to the model of Coulaloglou and Tavlarides (1977). Sovová (1981) suggested that a combination of both mechanisms of collision may be postulated. Following Coulaloglou and Tavlarides (1977), Lee *et al.* (1987) proposed a model based on the consideration that coalescence occurs if the contact time exceeds the coalescence time. They considered the coalescence time, as the time required for thinning plus the time of rupture. Tobin *et al.* (1990) presented the kinetic collision model. The concept is that in violent collisions the inertia of the drops is the governing factor and the effectiveness of the collision depends on the adequacy of the collision kinetic energy to accomplish film drainage. Prince and Blanch (1990) considered the collisions arising from turbulence, buoyancy and laminar shear. Their expression for the coalescence efficiency is based on the model of Coulaloglou and Tavlarides (1977). Chesters (1991) also applied the same relation for the efficiency of bubble coalescence as Coulaloglou and Tavlarides (1977), but their definition for the contact time and coalescence time is different. The coalescence efficiency in their model is based on the Weber number.

Lo (1996) incorporated the break-up model of Luo and Svendsen (1996) and the coalescence model of Prince and Blanch (1990) in his population balance. The predicted results were in broad agreement with the measured data. However the coalescence rate was too high and was scaled by a factor of 0.05.

Lehr and Mewes (2000) also used the break-up model of Luo and Svendsen (1996) and the coalescence model of Prince and Blanch (1990). Their model is able to predict the bubble size distribution in a bubble column including the formation of large bubbles at high superficial gas velocities. They implemented the transport equation in a commercial CFD code, to demonstrate the possibility of combining population balances with CFD. A dynamic two-fluid model was used and the calculations for three space coordinates were

performed for cylindrical bubble columns. Time averaging leaded to a stationary and axial symmetrical flow field that agrees with experimental results. Pohorecki *et al.* (2001) used a simplified version of the theoretical model developed by Prince and Blanch (1990). The results of the calculations were compared with experimental data and good agreement was found between calculated and experimental values.

In this thesis three different 3D Euler-Euler models were used to describe two-phase flows in bubble columns: A gas-liquid model, a gas-liquid model with the MUltiple-Size-Group (MUSIG) model for the gas phase and a gas-gas-liquid model. For the Euler-Euler models the commercial code CFX 4.4 was used. In all three Euler-Euler models a LES-turbulence model was incorporated. According to Deen (2001) a LES model gives better results compared to experimental results than the k-ε model. The MUSIG model, including population balances with a break-up and coalescence model, can be used to study the bubble size distribution in the column. All bubbles in this model have the same rise velocity. To study the effect of the different rise velocities of 'small' and 'large' bubbles a three-phase gas-gas-liquid system is also simulated.

4.2 Theory Euler-Euler model

In the Euler-Euler model the gas and liquid phases are described as continuous fluids which penetrate each other. For both phases the ensemble averaged continuity and momentum equations are solved. For phase *f* these equations can be written as:

$$\frac{\partial\left(\alpha_f \rho_f\right)}{\partial t} + \nabla \cdot \left(\alpha_f \rho_f \mathbf{u}_f\right) = 0 \tag{4. 1}$$

$$\frac{\partial\left(\alpha_f \rho_f \mathbf{u}_f\right)}{\partial t} + \nabla \cdot \left(\alpha_f \rho_f \mathbf{u}_f \mathbf{u}_f\right) = -\nabla \cdot \left(\alpha_f \tau_f\right) - \alpha_f \nabla P + \alpha_f \rho_f \mathbf{g} + \mathbf{F}_{IF,f} \tag{4. 2}$$

The stress term of phase *f* in equation 4.2 is described as follows:

$$\tau_f = -\mu_{eff,f}\left(\nabla \mathbf{u}_f + \left(\nabla \mathbf{u}_f\right)^T - \frac{2}{3}\mathbf{I}\left(\nabla \mathbf{u}_f\right)\right) \tag{4. 3}$$

where $\mu_{eff,f}$ is the effective viscosity of phase *f*.

The last term in equation 4.2 describes the ensemble averaged momentum exchange between the phases, due to interface forces. The interface force is composed of separable contributions originating from drag, lift and virtual mass and is given by:

$$\mathbf{F}_{IF,l} = -\mathbf{F}_{IF,g} = \mathbf{F}_{D,l} + \mathbf{F}_{L,l} + \mathbf{F}_{VM,l} \tag{4. 4}$$

The total drag per unit volume on the continuous phase is:

$$\mathbf{F}_{D,l} = \frac{3}{4}\alpha_g \rho_l \frac{C_D}{d_B}\left|\mathbf{u}_g - \mathbf{u}_l\right|\left(\mathbf{u}_g - \mathbf{u}_l\right) \tag{4. 5}$$

The drag coefficient C_D is a function of Re and Eo. Most drag relations are experimentally determined (see also Chapter 2). The drag curve for individual bubbles can be correlated for several distinct flow regimes.

In the viscous regime ($0 \leq \mathrm{Re} \leq 500\text{-}1000$) both the skin friction (due to viscous surface shear) and the form drag (due to pressure distribution around the body) are important. The drag coefficient for spherical bubbles continues to decrease monotonically with the Reynolds number. Several empirical correlations are available. Those available in the commercial package CFX were derived by Schiller and Nauman (1933), Ishii and Zuber (1979) and Ihme *et al*. (1972). These correlations are respectively give by:

$$C_D = \frac{24}{\mathrm{Re}}\left(1 + 0.15\,\mathrm{Re}^{0.687}\right) \tag{4. 6}$$

$$C_D = \frac{24}{\mathrm{Re}}\left(1 + 0.1\,\mathrm{Re}^{0.75}\right) \tag{4. 7}$$

$$C_D = \frac{24}{\mathrm{Re}} + 5.48\,\mathrm{Re}^{-0.573} + 0.36 \tag{4. 8}$$

These three relations are plotted in Figure 4.1 in which C_D vs. Re is given. The differences between these relations are small.

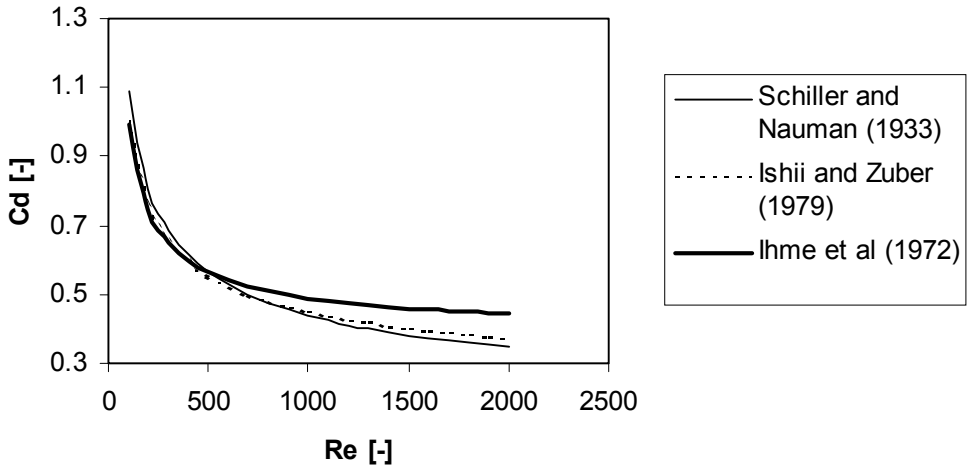

Figure 4.1: Comparison of 3 relations of C_D vs. Re.

The third region is the inertial region or turbulent region ($500\text{-}1000 \leq \mathrm{Re} \leq 1\cdot10^5\text{-}2\cdot10^5$). The form drag dominates in this region and bubbles become distorted. Ishii and Zuber (1979) gave the following relation for the drag coefficient in this region:

$$C_D = \frac{2}{3}\mathrm{Eo}^{1/2} \tag{4. 9}$$

where Eo is the dimensionless Eötvös number defined by:

$$\mathrm{Eo} = \frac{g d_B^2 \Delta\rho}{\sigma} \tag{4. 10}$$

It is noted that when equation 4.9 is used the drag force becomes independent of the bubble size, which is in agreement with the constant rise velocity that is found for large bubbles as can be seen in Figure 4.2.
In the Euler-Euler simulations described in this chapter, equation 4.9 is used for the drag relation.

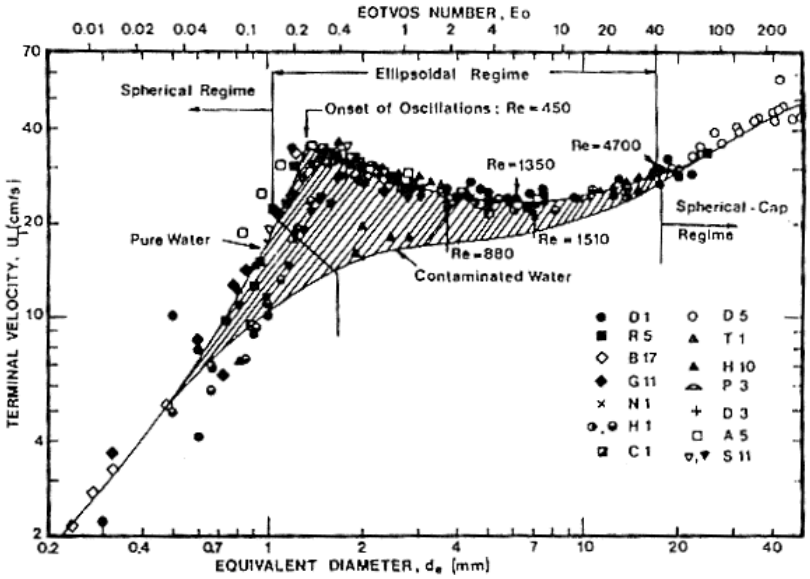

Figure 4.2: Terminal velocity of air bubbles in water at 20 °C.

Tomiyama (1998) gave the following relation for the C_D in a slightly contaminated system:

$$C_D = \max\left[\min\left[\frac{24}{\mathrm{Re}}\left(1+0.15\,\mathrm{Re}^{0.687}\right),\frac{72}{\mathrm{Re}}\right],\frac{8}{3}\frac{\mathrm{Eo}}{\mathrm{Eo}+4}\right] \tag{4. 11}$$

A bubble, rising in a non-uniform liquid flow field, experiences a transverse lift force due to vorticity, rotations of bubbles or shear. The lift force consists of two parts: The classical shear-induced lateral lift force and the wake induced lift force. Both forces act simultaneously on the bubble. For small, spherical bubbles the classical shear-induced lateral lift force dominates and for large, deformed bubbles the wake induced lift force dominates.

The lift force is perpendicular to the path of the bubble and is given by:

$$\mathbf{F}_{L,l} = \alpha_g \rho_l C_L \left(\mathbf{u}_g - \mathbf{u}_l\right) \times \nabla \times \mathbf{u}_l \tag{4. 12}$$

where C_L is the lift coefficient which is set to 0.5.

The resistance to acceleration of the bubble is due to an 'added' of 'virtual' mass of the liquid that has to be accelerated when a bubble accelerates. The virtual mass force is given in terms of relative acceleration of the phases:

$$\mathbf{F}_{VM,l} = \alpha_g \rho_l C_{VM} \left(\frac{D_g \mathbf{u}_g}{Dt} - \frac{D_l \mathbf{u}_l}{Dt} \right) \tag{4. 13}$$

with C_{VM} the virtual mass coefficient with a value of 0.5. The D_f/Dt operators denote the substantial time derivatives of phase f.

4.3 Turbulence model

The effective viscosity of the liquid phase $\mu_{eff,l}$ (equation 4.3) in the stress term of the momentum equation 4.2 is composed of three different contributions: The molecular viscosity, the turbulent viscosity and the viscosity due to bubble induced turbulence:

$$\mu_{eff,l} = \mu_{L,l} + \mu_{T,l} + \mu_{BIT,l} \tag{4. 14}$$

The effective gas viscosity is based on the effective liquid viscosity and is calculated as follows (Jakobsen *et al*., 1997):

$$\mu_{eff,g} = \frac{\rho_g}{\rho_l} \mu_{eff,l} \tag{4. 15}$$

Note that, the contribution of the diffusion term in the gas momentum will generally be very small due to the small density ratio.
There are several models for the bubble induced turbulence. In this work the model proposed by Sato and Sekoguchi (1975) was used:

$$\mu_{BIT,l} = \rho_l C_{\mu,BIT} \alpha_g d_B \left| \mathbf{u}_g - \mathbf{u}_l \right| \tag{4. 16}$$

where $C_{\mu,BIT}$ is a model constant and equal to 0.6.

To compare the results of the DBM and CFX in both models a LES turbulence model is implemented to calculate the turbulent viscosity.

Here the turbulent viscosity according to the LES model proposed by Smagorinksy (1963) is used. The equation for turbulent viscosity, i.e. the SGS viscosity, is given by:

$$\mu_{T,l} = \rho_l \left(C_S \Delta\right)^2 |\mathbf{S}| \tag{4. 17}$$

in which C_S is a constant with a value of 0.1, **S** the characteristic filtered rate of strain and $\Delta=(\Delta_x\Delta_y\Delta_z)^{1/3}$ the filter width.

4.4 Bubble size distribution

In most multiphase flow models, the dispersed phase is characterised by a single mean diameter. In reality a wide spectrum of bubble sizes and shapes exists, because of break-up and coalescence of the bubbles in the column of the dispersed elements.

Generally, in simulations of a gas-liquid system the bubbles can be divided into *N* size groups. Each of these size groups can be treated as a separate phase in a multiphase flow calculation. This multiphase flow model therefore consists of *N+1* separate phases and thus *N+1* sets of coupled continuity and momentum need to be solved. Because of the large number of equations involved, the number of size groups, which can be used in practical calculations, is limited typically to 2 or 3 size groups. As a result, the bubble size distribution cannot be represented adequately.

In CFX 4.4 the MUltiple-Size-Group (MUSIG) model developed by Lo (1996) can be used to handle dispersed multiphase flows in which the dispersed phase has a large variation in size. In the MUSIG model it is assumed that the bubbles of all size classes have the same rise velocity. This is a reasonable assumption for bubbles larger than 1 mm (see Figure 4.2). The multiphase flow model is reduced to a two-fluid approach with one velocity field for the continuous phase and one for the dispersed phase. The assumption of a common rise velocity has the favourable effect that only one set of equations is needed to describe the hydrodynamics of the gas phase. The continuity equations of the bubble size groups are retained and solved to represent the bubble size distribution.

MUSIG provides a framework in which the population balance method together with break-up, coalescence and turbulence models can be incorporated into CFD calculations. With this approach, it is possible to consider a large number of bubble size groups (10 to 20 bubble phases) and this gives a better representation of the size distribution.

Population balance methods are well-established techniques for computing the size distribution of the dispersed phase and accounting for break-up and coalescence. The continuity equation for size group *i* of the dispersed phase, used for the population is:

$$\frac{\partial}{\partial t}\left(\alpha_g \rho_g f_i\right) + \nabla \cdot \left(\alpha_g \rho_g \mathbf{u}_g f_i\right) = B_{BU,i} - D_{BU,i} + B_{C,i} - D_{C,i} \qquad (4.\ 18)$$

The first and second term of this equation respectively the rate of change and the convection of the bubble fraction. The four terms on the right hand side together form the rate of mass transfer into the size group due to break-up and coalescence. B_{BU} is the birth rate due to break-up of bubbles in size groups with larger bubbles. B_C is the birth rate due to coalescence of bubbles in size groups with smaller bubbles. D_{BU} and D_C are the death rate due to respectively break-up and coalescence of bubbles in size group *i*.

This equation has the form of the transport equation for a scalar variable, f_i, of the dispersed phase and can be solved numerically. The size distribution of the dispersed phase is defined by the variable f_i. The local Sauter mean diameter can be derived from:

$$d_{32} = \frac{1}{\sum_{i=1}^{N} \frac{f_i}{d_i}} \qquad (4.\ 19)$$

The Sauter mean diameter is used to calculate the drag force and other forces between the two phases.

The sources and sinks (*B* and *D* in equation 4.18) due to break-up and coalescence have to be defined to complete the model. In CFX 4.4 the default model for break-up is the model of Luo and Svendsen (1996). The default coalescence model is the one proposed by Prince and Blanch (1990).

4.4.1 Break-up model

The break-up model of Luo and Svendsen (1996) is described in full detail in Chapter 3 of this thesis. They developed a theoretical model for the break-up of drops and bubbles in turbulent dispersions. The model is based on the theory of isotropic turbulence and contains no unknown parameters. Here the model will be briefly summarised. Further details can be found in Chapter 3.

The birth rate of bubbles belonging to group *i* due to break-up of larger bubbles is:

$$B_{BU,i} = \sum_{j=i+1}^{N} g(V_j : V_i) n_{Bj} \tag{4. 20}$$

where $g(V_j:V_i)$ is the breakage rate of bubbles of volume V_j into bubbles of volume V_i and V_j-V_i, as described in Chapter 3 and n_{Bj} number of bubbles of group j per unit dispersed volume. $g(V_j:V_i)$ contains a callibration factor f_B for calibration of the model ($0 \leq f_B \leq 1$). The death rate of bubbles belonging to group *i* due to break-up to smaller bubbles is:

$$D_{BU,i} = g_i n_{Bi} \tag{4. 21}$$

where g_i is the breakage rate of bubbles of group i and n_i is the number of bubbles group i per unit dispersed volume.

4.4.2 Coalescence model

In Chapter 3 two different coalescence models of Chesters (1991) and Lee *et al* (1987) are described in detail. The default coalescence model in CFX 4.4 is the coalescence model of Prince and Blanch (1990). According to Prince and Blanch coalescence of two bubbles in turbulent flows occurs in three steps. First the bubbles collide, trapping a small amount of liquid between them. Then this liquid film separating the bubbles drains until it reaches a critical thickness. Finally the film ruptures and the bubbles coalesce. Two bubbles will coalesce, provided they remain in contact for a period of time sufficient for the liquid film between them to thin to the critical value necessary for rupture.

The coalescence frequency is given by the collision frequency multiplied by the coalescence efficiency:

$$Q_{ij} = f_C \theta_{ij} \lambda_{ij} \tag{4. 22}$$

where f_C is added for calibration of the model ($0 \leq f_C \leq 1$), θ_{ij} is the collision frequency and λ_{ij} is the coalescence efficiency.

Collisions may occur due to a variety of mechanisms. Prince and Blanch (1990) considered collisions arising from three different mechanisms: turbulence, buoyancy and laminar shear. In CFX only the turbulence collision model is included, which is given by:

$$\theta_{ij}^{T} = A_{ij} \left(\mathbf{u}_{ti}^2 + \mathbf{u}_{tj}^2 \right)^{1/2} \tag{4. 23}$$

where the collision cross-sectional area of the bubble is defined by:

$$A_{ij} = \frac{\pi}{4} \left(d_{Bj} + d_{Bi} \right)^2 \tag{4. 24}$$

The turbulent velocity in equation 4.23 is given by:

$$\mathbf{u}_t = 1.4 \varepsilon^{1/3} d_B^{1/2} \tag{4. 25}$$

with ε the energy dissipation rate.

When using the Smagorinsky (1963) model the energy dissipation rate can, after some manipulation, be written as follows:

$$\varepsilon = \frac{2 \mu_{T,l}^3}{\rho_l^3 \left(C_S \Delta \right)^4} \tag{4. 26}$$

The coalescence efficiency λ_{ij} is a function of the contact time between bubbles and the time required for bubbles to coalesce, the coalescence time. Coalescence will take place

if the contact time exceeds the coalescence time. For further details the reader is referred to Chapter 3.

The birth rate of bubbles belonging to group *i* due to coalescence of bubbles belonging to group *j* and group *k* is:

$$B_{C,i} = \frac{1}{2}\sum_{j=1}^{i}\sum_{k=1}^{i} Q_{jk} n_{Bj} n_{Bk} \tag{4. 27}$$

whereas the death rate of bubbles belonging to group *i* due to coalescence of bubbles belonging to group *i* and and group *j* is:

$$D_{C,i} = \frac{1}{2}\sum_{i=1}^{i}\sum_{j=1}^{i} Q_{ij} n_{Bi} n_{Bj} \tag{4. 28}$$

4.5 Boundary conditions and numerical implementation

In this work the commercial code CFX 4.4 (AEA Technology, England) is used for the Euler-Euler model. In CFX 4.4 closure relations for forces acting on a bubble and models for break-up, coalescence and the bubble size distribution are already implemented.
The Smagorinksy model and the averaging routines were implemented through the use of user Fortran following the work of Jakobsen (1997).

The boundary conditions at the inlet are defined as follows:

$$u_{y,g,in} = \frac{u_{g,s} W \times D}{\alpha_g A_{in}} \tag{4. 29}$$

with $u_{g,s}$ the superficial gas velocity and *W x D* the cross sectional area of the column. The gas inlet area A_{in} was implemented in a central area. In the standard case the size was 3x3 grid cells. A superficial gas velocity of 4.9 mm/s leads to a gas velocity at the inlet of 0.12 m/s. The time step in the simulations was $5.0 \cdot 10^{-3}$ s. For both phases no-slip boundary conditions are used for the confining solid walls.

The simulations were started with a pressure boundary at the outlet of the column. After 10,000 time steps the pressure boundary was changed into a degassing boundary. Due to the nature of this type of boundary condition it was not possible to start immediately with a degassing boundary. Details on these boundary conditions can be found in the CFX user manual.

In the simulations, a bounded third order accurate QUICK scheme was used for the discretisation of the convection terms, while the diffusion terms were discretised with the use of the second order accurate central differencing scheme.

4.6 Results

The model described in the previous sections was used to simulate the flow in a bubble column. In this section the results of the simulations are discussed.
Three different models are tested and compared in the Euler-Euler simulations: A gas-liquid model (G-L), a gas-gas-liquid model (G-G-L) and a gas-liquid model with the MUSIG model for the gas phase (MUSIG). For the gas-liquid model the time step, grid size and turbulence are investigated. The results of the gas-liquid model with MUSIG and the gas-gas-liquid model are compared to the gas-liquid model. In Table 4.1 an overview of the different cases is given.

Table 4.1: Overview of different simulation cases.

Case	CFX model	$\Delta x \Delta z$ [mm]	Δy [mm]	d_B [mm]	Δt [ms]	$\mu_{T,l}$
0	G-L	10	10	4.0	5.0	Eq. 4.18
1	G-L	5	5	4.0	5.0	Eq. 4.18
2	G-L	10	10	4.0	2.5	Eq. 4.18
3	G-L	10	10	4.0	5.0	0
4	MUSIG	10	10	0.0-10.0	5.0	Eq.4.18
5	G-G-L	10	10	2.0 and 6.0	5.0	Eq. 4.18
6	G-L	10	10	2.0	5.0	Eq. 4.18

The results of all three models are compared with experimental PIV results obtained by Deen (2001). The bubble column used by Deen (2001) had the dimensions of 0.15 x 0.15 x 0.45 and was filled with distilled water. Air was introduced into the column through a perforated plate. The plate contained 49 holes, with a diameter of 1 mm, which were positioned in the middle of the column at a square pitch of 6.25 mm. The superficial gas velocity was 4.9 mm/s.

The flow for each case was simulated for a period of 200 s. The data was time-averaged over the last 162.5 s.

4.6.1 Gas-liquid model

The first simulated Euler-Euler model is a two-phase model, a gas-liquid model. The gas phase consisted of bubbles with a diameter of 4.0 mm. The drag model of Ishii and Zuber (1979) was used (equation 4.9).

In Figure 4.3 the average vertical liquid velocity profiles and the vertical liquid velocity fluctuations of the standard case (case 0) are shown at a height of 0.255 m. As can be seen in this figure, the time averaged results become approximately constant after about 200 s of calculation time.

In case 1 the effect of the grid size is tested. The grid sizes are reduced by a factor of two for all directions. Figure 4.4 shows the average velocity profiles and the velocity fluctuations. In this figure it can be seen, that average vertical liquid velocity and the vertical liquid velocity fluctuations in the model with smaller grid sizes are lower. But the differences between the velocity profiles of the case with smaller grid sizes and the standard case are marginal. The results in this figure show, that the model is grid independent.

In Figure 4.5 snapshots of the liquid phase velocity fields and the instantaneous iso-surfaces of α_g = 0.03 of case 0 and case 1 are displayed. As can be seen in this figure the plume is more spread over the column when using a smaller grid. The liquid circulation is about the same.

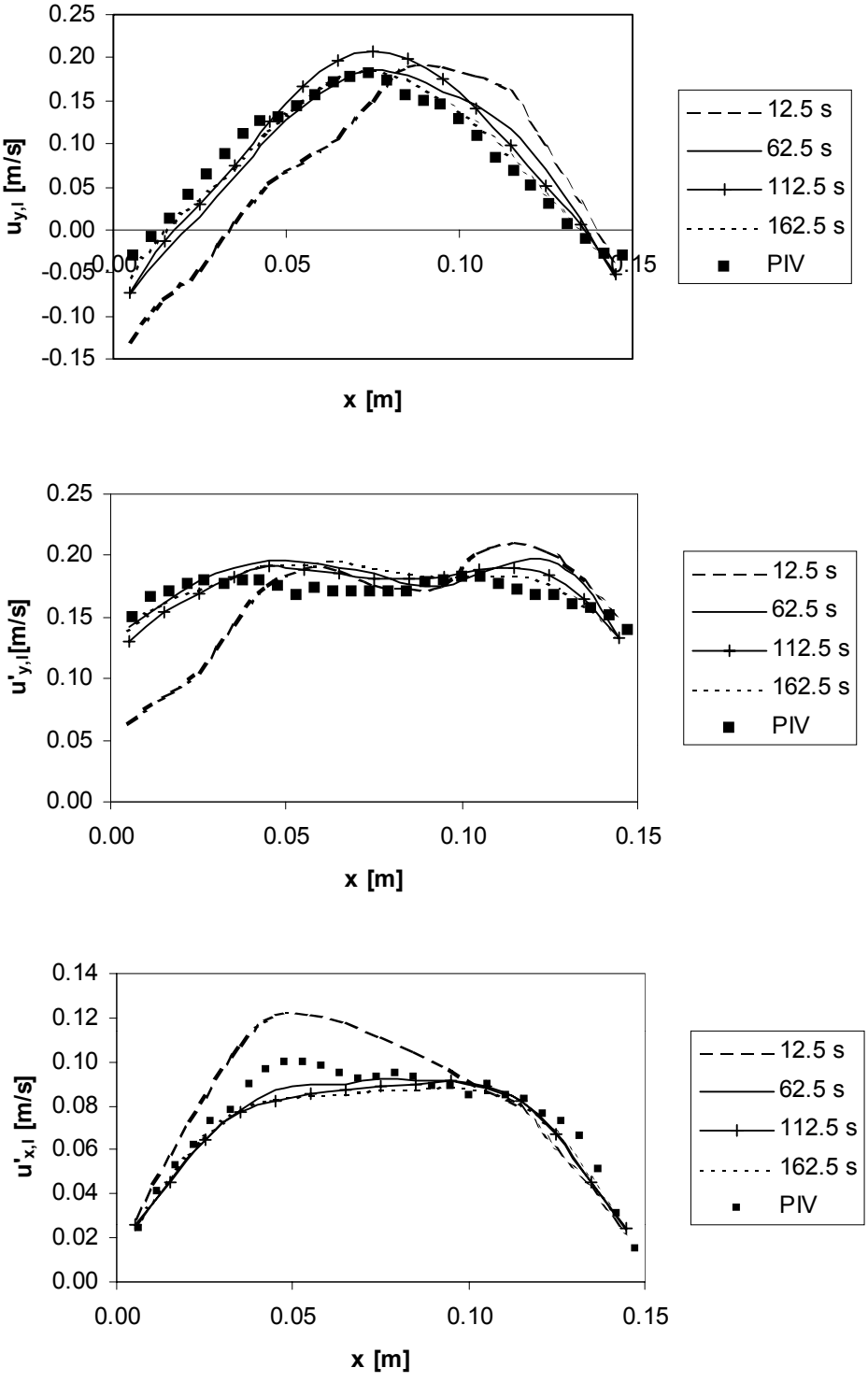

Figure 4.3: Comparison of the simulated and experimental average liquid velocity profiles for the standard case (see Table 4.1) at a height of 0.255 m and a depth of 0.075 m: Effect of the averaging period. Top: average liquid velocity; middle: vertical liquid velocity fluctuations; bottom: horizontal liquid velocity fluctuations.

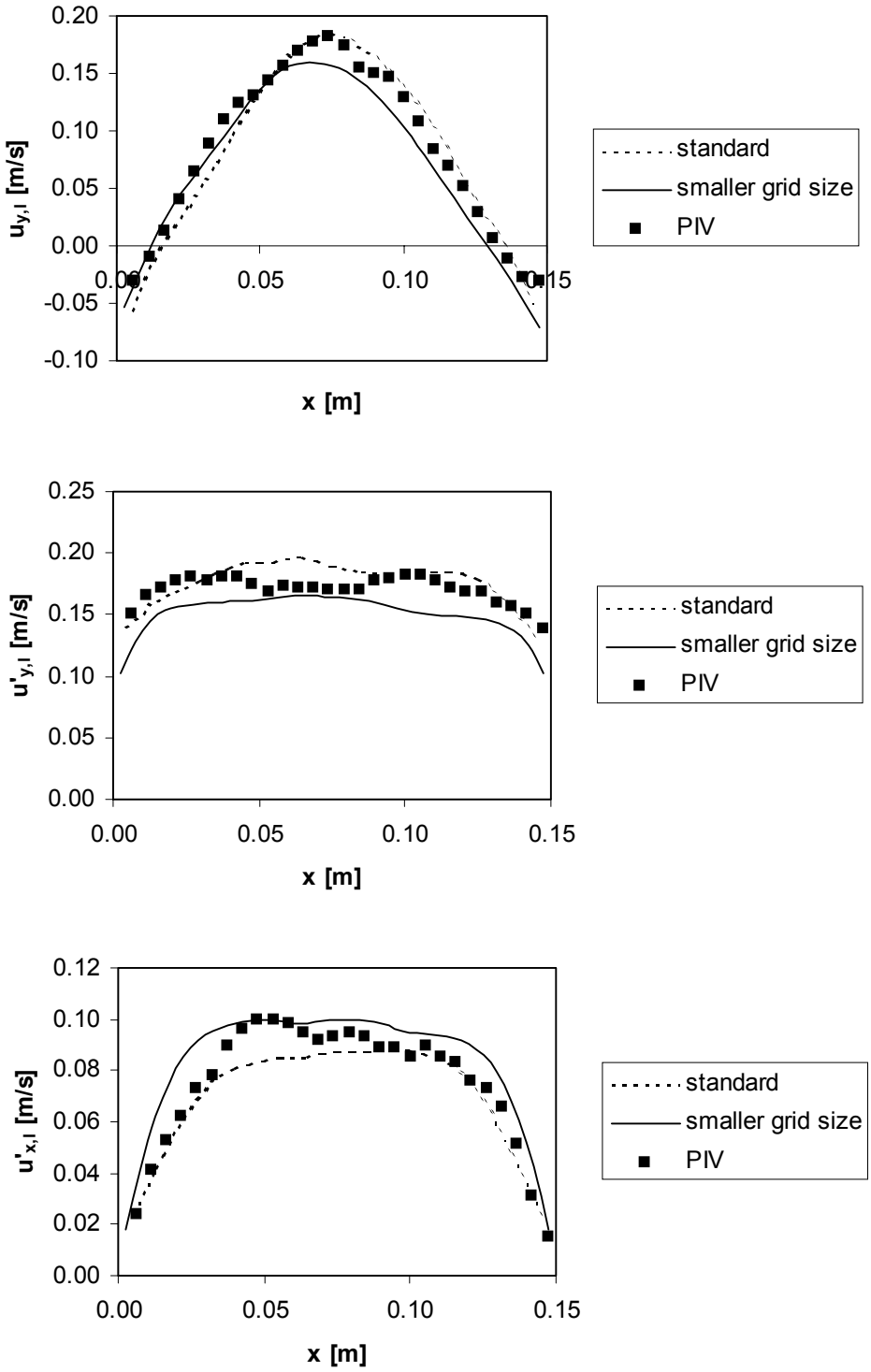

Figure 4.4: Comparison of the simulated and experimental average liquid velocity profiles for case 1 (see Table 4.1) at a height of 0.255 m and a depth of 0.075 m: Effect of the grid size. Top: average liquid velocity; middle: vertical liquid velocity fluctuations; bottom: horizontal liquid velocity fluctuations.

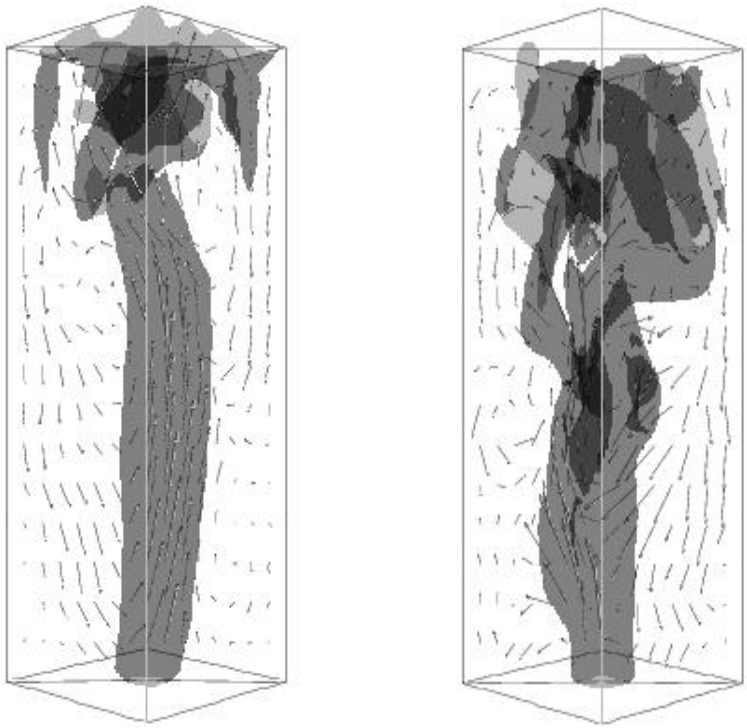

Figure 4.5: Snapshots of the liquid phase velocity fields and the instantaneous iso-surfaces of α_g = 0.03 after 200 s for case 0 and 1 (see Table 4.1).

In case 2 the effect of the time step is tested. The time step is changed from $5.0 \cdot 10^{-3}$ s to $2.5.0 \cdot 10^{-3}$ s. In Figure 4.6 a snapshot of the liquid phase velocity field and the instantaneous iso-surface of α_g = 0.03 case 1 is presented. As can be seen in this figure the plume is more spread over the column when using a smaller time step. The liquid circulation is about the same.

In Figure 4.7 the simulation results of the average velocity and the velocity fluctuations are shown. The average velocity is lower for the case with the smaller time step. The velocity fluctuation profile in the vertical direction also shows lower values in the case with small time step, which indicates an underprediction of the vertical plume dynamics. The differences between the velocity fluctuation profile in the horizontal direction of the standard case and the case with smaller time step is marginal.

Figure 4.6: Snapshot of the liquid phase velocity field and the instantaneous iso-surface of α_g = 0.03 after 200 s for case 2 (see Table 4.1).

Figure 4.8 shows the results of the simulations with and without LES turbulence model. As can be seen in this figure the average velocity profiles of the case with LES are much higher than in the case without LES. In the case in which LES is implemented the effective viscosity has an extra term and has a higher value compared to the case without LES. When the viscosity is higher, the movement of the plume is less and the average velocity in the centre of the column is higher. The velocity fluctuations in the vertical direction in the case with LES are lower than in the case without LES. For the horizontal direction the velocity fluctuations are higher in the case without LES.

In Figure 4.9 a snapshot of the liquid phase velocity field and the instantaneous iso-surface of α_g = 0.03 of case 3 are presented. As can be seen in this figure the plume is more evenly spread over the cross-sectional area of the column in the case without LES.

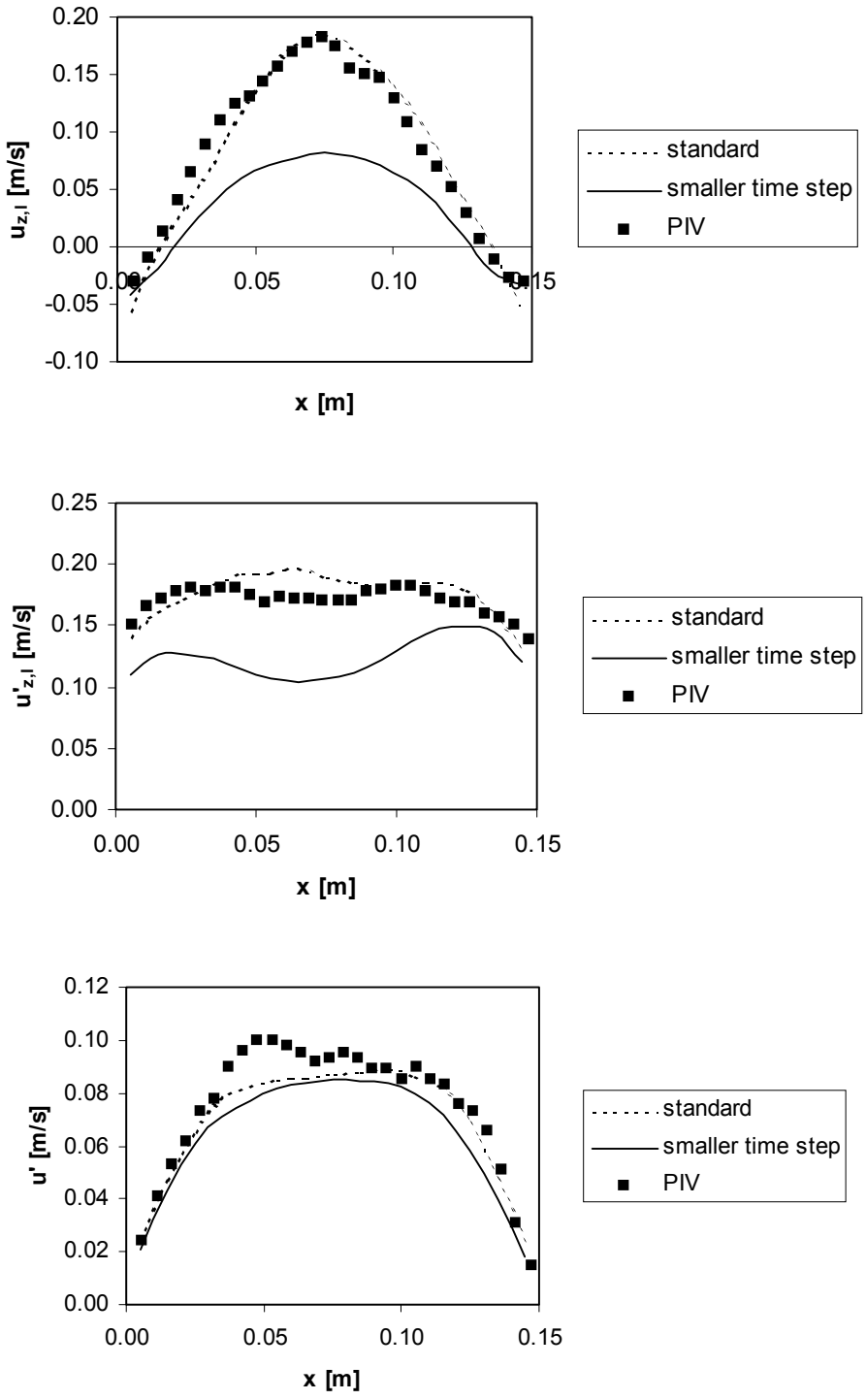

Figure 4.7: Comparison of the simulated and experimental average liquid velocity profiles for case 2 (see Table 4.1) at a height of 0.255 m and a depth of 0.075 m: Effect of the time step. Top: average liquid velocity; middle: vertical liquid velocity fluctuations; bottom: horizontal liquid velocity fluctuations.

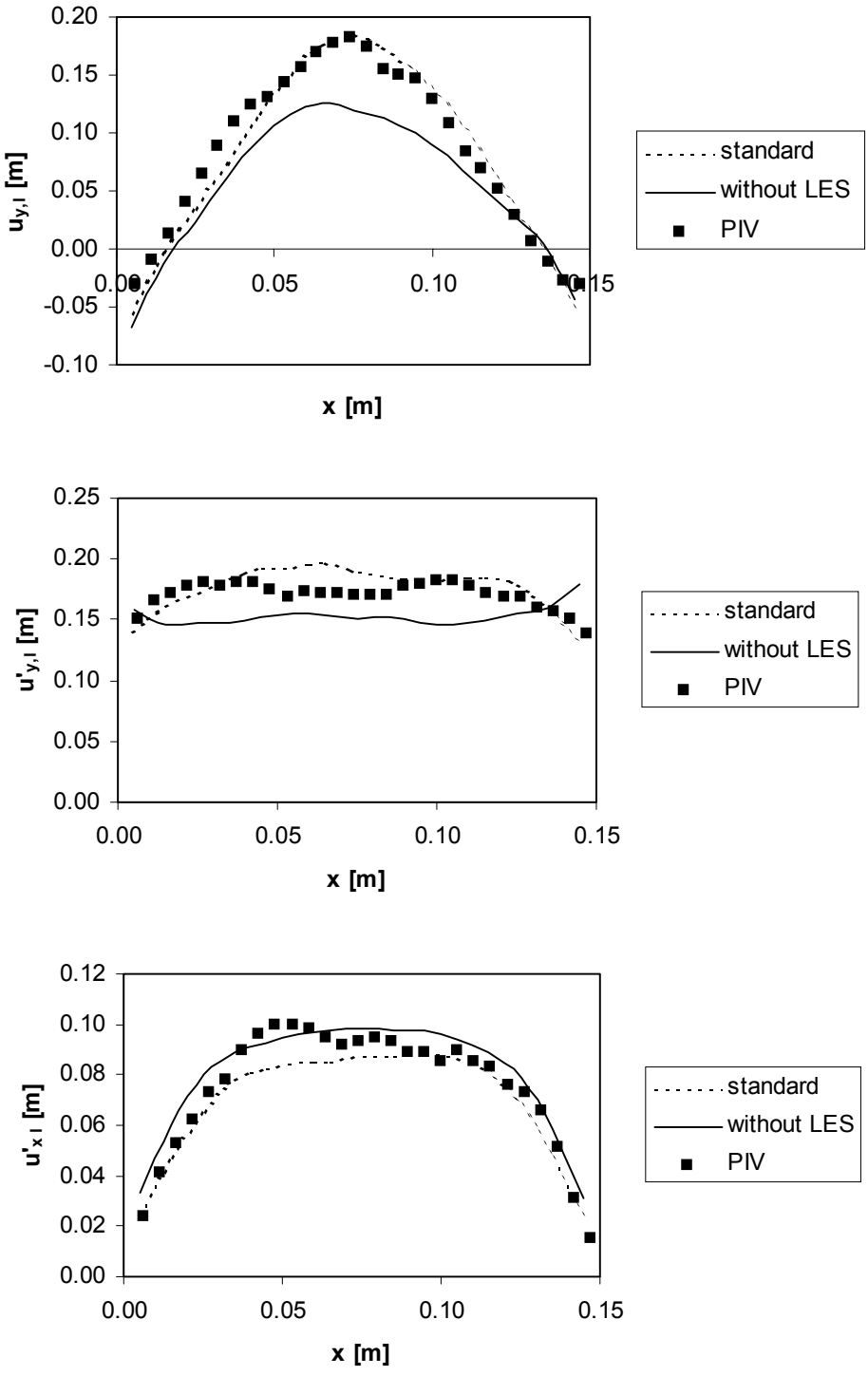

Figure 4.8: Comparison of the simulated and experimental average liquid velocity profiles for case 3 (see Table 4.1) at a height of 0.255 m and a depth of 0.075 m: Effect of LES. Top: average liquid velocity; middle: vertical liquid velocity fluctuations; bottom: horizontal liquid velocity fluctuations.

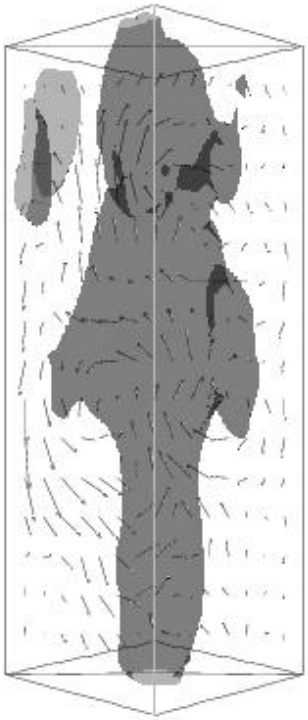

Figure 4.9: Snapshot of the liquid phase velocity field and the instantaneous iso-surface of α_g = 0.03 after 200 s for case 3 (see Table 4.1).

4.6.2 Gas-liquid system with MUSIG model

The second Euler-Euler model used here relies on a two-fluid description. In this model the MUSIG model was implemented in the gas phase, as described previously. The drag model of Ishii and Zuber (1979) was used (equation 4.9).
The bubbles in the gas phase were divided into 10 equally sized bubble size groups from 0.0 - 10.0 mm. All bubbles were entering the column with a diameter of 4.0 mm, the same diameter as in the gas-liquid model without MUSIG model. The break-up model used was the default model of Luo and Svendsen (1996) and the calibration factor for break-up had the default value of 1.0. For the coalescence model the default model of Prince and Blanch (1990) was used and the calibration factor for coalescence had the default value of 0.05.

Figure 4.10 shows the results of the average velocity profile and the velocity fluctuations for the standard case. The results are compared to the results of the gas-liquid phase without MUSIG model. The difference between model with and without MUSIG model

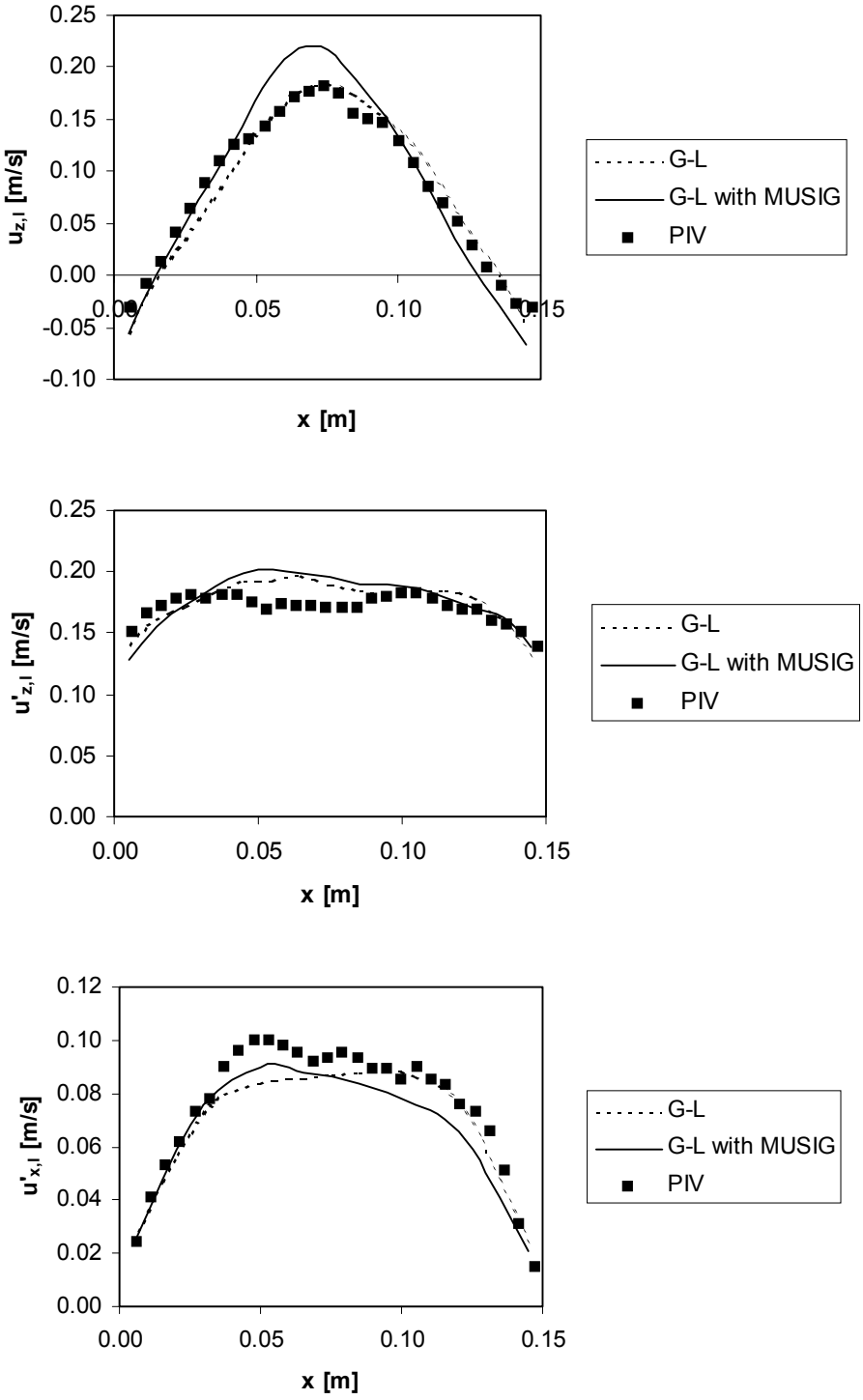

Figure 4.10: Comparison of the simulated and experimental average liquid velocity profiles case 0 and 4 at a height of 0.255 m and a depth of 0.075 m: Effect of MUSIG model. Top: average liquid velocity; middle: vertical liquid velocity fluctuations; bottom: horizontal liquid velocity fluctuations.

is about 15 %. The difference between the velocity fluctuation profiles between the case with and without MUSIG model is smaller. Therefore it can be concluded that the MUSIG model has small influence on the flow in the bubble column.

Figure 4.11 shows a snapshot of the liquid phase velocity fields and the instantaneous iso-surface of α_g = 0.03 of case 4. The standard case contains more bubbles in the top of the column. The bubble plume is the bottom of the column is about the same for the case with and without MUSIG model.

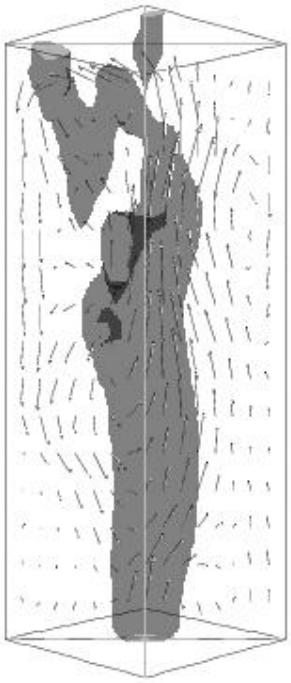

Figure 4.11: Snapshot of the liquid phase velocity field and the instantaneous iso-surface of α_g = 0.03 after 200 s for case 4 (see Table 4.1).

4.6.3 Gas-gas-liquid model

As was found in the previous section, the MUSIG model has small influence on the flow in the bubble column. All bubbles in this model have the same velocity. When equation 4.9 is used the drag force becomes independent of the bubble size, which is in agreement with the constant rise velocity that is found for large bubbles as evident from

Figure 4.2. For smaller bubbles however, the terminal velocity is smaller and another drag relation should be used.

To investigate the effect of the different bubble rise velocity of smaller bubbles a third Euler-Euler model is used. This is a three-phase gas-gas-liquid model or a three-fluid model. The gas phase was divided into two groups, one with smaller bubble diameters of 2 mm and one with larger bubble diameters of 6 mm. Half of the gas volume fraction of the bubbles at the inlet were 2 mm and the other half are 6 mm.

The bubbles in the small bubble phase were in the viscous regime ($0 \leq Re \leq 500$ to 1000). The drag relation used in this phase is the relation given by Schiller and Nauman (1933), equation 4.6. The bubbles in the large bubble phase were in the distorted regime ($500 - 1000 \leq Re \leq 1$ to 2×10^5). For this regime the drag relation given by Ishii and Zuber (1979), given by equation 4.9, was used.

In Figure 4.12 the average velocity profiles and the velocity fluctuations are shown. The results are compared to the standard gas-liquid model. As can be seen in the figure, the curve of the average liquid velocities of the gas-gas-liquid model lies lower than that of the gas-liquid model. This is due to the fact that the small bubbles are modelled with a different drag relation, which gives rise to lower slip velocities. This effect is confirmed in Figure 4.13, which shows lower average velocities with a high maximum in the middle. The oscillation of the plume is minor. The velocity fluctuation profile in the vertical direction also shows lower values in the case with small diameters and a high maximum in the middle. The velocity fluctuation profile in the horizontal direction shows higher values in the case with small diameters.

Figure 4.14 shows snapshots of the liquid phase velocity fields and the instantaneous iso-surface of $\alpha_g = 0.03$ of case 4 and 6. The bubble plume in the gas-gas-liquid model contains less gas than in the standard case. The bubble plume in the model with small bubble diameters shows hardly any movement of the bubble plume, as can also be seen in the average velocity profiles and velocity fluctuations.

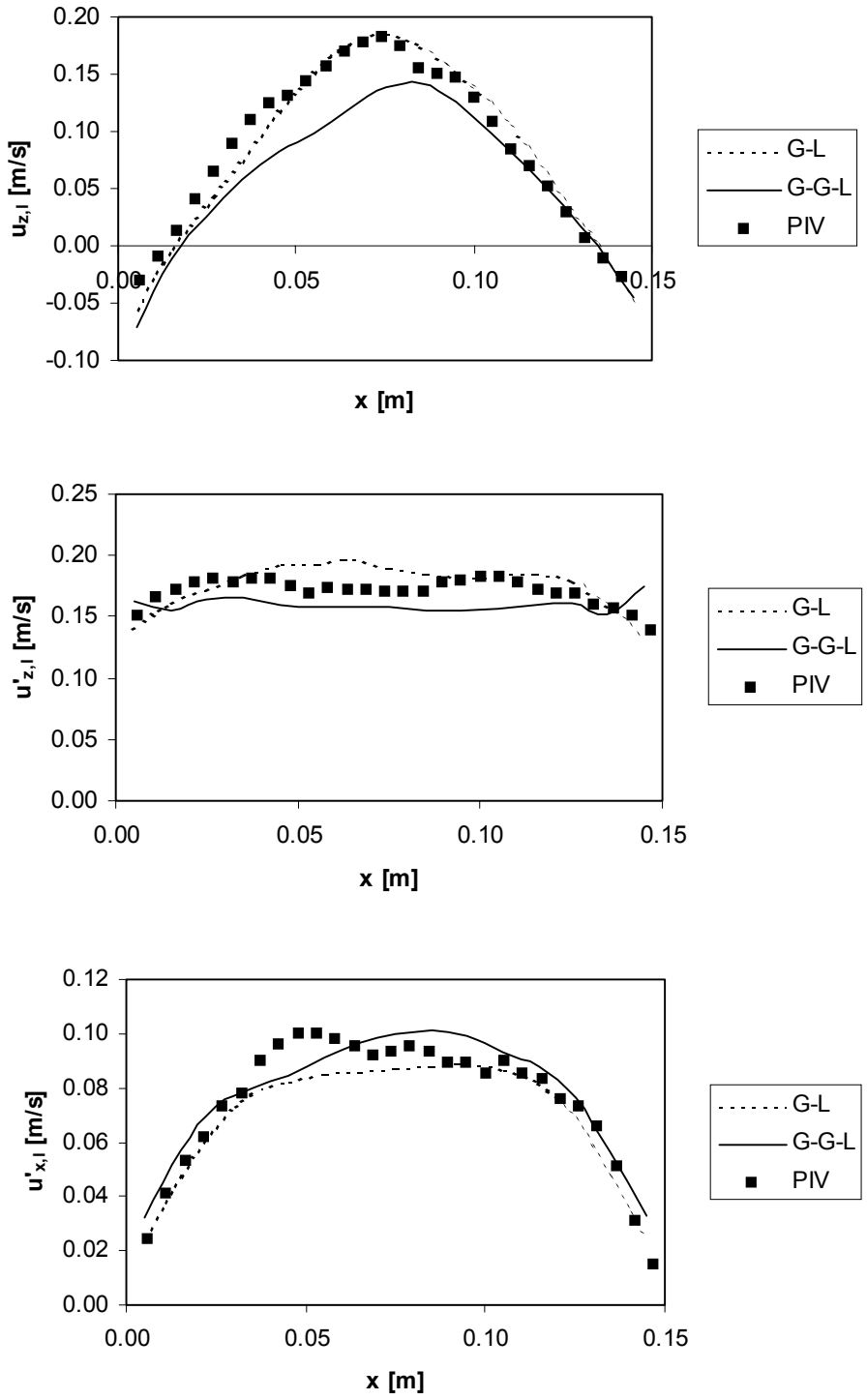

Figure 4.12: Comparison of the simulated and experimental average liquid velocity profiles case 0 and 5 at a height of 0.255 m and a depth of 0.075 m: Effect of number of gas phases. Top: average liquid velocity; middle: vertical liquid velocity fluctuations; bottom: horizontal liquid velocity fluctuations.

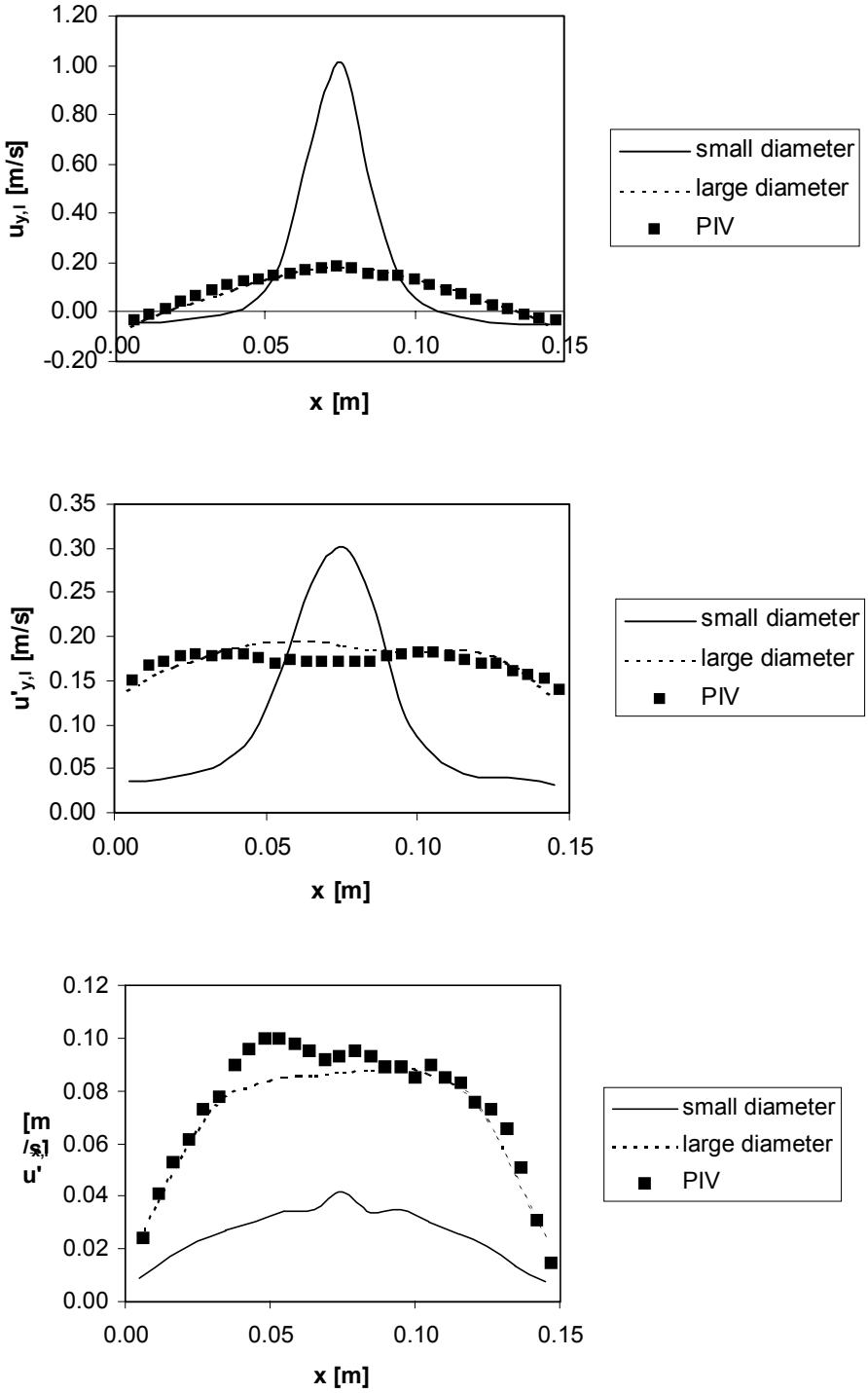

Figure 4.13: Comparison of the simulated and experimental average liquid velocity profiles case 0 and a case 6 at a height of 0.255 m and a depth of 0.075 m: Drag relation. Top: average liquid velocity; middle: vertical liquid velocity fluctuations; bottom: horizontal liquid velocity fluctuations.

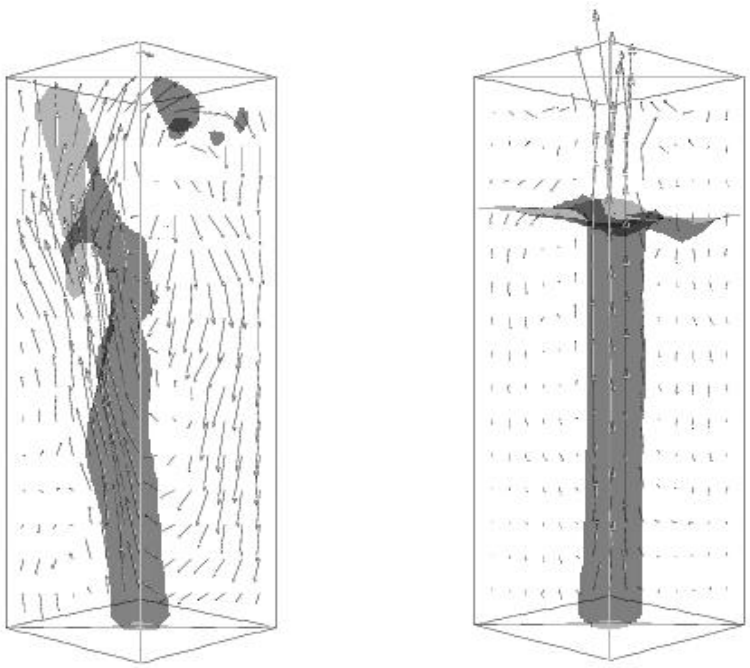

Figure 4.14: Snapshot of the liquid phase velocity field and the instantaneous iso-surface of α_g = 0.02 after 200 s for case 5 (see Table 4.1) (left) and case 6 (see Table 4.1) (right).

4.7 Results break-up and coalescence

The default break-up model in MUSIG is the model of Luo and Svendsen (1996). The default coalescence model is the model of Prince and Blanch (1990).
In order to investigate the influence of the coalescence model, the default model was replaces with the model of Chesters (1991), studied in Chapter 3:

$$\lambda = exp\left[-\frac{C_2}{2}\sqrt{We}\right] \tag{4. 30}$$

The bubble column used for the simulation in CFX was the same column described in the previous section. At different heights in the column (0.10, 0.20 and 0.30 m) the bubble size distribution is determined and the results are compared. The calibration factor for coalescence was set to a value of 1.0 in both cases.
The same column was also simulated with the discrete bubble model (see Chapter 3). In this model the coalescence model of Chesters (1991) is incorporated. In all three models the break-up model of Luo and Svendsen (1996) used.
In Figure 4.15 the results of the computed bubble size distributions are presented.

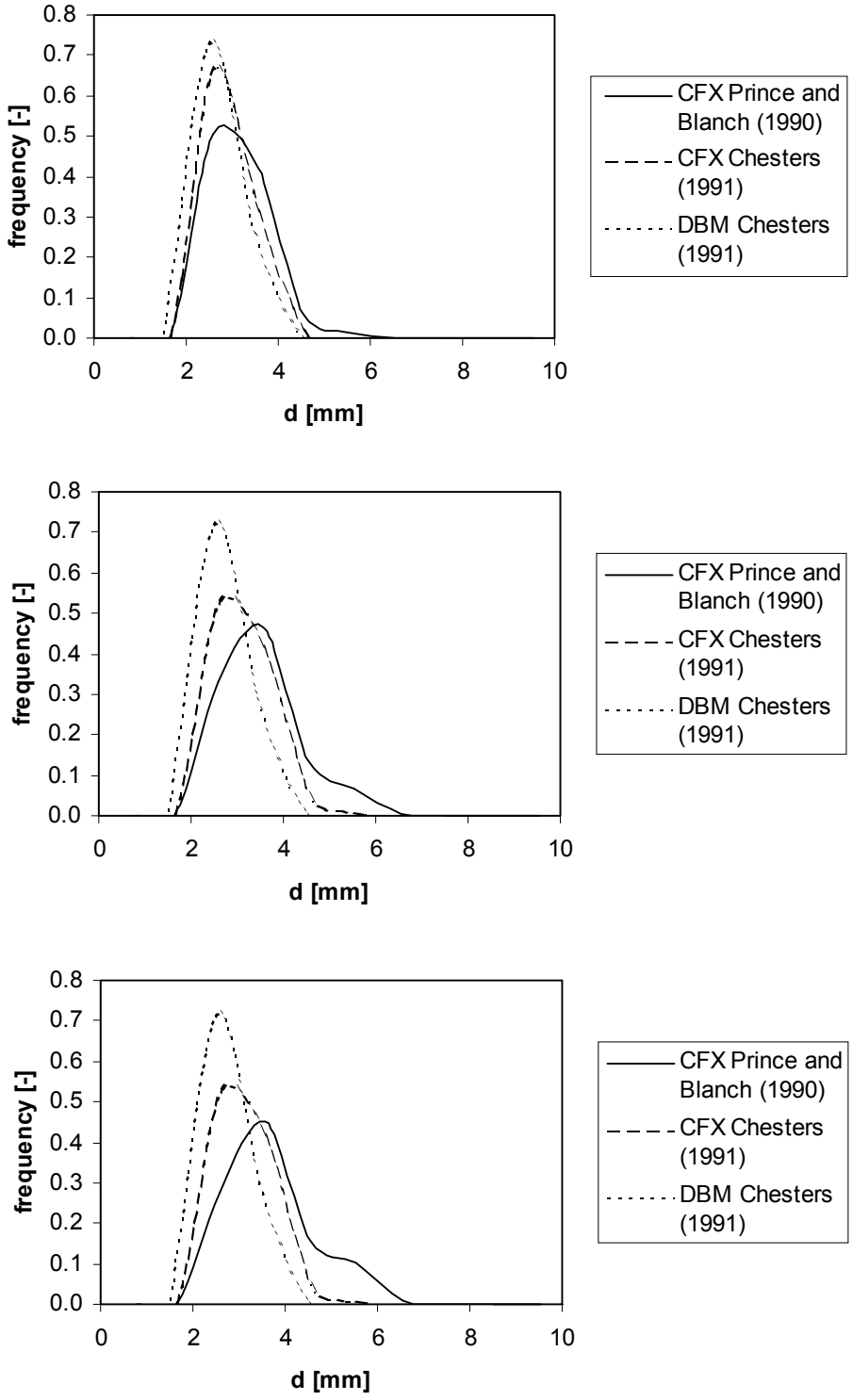

Figure 4.15: Bubble size distribution for three different cases at three different heights: Top: 0.10 m, middle: 0.20 m; bottom: 0.30 m.

In this figure it can be seen, that the bubbles in the DBM are the smallest and the bubble size distribution is the narrowest. The bubbles in the model of Prince and Blanch (1990) are the largest and the bubble size distribution is the widest. The coalescence rate for this model is clearly larger than that of the other two models. This can also be concluded from the change in the slope at larger bubble diameters. In CFX the bubble size increases more with increasing height in the column, compared with the DBM.

4.8 Conclusions

In this Chapter three different Euler-Euler models are used to describe two-phase flows in bubble columns: A gas-liquid model, a gas-gas-liquid model and a gas-liquid model with the MUSIG model for the gas phase. For the simulations of the Euler-Euler model the commercial code CFX 4.4 is used. In all three Euler-Euler models a LES-turbulence model is incorporated. The MUSIG model, including population balances with a break-up and coalescence model is used to study the bubble size distribution in the column. To study the effect of the different rise velocities of the bubbles a three-phase gas-gas-liquid system is simulated. The gas phase is divided into two groups, one with smaller bubble diameters of 2 mm and one with larger bubble diameters of 6 mm with different drag relations. The results of all three models are compared with experimental PIV results measured by Deen (2001) in a square bubble column filled with distilled water.
Good agreement was reached comparing the simulation results of the gas-liquid model to the experimental results. When using a smaller grid size the velocity and velocity fluctuations are lower, but the differences between the velocity profiles of the case with smaller grid sizes and the standard case are marginal.
The agreement between the simulation results and experimental results for the Euler-Euler model is better than for the Euler-Lagrange model (Chapter 3). This can probably be due to the differencing scheme, which is different in the Euler-Euler and Euler-Lagrange model. Another reason can be the use of the encounter model in the Euler-Lagrange model.

When the LES model is implemented the velocity and velocity are higher than in the case without LES. The effective viscosity in case of LES is higher due to the turbulence viscosity. In the gas-liquid model with MUSIG model the bubbles in the gas phase are divided into 10 equally sized bubble size groups from 0.0 - 10.0 mm. The break-up model used was the default model of Luo and Svendsen (1996), the coalescence model the

default model of Prince and Blanch (1990). The difference between the models with and without MUSIG model is very small because all size groups have the same rise velocity and thus the same drag relation. The curve of the average liquid velocities of the gas-gas-liquid model lies lower than that of the gas-liquid model. This is the effect of the smaller bubbles with a different drag relation. In this case the average velocity is lower with a high maximum in the middle of the column. The movement of the bubble plume is very weak, as can be concluded from the velocity fluctuations.

Simulation results of two different coalescence models, Prince and Blanch (1990) and Chesters (1991) are compared with simulation results of the DBM with the coalescence model of Chesters (1991) in a square column. In all models the break-up model of Luo and Svendsen (1996) is incorporated. In CFX the bubble size increases more with increasing height in the column.

The bubbles in the DBM are the smallest and the bubble size distribution is the narrowest. The bubbles in the model of Prince and Blanch (1990) are the largest and the bubble size distribution is the widest. As said in Chapter 3 the results of the DBM with the coalescence model of Chesters (1991) and the break-up model of Luo and Svendsen (1996) shows the best agreement with experimental results. The results of the Euler-Euler model with the models of Chesters (1991) and Luo and Svendsen (1996) are the best in agreement with the results of the DBM.

Chapter 5

IMAGE ANALYSIS IN PSEUDO 2D COLUMN

Abstract

In this chapter an imaging technique will be used to measure the bubble size distribution and mean diameter in a lab-scale pseudo 2D bubble column at different heights and different flow rates.
In distilled water the mean diameter increases with increasing height and with increasing flow rate in the column because of coalescence of the bubbles. The bubble size distribution moves to larger diameters with increasing height. The same is observed with increasing flow rate.
Octanol ($2.4 \cdot 10^{-4}$ M) added to the distilled water reduces the extent of coalescence. The mean diameter shows a weak increase with increasing height in the column which can be attributed to the decrease in hydrostatic pressure with increasing height. The mean diameter decreases with increasing flow rate, because only break-up occurs and coalescence is inhibited.

5.1 Introduction

Bubble columns are used as gas-liquid reactors in a variety of industrial processes. Despite the widespread applications of bubble columns and substantial research efforts, detailed knowledge on the hydrodynamics is still lacking. Bubble columns have been subject of research for many years and various researchers developed CFD models for gas-liquid bubble columns that can provide detailed information about the prevailing hydrodynamics.

In order to validate the CFD models, the simulation results should be compared to experimental data. For the validation of the break-up and coalescence models in both the Euler-Euler and Euler-Lagrange models, information about the bubble size distribution and the velocity maps of both phases are typically of interest.

Bubble sizes can be measured with different techniques. The most frequently used techniques are probe and imaging techniques. The probe techniques are known to influence the gas-liquid flow pattern, which is a disadvantage of this technique. The advantages of the imaging technique are the non-intrusiveness, the technique is not expensive and it maps the situation in the column without having to reconstruct the image from measured data. A disadvantage of this technique is that it can only be applied in pseudo 2D systems. Despite of this disadvantage the imaging technique has been applied in many studies for measuring bubble sizes (Pacek *et al*., 1994; Machon *et al*., 1997; Lage *et al*., 1999). Recent studies (Bröder *et al*., 2002 and Kluytmans, 2003) used a high speed camera to capture images. In all cases images are captures from a 2D column. The images are analysed and the bubble sizes are measured in different ways. In this chapter the imaging technique is used in a pseudo 2D column to measure the bubble size distribution and the bubble mean diameter.

5.2 Image analysis procedure

The image analysis described in this chapter is used to measure the bubble size distribution and the mean diameter of bubbles in a pseudo 2D bubble at different heights in the column and at different superficial gas velocities. The bubble sizes are determined by measuring ‘bubble shadows’ in shadow images, captured from the bubbles in the column with a digital camera. The analysis of the images is off line by the software called VisiSize Solo (AEA Technology, England).

A CCD camera generally records 8 bit images, which correspond to 255 grey levels, where 0 is black and 255 is white. Only images with sufficient contrast between the gas and the liquid can be analysed. The images in the case, where the column is illuminated from behind, have a light background with the bubbles appearing as dark objects in the field of view. It is important for the analysis that the edges of the bubbles are dark and distinct from the background. However, light areas in the centre of the bubble images will not affect the analysis. For both diameter analysis, the illumination of the image background should be as uniform as possible. The illumination of the image background must also be within a certain range for accurate analysis. To ensure that the illumination on the image is correct the peak in the background intensity histogram (Figure 5.1) should lie between the grey levels of 140 and 240 and should be reasonably narrow.

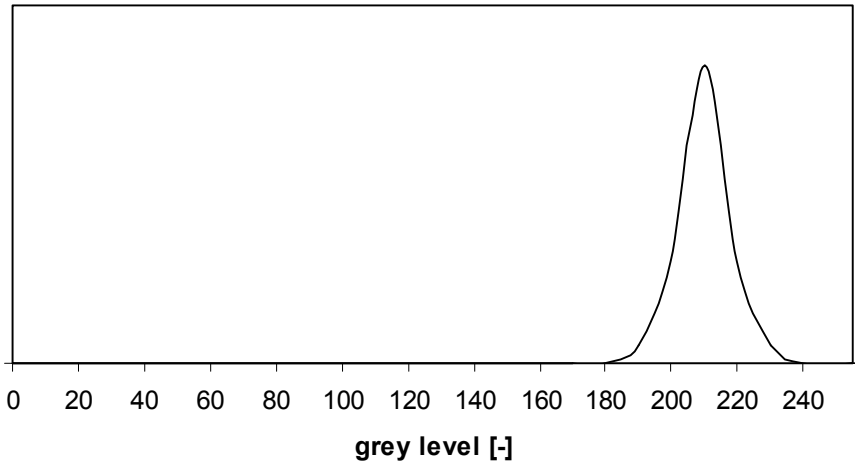

Figure 5.1: Background intensity histogram.

The VisiSize software uses a simple thresholded segmentation algorithm to identify and measure bubbles in an image. The images are thresholded in order to distinguish between the bubbles and the illumination background. The threshold level is the grey level above which pixels in the image can be assumed to be in the background. A threshold is chosen between 0 and 255; all pixels lower in value (darker) than the threshold are considered to belong to a bubble. The right threshold value for the measurements can be determined by using the background intensity histogram. In this histogram the grey level value is taken at which the background peak starts to rise. This is the minimum background level B. Since the profile of a small bubbles may not reach full darkness, in order to count small

bubbles, it is essential to set the threshold T just slightly below the minimum background level B, so a value of 10 is subtracted from the minimum background level B. But T must not be set higher than B, otherwise elements of the background will be identified as objects. Therefore it is important to choose the value of T carefully. A typical grey level histogram of an image looks like:

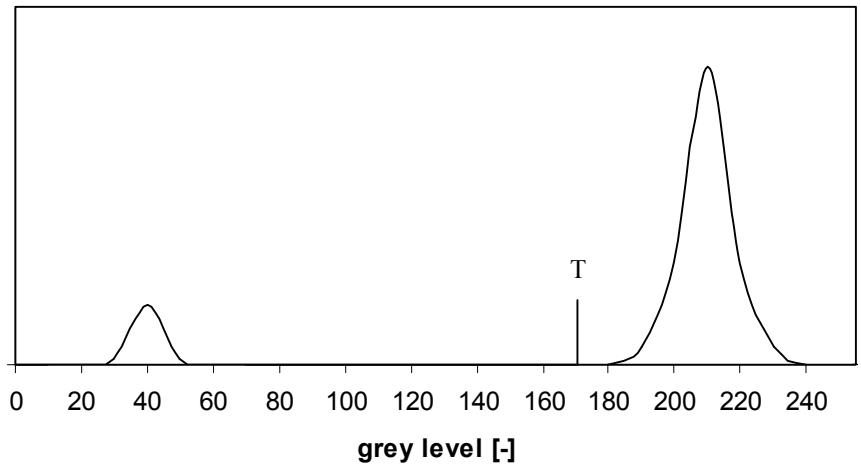

Figure 5.2: Grey level histogram for value of T.

The large peak in Figure 5.2 represents the background. The small peak represents the dark interiors of the larger bubbles (there may not be a foreground peak if the dark areas represent less than 1% of the image). The settings of T as shown will count most of the small objects.
The binary threshold value T has an effect on the results, and hence on the accuracy. It is very important to have always the same value for the threshold for the accuracy of the calculation of the bubble diameter. To understand the effect of the value of the threshold T, consider the grey level across one line of a typical image, that intersects three bubbles:

When T in Figure 5.3 has a lower value, the bubble sizes will be smaller (bubble 1 and 2) or bubbles are not counted (bubble 3).

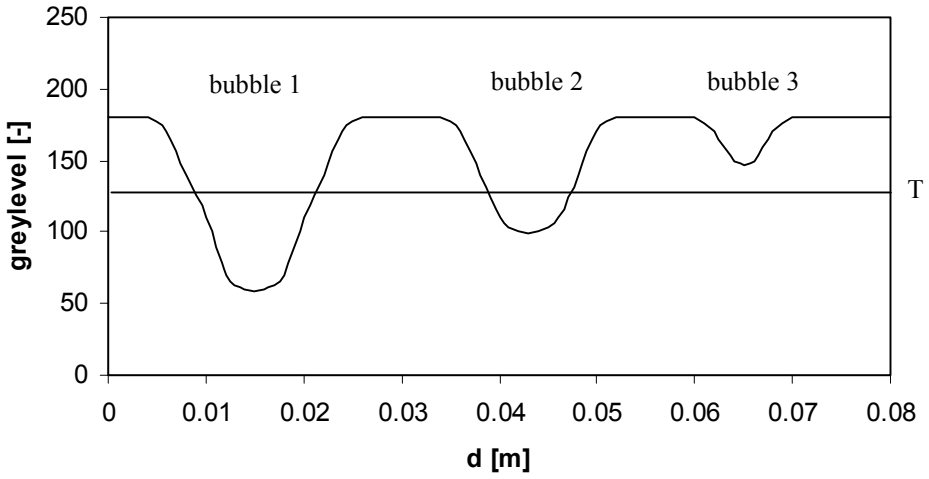

Figure 5.3: Effect of the value of threshold T.

The image is scanned from top to bottom, identifying dark segments on each line and associating them with the segments on the previous line. When a bubble is complete calculations are performed on the bubble.

For circular bubbles the diameter calculation is straightforward. For noncircular shapes, there are four different ways of characterising the bubble size (they are all equal for a spherical bubble). In the functions below A is the pixel area, P is the pixel perimeter and C is the microns/pixel calibration, also called the magnification.

Assuming that the bubble is a circle the pixel area is given by:

$$A_{pixel} = \pi \left(\frac{d_A}{2} \right)^2 \tag{5. 1}$$

where d_A is the bubble diameter based on the pixel area A_{pixel}

Therefore the equivalent diameter (in microns) is given by:

$$d_A = C \sqrt{\frac{4 A_{pixel}}{\pi}} \tag{5. 2}$$

Similarly using the perimeter P_{pixel}, then for a circle P_{pixel} is given by:

$$P_{pixel} = \pi d_P \tag{5. 3}$$

where d_p is the bubble diameter based on the pixel perimeter P_{pixel}
The equation for the equivalent circular perimeter is:

$$d_P = C \cdot \frac{P_{pixel}}{\pi} \tag{5. 4}$$

The Heywood diameter d_H is the smallest circle enclosing the particle (see Figure 5.4).

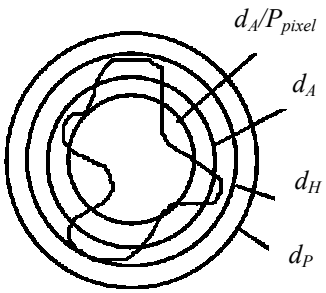

Figure 5.4: Definition of different diameters.

If the bubble is a perfect circle then $d_A=d_P$ such that $d_A/d_P=1$. The ratio d_A/d_P is a measure of the sphericity of the bubble and is computed as the shape factor in VisiSize Solo. Therefore using the equations 5.2 and 5.4 the sphericity is given as:

$$\frac{d_A}{d_P} = \frac{\frac{\sqrt{4A_{pixel}}}{\pi}}{\frac{P_{pixel}}{\pi}} = \frac{\sqrt{4\pi A_{pixel}}}{P_{pixel}} \tag{5. 5}$$

The software actually computes the shape factor as:

$$\left(\frac{d_A}{d_P}\right)^2 = \frac{4\pi A_{pixel}}{P_{pixel}^2} \tag{5. 6}$$

For a whole sequence of images the software can determine the bubble size distribution and the number mean diameter, the volume mean diameter and the Sauter mean diameter, respectively given by:
Number mean diameter (average diameter of all bubbles in the sample):

$$d_{10} = \frac{1}{N_B} \sum_{k=1}^{N_B} d_k \tag{5. 7}$$

Volume mean diameter (diameter of a bubble whose volume, if multiplied by the total number of bubbles, equals the total volume of the sample):

$$d_{30} = \left(\frac{1}{N_B} \sum_{k=1}^{N_B} d_k^3 \right)^{\frac{1}{3}} \tag{5. 8}$$

Sauter mean diameter (diameter of a bubble whose ratio of volume to surface area is the same as the complete sample):

$$d_{32} = \frac{\sum_{k=1}^{N_B} d_k^3}{\sum_{k=1}^{N_B} d_k^2} \tag{5. 9}$$

5.2.1 Image analysis parameter

Before starting any bubble distribution analysis, it is important that the image analysis parameters are set correctly. To set these parameters, one single image with a perfect circle is used for the purpose of callibration.
In these experiments a perfect circle with a diameter of exactly 15 mm is used to set the parameters. The area of the analysed images 0.09 x 0.09 cm. It is not possible to take a smaller area, because the lens cannot make sharp images closer to the bed. In this case a bubble of 1 mm has a diameter of 6 pixels and an area of 25 pixels. Assuming the error is half a pixel of the outer ring, the error of a bubble of 1 mm is 17.6 %. For a bubble of 4 mm (mean diameter of the bubbles in the column) the error is 4.4 %.

The pixel area of the smallest bubble, which will be measured in the image, the minimum pixel area, is set at 10 pixels. Bubbles, which appear in the same position on the screen in five consecutive images, are rejected. So any marks on the camera or lens will not be counted as real bubbles and are omitted form the bubble size distribution.

The bubbles images are overlapping each other in the captured image, because the bubbles are bouncing at the moment the image is captures or two bubble lay (partly) behind each other. In the two-dimensional image, this last point is seen as two bubbles overlapping each other. The higher the hold-up in the bubble column, the more bubbles are overlapping. VisiSize cannot distinguish the individual bubbles in a cluster of bubbles and will give only one (too large) diameter for these bubbles. To get accurate results a validation algorithm is used. For this algorithm a minimum shape factor is determined. Bubbles or clusters of bubbles with a shape factor lower than the minimum are discarded. The shape factor determines the degree of shape rejection used. The higher the value, the more spherical a bubble needs to be in order to be analysed.

In Figure 5.5 the Sauter mean diameter of a picture is calculated with different values of the minimum shape factor. Images are captured for 8 sec (2096 images) at a flow rate of $4.17 \cdot 10^{-5}$ m^3/s (superficial gas velocity = $7 \cdot 10^{-3}$ m/s; hold-up = 2.91 %). At low values of the shape factor also clusters of bubbles are analysed. When increasing the shape factor, these clusters are rejected and the Sauter mean diameter has a lower and more accurate value. At the shape factor > 0.95 the Sauter mean diameter increases again. In this case only a very few bubbles are analysed. When one of these bubbles is a large spherical bubble this will give a large Sauter mean diameter.
In order to remove all clusters of bubbles the shape factor was set at a value of 0.75.
The disadvantage of this shape factor is that some large bubbles are not analysed. The sphericity of large bubbles is sometimes lower than 0.75. Therefore the mean diameter will be somewhat lower than the actual value.

5.2.2 Accuracy

After calibration and determination of the shape factor some tests were done to check whether the VisiSize Solo software gives good values for the diameter of the bubbles. In these tests two sheets are used with printed circles and ellipses with known diameters. In

one sheet the circles and ellipses are printed separately and in the other sheet the circles are partly overlapping each other (see Figure 5.6).

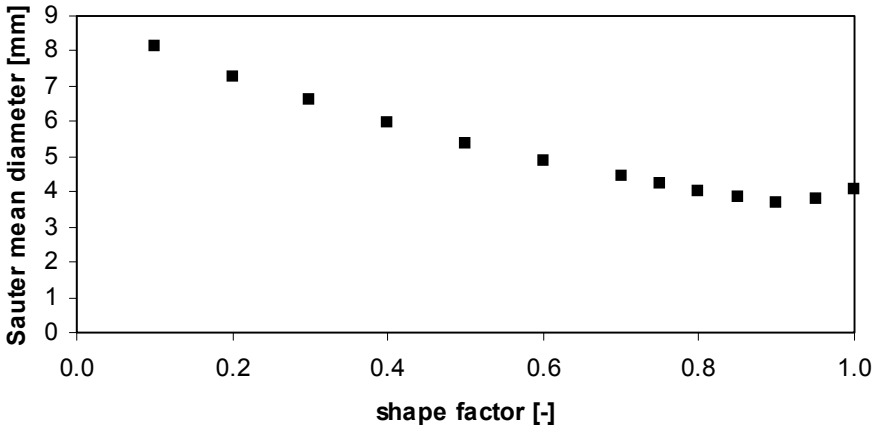

Figure 5.5: Experimental calculation of Sauter mean diameter at different shape factors.

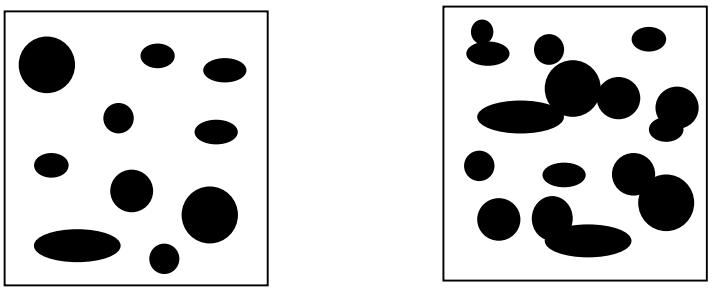

Figure 5.6: Sheets for testing overlap on the results of the measured bubble diameter.

In the case of overlapping circles the larger circles show more overlap than the smaller circles. The same situation can be seen in bubble columns: Larger bubbles show more overlap than smaller bubbles. Images are captured from both sheets and the images are analysed in VisiSize. In both cases VisiSize overestimates the circle sizes with about 8-10 %. So the rejection of clusters of bubbles because of overlap of the bubbles gives no larger error in the determination of the bubble size.

In order to be assured that the correct value of the bubble size distribution and the mean diameter is determined, the number of images/bubbles needs to be analysed. Images are captured for 8 sec (2096 images) at a flow rate of $4.17 \cdot 10^{-5}$ m^3/s (superficial gas

velocity = $7 \cdot 10^{-3}$ m/s; hold-up = 2.91 %). The mean diameters are determined after 200, 400, 600 etc. images. This value is compared with the previous determined value. If the deviation between the present and previous value is less than 1 %, it is assumed that the mean diameter has a constant value, which is independent of the remaining images.
Usually, the constant value is obtained after analysing about 600 images or 10.000 bubble images, as shown in Figure 5.7.

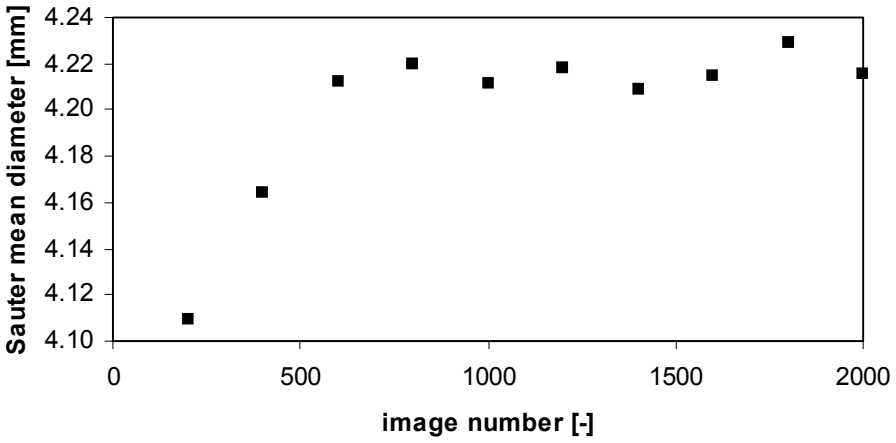

Figure 5.7: Experimental determination of minimum number of images (superficial gas velocity = $7 \cdot 10^{-3}$ m/s; hold-up = 2.91 %.

5.3 Experimental set-up

The imaging technique described in this chapter is used to study the bubble size distribution in a pseudo 2D column consisting of two parallel (distance 30 mm) plates (see Figure 5.8) with a height of 1.5 m and a width of 0.2 m. The column is filled with distilled water at a height of 1.4 m and the gas is fed at the bottom of the column through a porous plate (with pores ranging from 40-100 μm) (see Figure 5.9).

Digital images of the front side of the column are recorded with a high-speed Dalsa CA-D6-0512W camera (Tech5, The Netherlands) at a rate of 262 frames per second with a 50.0 mm lens. The camera resolution is 532H x 516V pixels. During the recording time, the images are stored in the memory of a PC. The working memory size of 1 GB limits the recording time to approximately 14 seconds. Digital images of the front side of the column are recorded with a high-speed Dalsa CA-D6-0512W camera (Tech5, The

Netherlands) at a rate of 262 frames per second with a 50.0 mm lens. The camera resolution is 532H x 516V pixels. During the recording time, the images are stored in the memory of a PC. The working memory size of 1 GB limits the recording time to approximately 14 seconds. The data is stored from the memory to the hard disk of a PC. The images are analysed off line with the software package VisiSize Solo (AEA Technology, England).

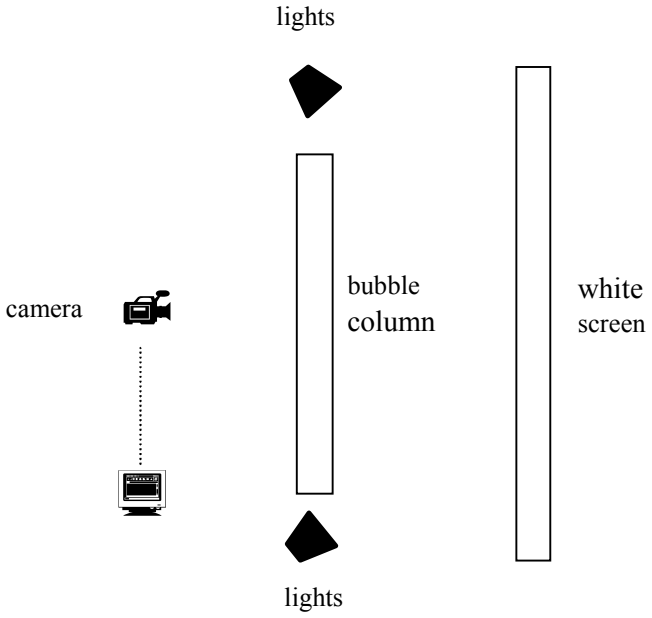

Figure 5.8: Experimental set-up of pseudo 2D column for image analysis.

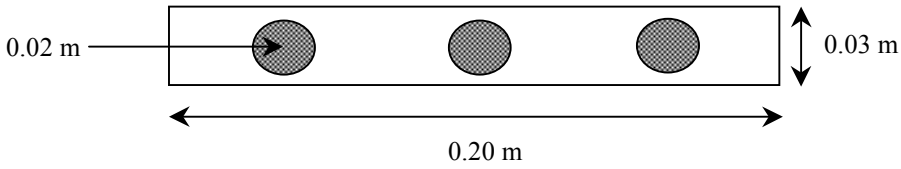

Figure 5.9: Bottom plate of the pseudo 2D column.

Because of the high frame rate and thus the fast shutter speed of the camera, enough light should be provided to capture the images with sufficient contrast. The illumination of the background should be as uniform as possible. On both sides of the column 3 halogen lights of 500 W each are used, which illuminated the column via indirect lighting on a white projector screen behind the column.

5.4 Experiments

The bubble size distribution and the number, volume and Sauter mean diameter were determined for different gas flow rates (superficial velocity) and for different heights in the column.
The overall gas hold-up is determined by measuring the liquid surface level expansion.
For all measurements the column is filled with distilled water at the same height. All measurements were carried out twice to test the accuracy of the measurements.

First the measurements have been carried out in distilled water for 6 different flow rates, shown in Table 5.1.

Table 5.1: Flow rates, hold-up and superficial gas velocity of video measurements with distilled water.

experiment	flow rate [m^3s^{-1}]	hold-up [%]	superficial gas velocity [$m\ s^{-1}$]
1	$0.83 \cdot 10^{-5}$	0.73	$1.39 \cdot 10^{-3}$
2	$1.67 \cdot 10^{-5}$	1.17	$2.78 \cdot 10^{-3}$
3	$2.50 \cdot 10^{-5}$	2.05	$4.17 \cdot 10^{-3}$
4	$3.33 \cdot 10^{-5}$	2.55	$5.56 \cdot 10^{-3}$
5	$4.17 \cdot 10^{-5}$	2.91	$6.94 \cdot 10^{-3}$
6	$5.00 \cdot 10^{-5}$	3.42	$8.33 \cdot 10^{-3}$

It was not possible to measure at higher superficial gas velocity, because in that case there are too many clusters of bubbles and hardly any separate bubbles could be distinguished on the image.

For all experiments the measurements were carried out at 5 different heights in the column: 0.15 m, 0.25, m, 0.50 m, 0.75 m, 1.00 m. It was not possible to measure closer to the nozzle, because no separate bubbles could be distinguished on the images due to excessive bubble-bubble overlap.
To inhibit coalescence the same measurements were performed in distilled water with octanol. Total coalescence inhibition is reached at 10^{-4} kmol m^{-3} (Zahradník et al, 1999). The column is filled with 8 litre distilled water, so 0.104 g octanol is needed to reach total coalescence inhibition. In these measurements 0.25 g octanol was used, to be sure that

total coalescence inhibition was reached. The surface tension of water with octanol was 0.0646 N/m.
The measurements were carried out at the same heights as for distilled water, but at different flow rates (Table 5.2).

Table 5.2: Flow rates, hold-up and superficial gas velocity of video measurements with distilled water and octanol.

experiment	**flow rate [$m^3 s^{-1}$]**	**hold-up [%]**	**superficial gas velocity [$m\ s^{-1}$]**
7	$0.42 \cdot 10^{-3}$	0.36	$0.69 \cdot 10^{-3}$
8	$0.83 \cdot 10^{-3}$	0.66	$1.39 \cdot 10^{-3}$
9	$1.25 \cdot 10^{-3}$	0.95	$2.08 \cdot 10^{-3}$
10	$1.67 \cdot 10^{-3}$	1.75	$2.78 \cdot 10^{-3}$

It was not possible to measure at higher superficial gas velocity in the case of distilled water with octanol. The bubbles are much smaller compared to the bubbles in distilled water. The hold-up in both cases is about the same, so the column contains much more bubbles in the case of distilled water with octanol.

First some measurements were performed for a few hours to be sure that the bubble size distribution and mean diameter reached constant values. In Figure 5.10 the results of the Sauter mean diameter vs the time can be seen. The Sauter mean diameter does not rise in time, and the error is ± 2%. It can be concluded that the amount of octanol in the water remains sufficiently high to inhibit coalescence effectively.

5.5 Results

In Figure 5.11 the results of the Sauter mean diameter at a superficial gas velocity of $5.56 \cdot 10^{-3}$ m s^{-1} in distilled water are shown at different heights in the column. Also the duplicate measurements can be seen in this Figure. The difference between the first measurements and the duplicates is maximum 2 %.

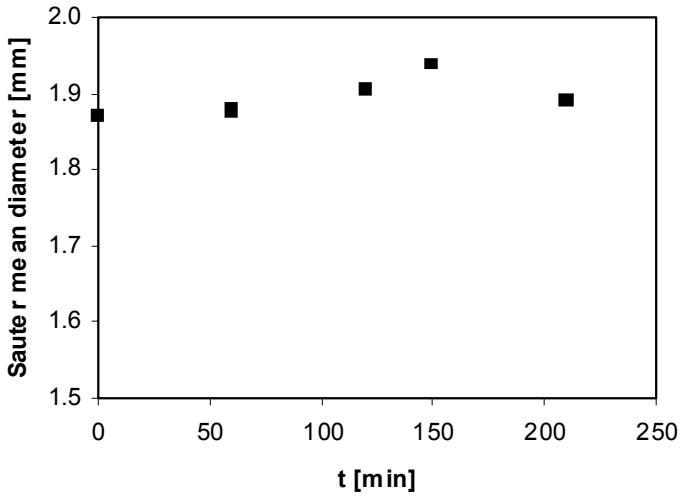

Fgure 5.10 Experimentally determined Sauter mean diameter vs. time for distilled water and octanol.

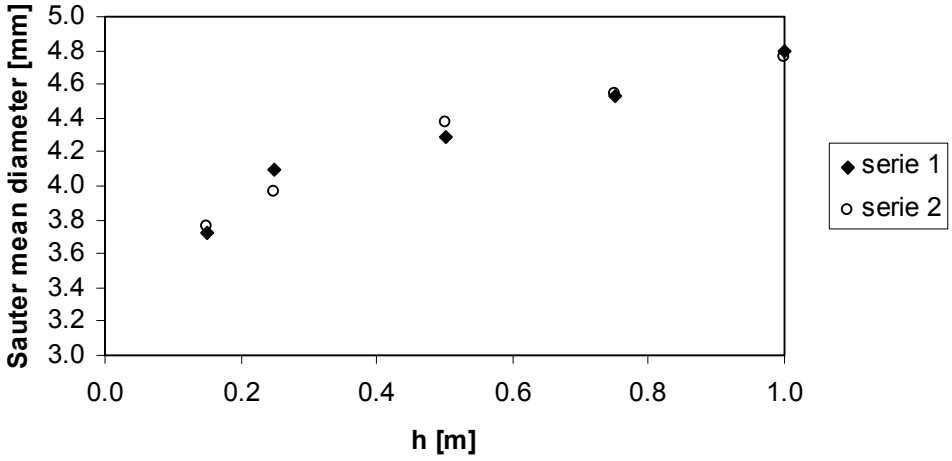

Figure 5.11: Experimentally determined Sauter mean diameter vs. height for a superficial gas velocity of $5.56 \cdot 10^{-3}$ m s^{-1}.

5.5.1 Distilled water

Figure 5.12 shows the number mean, volume mean and Sauter mean diameter vs. the height in the column for all applied flow rates. In Appendix 5A, Table 5A.1 the values obtained for the mean diameter at different heights are given. It can be concluded from the definition of the three different mean diameters, that number mean diameter < volume

mean diameter < Sauter mean diameter. This can also be seen in Table 5A.1 and by comparing the results shown in Figure 5.12.

The mean diameter increases with increasing height in the column. The increase of diameter is due to decreasing hydrostatic pressure and because of coalescence. The increase in diameter because of pressure is about 3% going from 15 cm to 100 cm. The higher their position in the column, the longer bubbles generally have resided in the column and the more opportunity they have had to coalesce. This explains why the Sauter mean diameter increases with height in the column.

The mean diameter increases with increasing flow rate. This is due to the fact that when the flow rate is higher, the gas fraction increases and the bubbles are closer together. Therefore more collisions between the bubbles occur, the chance for coalescence is higher and the diameter of the bubbles becomes larger.

For low flow rates ($0.83 \cdot 10^{-3}$ m^3 s^{-1}, $1.67 \cdot 10^{-3}$ m^3 s^{-1}, $2.50 \cdot 10^{-3}$ m^3 s^{1}), the slope of the line in the lower part of the column is steeper than in the higher part. The mean diameter of the bubbles increases more with increasing height in the lower part of the column. In the higher part of the column, the mean diameter is almost constant. In the lower part of the column the bubbles stay together in a plume (see Figure 5.13). The bubbles are close together and they collide very often and coalescence can occur. In the higher part of the column, the bubbles are spread through the whole column and no coalescence is observed. The hold-up is low and therefore there is more space between the bubbles. The bubbles do not collide very often and the chance for coalescence is lower.

Some differences can be seen between low flow rates ($0.83 \cdot 10^{-3}$ m^3 s^{-1}, $1.67 \cdot 10^{-3}$ m^3 s^{-1}, $2.50 \cdot 10^{-3}$ m^3 s^{1}) and high flow rates ($3.33 \cdot 10^{-3}$ m^3 s^{-1}, $4.17 \cdot 10^{-3}$ m^3 s^{-1}, $5.00 \cdot 10^{-3}$ m^3 s^{-1}). At high flow rates the mean diameter increases with increasing diameter. As observed in Figure 5.13 the bubbles only stay together in a plume for the first 0.25 m. For heights > 0.25 m the bubbles are spread over the whole column. The hold-up is high and the bubbles are close together in the whole column. The bubbles collide and the chance for coalescence to occur is high in the whole column.

In Figure 5.14 the bubble size distribution at a superficial gas velocity of $5.56 \cdot 10^{-3}$ m s^{-1} at different heights in the column can be seen.

The bubble size distribution appears to be approximately Gaussian:

$$f_x(C_x) = \frac{q}{(2\pi\sigma)^{\frac{1}{2}}} e^{\frac{-(d-\mu)^2}{2\sigma}} \qquad (5.\ 10)$$

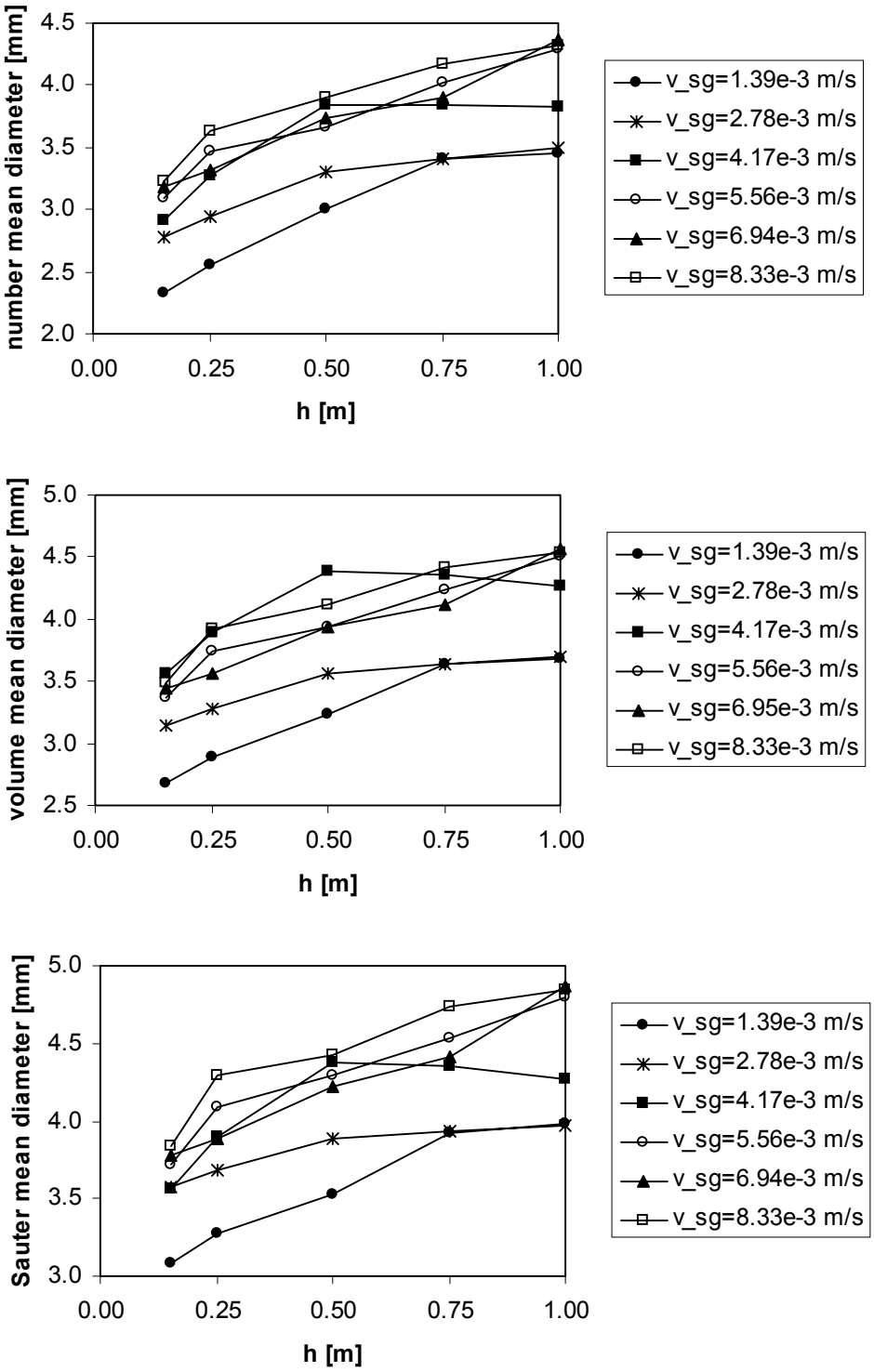

Figure 5.12: Experimental calculation of the mean diameter vs. height for different flows for distilled water. Top: number mean diameter; middle: volume mean diameter; bottom: Sauter mean diameter.

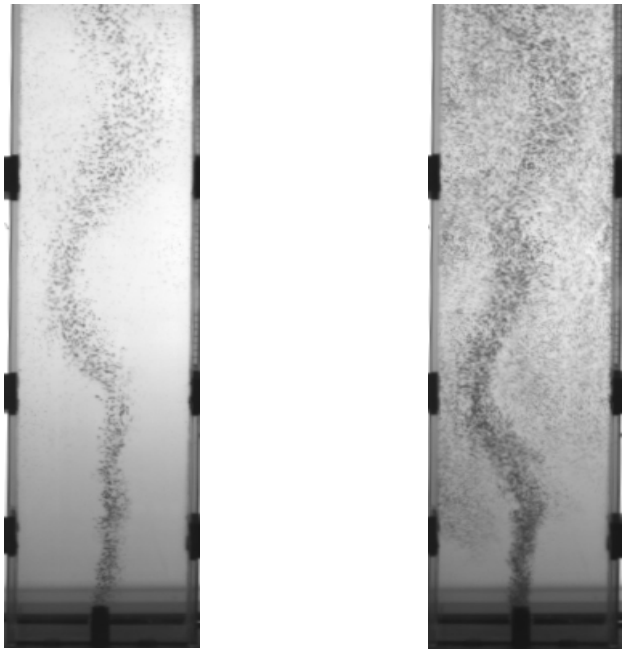

Figure 5.13: Experimental images of bubble plume in pseudo 2D column. Left: superficial gas velocity = $1.39 \cdot 10^{-3}$ m s^{-1}; right: superficial gas velocity = $5.56 \cdot 10^{-3}$ m s^{-1}.

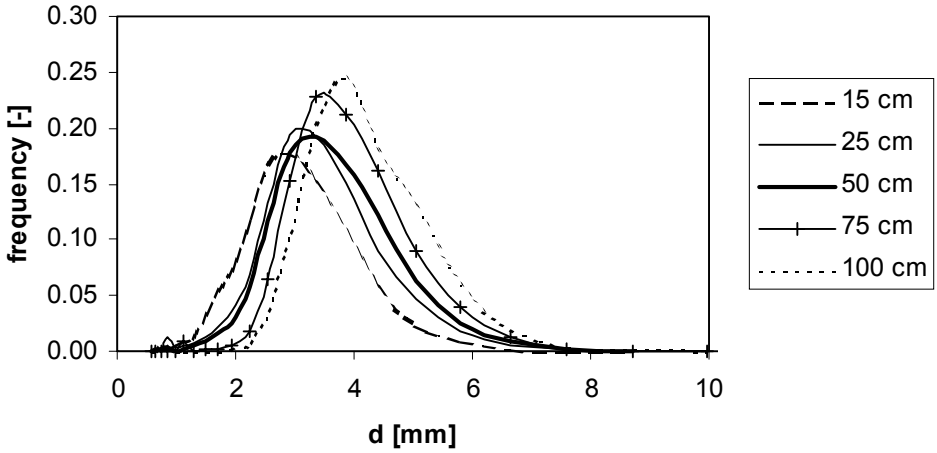

Figure 5.14: Experimentally determined bubble size distribution for distilled water at a superficial gas velocity of $5.56 \cdot 10^{-3}$ m s^{-1}.

with μ the ensemble mean diameter, σ the standard deviation and q a normalisation term. The mean diameter is calculated using the data given by VisiSize. Both number and volume distributions are fitted with the Gaussian distribution function. In Appendix 5A,

Table 5A.2 the standard deviation is given for the number size distribution for all flow rates and all heights in the column. In Appendix 5A, Table 5A.3 the same is reported for the volume size distribution.
As can be observed in Figure 5.14 and Table 5A.2 and 5A.3 the bubble size distribution moves to larger diameters, when increasing the height. The bubble size distribution is narrower and the maximum is higher in the top of the column. The total volume of the bubbles at the different heights in the column is equal, so the area under the distribution curve is the same for all different heights. As already explained the number of larger bubbles present in the top is higher than in the lower part of the column. Therefore the total number of bubbles in the top is lower and the number of larger bubbles in the top is relatively higher. Thus the maximum of the bubble size distribution is higher when increasing the height and the peak is narrower.

Figure 5.15 shows the bubble size distribution at a height of 0.50 m at different flow rates. As observed in this figure, the bubble size distribution moves to larger diameters when increasing the flow rate. The bubble size distribution is wider and the maximum decreases with increasing flow rates. This is due to the fact that at high flow rates more bubbles are present in the column, so more collisions between the bubbles occur and the chance for coalescence is higher. Therefore the number of larger bubbles is higher at higher flow rates and the bubble size distribution moves to larger diameters. At higher flow rates, larger bubbles are present, but also small bubbles, which did not coalesce. Thus the bubble size distribution is wider at higher flow rates and the maximum decreases.

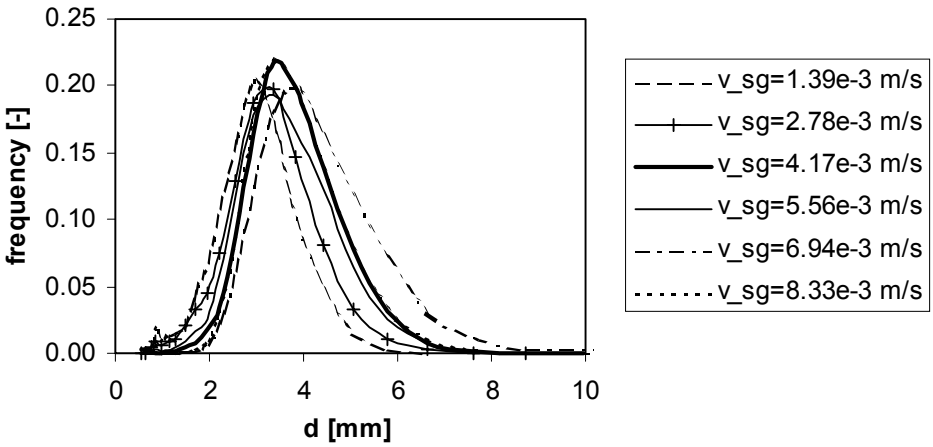

Figure 5.15: Experimentally determined bubble size distribution for distilled water at different gas flows.

5.5.2 Distilled water and octanol

Figure 5.16 shows the number mean, volume mean and Sauter mean diameter vs. the height in the column for all flow rates. In Appendix 5A, Table 5A.4 the values for the mean diameter of all flow rates at different heights are given.
The initial bubble diameter of the bubble coming into the column was 1.4 mm. The mean diameter shows a weak increase with increasing height in the column. This increase is probably only due to the decrease in hydrostatic pressure with increasing height.
The mean diameter decreases with increasing flow rate. This is the opposite for the case when only distilled water is used. In the case of water with octanol coalescence is inhibited, so when bubbles collide no coalescence, but bouncing will occur. When the flow rate is higher, more bubbles are present in the column and they cause more turbulence and more eddies. The number of collisions between bubbles and eddies is larger and the chance for breaking of bubbles is larger.

In Figure 5.17 the bubble size distribution at a superficial gas velocity of $1.39 \cdot 10^{-3}$ m s^{-1} at different heights can be seen. Also in this case the Gaussian distribution function is used to describe these bubble size distributions.
In Appendix 5A, Table 5A.5 the standard deviation is given for the number size distribution for all flow rates and all heights in the column. In Appendix 5A, Table 5A.6 the same is reported for the volume size distribution.
As can be observed in Figure 5.14 and Table 5A.5 and 5A.6 the bubbles increase a little when increasing the height, but this is only due to the decreasing hydrostatic pressure.

Figure 5.18 shows the bubble size distribution at a height of 0.50 m at different flow rates. As observed in this figure, the bubble size distribution moves to smaller diameters when increasing the flow rate. This is due to the fact that at high flow rates more bubbles are present in the column, so there is more turbulence and more eddies and more collisions between the bubbles and the eddies. Therefore the chance for break-up of bubbles is higher and the number of small bubbles is higher at higher flow rates. The bubble size distribution moves to smaller bubble diameters. At higher flow rates, smaller bubbles are present, but also larger bubbles, which did not break. Thus the bubble size distribution is wider at higher flow rates and the maximum decreases.

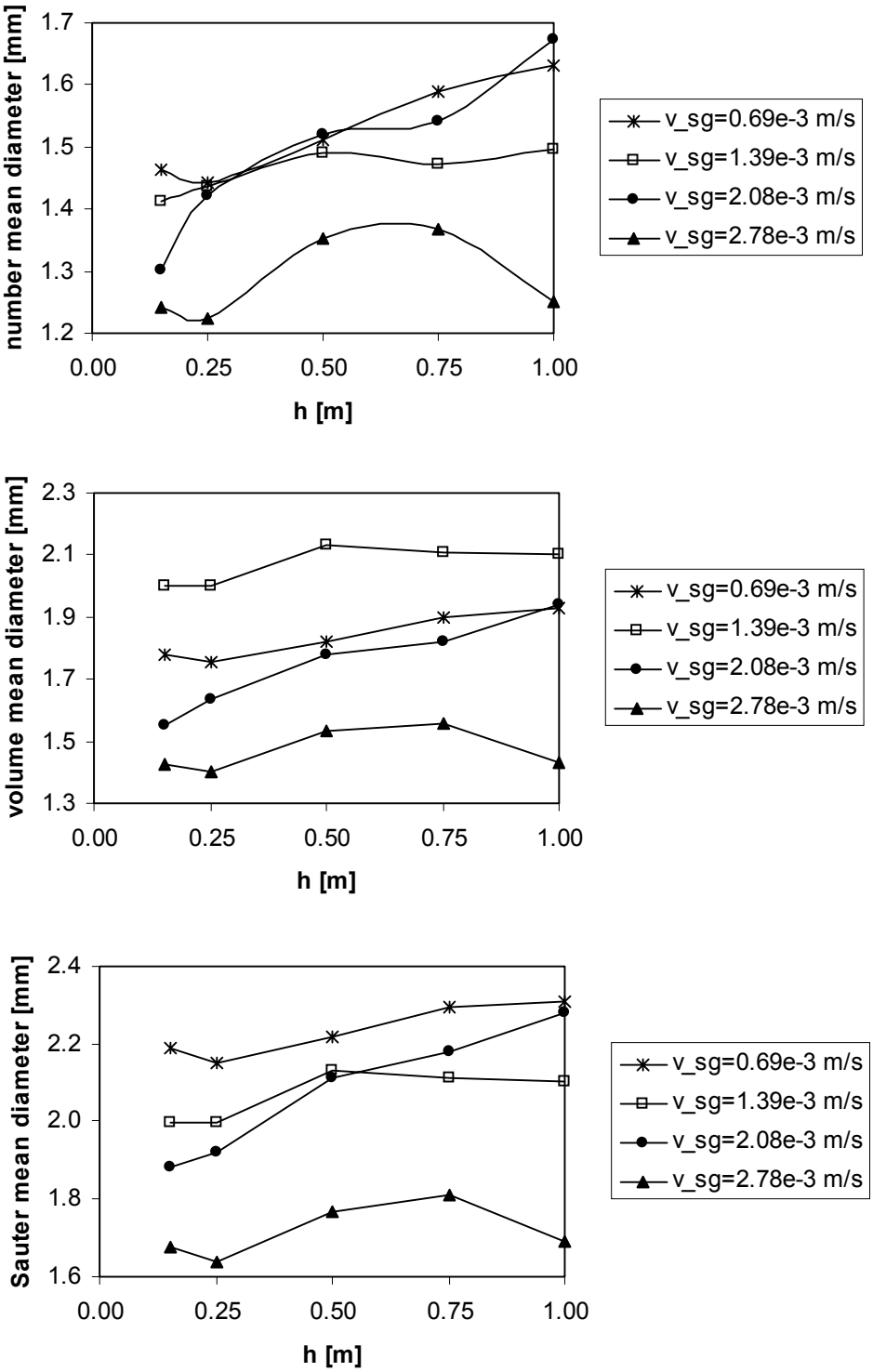

Figure 5.16: Experimental calculation of the mean diameter vs. height for different flows for distilled water and octanol. Top: number mean diameter; middle: volume mean diameter; bottom: Sauter mean diameter.

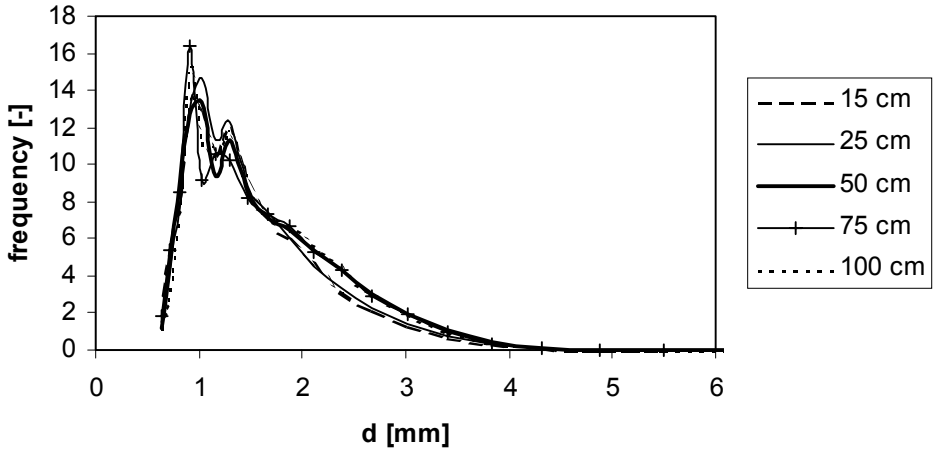

Figure 5.17: Experimentally determined bubble size distribution for distilled water and octanol at a superficial gas velocity of $1.39 \cdot 10^{-3}$ m s^{-1}.

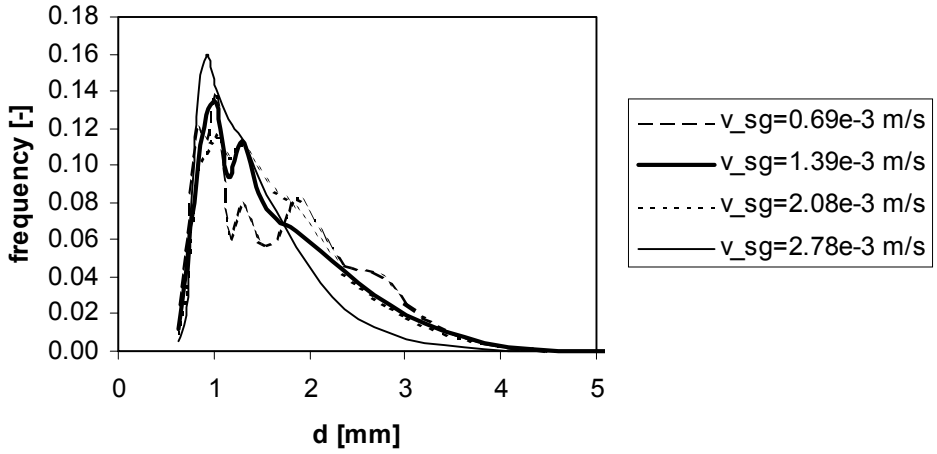

Figure 5.18: Experimentally determined bubble size distribution for distilled water and octanol at different gas flows.

5.6 Conclusions

In this chapter an imaging technique is used to measure the bubble size distribution and mean diameter in a lab-scale bubble column. This study shows that the imaging technique gives valuable information about the bubble size distribution and mean diameter at different flow rates and different heights in the column.

In distilled water the mean diameter increases with increasing height in the column because of coalescence of the bubbles. The higher their positions in the column, the

longer bubbles generally have resided in the column and the more opportunity they have had to coalesce.
The mean diameter increases with increasing flow rate. The higher the flow rate, the higher the gas fraction. Therefore more collisions between the bubbles occur, the chance for coalescence is higher and the diameter of the bubbles becomes larger.
The bubble size distribution moves to larger diameters, when increasing the height. The same is observed increasing the flow rate.

In distilled water with octanol ($2.4 \cdot 10^{-4}$ M) the mean diameter shows a weak increase with increasing height in the column due to the decrease in hydrostatic pressure with increasing height.
The mean diameter decreases with increasing flow rate. When the flow rate is higher, more bubbles are present in the column and they produce more turbulence and more eddies. The number of collisions between bubbles and eddies is larger and the chance for breaking of bubbles is larger.
The bubble size distribution moves a little to larger diameters when increasing the height and moves to smaller diameters when increasing the flow rate.

Appendix 5A: Experimental results of the mean diameter and standard deviation

Distilled water

Table 5A.1: Experimental results mean diameter with distilled water at different flow rates and different heights.

flow rate [m^3/s]	mean diameter [mm]	0.15 m	0.25 m	0.50 m	0.75 m	1.00 m
$0.83 \cdot 10^{-5}$	number	2.33	2.56	3.00	3.40	3.45
	volume	2.68	2.89	3.23	3.63	3.69
	Sauter	3.08	3.27	3.52	3.93	3.99
$1.67 \cdot 10^{-5}$	number	2.77	2.95	3.30	3.41	3.50
	volume	3.14	3.28	3.56	3.64	3.70
	Sauter	3.58	3.68	3.89	3.93	3.97
$2.50 \cdot 10^{-5}$	number	2.92	3.27	3.84	3.85	3.82
	volume	3.20	3.55	4.08	4.06	4.00
	Sauter	3.56	3.90	4.38	4.36	4.26
$3.33 \cdot 10^{-5}$	number	3.09	3.46	3.67	4.02	4.29
	volume	3.37	3.74	3.94	4.24	4.50
	Sauter	3.72	4.09	4.29	4.53	4.80
$4.17 \cdot 10^{-5}$	number	3.19	3.32	3.74	3.90	4.36
	volume	3.44	3.56	3.94	4.16	4.57
	Sauter	3.78	3.88	4.22	4.41	4.87
$5.00 \cdot 10^{-5}$	number	3.22	3.63	3.90	4.17	4.33
	volume	3.50	3.92	4.12	4.42	4.54
	Sauter	3.84	4.30	4.43	4.74	4.84

Table 5A.2: Standard deviation for number size distribution for distilled water.

flow rate [l/min]		0.15 m	0.25 m	0.50 m	0.75 m	1.00 m
$0.83 \cdot 10^{-3}$	θ_x	0.28	0.57	0.51	0.52	0.53
$1.67 \cdot 10^{-3}$	θ_x	0.36	0.50	0.54	0.50	0.50
$2.50 \cdot 10^{-3}$	θ_x	0.38	0.52	0.54	0.51	0.55
$3.33 \cdot 10^{-3}$	θ_x	0.41	0.52	0.56	0.53	0.53
$4.17 \cdot 10^{-3}$	θ_x	0.45	0.59	0.53	0.56	0.59
$5.00 \cdot 10^{-3}$	θ_x	0.44	0.55	0.56	0.58	0.54

Table 5A.3: Standard deviation for volume size distribution for distilled water.

flow rate [l/min]		0.15 m	0.25 m	0.50 m	0.75 m	1.00 m
$0.83 \cdot 10^{-3}$	θ_x	0.58	0.56	0.55	0.62	0.64
$1.67 \cdot 10^{-3}$	θ_x	0.67	0.63	0.59	0.65	0.66
$2.50 \cdot 10^{-3}$	θ_x	0.64	0.68	0.71	0.66	0.67
$3.33 \cdot 10^{-3}$	θ_x	0.64	0.70	0.72	0.70	0.78
$4.17 \cdot 10^{-3}$	θ_x	0.67	0.66	0.69	0.73	0.75
$5.00 \cdot 10^{-3}$	θ_x	0.72	0.74	0.78	0.79	0.76

Distilled water and octanol

Table 5A.4: Experimental results mean diameter with distilled water and octanol at different flow rates and different heights.

flow rate [l/min]	mean diameter [mm]	0.15 m	0.25 m	0.50 m	0.75 m	1.00 m
0.25	number	1.46	1.44	1.51	1.59	1.63
	volume	1.78	1.75	1.82	1.90	1.93
	Sauter	2.19	2.15	2.22	2.30	2.31
0.50	number	1.41	1.44	1.49	1.47	1.50
	volume	1.66	1.68	1.77	1.75	1.76
	Sauter	2.00	2.00	2.13	2.11	2.10
0.75	number	1.30	1.42	1.52	1.54	1.67
	volume	1.55	1.64	1.78	1.82	1.94
	Sauter	1.88	1.92	2.11	2.18	2.28
1.00	number	1.24	1.22	1.35	1.37	1.25
	volume	1.43	1.40	1.53	1.56	1.43
	Sauter	1.68	1.64	1.77	1.81	1.69

Table 5A.5: Standard deviation for number size distribution for distilled water and octanol.

flow rate [l/min]		0.15 m	0.25 m	0.50 m	0.75 m	1.00 m
$0.42 \cdot 10^{-3}$	θ_x	0.40	0.63	0.61	0.62	0.60
$0.83 \cdot 10^{-3}$	θ_x	0.29	0.51	0.59	0.59	0.58
$1.25 \cdot 10^{-3}$	θ_x	0.37	0.55	0.68	0.67	0.67
$1.67 \cdot 10^{-3}$	θ_x	0.34	0.62	0.46	0.43	0.52

Table 5A.6: Standard deviation for volume size distribution for distilled water and octanol.

flow rate [l/min]		0.15 m	0.25 m	0.50 m	0.75 m	1.00 m
$0.42 \cdot 10^{-3}$	θ_x	0.74	0.76	0.71	0.71	0.73
$0.83 \cdot 10^{-3}$	θ_x	0.78	0.75	0.72	0.71	0.72
$1.25 \cdot 10^{-3}$	θ_x	0.95	0.91	0.94	0.92	0.96
$1.67 \cdot 10^{-3}$	θ_x	1.00	0.88	0.78	0.92	1.52

Chapter 6

CONCLUSIONS AND RECOMMENDATIONS

Abstract

In this chapter the concluding remarks of this work are presented. The conclusions regarding the hydrodynamics in bubble columns studied with different models will be given. The imaging techniques used to validate the CFD models will also be discussed. In the final section an outlook on further research in the field of bubbly flows will be given.

6.1 Conclusions

Bubble columns are used in a variety of industrial processes. Despite the widespread application of bubble columns and substantial research efforts on their behaviour, detailed knowledge on the fluid dynamics is still lacking.
The objective of this thesis was to develop and improve computational fluid dynamics models (CFD models) that describe the time-dependent flow behaviour of gas-liquid flows in bubble columns. The models have been validated with experimental data.

Due to the complexity of the gas-liquid flow in a bubble column it appears almost impossible to develop a generalised computational fluid dynamic (CFD) model that accounts for all hydrodynamic phenomena in bubble columns. Therefore a 'hierarchy of models' is employed. This 'hierarchy of models' consists of a set of three types of CFD models and each model is used to study specific hydrodynamic phenomena.

Interface tracking models are the most detailed models in the 'hierarchy of models'. The interface tracking models used in this thesis are the 2D volume of fluid (VOF) model and the 2D and 3D front tracking model. These models have been used to study in detail the time-dependent behaviour of large bubbles rising in an initially quiescent liquid. The models solve the incompressible Navier-Stokes equations on a staggered Cartesian mesh using a one-fluid formulation to obtain the gas and liquid flow fields. The Youngs' VOF method reconstructs the gas-liquid interface from the local liquid fraction and the interface is 'tracked' through the Eulerian mesh. A known drawback of the Youngs' VOF model is the poor calculation of the surface tension force by the continuum surface force model (Brackbill *et al*., 1992), especially at points where the interface has a strong curvature compared to the computational mesh size. In this thesis a new surface tension model, the tensile force model, has been introduced into the VOF model. With this model is it possible to simulate very small bubbles (down to 1 mm diameter) in an air-water system. The front tracking method uses an unstructured dynamic mesh to represent the interface surface and tracks this interface explicitly by the interconnected marker points.
These models are used to calculate the forces acting on a bubble, i.e. the drag, lift and virtual mass forces, by using a force balance for a single bubble. The results are compared to relations from literature. The relations for these forces can be used as closure relations for less detailed models such as Euler-Lagrange and Euler-Euler models. The drag coefficients for small bubble diameters (< 2 mm), calculated with the 2D VOF model, are very close to the relations of Tomiyama (1998) and Ishii & Zuber (1979). For

larger bubble diameters (> 2 mm) the drag coefficients are very close to the relation of Grace *et al.* (1976). The drag coefficients in the 3D front tracking model for bubbles larger than 7 mm are higher than in the 2D VOF model where the equation for a sphere is used to calculate the drag coefficient. When the equation for a cylinder is used to calculated the drag coefficient for the 2D VOF model, the drag coefficients of the 3D front tracking model and the 2D VOF model are close together.
The virtual mass force can only be calculated for the first part of the simulation when the bubble accelerates. For the 2D VOF model the value obtained for the virtual mass coefficient is typically around 1.1. This value for bubbles in 2D systems is in agreement with literature (Auton, 1988; Lamb, 1932). For the 3D front tracking model the virtual mass coefficient is around 0.6, the value for 3D systems (Auton, 1983). The deviation from the theoretical value of spherical bubbles is probably caused by minor deformation of the bubble.
The lift force was studied using a 2D front tracking model. A bubble in a linear shear field does not rise in a straight line, but oscillates in the horizontal direction and moves to one side of the column. A bubble of 8 mm moves to the side with the highest slip velocity and a bubble of 10 mm moves to the side with the lowest slip velocity. When using a lower shear rate, the movement of the bubble is smaller. The horizontal velocity shows large oscillations due to the oscillating movement of the bubble in the column and is oscillating between a negative and a positive value. Due to the change in horizontal velocity, the lift coefficient changes accordingly. The average lift coefficient for a bubble of 8 mm is positive and the average lift coefficient for a bubble of 10 mm is negative. The values are higher than the values reported in literature (Tomiyama, 1998). The shape of a bubble of 8 mm is approximately ellipsoidal during the oscillations. The shape of a bubble of 10 mm changes during the oscillations. The bubble is ellipsoidal and during the turn the shape changes to wobbling. This is probably the reason for the observed differences in the lift coefficient.

The next level in the 'hierarchy of models' is the Euler-Lagrange model, also called discrete bubble model (DBM). A discrete bubble model was used to investigate the hydrodynamics, coalescence and break-up occurring in bubble columns. The 3D DBM code, developed by Delnoij (1999), was extended to incorporate models describing the coalescence and break-up along with a closure model for the turbulence. The model incorporates all relevant forces acting on a bubble in a liquid.
Simulation results of the model with LES are compared to experimental particle image velocimetry (PIV) results measured by Deen (2001) in square column. The velocity and

velocity fluctuations of the simulation are predicted somewhat too high compared to the PIV results. The difference between the simulation results and the experiments is 7 %. The difference between the simulation and PIV results are marginal in cases with a smaller time step or smaller grid size.
When the LES model is implemented the average velocity and velocity fluctuations of the liquid phase are much higher than in the case without LES. The effective viscosity in the case with LES is higher due to the turbulent viscosity. Low viscosities lead to less dampening of the bubble plume dynamics and this in turn leads to flatter average liquid phase velocity profiles. The average velocity also increases when implementing bubble induced turbulence, due to an increase in the effective viscosity. The influence of the sub-grid scale velocity is negligible.
Reducing the lift coefficient to 0.3 (instead of 0.5, which is the value given in the literature) gives much higher average velocity and velocity fluctuations than in the case with C_L=0.5. In case of a smaller lift coefficient the spreading of the plume is less and therefore the dynamics of the plume are reduced, which leads to a higher average velocity in the centre of the column.
When using LES, the agreement between the simulation and experimental results is better when using a time step of $0.5 \cdot 10^{-3}$ s, a grid size of 0.01 m in all directions and a lift coefficient of 0.5. Implementing bubble induced turbulence gives worse results.

The DBM is extended with the coalescence model of Chesters (1991) and Lee *et al.* (1987) and the break-up model of Luo and Svendsen (1996) to study the bubble size distribution. The results are compared to experimental results, measured with a digital image technique and PIV in a pseudo 2D bubble column with an air-water system.
The break-up model of Luo and Svendsen (1996) and others were developed for $\varepsilon > 0.5$ m^2 s^{-3}. In bubble columns with low gas flows and low turbulence intensities the energy dissipation is in the order of 10^{-2} m^3 s^{-1}. When these energy dissipation rates are used in the break-up model, hardly any break-up occurs. In the simulations break-up only occurs in the top of the column, when the energy dissipation is > 10^{-1} m^3 s^{-1} and the diameter of the bubble is large (> 5 mm).
When either of the coalescence models is used, the mean diameter is overpredicted, due to the fact that hardly any break-up occurs. The number of collisions between two bubbles that result in coalescence is 43 % with the coalescence model of Chesters and 85 % with the coalescence model of Lee *et al.* (1987). Most of the coalescence occurs in the lower part of the column. The results of the coalescence model of Chesters (1991)

combined with the break-up model of Luo and Svendsen (1996) are closer to the experimental results.
When changing the superficial gas velocity the coalescence efficiency is still the same, but the number of collisions and thus of coalescence changes. The higher the superficial gas velocity, the more collisions occur in the column. Therefore the differences between the simulated mean diameters and the experiments at higher superficial gas velocity are higher. The bubble size distribution is wider at higher superficial gas velocity.
Further research is necessary to solve the differences between the experiments and the simulations.

In Euler-Euler models the different phases are treated as interpenetrating fluids and the ensemble averaged mass and momentum conservation equations are solved to describe the time-dependent motion of the phases. For the simulations with the Euler-Euler model the commercial code CFX 4.4 is used. Three different Euler-Euler models are used to describe two-phase flows in bubble columns: A gas-liquid model, a gas-gas-liquid model and a gas-liquid model with the MUSIG model for the gas phase. In all three Euler-Euler models a LES-turbulence model is incorporated. The MUSIG model, including population balances with a break-up and coalescence model, is used to study the bubble size distribution in the column. To study the effect of the different rise velocities of the bubbles a three-phase gas-gas-liquid system is simulated. The gas phase is divided into two groups, one with a diameter of 2 mm and one with a diameter of 6 mm. The drag relation used for both groups is different. The results of all three models are compared with experimental PIV results measured by Deen (2001) in a square bubble column filled with distilled water.
Good agreement was reached comparing the simulation results of the gas-liquid model to the experimental results. When using a smaller grid size the liquid velocity and velocity fluctuations are lower, but the differences between the velocity profiles of the case with smaller grid sizes and the standard case are marginal. In the case with a smaller time step the average velocity profile is lower than in de standard case. The velocity fluctuations in the vertical direction are lower, but the difference between the fluctuations in the horizontal direction between the case with smaller time step and the standard case is negligible.
When the LES model is implemented the liquid velocity and velocity fluctuations are much higher than in the case without LES, as could also be seen in DBM. The effective viscosity in case of LES is higher due to the turbulence viscosity.

In the gas-liquid model with MUSIG model the bubbles in the gas phase are divided into 10 equally sized bubble size groups from 0.0 - 10.0 mm. The default break-up model used was the model of Luo and Svendsen (1996), the default coalescence model the model of Prince and Blanch (1990). The difference between the models with and without MUSIG model is small because all size groups have the same rise velocity and thus the same drag relation.
The curve of the average liquid velocities of the gas-gas-liquid model is smaller than for the gas-liquid model. This is the effect of the smaller bubbles with a different drag relation. In this case the average velocity is lower with a high maximum in the middle part of the column. The movement of the bubble plume is very small, as can be concluded from the velocity fluctuations.
Simulation results of two different coalescence models, of Prince and Blanch (1990) and Chesters (1991), are compared with simulation results of the DBM with the coalescence model of Chesters (1991) in a square column. In all models the break-up model of Luo and Svendsen (1996) is incorporated. The bubbles in the DBM are the smallest and the bubble size distribution is the narrowest. The bubbles in the model of Prince and Blanch (1990) are the largest and the bubble size distribution is the widest. As said previously the results of the DBM with the coalescence model of Chesters (1991) and the break-up model of Luo and Svendsen (1996) shows the best agreement with experimental results. The results of the Euler-Euler model with the models of Chesters (1991) and Luo and Svendsen (1996) are the best in agreement with the results of the DBM. The bubbles in the Euler-Euler model with the models of Prince and Blanch (1990) and Luo and Svendsen (1996) are too large.

An imaging technique is used to validate the CFD models experimentally. In this imaging technique the bubble size distribution and the mean diameter of the bubbles are measured with a digital high-speed camera in a lab-scale bubble column. This work shows that the imaging technique gives valuable information about the bubble size distribution and mean diameter at different flow rates and different heights in the column.
In distilled water the mean diameter increases with increasing height in the column because of coalescence of the bubbles. The higher their positions in the column, the longer bubbles generally have resided in the column and the more opportunity they have had to coalesce.
The mean diameter increases with increasing flow rate. The higher the flow rate, the higher the gas fraction. Therefore more collisions between the bubbles occur, the chance for coalescence is higher and the diameter of the bubbles becomes larger.

In distilled water with a very small amount of octanol ($2.4 \cdot 10^{-4}$ M) to inhibit coalescence the mean diameter shows a little increase with increasing height in the column due to the decrease in hydrostatic pressure.
The mean diameter decreases with increasing flow rate. When the flow rate is higher, more bubbles are present in the column and more turbulence is generated. The number of collisions between bubbles and eddies is larger and the chance for breaking of bubbles is larger.
The bubble size distribution moves a little to larger diameters when increasing the height and moves to smaller diameters when increasing the flow rate.

6.2 Recommendations

6.2.1 Interface tracking models

The volume of fluid model and the front tracking model can be used very well to derive equations for the forces acting on bubbles rising in a liquid. The volume of fluid model is improved by using the tensile force model instead of the continuum surface force model to calculate the surface tension. A second improvement is the use of a smoothened colour function for the calculations of the liquid fraction.
A disadvantage of the front tracking model is that the volume of the bubble is not intrinsically conserved. The bubble volume slowly changes in time, due to the method used to move the interface and the re-meshing of the interface mesh. Therefore the next step in the front tracking model is to improve the conservation of volume by e.g. changing the remeshing of the interface.

In the simulations in this thesis the bubble is placed at some point in the column as a sphere. When starting the simulation the bubble starts to rise and to deform. To reach a better approach to real bubble columns and to do further research on the time-dependent behaviour of bubbles the simulated bubble should enter the column through a nozzle. In that case the shape of the bubble is better described.

In this thesis closure relations for the drag, lift and virtual mass force of a bubble rising in a liquid are derived. The drag and virtual mass force are studied for small and large bubbles in a 2D and 3D model. Further research on the lift force for small bubbles (< 8 mm) and the lift force of bubbles in 3D models is necessary.

Another subject to study is the influence of bubbles on the behaviour of other bubbles. By doing simulations with detailed models such as VOF and front tracking, the influence of neighbouring bubbles on the shape and dynamics of the rising bubble can be studied. These closure relations can be used in Euler-Lagrange and Euler-Euler models, which often ignore the presence of surrounding bubbles.

The bubble behaviour can be influenced by coalescence with neighbouring bubbles or break-up of the bubble. When the VOF model will be used to study coalescence and break-up a more detailed description of the interface dynamics is necessary. In VOF coalescence and break-up now occurs as a result of the interface reconstruction. When the interfaces of two bubbles are in one cell, the bubbles immediately coalesce. A first step to use VOF to study coalescence and break-up is to develop an algorithm that allows for more than one interface in a cell, which will be a difficult task. Another step to a probable solution for solving the problem of two interfaces in one cell is to use a very fine local grid at the interface. In this way the film between two bubbles and the neck of a breaking bubble can probably be solved in the simulations.
In the front tracking model it is already possible to have more than one interface in a cell. The problem in this model is the restructuring of the interface meshes when coalescence or break-up occurs.

6.2.2 Discrete bubble model

The relations for the drag, lift and virtual mass forces derived with the VOF model and the front tracking model can be implemented in the DBM. Different relations can be used for different diameters and shapes of the bubbles. When using time-dependent relations of the drag and lift coefficient, the oscillating behaviour of the bubbles can be described.
The DBM can be used very well to investigate which break-up and coalescence model gives the best results compared to experimental results, because in this model all bubbles can be tracked individually. In this thesis the break-up model of Luo and Svendsen (1996) was implemented. An important parameter in this break-up model and also in other models in the literature is the energy dissipation. The models in literature are based on fact that the energy input, given by the turbulent kinetic energy of an eddy, should be large enough to provide the increase of the bubble surface energy. In the bubble column with small gas flow rates used in this thesis the energy dissipation is low. Due to this low energy dissipation in the simulations hardly any break-up occurs. In the experimental

results could be seen, that break-up occurs, even at low gas flows. Probably also another mechanism causes break-up in bubble column. If this is the case, the model of Luo and Svendsen (1996) and others cannot be used to study break-up of bubbles at low gas flows. Possibly a new break-up model should be developed, in which not only the turbulent kinetic energy is included, but also other parameters. One can think of the time duration of the interaction and the stability of the bubble.
In the snap shots of the bubble plumes in the pseudo 2D model could be seen, that the bubbles are rising in a line behind each other and the bubble plume is not oscillating at small gas flows. This can be the effect of the large grid size. Probably the time between the bubbles coming into the column through the nozzle also influences the bubble plume behaviour.

DBM with coalescence and break-up model can be used to investigate the complex behaviour involving hydrodynamics, mass transfer and chemical reactions in a gas-liquid bubble column reactor. With this extension the model can be used to simulate bubble columns used as chemical reactors.

6.2.3 Two-fluid model

The bubble size distribution is also relevant in the context of the Euler-Euler model. The break-up and coalescence models studied in DBM can also be incorporated in the two-fluid model and validated with experimental results. Although experimental results obtained in a pseudo 2D column were available, it was not possible to compare these with CFX simulations, since CFX failed to converge for this particular problem. Further research on the bubble size distribution and break-up and coalescence of bubbles in the Euler-Euler model is necessary. When it is possible to measure the bubble size distribution in a 3D column experimentally, these results can be compared to simulation results of the Euler-Euler model.

The relations for the drag, lift and virtual mass forces derived with the VOF model and the front tracking model can be implemented in the two-fluid model. Different relations can be used for different diameters and shapes of the bubbles.
An important point using different drag relations is the influence of the different rise velocity of bubbles with different diameters. This difference is only important in the case both very small and large bubbles are present. When all bubbles are in the range of 4-10

mm, the rise velocity is approximately constant. A combination of the gas-gas-liquid model, used in this thesis, with the MUSIG model can be investigated. In both gas phases the MUSIG model can be incorporated. The gas-gas-liquid model can be used for the difference in rise velocity and the MUSIG model for the population balances.

The two-fluid model with coalescence and break-up model can be used to investigate the complex behaviour involving hydrodynamics, mass transfer and chemical reactions in a gas-liquid bubble column reactor. With this extension the model can be used to simulate bubble columns used as chemical reactors.

Nomenclature

A	surface [m^2]
A_h	Hamacker constant [J]
A_{pixel}	pixel area [m^2]
B_{BU}	birth rate break-up [m^{-3} s^{-1}]
B_C	birth rate coalescence [m^{-3} s^{-1}]
C	constant [-]
C_D	drag coefficient [-]
C_k	number density of particle [-]
C_L	lift coefficient [-]
C_S	constant sub-grid scale model [-]
C_{VM}	virtual mass coefficient [-]
$C_{\mu,BIT}$	constant bubble induced turbulence model [-]
c_f	increase coefficient of surface area [-]
D	column depth [m]
D_{BU}	death rate break-up [m^{-3} s^{-1}]
D_C	death rate coalescence [m^{-3} s^{-1}]
D_c	column diameter or hydraulic diameter [m]
d	diameter bubble [m]
d_{10}	number mean diameter [m]
d_{30}	volume mean diameter [m]
d_{32}	Sauter mean diameter [m]
d_A	bubble diameter based on pixel area [m]
d_{ab}	equivalent bubble diameter [m]
d_e	volume equivalent sphere diameter for drop or bubble [m]
d_H	Heywood diameter [m]
d_P	bubble diameter based on pixel perimeter [m]
E	energy spectrum [m^3 s^{-2}]

e	energy of individual eddies [J]
$\overline{e}$	mean energy of individual eddies [J]
$\overline{e}_i$	increase of surface energy due to a bubble breakage [J]
F	liquid volume fraction [-]
$\mathbf{F}_{1\text{-}2}$	force exterted on interface between point 1 and 2 [N]
$\mathbf{F}_{Buoyancy}$	buoyancy force [N]
$\mathbf{F}_D$	drag force [N]
$\mathbf{F}_G$	gravitational force [N]
$\mathbf{F}_{IF}$	total interfacial force [N]
$\mathbf{F}_L$	lift force [N]
$\mathbf{F}_P$	pressure force [N]
$\mathbf{F}_{SF}$	volumetric surface tension force [N]
$\overline{\mathbf{F}}_{SF}$	smoothed surface tension force [N]
$\mathbf{F}_{tot}$	total force [N]
$\mathbf{F}_{VM}$	virtual mass force [N]
f_B	calibration factor for break-up [-]
f_C	calibration factor for coalescence [-]
f_{BV}	breakage volume fraction [-]
f_q	fraction of the dispersed phase volume fraction in the q^{th} group [-]
$\mathbf{g}$	gravitational constant [m s^{-2}]
g	total breakage rate [s^{-1}]
H	dimensionless group [-]
h	grid spacing [m]
h_f	final film thickness [m]
h_i	initial film thickness [m]
$\mathbf{I}$	unity vector [-]
J	dimensionless group [-]
k	wave number [-]
k_{sgs}	sub-grid scale kinetic energy [m^2 s^2]
L	length [m]
$l_\perp$	length perpendicular to the x,y-surface [m]
M	surface immobility parameter [-]
m	mass [kg]
N_B	number of bubbles [-]
N_{pixels}	number of pixels [-]

N_S	source density [-]
N_t	number of time steps [-]
NX	number of cells in x-direction [-]
NY	number of cells in y-direction [-]
n	number of grid cells [-]
$\mathbf{n}$	normal of gas-liquid interface [-]
n_B	number of bubbles per unit dispersed volume [m^{-3}]
$\dot{n}_{\lambda_e}$	number of eddies per unit reactor volume [m^{-4}]
$\tilde{\mathbf{n}}$	unit normal of gas-liquid interface [-]
P	pressure [N m^{-2}]
P_{BU}	break-up probability [-]
P_{pixel}	pixel perimeter [m]
p_e	kinetic energy distribution [-]
Q	coalescence frequency [m^3 s^{-1}]
r	radius [m]
$\mathbf{r}$	position of bubble [m]
r_d	radius of the liquid film disc [m]
r_{ab}	equivalent bubble radius [m]
rnd	random number [-]
$\mathbf{S}$	characteristic filtered rate of strain [s^{-1}]
Δs	surface area [m^2]
$\mathbf{T}$	tensile force [N]
t	time [s]
$\mathbf{t}$	tangential unit vector
t_{ab}	time step to solve collision between bubbles [s]
t_c	coalescence time [s]
t_{flow}	time step to solve flow field [s]
t_{bub}	time step to solve forces acting on bubbles [s]
t_d	drainage time [s]
t_r	rupture time [s]
u	velocity [m s^{-1}]
$\mathbf{u}$	liquid velocity [m s^{-1}]
$\mathbf{u}_{gs}$	liquid velocity grid scale [m s^{-1}]
$\mathbf{u}_I$	velocity in interrogation area [m s^{-1}]
$\mathbf{u}_{sgs}$	liquid velocity sub-grid scale [m s^{-1}]
$\mathbf{u}_t$	turbulent velocity [m s^{-1}]

$\mathbf{u}_{\lambda_e}$	turbulent velocity of eddy [m s^{-1}]
$\overline{u}$	time-averaged mean velocity [m s^{-1}]
$\overline{u}'$	velocity fluctuations [m s^{-1}]
V	volume [m^{-3}]
v	gas velocity/ bubble velocity [m s^{-1}]
v_B	bubble velocity [m s^{-1}]
v_{sg}	superficial gas velocity [m s^{-1}]
W	column width [m]
x	position [m]
x	x-direction [-]
x_B	bubble position in x-direction [m]
$\overline{\mathbf{x}}$	centre of distribution function [m]
$\mathbf{x}_i$	boundary of integration step in i-direction [m]
$\mathbf{x}_j$	boundary of integration step in j-direction [m]
x_{random}	random number [-]
y	y-direction [-]

Greek symbols

α	volume fraction [-]
α_c	universal constant [-]
α_{low}	minimum volume fraction of the liquid [-]
$\tilde{\beta}$	constant [-]
χ	dimensionless energy [-]
χ_c	dimensionless energy [-]
Δ_x	grid spacing in horizontal direction [m]
Δ_y	grid spacing in lateral direction [m]
Δ_z	grid spacing in vertical direction [m]
ε	energy dissipation [$m^2\ s^{-3}$]
Φ	interface momentum transfer / total interfacial force [$N\ m^{-3}$]
γ	shear rate [s^{-1}]
Γ	gamma function [-]
κ	surface curvature [m^{-1}]
λ	coalescence efficiency [-]
λ_e	eddy size [m]
λ_{ms}	eddy size of viscous dissipation [m]
μ	viscosity [$kg\ m^{-1}\ s^{-1}$]
μ_{BIT}	bubble induced turbulence viscosity [$kg\ m^{-1}\ s^{-1}$]
μ_L	molecular viscosity [$kg\ m^{-1}\ s^{-1}$]
μ_T	turbulent viscosity [$kg\ m^{-1}\ s^{-1}$]
μ_{eff}	effective viscosity [$kg\ m^{-1}\ s^{-1}$]
μ_w	viscosity of water [$kg\ m^{-1}\ s^{-1}$]
θ	collision rate [$m^{-3}\ s^{-1}$]
θ^T	collision rate due to turbulence[$m^{-3}\ s^{-1}$]
ρ	density [$kg\ m^{-3}$]
σ	surface tension [$N\ m^{-1}$]
τ	stress tensor [$kg\ m^{-1}\ s^{-2}$]
τ_c	contact time [s]
ξ	size ratio between eddy and bubble [-]
ζ^i_{cell}	volume fraction of i^{th} bubble in cell [-]
Ω_B	breakage rate [$m^{-3}\ s^{-1}$]
$\dot{\omega}_{\lambda_e}$	collision frequency between eddy and bubble [$m^{-4}\ s^{-1}$]

Subscripts

1	image 1
2	image 2
2*D*	two-dimensional
3*D*	three-dimensional
a	bubble a
ab	colliding bubble pair
aftercollision	after collision
B	bubble
b	bubble b
cell	cell
g	gas
f	phase f
$\hbar$	time step
i	cell i in x-direction
i	bubbles in group i
in	inlet
j	bubbles in group j
j	cell j in y-direction
k	bubbles in group k
k	bubble number in sample
l	liquid
ℓ	edge
m	marker
masscentre	centre of mass
min	minimum
p	projected
q	bubble number in cell
rel	relative
s	superficial
slip	slip velocity
x	x-direction
y	y-direction

Dimensionless numbers

Eo	Eötvös number
M	Morton number
Re	Reynolds number
We	Weber number

Bibliography

Angelidou, C., Psimopoulos, M., Jameson, G.J., 1979, Size distribution functions of dispersions, *Chem. Eng. Sci.*, **34**, 671-676

Auton, T.R., 1983, *The dynamics of bubbles, drops and particles in motion in liquids*, Ph. D. Thesis, University of Cambridge, Cambridge, United Kingdom

Auton T.R., 1987, The lift force on a spherical body in a rotational flow, *J. Fluid Mech.*, **183**, 199-218

Batchelor, G.K., 1982, *The theory of homogeneous turbulence*, Cambridge Univ. Press, Cambridge, England

Becker, S., Sokolichin, A., Eigenberger, G., 1994, Gas-liquid flow in bubble columns and loop reactors: Part II. comparison of detailed experiments and flow simulations, *Chem. Eng. Sci.*, **49**, 5747-5762

Brackbill, J.U., Kothe, B., Zemach, C., 1992, A continuum method for modeling surface tension, *J. Comp. Physics*, **100**, 335-354

Braida, L., 1956, M.Sc Thesis, University of Toronto

Bröder, D. and Sommerfeld, M., 2002, Visual study of bubble-bubble interaction with a high-speed camera, 10th Workshop on two-phase flow predictions, Merseburg, Germany

Bunner, B. and Tryggvason, G., 1997, Simulations of Large Bubble Systems, ASME Fluids Engineering Division Summer Meeting, Vancouver, Canada

Centrella, J. and Wilson, J.R., 1984, Planar numerical cosmology. II. The difference equations and numerical tests, *Astrophys. J. Suppl. Ser.*, **54**, 229-249

CFX user manual, AEA Technology, United Kingdom

Chesters, A.K. and Hofman, G., 1982, Bubble coalescence in pure liquids, *Appl. Sci. Res.*, **38**, 352-361

Chesters, A.K., 1991, The modelling of coalescence processes in fluid-liquid dispersions: a review of current understanding, *Trans. IChemE*, **69**, 259-270

Clift, R., Grace, J.R., Weber, M.E., 1978, *Bubbles, drops and particles*, Academic Press, New York

Coulaloglou, C.A. and Tavlarides, L.L., 1977, Description of interaction processes in agitated liquid-liquid dispersions, *Chem. Eng. Sci.*, **32**, 1289-1297

Darmana, D., Deen, N.G., Kuipers, J.A.M., 2004 , Detailed Modeling of Hydrodynamics, Mass transfer and Chemical Reactions in a Bubble Column using a Discrete Bubble Model, in preparation

Deckwer, W.-D., 1992, *Bubble column reactors*, John Wiley & Sons Ltd, Chicester, England

Deen, N.G., 2001, *An experimental and computational study of fluid dynamics in gas-liquid chemical reactors*, Ph.D. Thesis, Aalborg University, Esbjerg, Denmark

Deen, N.G., Solberg, T., Hjertager, B.H., 2001, Large eddy simulation of the gas-liquid flow in a square cross-sectioned bubble column, *Chem. Eng. Sci.*, **56**, 6341-6350

Deen, N.G., van Sint Annaland, M., Kuipers, J.A.M., 2004, Multi-scale modeling of dispersed gas-liquid two-phase flow, submitted to *Chem. Eng. Sci*.

Delnoij, E., Lammers, F.A., Kuipers, J.A.M., Van Swaaij, W.P.M., 1997, Dynamic simulation of dispersed gas-liquid two-phase flow using a discrete bubble model, *Chem. Eng. Sci.*, **52**, 1429-1458

Delnoij, E., 1999, *Fluid dynamics of gas-liquid bubble columns. A theoretical and experimental study*, Ph.D. Thesis, University of Twente, Enschede, The Netherlands

Devanathan, N., Dudukovic, M.P., Lapin, A., Lübbert, A., 1995, Chaotic flow in bubble column reactors, *Chem. Eng. Sci.*, **50**, 2661-2668

Goldschmidt, M.J.V., 2001, *Hydrodynamic modelling of fluidised bed spray granulation*, Ph.D. Thesis, University of Twente, Enschede, The Netherlands

Grace, J.R., 1973, Shapes and velocities of bubbles rising in infinite liquids *Trans. IChemE*, **51**, 116-120

Grace, J.R., Wairegi, T., Nguyen, T.H., 1976, Shapes and velocities of single drops and bubbles moving freely through immiscible liquids, *Trans. IChemE*, **54**, 167-173

Ginzburg, I., Wittum, G., 2001, Two-phase flows on interface refined grids modeled with VOF, staggerd finite volumes, and spline interpolants, *J. Comp. Phys.*, **166**, 302-335

Hawley, J.F., Smarr, L.L., Wilson, J.R., 1984, A numerical study of nonspherical black hole accretion. II. Finite differencing and code calibration, *Astrophys. J. Suppl. Ser.*, **55**, 211-246

Hesketh, R.P., Etchells, A.W., Russell, T.W.F., 1991a, Experimental observations of bubble breakage in turbulent flow, *Ind. Eng. Chem. Res.*, **30**, 845

Hirt, C.W. and Nichols, B.D., 1981, Volume of Fluid (VOF) method for the dynamics of free boundaries, *J. Comp. Phys.*, **39**, 201-225

Hoomans, B.P.B., Kuipers, J.A.M., Briels, W.J., van Swaaij, W.P.M., 1996, Discrete particle simulation of bubble and slug formation in a two dimensional gas-fluidised bed: a hard sphere approach, *Chem. Eng. Sci.*, **51**, 99-118

Ida, M., 2000, An improved unified solver for compressible and incompressible fluids involving free surfaces. Part I. Convection**,** *Comp. Phys. Comm.,* **132***,* 44-65

Ida, M., 2003, An improved unified solver for compressible and incompressible fluids involving free surfaces. II. Multi-time-step integration and applications, *Comp. Phys. Comm.*, **150**, 300-322

Ihme, F., Schmidt-Traub, H., Brauer, H., 1972, *Chemie-Ing.-Techn.*, **44**, 306

Ishii, M. and Zuber, N., 1979, Drag coefficient and relative velocity in bubbly, droplet or particulate flows, *AIChE J*, **25**, 843-855

Jakobsen, H.A., Sannæs, B.H., Grevskott, S., Svendsen, H.F., 1997, Modeling of vertical bubble-driven flows, *Ind. Eng. Chem. Res.*, **36**, 4052-4074

Kirkpatrick, R.D. and Lockett, M.J., 1974, The influence of approach velocity on bubble coalescence, *Chem. Eng. Sci.*, **29**, 2363-2373

Kluytmans, J.H.J., 2003, *An airlift loop redox cycle reactor for alcohol oxidations: Hydrodynamics, mass transfer and reactor design*, Ph.D. Thesis, Technical University of Eindhoven, The Netherlands

Kothe, D.B., Mjolsness, R.C., Torrey, M.D., 1991*, RIPPLE: a computer program for incompressible flows with free surfaces*, Los Alamos National Laboratory, Report LA-12007-MS

Kothe, D.B. and Rider, W.J., 1995a*, Comments on modeling interfacial flows with volume-of-fluid methods*, Technical Report LA-UR-3384, Los Alamos National Laboratory

Kothe, D.B. and Rider, W.J., 1995b, Practical considerations for interface tracking methods, *6th ISCFD*

Kuboi, R., Komasawa, I., Otake, T., 1972a, Behavior of dispersed particles in turbulent liquid flow, *J. Chem. Eng. Japan*, **5**, 349

Kuboi, R., Komasawa, I., Otake, T., 1972b, Collision and coalescence of dispersed drops in turbulent liquid flow, *J. Chem. Eng. Japan*, **5**, 423

Kuipers J.A.M., van Duin, K.J., van Beckum, F.P.H., van Swaaij, W.P.M., 1993, Computer simulation of the hydrodynamics of two-dimensional gas-fluidized bed, *Computers Chem. Eng.*, **17**, 839-858

Kuipers, J.A.M. and van Swaaij, W.P.M., 1997, Computational fluid dynamics applied to chemical reaction engineering, *Rev. Chem. Eng.*, **13**, 3

Kumar, S., Kumar, R., Gandhi, K.S., 1993, A new model for coalescence efficiency of drops in stirred dispersion, *Chem. Eng. Sci.*, **48**, 2025-2038

Lafaurie, B., Nardone, C., Scardovelli, R., Zaleski, S., Zanetti, G., 1994, Modelling merging and fragmentation in multiphase flows with SURFER, *J. Comput. Phys.*, **113**, 134-147

Lage, P.L.C. and Espósito, R.O., 1999, Experimental determination of bubble size distribution in bubble columns: prediction of mean bubble diameter and gas hold up, *Powder Tech.*, **101**, 142-150

Laín, S., Bröder, D., Sommerfeld, M., 2001, Numerical simulations of the hydrodynamics in a bubble column: quantitative comparisons with experiments. In *Fourth Int. Conf. on Multiphase Flow*, *ICMF-2001*, New Orleans, USA

Lapin, A., Lübbert, A., 1994, Numerical simulation of the dynamics of two-phase gas-liquid flows in bubble columns, *Chem. Eng. Sci.*, **49**, 3661-3674

Lee, C.-H., Erickson, L.E., Glasgow, L.A., 1987, Bubble breakup and coalescence in turbulent gas-liquid dispersion, *Chem. Eng. Comm.*, **59**, 65-84

Lehr, F. and Mewes, D., 2000, A transport equation for the interfacial area density applied to bubble column, *16th International Symposium on Chemical Engineering*, Cracow, Poland

Levich, V.G., 1962, *Physicochemical hydrodynamics*, Prentice Hall, Englewood Cliff, NJ

Li, D., 1994, Coalescence between two small bubbles or drops, *J. Coll. Interf. Sci.*, **163**, 108-119

Lo, S.M., 1996, *Application of the MUSIG model to bubbly flows*, AEAT-1096, AEA Technology, United Kingdom

Luo, H. and Svendsen, H.F., 1996, Theoretical model for drop and bubble breakup in turbulent dispersions, *AIChE J*, **42**, 1225-1233

Machon, V., Pacek, A.W., Nienow, A.W., 1997, Bubble size in electrolyte and alcohol solution in a turbulent stirred vessel, *Trans. IChemE*, **75**, 339-348

Mason, P.J. and Callen, N.S., 1986, On the magnitude of the subgrid-scale eddy coefficient in large-eddy simulations of turbulent channel flow, *J. Fluid Mech.*, **162**, 439-462

Menzel, T., 1990, *Die Reynolds-schubspannung als wesentlicher parameter zur modellierung der strömungsstruktur in blasensäulen und airliftschlaufreaktoren*, Ph.D. Thesis, VDI Verlag, Düsseldorf

Mudde, R.F. and Simonin, O., 1999, Two- and three-dimensional simulations of a bubble plume using a two-fluid model, *Chem. Eng. Sci.*, **54**, 5061-5069

Nambiar, D.K.R., Kumar, R., Das, T.R., Gandhi, K.S., 1992, A new model for the breakage frequency of drops in turbulent stirred dispersions, *Chem. Eng. Sci.*, **34**, 2989-3002

Narsimhan, G., Gupta, J.P., Rankrishna, D., 1979, A model for transitional breakage probability of droplets in agitated lean liquid-liquid dispersions, *Chem. Eng. Sci.*, **34**, 257-265

Noh, W.F., Woodwart, P.R., 1976, SLIC (simple line interface calculation method), In: *Lecture note in physics*, A.I. van de Voren en P.J. Zandbergen (Eds.), 330

Odar, F. and Hamilton, W.S., 1964, Forces on a sphere accelerating in a viscous liquid, *J. Fluid Mech.*, **18**, 302-314

Pacek, A.W., Moore, I.P.T., Nienow, A.W., 1994, Video technique for measuring dynamics of liquid-liquid dispersions during phase inversion, *AIChE J.*, **40**, 1940-1949

Patankar, S.V., 1980, *Numerical heat transfer and fluid flow*, Taylor & Francis

Peskin, C.S., 1977, Numerical analysis of blood flow in the heart, *J. Comp. Phys.*, **25**, 220-251

Pfleger, D., Gomes, S., Gilbert, N., Wagner, H., 1999, Hydrodynamic simulations of laboratory scale bubble columns fundamental studies of the Eulerian-Eulerian modelling approach, *Chem. Eng. Sci.*, **52**, 4473-4484

Pilliod Jr, J.E., 1992, *An analysis of piecewise linear interface reconstruction algorithms for volume-of-fluid methods*, Master's Thesis, University of California at Davis

Prince, M.J. and Blanch, H.W., 1990, Bubble coalescence and break-up in air-sparged bubble columns, *AIChE J.*, **36**, 1485-1499

Prosperetti, A., 2001, Navier-Stokes numerical algorithms for free-surface flow computations: An overview, Proceedings of the CISM Course on *Drop-Surface Interactions*

Rider, W.J. and Kothe, D.B., 1995, *Stretching and tearing interface tracking methods*, Los Alamos National Laboratory

Rider, W.J., Kothe, D.B., Jay Mosso, J., Cerutti, J.H., Hochstein, J.I., 1995*, Accurate solution algorithms for incompressible multiphase flows*, Technical Report AIAA 95-0699, AIAA

Ross, S.L., and Curl, 1973, Measurement and models of dispersed phase mixing process, *Joint Chem. Eng. Conf.*, paper 29b, Vancouver

Ruckenstein, E. and Jain, R.K., 1974, Spontaneous rupture of thin liquid films, *J. Chem. Soc. Faraday II*, **70**, 132-147

Rudman, M., 1997, Volume-tracking methods for interfacial flow calculations, *Int. J. Num. Methods in Fluids*, **24**, 671-691

Rudman, M., 1998, A volume-tracking method for incompressible multifluid flows with large density variations, *Int. J. Num. Methods in Fluids*, **28**, 357-378

Saffman, P.G. and Turner, J.S., 1956, On the collision of drops in turbulent clouds, *J. Fluid Mech.*, **1**, 16

Sagert, N.H. and Quinn, M.J., 1976, The coalescence of H_2S and CO_2 bubbles in water, *Can. J. Chem. Eng.*, **54**, 392-398

Sankaranarayanan, K., Shan, X., Kevrekidis, I., Sundaresan, S., 1999, Bubble flow simulations with the lattice Boltzmann method, *Chem. Eng. Sci.*, **54**, 4817-4823

Sankaranarayanan, K., Shan, X., Kevrekidis, I., Sundaresan, S., 2002, Analysis of drag and virtual mass forces in bubbly suspensions using an implicit formulation of the lattice Boltzmann method, *J. Fluid Mech.*, **452**, 61-96

Sato, Y. and Sekoguchi, K., 1975, Liquid velocity distribution in two-phase bubble flow, *Int. J. Multiphase Flow*, **2**, 79-95

Scardovelli, R. and Zaleski, S., 1999, Direct numerical simulation of free-surface and interfacial flow, *Annu. Rev. Fluid Mech.*, **31**, 567-603

Schiller, L. and Nauman, A., 1933, *VDI Zeits.*, **77**, 318

Shahbazi, K., Paraschivoiu, M., Mostaghimi, J., 2003, Second order accurate volume tracking based on remapping for triangular meshes, *J. Comp. Phys.*, **188**, 100-122

van Sint Annaland, M., Deen N.G., Kuipers, J.A.M., 2003, Multi-Level Modelling of Dispersed Gas-Liquid Two-Phase Flows, *Series: Heat and Mass Transfer*, eds. M. Sommerfeld, Springer-Verlag, 139-157

Smagorinksy, J., 1963, General circulation experiments with the primitive equations, *Mon. Weather, Rev.*, **91**, 99-165

Sokolichin, A. and Eigenberger, G., 1994, Gas-liquid flow in bubble columns and loop reactors: Part I. Detailed modelling and numerical simulation, *Chem. Eng. Sci.*, **49**, 5735-5746

Sokolichin, A., Eigenberger, G., Lapin, A., Lübbert, A., 1997, Dynamic numerical simulation of gas-liquid two-phase flows. Euler/Euler versus Euler/Lagrange, *Chem. Eng. Sci.*, **52**, 611-626

Sokolichin, A. and Eigenberger, G., 1999, Applicability of the standard k-ε turbulence model to the dynamic simulation of bubble columns: Part i. Detailed numerical simulations, *Chem. Eng. Sci.*, **54**, 2273-2284

Sovová, H., 1981, Breakage and coalescence of drops in a batch stirred vessel - II Comparison of models and experiments, *Chem. Eng. Sci.*, **36**, 1567-1573

Sussman, M., Puckett, E.G., 2000, A coupled level set and volume-of-fluid method for computing 3D and axisymmetric incompressible two-phase flow, *J. Comp. Phys.*, **161**, 301-337

Sussman, M., 2003, A second order coupled level set and volume-of-fluid method for computing growth and collapse of vapor bubbles, *J. Comp. Phys.*, **187**, 110-136

Tennekes, H. and Lumley, J.L., 1972, *A first course in turbulence*, The MIT Press, Cambridge, MA

Tomiyama, A., Zun, I., Sou, A., Sakaguchi, T., 1993, Numerical analysis of bubble motion with the VOF method, *Nucl. Eng. Des.*, **141**, 69-82

Tomiyama, A., Zun, I., Higaki, H., Makino, Y., Sakaguchi, T., 1997, A three-dimensional particle tracking method for bubbly flow simulation, *Nucl. Eng. Des.*, **175**, 77-86

Tomiyama, A., 1998, Struggle with computational bubble dynamics, *Third International Conference on Multiphase Flow, ICMF'98*, Lyon, France

Trapp, J.A. and Mortensen, G.A., 1993, A discrete particle model for bubble slug two phase flow, *J. Comp. Physics*, **107**, 367-377

Tryggvason, G., 2001, *Embedded interface methods applications*, Short course "Modelling and computation of multiphase flows, Part IIB. Multiphase-Flow CFD", Swiss Federal Institute of Technology (ETH), Zurich, Switzerland

Tryggvason, G., Bunner, B., Esmaeeli, A., Juric, D., Al-Rawahi, N., Tauber, W., Han, J., Nas, S., Jan, Y.-J., 2001, A front-tracking method for the computations of multiphase flow, *J. Comp. Phys.*, **169**, 708-759

Unverdi, S.O., Tryggvason, G., 1992, A front-tracking method for viscous, incompressible, multi-fluid flows, *J. Comput. Phys.*, **100**, 25-37

Walter, J.F. and Blanch, H.W., 1986, Bubble break-up in gas-liquid bioreactors: Break-up in turbulent flows, *Chem. Eng. J.*, **32**, B7-B17

Westerweel, J., 1997, Fundamentals of digital particle image velocimetry, *Meas. Sci. Tech.*, **8**, 1379-1392

Westerweel, J., Dabiri, D., Gharib, M., 1997, The effect of a discrete window offset on the accuracy of cross-correlation analysis of digital PIV recording, *Exp. in Fluids*, **23**, 20-28

Youngs, D.L., 1982, Time-dependent multi-material flow with large fluid distortion, *Numerical Methods for Fluid Dynamics*, in K.W. Morton and M.J. Baines (eds), New York, 273-285

Zaleski, S., 2001, *Multiphase-flow CFD with Volume of Fluid (VOF) methods*, Short course "Modelling and computation of multiphase flows, Part IIB. Multiphase-Flow CFD", Swiss Federal Institute of Technology (ETH), Zurich, Switzerland

Dankwoord

En dan ben ik nu aangekomen bij bijna het laatste, maar zeker niet het minst belangrijke onderdeel van dit proefschrift: Het Dankwoord. Ik denk dat deze bladzijden de meest gelezen zullen zijn van dit proefschrift en daarom zal ik ook bij deze laatste pagina's nog even mijn uiterste best doen.
Ik wil alle mensen, die een bijdrage hebben geleverd aan de totstandkoming van dit werk, heel hartelijk bedanken. En daarbij hoop ik niemand te vergeten.

Als eerste wil ik mijn promotor, Hans Kuipers, bedanken voor de mogelijkheid een promotieproject in zijn groep uit te voeren. Door deze mogelijkheid is mijn belangstelling voor onderzoek aangewakkerd en ik ben nog steeds blij dat ik de keuze heb gemaakt om te gaan promoveren. De kennis van Hans op CFD-gebied heeft een grote bijdrage geleverd aan het slagen van dit project. Ook wil ik mijn assistent-promotor Niels Deen bedanken voor zijn inbreng en begeleiding tijdens de laatste twee jaren van mijn promotie. Ik heb veel geleerd van zijn kennis op het gebied van gas-vloeistofstroming en zijn kritische blik op de resultaten is dit proefschrift zeer ten goede gekomen. Niels, ik heb het altijd leuk gevonden met je samen te werken. Daarnaast wil ik Martin van Sint Annaland bedanken voor zijn inzet en begeleiding tijdens de eerste twee jaren van mijn promotie. Zijn nieuwe ideeën bij het oplossen van problemen zijn van groot belang geweest voor het vervolg van het project.

Ik wil Akzo Nobel bedanken voor de financiële ondersteuning van dit promotie-onderzoek. Mijn dank gaat daarbij uit naar Erik Delnoij, voor zijn interesse en kritische blik tijdens de eerste twee jaren van mijn promotie en naar Mathijs Goldschmidt, voor zijn bijdrage en ondersteuning tijdens de laatste twee jaren.

Twee afstudeerders hebben een belangrijke bijdrage geleverd aan onderwerpen in dit proefschrift. Rutger Lempens heeft in het VOF model gekeken naar de krachten, die op bellen werken. Vanwege een groot aantal numerieke problemen was dit een zeer lastige opgave. Het is niet makkelijk om twee maanden lang te staren naar een belletje dat niet wil opstijgen. Rutger, bedankt voor je inzet. Hans Noorlag wil ik bedanken voor zijn grote bijdrage aan de resultaten van het DBM. Hij heeft met zijn kritische blik een groot deel van de problemen met de botsingen van bellen in dit model opgelost. Hans, ik hoop dat je niet al te veel nachtmerries hebt gehad van het tellen van bellen en hun botsingen.

Verder wil ik Wouter Tromp bedanken voor zijn bedrage aan de PIV metingen tijdens zijn opdracht voor Practicum Proceskunde. Er zijn mooie resultaten uitgekomen, die ik helaas niet in dit proefschrift kon verwerken.

Vervolgens wil ik al mijn collega's bij FAP en OOIP bedanken, die mij op vele manieren hebben geholpen bj mijn project. Michiel, bedankt voor je vele hulp bij het werken met Unix en het verbeteren van het VOF model en het DBM. Door je kennis over gas-vloeistofsystemen was het goed om met jou hierover te discussiëren. Ik vond het prettig om samen met jou als 'bellen-mens' te werken tussen alle 'ballen-mensen'. Dadan, also your support as new 'bubble-person' in the group during the last year of my promotion was very welcome. Thanks to your help with the DBM the last problems were solved. It was very pleasant to work with you and good luck with your research. Verder wil ik Albert en Jeroen heel erg bedanken voor al hun hulp en steun bij alle grote en kleine, belangrijke en minder belangrijke vragen. Ik ben blij dat ik altijd jullie kantoor binnen kon lopen voor al mijn vragen. Of het nu ging over Unix, Windows, bellen of ballen, jullie probeerden mij altijd te helpen. I would like to thank Dhaneshwar (Dani) for his support with CFX. It was very pleasant to have you as a roommate during the four years of this project. Daarnaast wil ik Toine bedanken voor alle hulp en discussies over gas-vloeistofsystemen. Toine, ook jouw kantoor kon ik altijd binnenlopen voor allerlei vragen. Jammer dat we de ultrasone techniek niet verder konden gebruiken in de bellenkolom. Duco wil ik bedanken voor zijn korte samenwerking bij het testen van de ultrasone techniek in de platte kolom. Duco, het was erg gezellig om met jou samen te werken.

De experimentele resultaten waren nooit tot stand gekomen zonder het bekwame werk van de technici, Gerrit Schorfhaar, Wim Leppink, Benno Knaken en Henk-Jan Moed. Gerrit, ik wil je heel hartelijk bedanken voor de mooie bellenkolom die je hebt gemaakt. Het was erg plezierig om daarbij met jou samen te werken. Wim, jouw ideeën hebben mijn geholpen om de puntjes op de i te zetten. Benno wil bedanken voor zijn hulp bij de ultrasone techniek en voor het lijmen van de kolom. Henk-Jan bedank ik voor alle kleine tussendoortjes. En Robert Meijer wil ik bedanken voor zijn electo-technische en computerondersteuning. Dankzij jullie hulp zijn mijn opstelling en ik tv-beroemdheden geworden.

Ook wil ik de secretaresses hartelijk danken: Brigitte Sanderink, Ria Hofs-Winkelman en Nicole Haitjema. Zij hebben op de achtergrond veel ondersteuning gegeven en hadden ook altijd tijd voor een informeel en belangstellend praatje.
Martin van Sint Annland verzorgde de afhandeling van de financiën. Bedankt.

Ik heb een bijzonder goede tijd gehad bij de Vlugtheuvel. Ik heb vele goede herinneringen aan alle borrels, het vakgroepvolleybal, het zeilen, skiën, wadlopen, karten, bowlen en andere activiteiten. Hiervoor wil ik alle collega's, studenten, Twaio's en andere medewerkers die de afgelopen vier jaar bij de Vlugtheuvel hebben rondgelopen heel hartelijk bedanken. Zonder jullie aanwezigheid was mijn promotietijd toch een stuk minder leuk en enerverend geweest.

Verder wil ik hierbij ook mijn paranimfen Petra en Ylva bedanken. Ik vind het als promovenda erg leuk om twee vrouwelijke paranimfen te hebben. Petra, heel erg bedankt voor de steun en belangstelling de afgelopen jaren. Ik kon altijd mijn verhaal bij jou kwijt, via mail of telefoon.
Ylva, ook jij heel erg bedankt voor alle steun en belangstelling, ook al begreep je er misschien soms niet veel van. Hoewel de afstand groot was (Maastricht-Enschede of Zweden-Enschede), leek de afstand veel kleiner door contact via computer en telefoon.

En dan een speciaal woord van dank voor mijn ouders. Ook al konden jullie je volgens mij geen voorstelling maken waar ik nu precies mee bezig was, ik heb altijd heel veel steun aan jullie gehad. Ik kon altijd mijn verhaal bij jullie kwijt en jullie belangstelling was geweldig. Ik ben erg blij dat jullie mij vier jaar geleden hebben geholpen bij de keuze om te gaan promoveren, want dit is een goede keuze geweest.

En als laatste wil ik Sven bedanken. Door jouw aanwezigheid tijdens de laatste periode van mijn promotie en in de periode daarna ben je een hele grote steun. Sven, jij hebt altijd een luisterend oor en een goed advies, waar ik op kan bouwen en op terug kan vallen. Uiteraard wil ik je ook nog even extra bedanken voor het maken van de omslag van het proefschrift. En we gaan vast en zeker een erg goede toekomst tegemoet met z'n tweeën.

Allemaal ontzettend bedankt!

Levensloop

Esther van den Hengel werd geboren op 26 mei 1976 in Langeveen, waar zij ook de lagere school bezocht. Van 1989 tot 1994 bezocht zij het Pius X College te Almelo, waar zij in 1994 haar VWO diploma behaalde.

In september 1994 begon zij met de studie Chemische Technologie aan de Universiteit Twente in Enschede. In het kader van deze opleiding liep zij van augustus tot november 1998 stage bij Schering AG in Berlijn, Duitsland. In augustus 1999 studeerde zij af bij de vakgroep Ontwikkeling en Ontwerp van Industriële Processen (OOIP) op het onderwerp “Oxidatieve dehydrogenering van propaan”.

In oktober 1999 trad zij in dienst bij de werkeenheid Fundamentele Aspecten van de Proceskunde (FAP) om als promovendus (AIO) een promotieonderzoek te verrichten op het gebied van gas-vloeistof twee-fasenstroming. De resultaten van dit onderzoek vormen de basis voor dit proefschrift.

In januari 2004 trad zij in dienst bij TNO Prins Mauritslaboratorium in Rijswijk.